Populations of low mass X-ray binaries in the galaxies Centaurus A and Andromeda

Rasmus Voss

München 2007

Populations of low mass X-ray binaries in the galaxies Centaurus A and Andromeda

DISSERTATION

der Fakultät für Physik der Ludwigs-Maximilians-Universität München
zur Erlangung des Grades
Doktor der Naturwissenschaften
Dr. rer. nat.

vorgelegt von

Rasmus Voss
von
Kopenhagen, Dänemark

München, den 5 März 2007

1. Supervisor: Prof. Dr. Rashid Sunyeav
2. Supervisor: Dr. Marat Gilfanov

Examination committee:

1st referee:	Prof. Dr. Rashid Sunyeav
2nd referee:	Prof. Dr. Thomas Gehren
Head of committee:	Prof. Dr. Martin Fässler
	Prof. Dr. Dorothee Schaile

Day of oral examination: May 4th, 2007

Summary

The subject of this dissertation is the observational and theoretical study of the populations of low mass X-ray binaries in external galaxies.

The goal of the observational part is to study the luminosity function and spatial distribution of low mass X-ray binaries to the faintest possible limit, and in different types of galaxies. It is based on the analysis of a large number of archival observations from the *Chandra* X-ray observatory. We select an elliptical galaxy, Centaurus A, and a spiral galaxy, Andromeda. Both are the nearest galaxy of their type, massive enough to contain a significant number of low mass X-ray binaries. After correction for the incompleteness effects we constrain the low mass X-ray binary luminosity function in Centaurus A down to $L_x \sim 2 \times 10^{36}$ erg s^{-1}, 5-10 times lower than in previous studies of elliptical galaxies. For Andromeda we study the luminosity function down to $L_x \sim 10^{35}$ erg s^{-1}. For both galaxies we show that the luminosity function of low mass X-ray binaries flattens below $\log(L_x) \sim 37.5$ to the $dN/dL \propto L^{-1}$ law in agreement with the behaviour found earlier in the Milky Way and nearby galaxies. With the exception of the central part of the Andromeda galaxy the spatial distribution of the low mass X-ray binaries is consistent with the distribution of stellar mass as traced by the K-band light observed in the 2MASS survey. We find, however, that in Andromeda the specific frequency, per unit stellar mass, of X-ray point sources increases dramatically in the inner $\sim$ 1 arcmin (corresponding to $\sim$ 200 pc) of the galaxy. The distribution of the surplus sources follows ρ_*^2 profile, in contrast to the $\propto \rho_*$ profile observed outside the central arcmin and in Centaurus A. This suggests that the sources are formed through dynamical interactions in the high stellar density environment of the inner bulge. This is the first evidence of dynamical formation of low mass X-ray binaries near the centre of a galaxy, similar to the processes known to take place in globular clusters. This interpretation is further supported by the fact that the luminosity function of surplus sources near the center of M31 is similar to that of globular cluster sources, with a clear lack of faint sources, below $\sim 10^{36}$ erg s^{-1}. This is different from the L^{-1} luminosity distribution of field sources, presumably primordial low mass X-ray binaries, indicating a different origin.

Motivated by the observational results, in the theoretical part of this dissertation, we investigate dynamical formation of low mass X-ray binaries, paying particular attention to the high stellar velocity regime characteristic for galactic bulges, which has not been previously explored. We carry out a detailed population synthesis using both analytical calculations and Monte Carlo simulations. Our calculations suggest that the majority of the surplus sources are formed in tidal captures of black holes

by main sequence stars of low mass, $M_* \lesssim 0.4 M_\odot$, with some contribution of neutron star systems of the same type. Due to the small size of the accretion discs, a fraction of such systems may be persistent X-ray sources. Some of the sources may be ultra-compact X-ray binaries with helium star/white dwarf companions. We also predict a large number of faint transients, both neutron star and black hole systems, within ~ 1 arcmin from the Andromeda galactic centre. Finally, we consider the population of dynamically formed binaries in Galactic globular clusters, emphasizing the differences between the low mass X-ray binary formation processes in these compared to the formation processes in the central parts of galaxies.

Acknowledgements

First I would like to thank my neurologist for making me sleep better.

The last years working on this dissertation have been hard for me in many ways, and I would like to thank all the persons, who have helped me get through this time. Without your love, friendship, support and help I might not have held through to the end.

I would like to thank my parents, Erling and Kirsten. From a distance you have always shown interest in my situation, and spent much time and effort to help me through problems or at least offer moral support. You have even tried to understand what I am working on! I also thank my brother Jeppe, who has brought me great comfort over the years, his wife Cathrine, and their two wonderful children, Christoffer and Filippa.

My closest friends here in Munich have been Cecilia, Marco and Paola. All three of you have done more for me than what can be expected from friends. Even if you have had plenty of problems of your own, you have helped me through some very dark periods. In some of those periods I have neglected our friendship, but you stood by me anyway. I have enjoyed every moment we spent together.

I lot of other friends deserves thanks also. Especially Dimitrios, Jens, Gert, Carlos, Jorge, Patricia, Karina, Anja, Josefa, Dani and my two flatmates, Nico and Sigurd. I thank you for your friendship, interesting discussions, fun parties and plenty of good times spent together. Also thanks to the rest of my friends, who I will not mention out of fear of forgetting someone.

I thank Rashid Sunyaev for giving me the opportunity to work in his group at MPA, and Marat Gilfanov for spending so much time and effort on your careful supervision of my projects. Aside from my supervisors, I would like to thank Dimitrios, Gert and Jens for general discussions about our work, and Yu-Ying and Aurora for discussions about X-ray analysis.

Finally I would like to thank Stefania for making me sleep better.

Contents

1 Introduction

A low mass X-ray binary (LMXB) consists of a compact object, either a neutron star (NS) or a black hole (BH), and a donor star of low mass $\lesssim 1 M_{\odot}$. The compact object accretes matter from its companion, and in the accretion process X-ray emission is produced, hence the name. Despite most stars being in multiple systems, LMXBs are rare objects due to the very special evolution necessary for a binary to reach this state. LMXBs are exciting objects, as they offer unique insights on a broad range of astrophysical processes. Some of these are the production and structure of compact objects, emission of gravitational waves, mass transfer, accretion disks, jets and production of high energy emission. Over the past decades the study of LMXBs has therefore received massive attention. Especially the strong evolution of the capabilities of X-ray telescopes has contributed to the momentum of the research.

X-ray binaries (either LMXBs or high mass X-ray binaries (HMXBs) that have more massive companions stars, $\gtrsim 8 M_{\odot}$) are among the brightest objects in the sky at $\sim$ few keV energies, and they were detected by the first X-ray missions launched to space (Giacconi et al., 1962). Since then they have been studied extensively through a number of satellite missions, including *UHURU*, *ARIEL V*, *Ginga*, *EXOSAT*, *ROSAT* and *RXTE*. With these missions it was possible to greatly enhance the understanding of the X-ray binary population in the Milky Way ($\sim$ 300 sources). Having determined the source positions with the X-ray telescopes, it also became possible to study the sources in other wavelengths, thereby learning about the companion stars and the accretion disks. This way it was learned that $\sim$ 150 of the Galactic X-ray sources are LMXBs, and that 13 of these reside in globular clusters.
Studies of X-ray binaries outside the Milky Way were impossible due to the limited sensitivity and/or spatial resolution of the telescopes. The sources in the Milky Way are spread over the sky, and with most instruments it is therefore only possible to observe one source at a time. Moreover, the distances to the sources, as well as incom-

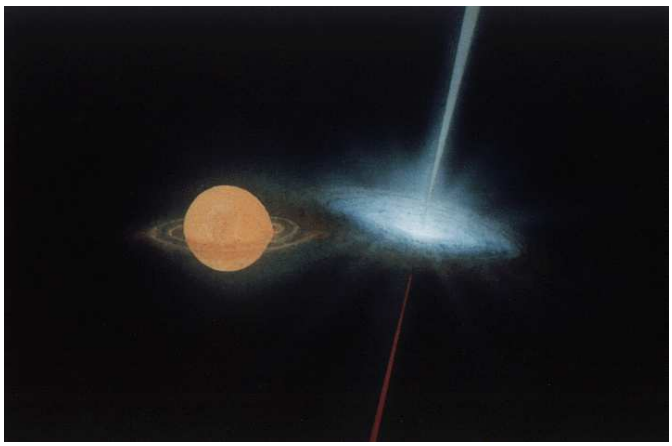

Figure 1.1: Artists impression of an LMXB. Credit: NASA

pleteness effects, are difficult to estimate. Furthermore, the evolution of LMXBs is complicated, leading to a wide range of LMXB types, with different properties, which makes any accurate theoretical modeling difficult. However, with the advent of *Chandra* and *XMM-Newton* the situation changed dramatically, as it became possible to uniformly observe large numbers of LMXBs in external galaxies (Fabbiano, 2006).

In this introduction we first present a quick overview of LMXBs (section 1.1). We focus on the processes governing the formation and evolution of the systems. In the second part of the introduction (section 1.2), we present an overview of the observational results obtained from X-ray studies of LMXBs in external galaxies. In the end of the introduction we give an overview of the work laying the ground for this dissertation.

1.1 Low mass X-ray binaries

An LMXB contains a star of low mass, $\lesssim 1 M_{\odot}$, in orbit with a BH or an NS. As mass is transferred from the companion star to the compact object, it is accreted and X-rays are emitted. For mass to be transferred, the companion star has to fill its Roche-lobe, as the wind from a low mass star is not enough to power the X-ray sources. The mass transfer can be sustained in two ways, either by the expansion of the low mass star as it evolves off the main sequence, or by the loss of orbital angular momentum due to gravitational radiation and magnetic braking. We begin this section with a description of the basic concepts of close binary evolution involved. This is followed by an overview of the evolution of LMXBs. The possible formation scenarios are discussed in the end, as a basic knowlegde of LMXB evolution is needed in order to understand these, and because LMXB formation is currently the least understood part of the evolution.

1.1.1 The Roche-lobe

In a binary system the two stars are affected by each others gravity. The shape of the stars follow the equipotential surfaces of the rotating binary, see figure 1.2. As one moves away from the stellar centres the surfaces become more and more pearshaped, until the point where the two surfaces touch one another, in the so-called first Lagrangian point L_1. At this point the gravity of the two stars cancel. The equipotential surface touching this point is called the Roche-lobe (RL) of the stars. If the size of a star is large enough for the star to fill its RL, matter will flow through L_1 and be caught by the gravity of the companion star. This is known as RL-overflow. The radius R_* of a star exactly filling its RL can be found from (Eggleton, 1983)

$$\frac{R_*}{a} = \frac{0.49}{0.6 + q^{2/3}\ln(1 + q^{-1/3})}, \tag{1.1}$$

where a is the orbital separation of the binary and $q = M_a/M_d$ is the mass ratio of the two stars (M_d being the mass of the donor and M_a the mass of the accretor). While this equation is valid over the entire range of mass ratios, an alternative and simpler equation is sufficiently accurate for LMXBs, where $M_d < M_a$ (Paczynski, 1971):

$$\left(\frac{R_*}{a}\right)^3 = (0.46)^3 \frac{M_d}{M_d + M_a}. \tag{1.2}$$

1.1.2 Accretion by compact objects

When mass is transferred through L_1 into the potential well of the compact object, it settles into a disk. This was first studied by Shakura & Sunyaev (1973), who described a geometrically thin, optically thick disk of gas, in which viscosity transports angular momentum outwards, thereby allowing matter to be accreted by the central compact object. The energy released during this process is emitted from the surface of the disk. The disk temperature follows $T \sim R^{-3/4}$ in a stationary viscously heated disk and $T \sim R^{-1/2}$ in an illuminated disk. Therefore X-rays are predominantly emitted from the inner regions. This general picture is still valid, while the theory has advanced significantly. For a comprehensive overview of accretion disks, see Frank et al. (2002).

For systems with relatively large mass transfer rates, the accretion disk is stable, and the sources will be persistent in X-ray emission. If the accretion is below a certain threshold, the disk will be unstable, and the source will be transient, only being luminous in X-rays in intervals, separated by long periods of quiescence. This is due to a thermal-viscous instability that appears at a temperature where hydrogen becomes partially ionized. Only for very high accretion rates can the temperature be kept above this value out to the outer edge of the disk. However, for NS and BH accretors, X-ray irradiation can heat the disk enough for the limiting accretion rate to

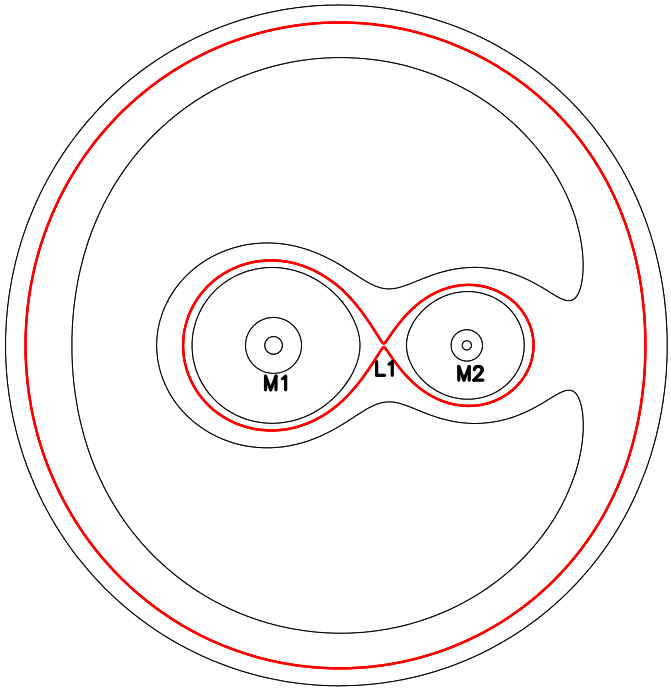

Figure 1.2: The equipotential lines in a binary with two stars with $M_1 = 2M_2$, in a circular orbit. The inner red line indicates the RLs of the two stars.

be significantly lower (van Paradijs & McClintock, 1995; Dubus et al., 1999). In our work, the instability criterion of Dubus et al. (1999) was used. This is given by

$$\dot{M}_{crit}^{irr} \simeq 3.2 \cdot 10^{-8} \left(\frac{M_a}{M_\odot}\right)^{0.5} \left(\frac{M_d}{M_\odot}\right)^{-0.2} P_{hr}^{1.4} \cdot \left(\frac{C}{5 \cdot 10^{-4}}\right)^{-0.5} M_\odot/yr \qquad (1.3)$$

Where C is given the "typical value" of $5 \cdot 10^{-4}$. It is obvious that there is a strong dependence on the orbital period P_{hr} (in hours) due to the fact that larger disks have lower temperatures, and outer edges that are further from the irradiation source (the vicinity of the compact object).

For very high accretion rates the accretion is limited by the radiation pressure produced by the infalling matter. If this pressure is stronger than the gravitational attraction of the compact object, the material is dispersed rather than accreted. For spherically symmetric emission, the limiting luminosity (called the Eddington luminosity) is given by

$$L_{Edd} = \frac{4\pi G M m_e c}{\sigma_T} \qquad (1.4)$$

where G is the gravitational constant, M is the mass of the accreting object, m_e is the mass per electron of the accreting gas, c is the speed of light and σ_T is the Thomson cross-section. For a 1.4 $M_\odot$ NS and accreting hydrogen rich matter the Eddington

luminosity is $\sim 2 \cdot 10^{38}$ erg s^{-1}.

The reaction of the orbit to the mass transfer can be found from the conservation of angular momentum. Assuming a circular orbit, the angular momentum of a binary is given by

$$J_{orb} = \frac{M_d M_a \Omega a^2}{M_d + M_a}, \tag{1.5}$$

where Ω is the orbital angular velocity, $\Omega = \sqrt{G(M_d + M_a)/a^3}$. Differentiating this, one finds

$$\frac{\dot{a}}{a} = 2\frac{\dot{J}_{orb}}{J_{orb}} - 2\frac{\dot{M}_d}{M_d} - 2\frac{\dot{M}_a}{M_a} + \frac{\dot{M}_d + \dot{M}_a}{M_d + M_a}. \tag{1.6}$$

From this equation it is evident that in the absence of mass and angular momentum loss from the binary, the orbital separation increases as response to the mass transfer if $M_d < M_a$ (as is the case in LMXBs). To sustain mass transfer, it is therefore necessary that either angular momentum is lost from the binary, or that the donor star increases its size. To estimate the mass transfer rate in the absence of changes in the radius of the donor star, we assume conservative mass transfer, meaning that all mass lost by the donor star is accreted by the compact object, ($\dot{M}_p = -\dot{M}_s$), and substitute the logarithmic derivative of equation 1.2 into equation 1.6. From this we get

$$\frac{\dot{R}_*}{R_*} = 2\frac{\dot{J}_{orb}}{J_{orb}} - 2\left(1 - \frac{M_d}{M_a}\right)\frac{\dot{M}_d}{M_d} + \frac{1}{3}\frac{\dot{M}_d}{M_d}. \tag{1.7}$$

Approximating the mass-radius relationship of the donor star as $R_d \propto M_d^n$,[1] gives

$$\dot{R}_d/R_d = n\dot{M}_d/M_d. \tag{1.8}$$

The mass transfer rate can be found from

$$\frac{\dot{J}_{orb}}{J_{orb}} = \left(\frac{5}{6} + \frac{n}{2} - \frac{M_d}{M_a}\right)\frac{\dot{M}_d}{M_d} \equiv D\frac{\dot{M}_d}{M_d}. \tag{1.9}$$

If $D > 0$ mass transfer is stable, otherwise it is unstable.

1.1.3 Expansion of the donor star

A star on the main sequence (MS) burns hydrogen to helium in the centre. When a star has exhausted the hydrogen in the centre, the star quickly begins to expand drastically; it becomes a red giant. If the star is in a binary, the expansion can at some point cause the star to fill its RL (depending on the orbital separation), and mass will be transferred to the companion star. Unless the original orbit is so tight that the mass transfer commences before any significant expansion of the star has occured, the orbit will be so wide that the mechanisms of angular momentum loss described above are believed to be insignificant. The mass transfer is therefore solely driven by the further

[1] For stars of $\sim M_\odot$ in thermal equilibrium, the radius is approximately proportional to the mass, and therefore $n \sim 1$

expansion of the star, as nuclear burning proceeds. As long as $\dot{R}_d > 0$ mass transfer is on. As soon as $\dot{R}_d < 0$ it turns off on a timescale $\tau \sim \frac{H}{R_d} \cdot \mid \frac{R_d}{\dot{R}_d} \mid$, where H is the pressure scale height. The lifetime of an LMXB with a red giant donor is comparable to the time remaining on the red giant branch at the onset of mass transfer, typically < 100 Myr. Due to the relatively wide orbits, the accretion disks are large, and from equation 1.3 it is evident that all such systems are transient.

1.1.4 Angular momentum loss

Neglecting the possible effects of mass loss from the LMXBs there are two effects that can decrease the angular momentum of a binary[2]: Gravitational radiation and magnetic braking.

Gravitational radiation was predicted by Einstein shortly after he formulated his general theory of relativity (Einstein, 1916, 1918). The quadrupole moment of a system of moving masses causes the emission of gravitational waves (Landau & Lifshitz, 1950). For a system of two pointmasses in a gravitationally bound circular orbit[3], the change in angular momentum J_{orb} due to the gravitational radiation can be described by (Peters, 1964)

$$\frac{\dot{J}_{GR}}{J_{orb}} = -\frac{32}{5}\frac{G^3}{c^5}\frac{M_d M_a (M_d + M_a)}{a^4}, \tag{1.10}$$

where c is the speed of light and G is the gravitational constant.

Magnetic braking is believed to take place when the donor star is a main sequence star with a convective envelope ($0.4 - 1.5 M_\odot$). Such stars emit stellar winds and out to a distance $\gtrsim$few stellar radii, the winds are forced to co-rotate with the stars, due to the magnetic fields. It is generally believed that the winds thereby carry away enough angular momentum to slow the spin of the stars, while the mass loss rate is negligible. In a close binary tidal forces keep the stars in co-rotation, and the angular momentum lost from one of the stars is therefore taken from the orbital angular momentum of the system.

Various formulations of the theory exist and the strength of the process is still a subject of debate (see e.g. Ivanova & Taam, 2003). In this work we use the formulation of Rappaport et al. (1983), in which the angular momentum loss $\dot{J}_{MB}$ is given by

$$\frac{\dot{J}_{MB}}{J_{orb}} = -1.84 \cdot 10^{-8}\mathrm{s}\left(\frac{M_a + M_d}{M_a}\right)\left(\frac{R_d}{R_\odot}\right)^4 \omega^2 \left(\frac{R_\odot}{a}\right)^2, \tag{1.11}$$

where R_d is the radius of the donor star, ω is the angular velocity of the binary orbit. This is a variation of the magnetic braking law of Verbunt & Zwaan (1981) assuming that the donor star has a thin convective envelope.

[2] We ignore here the fact that encounters with other stellar objects can strongly influence the binary orbits. This is discussed in chapter 4.

[3] Due to tidal interactions, virtually all binaries close enough for mass exchange to take place are circular. The equations for the evolution of eccentric orbits can be found in Peters (1964).

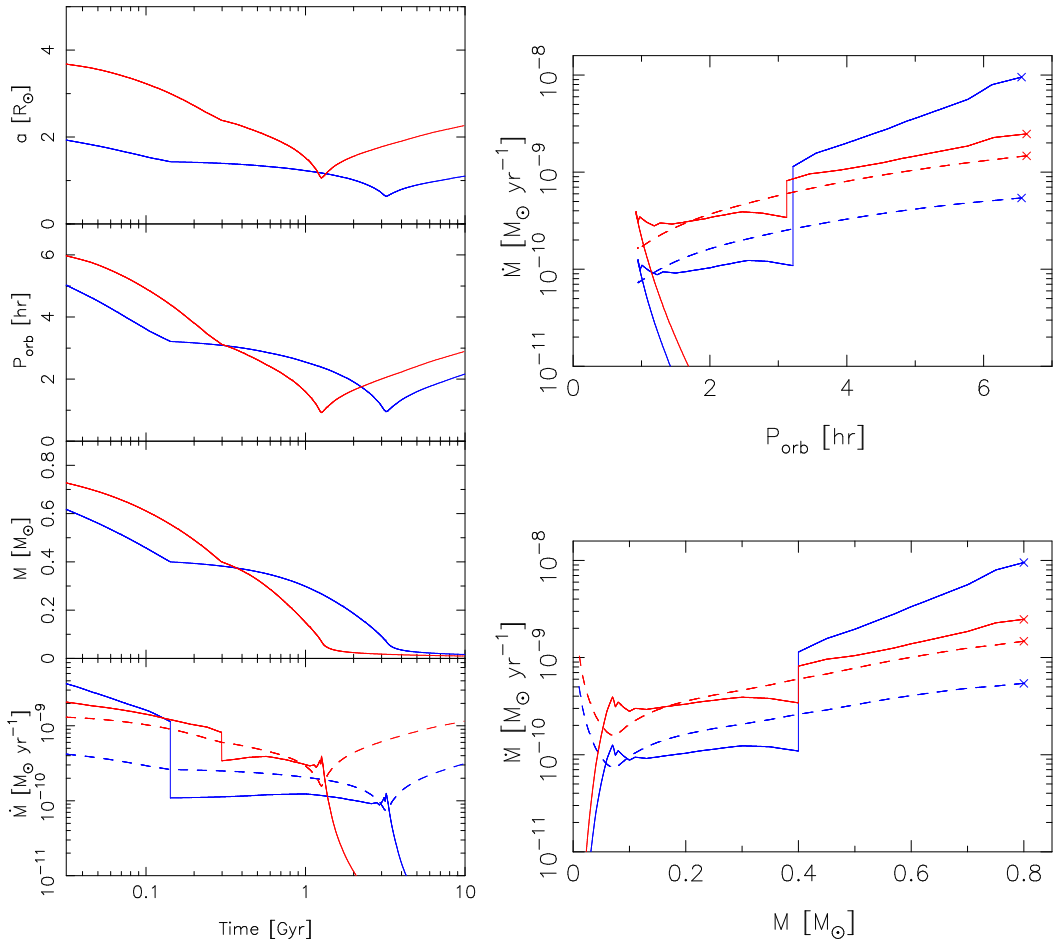

Figure 1.3: The evolution of an LMXB initially consisting of a 0.8 $M_\odot$ star and either an 1.4 $M_\odot$ NS (blue lines) or a 10 $M_\odot$ BH (red lines). Mass transfer is assumed to be conservative, i.e. all matter lost by the donor star is accreted by the compact object. On the left is shown the evolution of four parameters with time. These are the orbital separation a, the orbital period P_{orb}, the mass of the donor star M and the mass transfer rate $\dot{M}$. On the right is shown the mass transfer rate as a function of the orbital period of the LMXB (top) and as a function of the mass of the donor star (bottom). In both plots, $t = 0$ is marked by crosses. In the three plots showing the mass transfer rate, also the critical rate for disk stability (below which LMXBs are transient) according to equation 1.3 is shown (dashed lines).

1.1.5 Evolution of LMXBs with main sequence donors

Together with the mass-radius relationship of MS stars, it is now possible to use the equations above to follow the evolution of MS-LMXBs from the initial Roche-lobe contact. In this approach it is being neglected that the stars are out of thermal equilibrium, which for high mass transfer rates can cause significant deviations from the given mass-radius relationship. In figure 1.3 we show the evolution of a typical LMXB initially consisting of a $0.8M_\odot$ MS star and either an NS or a 10 $M_\odot$ BH,

using the mass-radius relationship of Baraffe et al. (2003, 1998). The mass transfer is assumed to be conservative. At the end of the evolution, the mass of the NS is therefore 2.2 $M_\odot$ and that of the black hole 10.8$M_\odot$. To begin with, the LMXB is mainly driven by magnetic braking. For NS accretors, the mass transfer rate is high, only slightly sub-Eddington, and such LMXBs are therefore bright persistent sources, whereas the mass transfer rate for BHs is lower, close to the critical rate. In fact all the observed LMXBs with BH accretors are transient. As the mass of the donor star decreases, the orbital period decreases, and so does the mass transfer rate. After a few 100 Myr[4] the donor star reaches $\sim 0.4M_\odot$[5], and magnetic braking ceases to be effective. During the evolution, the donor star has been pushed out of thermal equilibrium by the mass loss, and as an effect of this, the radius is increased[6]. As angular momentum is now lost by gravitational radiation alone, the mass transfer rate drops significantly. As the star regains thermal equilibrium, the radius of the star decreases, and RL overflow ceases, until gravitational radiation has decreased the orbit enough for the star to fill its RL again. This might give rise to a "period gap", in which the LMXB is not emitting X-rays, around an orbital period of 3 hr. While this period gap is clearly seen for cataclysmic variables, it is highly debated whether it exists for LMXBs. The observed period distribution of LMXBs does not show a statistically significant period gap. When RL overflow occurs again the mass transfer rate is so low, that also the LMXBs with NS accretors become transient. Over the following 1-3 Gyr the donor star loses most of its mass. Around a mass of $0.1M_\odot$ there may be a stage at which the LMXB might become persistent again, for $\sim$ 300 Myr. Also around this mass, hydrogen burning ceases and the donor star becomes a brown dwarf. With further mass loss, the radius of the brown dwarf increases $R_d \sim M_d^{-1/3}$, and the mass transfer rate drops significantly below the transiency threshold.

1.1.6 Ultra-compact X-ray binaries

LMXBs can also have white dwarf (WD) donors. Such LMXBs are called ultra-compact X-ray binaries (UCXBs). Due to the small radii of WDs, RL-overflow can only occur if the orbital separation is very small, that is at orbital periods of a few minutes. For the more compact of such systems, gravitational radiation is strong, causing highly super-Eddington accretion rates. Due to the inverse mass-radius relationship of degenerate stars, the radius (and with it the orbital separation) increases in response to the mass transfer. Quickly the WD mass is reduced from the original mass (between 0.1 and $\sim 1.3M_\odot$) to $\sim 0.06M_\odot$ at an orbital period of $\sim$ 10 minutes. During the following $\sim$ 100 Myr, the orbital period increases to $\sim$ 1 hour, while the X-ray luminosity drops from $\sim 10^{38}$ erg s^{-1} to $\sim 10^{36}$ erg s^{-1}. Further expansion leads to mass transfer rates below the transiency threshold. For a thorough investigation of UCXB evolution, see Deloye & Bildsten (2003); Bildsten & Deloye (2004).

[4] As noted above the strength of magnetic braking is currently subject of debate, and the lifetime of this stage is strongly dependent on this.

[5] This value of this limit depends on the evolutionary state of the star and on how far the star is from thermal equilibrium.

[6] In the evolution depicted in figure 1.3, equilibrium stellar models were used, and this effect is therefore not included.

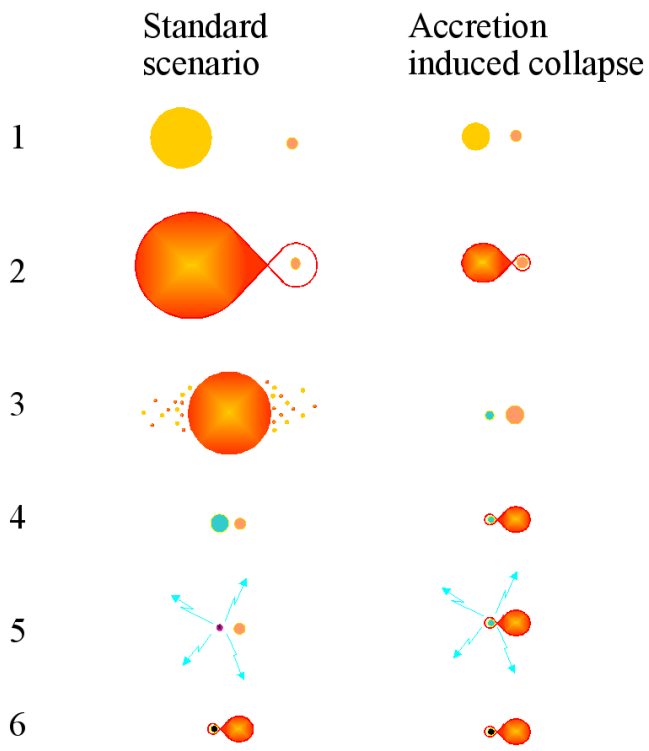

Figure 1.4: Examples of the two LMXB formation channels in the field of a galaxy. For the standard scenario, the stages are: (1) A binary consisting of a massive star, $> 8M_{\odot}$, and a low mass star, $< 1M_{\odot}$. (2) The massive star evolves to fill its RL and mass transfer commenses. (3) The low mass star spirals in through the envelope of the massive star, and the envelope is expelled. (4) A binary consisting of a helium star (the core of the massive star) and the low mass star is created. (5) The helium star explodes as a supernova. (6) The low mass star fills its RL and transfers mass to the NS born in the supernova explosion. For the accretion induced collapse scenario, the stages are: (1) A binary consisting of a star with a mass of $\sim 2M_{\odot}$, and a star of slightly lower mass, $\sim 1.5M_{\odot}$. (2) The more massive star evolves to fill its RL and transfers mass to the less massive star through stable mass transfer. (3) A binary consisting of a white dwarf (the core of the donor star) and the secondary star. (4) Due to orbital decay the secondary star fills its RL and transfers mass to the white dwarf. (5) The accretion causes the white dwarf to exceed the Chandrasekhar mass and it explodes as a supernova. (6) The secondary star transfers mass to the NS born in the supernova explosion.

1.1.7 Formation of LMXBs

There are several ways of forming LMXBs, and the relative contributions of the various paths is a subject of debate. In the field of a galaxy there are two ways to produce LMXBs (see e.g. van den Heuvel, 1992):

1. The standard scenario for the formation of LMXBs (depicted in the left part of

figure 1.1.7) starts with a binary consisting of a massive star ($M \gtrsim 8M_\odot$) and a star of low mass ($M \lesssim 8M_\odot$) in a relatively wide orbit. The evolutionary timescale of the massive star is much shorter than that of the low mass star, and it evolves off the MS rapidly increasing its radius. As it fills its Roche-lobe, mass transfer begins. As $M_d > M_a$ the mass transfer causes a decrease of the orbital separation (see equation 1.6) which further increases the mass transfer. This leads to a run-away process, in which the less massive star spirals in through the envelope of the giant star, in what is called common envelope (CE) evolution (Paczynski, 1976; Ostriker, 1976). During the spiral in, energy and angular momentum is transferred to the envelope and if the energy is sufficient to expel the envelope, this results in a binary consisting of a helium (HE) star and the low mass star in a tight orbit. After a short time the HE-star explodes as a supernova (type Ib/c). The formation of an LMXB depends on the final orbit of the two stars, which is governed by two processes: (i) The ejection of a large amount of mass from the system, with the specific angular momentum of the former donor star as it undergoes a type Ib/c supernova explosion, causes the orbit to become eccentric or even disrupts of the binary. (ii) It is known that asymmetries in the supernova explosions gives the newborn NS a "kick" velocity of the order of 100 km s^{-1}. The effect of the kicks depends on the direction and the strength of it. In general they enhance the probability of the disruption of a binary, but in some cases they can lead to tightly bound binaries.

2. Another possibility is the accretion induced collapse scenario (depicted in the right part of figure 1.1.7), which starts with a binary consisting of two stars, each with a mass below $\sim$ few $M_\odot$. The more massive star exhausts hydrogen in the centre and turns off the MS, mass transfer is initiated, and if $q \gtrsim 0.4$, the mass transfer is dynamically stable (Bhattacharya & van den Heuvel, 1991). In this process, the donor star loses all its entire hydrogen envelope leaving only the core, a WD. This way a WD-MS binary is born. A second mass transfer event, now from the MS star to the WD, can bring the WD mass above the Chandrasekhar mass[7], causing it to collapse into an NS in a supernova explosion. For a ONeMg WD this leads to the formation of an NS in a type II supernova explosion.

For the NS (or BH)-MS star binaries created, the subsequent evolution depends on the orbital separation. If it is small, magnetic braking can bring the MS star into contact, thereby creating an MS LMXB. Otherwise, Roche-lobe contact will be reached when the star evolves to the red giant branch (RGB), in which case a short-lived and transient RGB LMXB is formed, see above. For a small range of orbital periods, mass transfer begins approximately at the time when the MS star evolves off the MS. As the cores of such stars is depleted of hydrogen and consists mainly of degenerate helium, they are compact enough for the binaries to evolve to periods of $\sim$ 10 minutes,

[7] Above this mass, the pressure from a degenerate electron gas is not high enough to support the WD.

becoming UCXBs (however, without the initial super-Eddington mass transfer rate described in section 1.1.6). For a 1 $M_\odot$ star the initial period range is $\sim 13 - 18$ hr (Podsiadlowski et al., 2002; van der Sluys et al., 2005).

Both scenarios above require rather specific circumstances to be fulfilled in order to create LMXBs. The standard scenario, especially the evolution in the common envelope, requires finetuning of the parameters, and also the distribution of supernova kicks is problematic. For the accretion induced collapse model, the problem is that the accretion on the WD causes the ignition of hydrogen flashes, and for most accretion rates, more material is lost in these flashes, than is accreted.

Both of the above formation scenarios involve primordial binaries, and are independent of the environment around the binary. They can therefore be formed anywhere in galaxies, and it has been shown by Gilfanov (2004) that the specific frequency per stellar mass in nearby galaxies is $\sim$ constant. In the following we call such binaries "primordial LMXBs".
In contrast to these there exists a population of "dynamically formed LMXBs", the formation of which relies on stellar interactions in very densely populated regions, such as globular clusters (GCs) or the central parts of galaxies. Their existence was first realized based on the fact that the ratio of the number of X-ray binaries to stellar mass is $\sim$ two orders of magnitude higher in GCs than in the Galactic disk (Clark, 1975). The three most important formation channels are:

1. The tidal capture of a neutron star (NS) by a single star on the MS. A close passage of the two stars induces oscillations in the MS star, and the energy for this is taken from the orbital energy. If the energy of the oscillations exceeds the originally positive orbital energy, the stars are captured in a bound orbit (Fabian et al., 1975).

2. The collision between an NS and an evolved single star on the subgiant or red giant branch (RGB) or the asymptotic giant branch (AGB) can lead to the formation of an X-ray binary, in which the donor star is a white/brown dwarf or a helium star, depending on the evolutionary stage of the evolved star before the collision (Ivanova et al., 2005). In the case of a white dwarf donor an ultra compact X-ray binary is formed. In this scenario, orbital energy is transferred to the envelope of the evolved star, which is expelled, leaving the NS and the core of the evolved star in a bound orbit (Verbunt, 1987).

3. In an exchange reaction, an NS exchanges place with a star in a pre-existing binary during a close binary-single encounter (Hills, 1976).

The dynamical formation of LMXBs is investigated in detail in chapter 4.

1.2 X-ray observations of LMXBs in galaxies

Having reviewed the basic processes governing the formation and evolution of LMXBs, we now turn the attention to the observations of LMXBs in galaxies. This section is

Figure 1.5: Artists impression of *Chandra*. Credit: *Chandra* X-ray center.

not intended to be a complete review of the observations of LMXBs (for a comprehensive review, see Lewin & van der Klis (2006), and for a discussion of extra-Galactic sources, see Fabbiano (2006)). Instead the purpose is to present an overview of the recent developments that motivate the studies presented in this dissertation.

While the *Einstein Observatory* gave the first detection of X-ray sources in other galaxies, and *ROSAT* and *ASCA* expanded the knowledge, it was first with *Chandra* and *XMM-Newton* that it became possible to study in detail the properties of the X-ray point sources in nearby galaxies. *XMM-Newton* has a large collecting area, combined with good energy resolution, making it very useful for studies of the nearest galaxies. While *Chandra* is inferior in these respects, it has much better angular resolution, $\sim$ 0.5 arcsec on the axis, and it is therefore possible to study X-ray binaries in galaxies as distant as 30 Mpc. The advent of these telescopes has therefore greatly increased the knowlegde of the populations of LMXBs in galaxies, and has sparked new life in discussions about the formation and evolution of LMXBs. Two of the most important observable distributions are the luminosity function and the spatial distribution of the observed sources. Due to the distance of most of the galaxies, most observations of extra-Galactic LMXBs are limited by the photon statistics, inhibiting spectral fitting. Instead it is necessary to rely on more simple tools, such as photometric diagrams.

1.2.1 The LMXB-stellar mass relation

The fraction of double stars that develop into primordial LMXBs is believed to be relatively independent of the stellar environment, albeit with some sensitivity to the metallicity (the fraction of mass in atoms heavier than helium), the initial mass function (the distribution of stellar masses for newborn stars) and the star formation history of the population. In the absence of significant differences in the binary fraction, the number of primordial LMXBs therefore only depends on the stellar mass. This is in contrast to HMXBs, the number of which is mainly related to the star formation rate (SFR), as they are very young objects. This is a useful way to distinguish between the two types of objects, in the absence of good quality spectra or optical counterparts, which is mostly the case for sources in external galaxies. In general old stellar envi-

ronments like the bulges of spiral galaxies as well as elliptical galaxies (and globular clusters) have little star formation, and the majority of the sources in the $10^{35} - 10^{39}$ erg s^{-1} luminosity range are therefore LMXBs. Based on these considerations, it was predicted that LMXBs should be present in early type galaxies (Fabbiano, 1989), but only with the *Chandra* observation of NGC4697 was such a population confirmed (Sarazin et al., 2000). Further studies of individual early type galaxies quickly confirmed the conclusions (e.g. Blanton et al., 2001; Kraft et al., 2001). Similarly, studies of the bulge of the nearby spiral galaxy Andromeda (M31), confirmed the presence of a large number of LMXBs there (Garcia et al., 2000; Shirey et al., 2001).

Gilfanov (2004) studied the populations of LMXBs in a sample of nearby galaxies of various morphological type with *Chandra*, comparing the spatial distribution and number of sources with the mass distribution, as indicated by K-band observations. The study concluded that the spatial distribution of LMXBs does indeed follow the mass distribution, and that the number of LMXBs with $L_x > 10^{37}$ erg s^{-1} is ~ 14 LMXBs per $10^{10} M_{\odot}$.
In regions where there might be a mixture of LMXBs and other types of sources, it is therefore possible to separate the contributions statistically, by studying the differences between the distribution of X-ray sources and the distribution of K-band light.

1.2.2 The X-ray background

Outside the nearby galaxies, the X-ray sky is relatively uniform. In recent years the majority of this Cosmic X-ray background (CXB) (at ~ 1 keV)[8] has been resolved into discrete sources (mainly AGNs) by deep *Chandra* and *XMM-Newton* surveys (e.g. Mushotzky et al., 2000; Hasinger et al., 2001; Giacconi et al., 2002; Alexander et al., 2003). While the spectral properties of some of the CXB sources can be used to distinguish them from X-ray binaries, this is not possible for the majority of them (especially due to the low photon counts of many of the sources). The normalization of the background is low enough, that it does not compromise studies of the most luminous sources, or when only considering sources within the central regions of galaxies. For studies of the faint sources in galaxies, or for studies that include sources further away from the centre of a galaxy, it is necessary to take the CXB sources into account. Due to the difficulties of distinguishing the type of individual sources, this is best done statistically, using the fact that the spatial distribution of the CXB sources is flat (at least for the angular scales relevant for studies of single galaxies), while the spatial distribution of LMXBs follows the distribution of mass in the galaxy. This method was used in the studies presented in the following chapters of this dissertation.

1.2.3 Sources in globular clusters

It is a well known fact that the ratio of the number of LMXBs to stellar mass is $\sim$ two orders of magnitude higher in GCs than in the Galactic disk (Clark, 1975). This is due to the fact that in GCs, LMXBs can be dynamically formed (see section

[8] At 10 keV the resolved fraction of the background is $\sim 60\%$.

1.1.7). In recent years it has been realized that in galaxies with old stellar populations, a large fraction, 20-70%, of all the LMXBs resides in GCs (e.g. Sarazin et al., 2000; Kundu et al., 2002; Jordán et al., 2004; Kim, E. et al., 2006; Sivakoff et al., 2006), and that it is ~ 3 times more probable to find an LMXB in a red (metal-rich) GC than in a blue (metal-poor) GC, in accordance with what was previously observed in the Milky Way (Grindlay, 1993; Bellazzini et al., 1995). Due to the high fraction of LMXBs residing in GCs, together with the problems concerning the formation channels of primordial LMXBs (see section 1.1.7), it has been suggested that all LMXBs were originally formed in GCs (White et al., 2002). The LMXBs observed in the field would then either have escaped the GCs, or the GCs would have been tidally disrupted by gravitational interactions with the host galaxy. While this issue is not resolved, observations relating the specific frequency of GCs in galaxies to the fraction of LMXBs formed in GCs indicate that the majority of the field LMXBs are indeed primordial (Juett, 2005). Also the fact that the spatial distribution of primordial LMXBs is consistent with the spatial distribution of mass in galaxies (Gilfanov, 2004) is difficult to explain if all sources were formed in GCs.
It is important to take the spatial distribution of the LMXBs in GCs into account, when comparing with the stellar mass in galaxies, due to the differences in the distributions.

1.2.4 The luminosity function of LMXBs

An effective astrophysical tool for studying the populations of objects, for which few physical parameters are observable, is the luminosity function (LF). While it is simple to observe the LF of a sample of objects, the comparison with theoretical models can provide useful constraints on the physical processes working in the objects.
Grimm et al. (2002) performed a study of the LFs of X-ray binaries in the Milky Way using data from *RXTE ASM*. They showed that whereas the LF of HMXBs is well approximated by a single powerlaw, the LF of LMXBs steepens towards higher fluxes. In the subsequent study of Gilfanov (2004), in which also LMXBs from nearby galaxies were included, it was found that the LF of LMXBs was adequately modelled by powerlaws with different slopes in three luminosity regimes, -1 below $L_x \sim 1.9{\cdot}10^{37}$ erg s^{-1}, -1.86 above this luminosity and a sharp cut-off at $L_x \gtrsim 5 \cdot 10^{38}$ erg s^{-1}.

However, the statistical significance of the bright-end break was not very high, and from a thorough study of the bright end of the luminosity function in 14 early type galaxies, Kim & Fabbiano (2004) concluded that the LMXB LF ($>$few$\times 10^{37}$ erg s^{-1}) is consistent with a single powerlaw[9] with a slope of 2.1. The issue of a bright-end break is still unresolved. The universality of the break at the faint end is also controversial. As there are many more LMXBs around this luminosity than at the bright end of the LF, the break has been unambiguously observed in old stellar populations in nearby galaxies (see e.g. Kong et al., 2003; Gilfanov, 2004). However, the break luminosity is below the detection limit for almost all massive early type galaxies (except for Centaurus A, see chapter 2). Based on long-exposure observations of the two elliptical galaxies NGC 3379 and NGC 4278, it has recently been claimed that there is no break

[9] A broken powerlaw with a break at $5.0 \cdot 10^{38}$ erg s^{-1} improves the fit, but is not statistically necessary.

at this luminosity in elliptical galaxies[10] (Kim, D.-W. et al., 2006).

According to Postnov & Kuranov (2005), for a population of LMXBs with MS donors a differential powerlaw slope of -1 below $\sim 10^{37}$ erg s^{-1} can be obtained if the mass transfer is driven by gravitational radiation alone, whereas the steeper slope above this luminosity can be explained by mass transfer driven by magnetic braking. In UCXBs, the donors are WDs, and the mass transfer is driven by gravitational radiation alone. For these systems models have been succesful in explaining the bright end of the LF (Bildsten & Deloye, 2004), but no modeling of the LF at lower luminosities has been reported so far.

1.3 Motivation and outline

This dissertation consists of 3 separate studies, intended for publication in the journals `Astronomy & Astrophysics` and `Monthly Notices of the Royal Astronomical Society`. The focus is on the overall properties of the populations of LMXBs in external galaxies with old stellar populations (elliptical galaxies and the bulges of spiral galaxies). The main objectives of the studies are to increase the knowledge of the LFs (especially the faint end) and spatial distribution of LMXBs in different galaxies, and to investigate the dynamical formation of LMXBs in various environments.

As it has been contested that the shape of the LMXB LF follows the shape given in Gilfanov (2004) in elliptical galaxies (see section 1.2.4) it was important to perform a detailed investigation of the faint end of the LF in an elliptical galaxy. Unfortunately all regular elliptical galaxies massive enough to contain the needed number of LMXBs are so distant, that with moderate observation time the faintest observable point sources have $L_x \sim 10^{37}$ erg s^{-1} (similar to the luminosity of the contested break in the LF). Instead we chose to study the relatively close (3.5 Mpc) elliptical galaxy Cen A, in which it is possible to observe sources to $L_x \sim 10^{36}$ erg s^{-1}. While this is not a "clean" elliptical galaxy[11], the population of LMXBs is not expected to be much different from the population in more regular ellipticals. To constrain the LF to the lowest possible luminosity, we developed methods to correct for incompleteness effects and for the contamination by CXB sources, utilizing the spatial distribution of the two kinds of sources. This observational study, published in `Astronomy & Astrophysics` (Voss & Gilfanov, 2006), is presented in chapter 2.

The bulge of the nearest spiral galaxy, M31, hosts a large number of LMXBs (Gilfanov, 2004; Kong et al., 2003; Kaaret, 2002; Pietsch et al., 2005). At a distance of 780 kpc (Stanek & Garnavich, 1998; Macri, 2001), the source population can be studied to a limiting luminosity of $\sim 10^{35}$ erg s^{-1}. At the same time this distance is far enough, that a large fraction of the bulge can be covered in a single *Chandra*

[10] Actually they conclude that there is no break at the somewhat higher luminosity $5.0 \cdot 10^{37}$ erg s^{-1}. In this investigation, the completeness limits are 10^{37} and $3 \cdot 10^{37}$ erg s^{-1} for NGC 3379 and NGC 4278, respectively.

[11] In the inner part of Cen A there is an extended disk of dust, as well as evidence of star formation. Furthermore a jet extends from the nucleus, and buoyant bubbles of gas have been observed.

observation. M31 is therefore ideal for a deep study of the properties of the LMXB populations, to further constrain the LF of LMXBs in spiral galaxies, to search for differences between the primordial LMXBs and the dynamically formed ones and to study how precisely the spatial distribution follows the mass distribution. A large number of X-ray studies were previously performed, both with *Chandra* (e.g. Gilfanov, 2004; Kong et al., 2003; Kaaret, 2002) and with *XMM-Newton* (e.g. Pietsch et al., 2005; Trudolyubov & Priedhorsky, 2004). However since then, the number of observations has increased significantly, making it possible to combine many observations to get long exposure time. Furthermore previous studies did not account for the effects of the CXB sources, which is significant for large parts of the bulge. We therefore used the methods developed for the study of Cen A, to perform a deep study of the X-ray point sources in the bulge of M31. This observational study, submitted for publication in `Astronomy & Astrophysics` (Voss & Gilfanov, 2007a), is presented in chapter 3.

In the study of M31, we found that there is a clear overdensity of sources with $L_x > 10^{36}$ erg s^{-1} within 1 arcmin of the centre of M31. We investigated different explanations for this overdensity and came to the conclusion that it was due to dynamical formation of LMXBs in the high-density bulge environment, similar to the processes responsible for the formation of LMXBs in globular clusters. The theory of the different paths of dynamical interactions has been investigated for globular clusters (e.g. Bellazzini et al., 1995; Ivanova et al., 2005). However there is currently no real population synthesis with clear predictions regarding the number of sources produced. We therefore performed a study, comparing the effectiveness of the three main channels of LMXB formation, making use of the existing theories, and used the results to calculate predictions for the Galactic GCs. As there were previously no observational studies suggesting that dynamical interactions are important in the central parts of galaxies, the theories had not been extended to this kind of environment. In the inner bulge of M31, the density is lower than in the centre of massive GCs, and the velocity dispersion is almost an order of magnitude higher, $\sigma_{1D} \sim 150$ km s^{-1} (McElroy, 1983; Widrow et al., 2003). This causes the rate of dynamical interactions per unit mass to be much lower. On the other hand, the mass of the inner bulge of M31 is so large $\sim 10^{10} M_\odot$ that a considerable number of LMXBs can still be formed this way. Furthermore there is no mass segregation, and whereas a large fraction of NSs and most likely almost all BHs escape GCs, they remain in the bulge. Therefore the ratios of NSs and BHs to normal stars are very different there. We therefore performed an extensive study of the dynamical formation of LMXBs in the high stellar velocity dispersion environment of galactic bulges, and used this to calculate predictions for the bulge of M31. This theoretical study, submitted to `Monthly Notices of the Royal Astronomical Society` (Voss & Gilfanov, 2007b), is presented in chapter 4.

In the final chapter (chapter 5) we summarize the main conclusions of the studies presented in the preceding chapters.

Bibliography

Alexander, D.M., Bauer, F.E., Brandt, W.N., et al., 2003, AJ, 126, 539

Baraffe I., Chabrier G., Barman T. S., Allard F., Hauschildt P. H., 2003, A&A, 402, 701

Baraffe I., Chabrier G., Allard F., Hauschildt P. H., 1998, A&A, 337, 403

Bellazzini M., Pasquali A., Federici L., Ferraro F. R., Fusi Pecci F., 1995, ApJ, 439, 687

Bhattacharya, D., van den Heuvel, E.P.J., 1991, Phys. Reports, 203, 1

Bildsten L., Deloye C. J., 2004, ApJ, 607, L119

Blanton, E.L., Sarazin, C.L., Irwin, J.A., 2001, ApJ, 552, 106

Clark G. W., 1975, ApJ, 199, L143

Deloye C. J., Bildsten L. 2003, ApJ, 598, 1217

Dubus, G., Lasota, J.-P., Hameury J.-M., Charles, P. 1999, MNRAS, 303, 139

Eggleton, P.P., 1983, ApJ, 268, 368

Einstein, A. 1916, Sb. Preuss. Akad. Wiss. 688

Einstein, A. 1918, Sb. Preuss. Akad. Wiss. 154

Fabian A. C., Pringle J. E., Rees M. J., 1975, MNRAS, 172, 15

Fabbiano, G., 1989, ARA&A, 27, 87

Fabbiano, G., 2006, ARA&A, 44, 323

Frank, J., King, A., Raine, D., 2002, Accretion power in astrophysics (Cambridge University Press)

Garcia, M.R., Murray, S.S., Primini, F.A., Forman, W.R., McClintock, J.E., Jones, C., 2000, ApJ 537, L23

Giacconi, R., Gursky, H., Paolini, F.R., Rossi, B.B. 1962, Physical Review Letters, 9, 439

Giacconi, R., Zirm, A., Wang, J.X., et al., 2002, ApJS, 139, 369

Gilfanov M., 2004, MNRAS, 349, 146

Grimm, H.-J., Gilfanov, M., Sunyaev, R., 2002, A&A, 391, 923

Grindlay J., ASP conf. Ser. 48, The Globular Clusters-Galaxy connection, ed. G. H. Smith & J. P. Brodie (San Francisco:ASP), 156

Hasinger, G., Altieri, B., Arnaud, M., et al., 2001, A&A, 365, 45 2004, MNRAS, 349, 146

Hills J. G., 1976, MNRAS, 175, 1

Ivanova, N., Taam, R.E., 2003, ApJ, 599, 516

Ivanova N., Rasio F. A., Lombardi J. C., Dooley K. L., Proulx Z. F., 2005, ApJ, 621, L109

Jordán, A., Côté, P., Ferrarese, L., et al., 2004, ApJ, 613, 279

Juett, A.M., 2005, ApJ, 621, L25

Kaaret, P., 2002, ApJ, 578, 114

Kim, D.-W., Fabbiano, G., 2004, ApJ, 611, 846

Kim, D.-W., Fabbiano, G., Kalogera, V., et al., 2006, ApJ, 652, 1090

Kim, E., Kim, D.-W., Fabbiano, G., Lee, M.G., Park, H.S., Geisler, D., Dirsch, B., 2006, ApJ, 647, 276

Kong, A.K.H., Di Stefano, R., Garcia, M.R., Greiner, J. 2003, ApJ, 585, 298

Kraft, R.P., Kregenow, J.M., Forman, W.R., Jones, C., Murray, S.S., 2001, ApJ, 560, 675

Kundu, A., Maccarone, T.J., Zepf, S.E., 2002, ApJ, 574, L5

Landau, L., Lifshitz, E., 1959, The Classical Theory of Fields, Addison-Wesley, Massachusetts, chapter 11

Compact stellar X-ray sources. Edited by Walter Lewin & Michiel van der Klis. Cambridge Astrophysics Series, No. 39. Cambridge, UK: Cambridge University Press

Macri, L.M. 2001, ApJ, 549, 721

McElroy D. B., 1983, AJ, 270, 485

Mushotzky, R.F., Cowie, L.L., Barger, A.J., Arnaud, K.A., 2000, Nature, 404, 459

Ostriker, J., 1976, in: Structure and Evolution in Close Binary Systems, eds: P.P. Eggleton, S. Mitton, J. Whealan, IAU Symp. 73, p. 206

Paczynski, B., 1971, ARA&A, 9, 183

Paczynski, B., 1976, in: Structure and Evolution in Close Binary Systems, eds: P.P. Eggleton, S. Mitton, J. Whealan, IAU Symp. 73, p. 75

Peters P.C., 1964, Phys. Rev., 136, B1224

Pietsch, W., Freyberg, M.J., Haberl, F., 2005, A&A, 434, 483

Podsiadlowki P., Rappaport S., Pfahl E. D., 2002, ApJ, 565, 1107

Postnov, K.A., Kuranov, A.G. 2005, Astro. Lett., 31, 7

Rappaport S., Verbunt F., Joss P. C., 1983, ApJ, 275, 713

Sarazin, C.L., Irwin, J.A., Bregman, J.N., 2000, ApJ, 544, L101

Shakura, N., Sunyaev, R., 1973, A&A, 24, 337

Shirey, R., Soria, R., Borozdin, K., et al., 2001, A&A, 365, 195

Sivakoff, G.R., Jordán, A., Sarazin, C.L., et al., 2006, astro-ph/0611237

Stanek, K.Z., & Garnavich, P.M. 1998, ApJ, 503, 131

Trudolyubov, S., Priedhorsky, W., 2004, ApJ 616, 821

van den Heuvel, E. P. J., 1992, in Saas-Fee advanced course 22, Interacting Binaries, ed. H. Nussbaumer & A. Orr (Springer-Verlag), 263

van der Sluys, M.V., Verbunt, F., Pols, O., 2005, A&A, 431, 647

van Paradijs, J., McClintock J.E. 1995, in Lewin, W.H.G., van Paradijs, J., van den Heuvel, E.P.J., eds, X-ray Binaries, Cambridge University Press, Cambridge, P. 58

Verbunt F., 1987, ApJ, 312, L23

Verbunt F., Zwaan C., 1981, A&A, 100, 7

Voss R., Gilfanov M., 2006, A&A, 447, 71

Voss R., Gilfanov M., 2007a, Preprint (astro-ph/0610649)

Voss R., Gilfanov M., 2007b, Submitted to MNRAS

White, R.E., Sarazin, C.L., Kulkarni, S.R. 2002, ApJ, 504, L31

Widrow L. M., Perrett K. M., Suyu S. H., 2003, ApJ, 588, 311

2

The luminosity function of X-ray point sources in Centaurus A

Astronomy & Astrophysics, 447, 71, 2006

R. Voss & M. Gilfanov

Abstract

We have studied the X-ray point source population of Centaurus A (NGC 5128) using data from four archival *CHANDRA* observations. We detected 272 point-like X-ray sources within a radius of 10 arcmin from the centre. Approximately half of these are CXB sources, with the remaining half being LMXBs. The spatial distribution of the LMXBs, both azimuthally averaged and 2-D, is consistent with the distribution of the K-band light observed in the 2MASS survey. After correction for the incompleteness effect we constrain the LMXB luminosity function down to $\sim 2 \times 10^{36}$ erg s^{-1}, much lower than previous studies of LMXBs in elliptical galaxies. The obtained XLF flattens significantly below $L_X \sim 5 \times 10^{37}$ erg s^{-1} and follows the $dN/dL \propto L^{-1}$ law in agreement with the behaviour found earlier for LMXBs in the Milky Way and in the bulge of M31.

2.1 Introduction

CHANDRA observations of the bright end, $\log(L_X) \gtrsim 37.5-38$, of X-ray point source populations in nearby elliptical galaxies found a rather steep luminosity distribution with a differential power law index in the $\sim 1.8-2.5$ range (e.g. Colbert et al., 2004; Kim & Fabbiano, 2004). This is noticably steeper than X-ray luminosity function (XLF) slopes in spiral and starburst galaxies, ~ 1.6 (Grimm et al., 2003). This difference reflects the difference in the composition of the X-ray populations in the early and late type galaxies, dominated by low- and high-mass X-ray binaries, respectively. Extension of the luminosity range available for the study down to $\log(L_X) \sim 36$ revealed a much more complex shape of the XLF of low-mass X-ray binaries (LMXBs). It has been shown to flatten considerably at the faint end and to follow the $dN/dL \propto L^{-1}$ power law below $\log(L_X) \lesssim 37-37.5$ (Gilfanov, 2004). Motivated by observational results, Bildsten & Deloye (2004) and Postnov & Kuranov (2005) suggested that the slope of the LMXB XLF in different luminosity regimes is defined by predominantly different sub-types of low-mass X-ray binaries. In the sample of Gilfanov (2004) the faint end of the LMXB XLF was represented by the bulges of two spiral galaxies only – the Milky Way and M31. On the other hand, the X-ray binaries in elliptical galaxies and spiral bulges could be formed by different mechanisms and have different evolution histories and, consequently, different luminosity distributions. It is therefore important to complement theoretical advances in understanding the XLF of X-ray binaries with firm observational constraints on its behaviour based on a broad range of galactic types, especially at the low luminosity end.

Centaurus A (Cen A) is candidate for such a study. It is massive enough to contain a sufficient number of LMXBs and, on the other hand, is sufficiently nearby to reach luminosities below $\sim 10^{37}$ erg s^{-1} with moderate observing times. It has been widely studied in X-rays, and it has been observed 10 times with *CHANDRA*. These observations have been used to obtain information about the nucleus (Evans et al., 2004), the interstellar medium (Kraft et al., 2003), the jet (Kraft et al., 2002; Hardcastle et al., 2003) the shell structures (Karovska et al., 2002) and the off-centre point source population (Kraft et al., 2001). The objective of the present study is the population of LMXBs in Cen A, namely their spatial and luminosity distribution. Studying the latter, we will focus specifically on the low luminosity domain, $\log(L_X) \sim 36.5-37.5$, whose importance has been emphasized above. Combining 4 observations and accurate incompleteness correction enabled us to investigate sources with luminosity by a factor of $\sim 5-10$ lower than in previous studies.

Cen A has a strongly warped dust disc with evidence for star formation, and optical images show a system of filaments and shells. This is probably due to a recent merger (Schiminovich et al., 1994). It is the nearest active galaxy and is considered to be the prototypical Faranoff-Riley class I radio galaxy. It has a very compact nucleus, most likely an accreting massive black hole, with strongly varying intensity. Emanating from this nucleus are milliarcsecond radio jets and a subrelativistic radio/X-ray jet extend ~ 6 arcmin towards NE of the nucleus. Radio lobes extending NE and SW are seen. An exhaustive review of Cen A can be found in Israel (1998).

The paper is structured as follows. In Sect. 2 we describe the data sets and the basic

Table 2.1: The *CHANDRA* observations used in this paper.

Obs-ID	Date	Instrument	Exp. Time	R.A.	Dec.	Data Mode
0316	1999 Dec 05	ACIS-I	36.18 ks	13 25 27.61	−43 01 08.90	FAINT
0962	2000 May 17	ACIS-I	36.97 ks	13 25 27.61	−43 01 08.90	FAINT
2987	2002 Sep 03	ACIS-S	45.18 ks	13 25 28.69	−43 00 59.70	FAINT
3965	2003 Sep 14	ACIS-S	50.17 ks	13 25 28.70	−43 00 59.70	FAINT

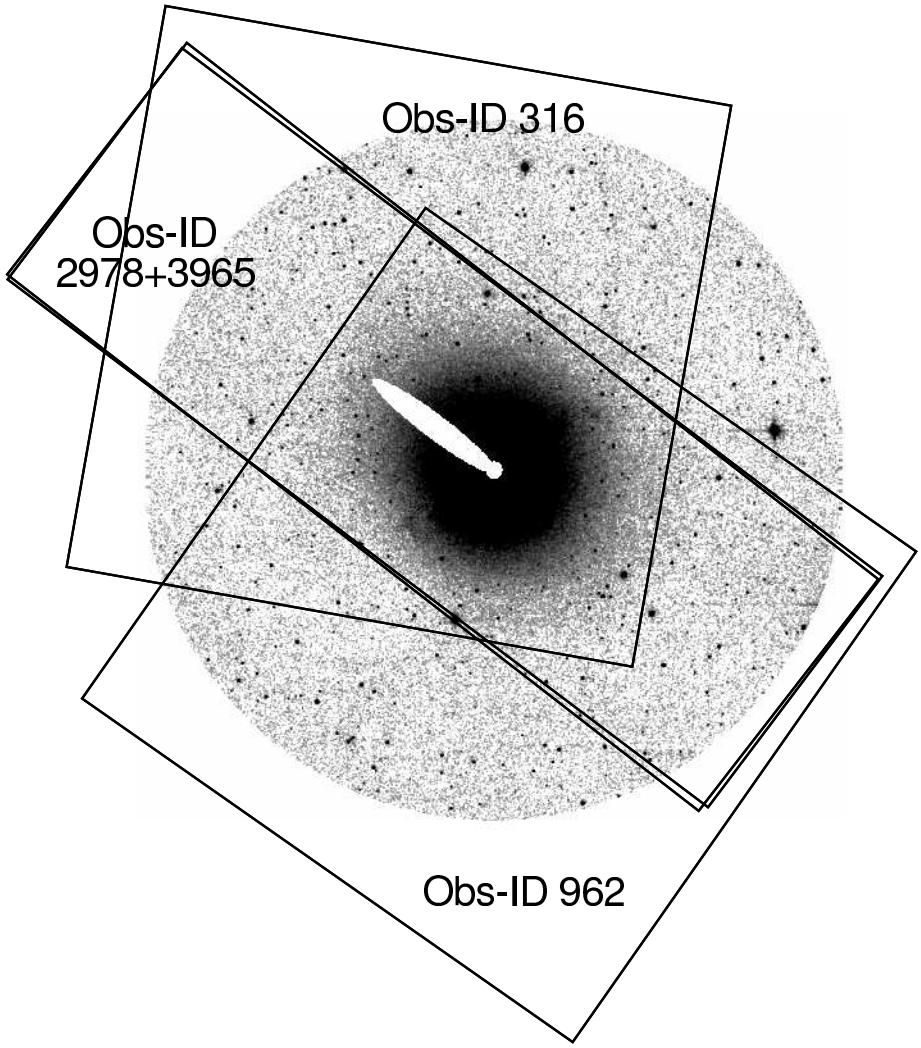

Figure 2.1: The 2MASS K-band image of the region of Cen A analysed in this paper. The radius of the image is 10 arcmin. Also shown are the areas covered by the four *CHANDRA* observations.

data preparation and analysis. The source list cleaning procedures are presented in Sect. 3, together with source identifications. In this section we also deal with possible periodic variability of the most luminous sources. The properties of the population of X-ray binaries, as well as the background X-ray sources are analysed and compared with previous studies in Sect. 4, including the spatial distribution of the sources and their luminosity function. Sect. 5 gives the conclusions. We adopt a distance of 3.5 Mpc to Cen A, and that (R.A.,Dec.) = (13 25 27.6, -43 01 08.8) is the centre of the galaxy.

2.2 Data analysis

The analysis in this paper is based on four *CHANDRA* observations, two of them made with the ACIS-I array (OBS-ID 316 and 962), and the other two with the ACIS-S array (OBS-ID 2978 and 3965). Information about the observations is listed in Table 2.1; their fields of view overlaid on the K-band image of the galaxy are shown in Fig.2.1.

Together these four observations cover most of Cen A within a 10 arcmin radius from the centre. The data preparation was done following the standard CIAO[1] threads (CIAO version 3.1; CALDB version 2.28), and limiting the energy range to 0.5-8.0 keV. The ACIS chips sometimes experience flares of enhanced background. For point source detection and luminosity estimation it is not necessary to filter out weak flares, since the increased exposure time outweighs the increased background. We did not find any flares strong enough to filter them out.

We used CIAO wavdetect to detect sources. This program is the most widely used for point source detection in *CHANDRA* data. Some of the parameters we have changed from the default values. Most important are the scales. We have used the $\sqrt{2}$-series from 1.0 to 8.0. This gives a wide enough range of source sizes to account for the variation in point spread function (PSF) from the inner parts of Cen A to the parts 10 arcmin from the centre as well as enough middle scales. We also used maxiter=10, iterstop=0.00001 and bkgsigthresh=0.0001. The effect of changing these parameters is that more iterations are done in the process of removing sources when creating backgound files, at the expense of computing time. Finally we set the parameter eenergy=0.8 (the encircled fraction of source energy used for source parameter estimation), which gives larger areas for source parameter estimation at the risk of source merging, see Sect. 3.

First we detected sources in the inner region of Cen A covered by all four observations. From these sources we then chose 40 that are bright enough to have the positions determined precisely and that existed in all four observations. We used these sources to determine the average positions of the sources and the offsets for the individual observations. The statistical uncertainties of the source positions are typically 0.3−0.5 pixel. Assuming that the errors are uncorrelated gives an uncertainty of ∼0.05 pixel in the calculated offsets of the observations. Using CIAO dmtcalc we then corrected the aspect and events file for each observation. The corrections applied are listed in Table 2.2. This step was performed in order to make the observations aligned for

[1] http://cxc.harvard.edu/ciao/

Table 2.2: The corrections applied to the *CHANDRA* aspect files to align the observations.

Obs-ID	Correction West	Correction North
0316	−0.73 pixel*	−0.42 pixel
0962	+1.58 pixel	+1.44 pixel
2978	−0.53 pixel	−0.18 pixel
3965	−0.31 pixel	−0.85 pixel

*1 pixel is 0.492 arcsec

combination, not to get better absolute astrometry, which will be dealt with in Sect. 3.

We used CIAO reproject_events to reproject observations 316, 962 and 2978 into the sky coordinates of observation 3965. The files were then merged and the wavdetect task was applied again to the combined image. The output count rate for each detected source is calculated inside a source cell and the local background is subtracted. For each source we extracted the PSF using CIAO psfextract task and calculated the percentage of the counts expected to lie inside each source cell. This was done for each of the four observations, and the result was averaged using the values of the exposure maps as weights. For most sources this percentage is above 97 per cent, and only four sources have values lower than 70 per cent. An exposure map was created for each of the observations, assuming the energy distribution to be a powerlaw with photon index of 1.7 and Galactic absorption of $8.4\times10^{20}\mathrm{cm}^{-2}$ (Dickey & Lockman, 1990). We assumed the same spectrum to convert the observed count rates to unabsorbed source luminosities.

In the very inner parts of Cen A there is strong X-ray emission from hot gas and the central AGN. At the same time there is a large number of point sources within a small area making crowding a serious problem. We have therefore excluded the area within a radius of 30 pixels ($\sim$ 15 arcsec) from the centre of the galaxy.

Simulations using the observed source distribution as input show that excluding this inner region limits crowding to less than 4% of the sources (sec. 2.A.1). Also the part of the galaxy dominated by the X-ray jet has been excluded. The excluded regions are evident from Fig.2.1.

In each of the four observations, readout streaks caused by the bright central region of Cen A are seen. As in different observations they cover different regions of the image, for each streak we have searched for sources and estimated their parameters using a combined image of the observations, excluding the one containing this streak.

To check for differences between the four observations and between the individual observations and the combined observation, we have created the cumulative point source luminosity function for each, taking only sources from the central region, where all four observations overlap, see Fig. 2.1. The results can be found in Fig. 2.2. A large fraction of the sources are variable. For these sources, using the luminosities estimated from the combined image is equal to using the average luminosities. We

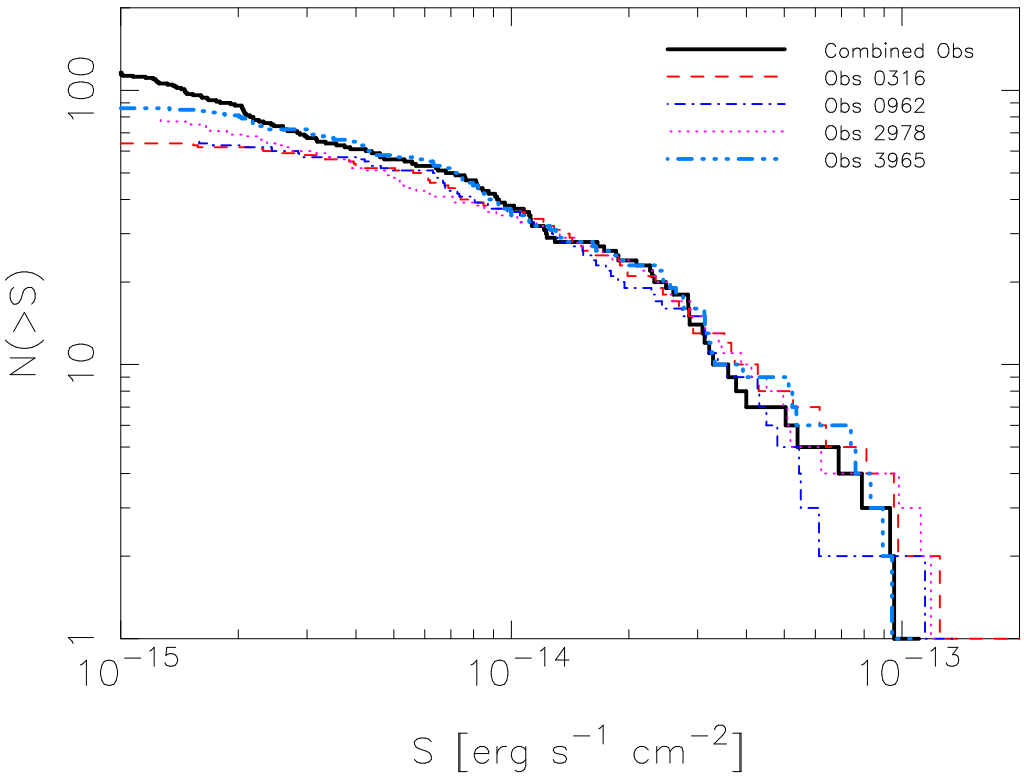

Figure 2.2: Comparison of the cumulative $\log(N) - \log(S)$ distribution found in each of the separate observations and in the combined image. Only sources from the inner region, contained in all four observations, have been used and incompleteness correction has not been applied. The incompleteness begins to have effect at a few $\times 10^{-15}$ erg $s^{-1}cm^{-2}$ for the combined image and at $\sim 7 - 8 \times 10^{-15}$erg $s^{-1}cm^{-2}$ for the individual observations.

used the Kolmogorov–Smirnov (KS)-test to compare the $\log(N) - \log(S)$ distribution obtained in the individual observations with that based on the combined data. To minimize incompleteness effects only sources with fluxes higher than $3{\cdot}10^{-15}$ erg s^{-1} cm^{-2} were used. The lowest probability found was 68 per cent (for Obs-ID 316). This confirms that the source variability does not modify the flux distribution of the point sources in a galaxy like Cen A at a detectable level.

2.3 The source list

Several effects can compromise the source list generated from CIAO wavdetect. This includes extended sources and false sources due to background fluctuations. The background due to the diffuse emission is high, especially in the inner parts of Cen A, and many structures can be seen in the image. The "bubble" ∼5 arcmin south-west of the centre is an example (Kraft et al., 2003). Some of these structures might be misinterpreted as point sources. We have visually inspected the images and for each source

compared the photon distribution with the distribution expected from the PSF. As a result we rejected 18 sources. As indicated by the shapes, none of the rejected sources is likely to be a supernova remnant. Some of the rejected sources are filamentary structures in the diffuse component and the rest are caused by local variations in the emission of the diffuse component. The characteristic length scale of the latter is $\gtrsim$100 pc. Due to the low luminosity of the rejected sources, it is not possible to classify them according to their spectra.

Another potential problem could be merging of sources. We have used a high value (80 per cent) of the enclosed percentage of PSF in CIAO wavdetect because it gives a good estimation of source parameters. On the other hand, such a high value in some cases leads to two sources being detected as one source. To check for this, we ran CIAO wavdetect again with smaller enclosed percentages of the PSF. We find no sources that are merged because of the high enclosed percentage of the PSF.

After the filtering, the final list of X-ray sources contains 272 objects. It is presented in Table 2.5. Kraft et al. (2001) analysed the two ACIS-I observations of Cen A (Table 2.1) and detected 246 X-ray sources. Of these, 205 sources are located within $r < 10$ arcmin of the center of the galaxy analysed here. 184 of these sources are in our source list, which therefore contains 90 previously undetected sources. The $\sim 1/3$ increase in the total number of detected sources is due to a factor of $\gtrsim 2-4$ increase in the exposure time of the main body of the galaxy (Fig.2.1, Table 2.1).

2.3.1 Background and foreground sources

A fraction of the detected sources are foreground or background objects. Some (but not all) of them can be identified using either their X-ray spectra, or from observations at other wavelengths. Since this paper concerns the statistical properties of the X-ray point source population, we have adopted the following strategy. We exclude foreground sources as much as possible (6 such sources are excluded, see Sect. 2.3.2), but do not attempt to remove background sources, which are by far the most significantly contaminating factor (about half of the detected sources are background sources, see Sect. 2.4.3). Their contribution to the surface brightness and luminosity distributions is instead taken into account in the statistical sense, based on the results of the cosmic X-ray background (CXB) source counts.

2.3.2 Optical identifications

We check the absolute astrometry using USNO-B1.0 (Monet et al., 2003) and GSC 2.2 (Morrison et al., 2001) catalogues. We find that for a search radius of 2.0 arcsec the rms deviation of the positions is 1.1 arcsec. This is comparable to the quoted positional uncertainties of the optical catalogues as well as that of the Chandra X-ray source list, confirming reasonable astrometric accuracy of the latter. Adding a systematic shift of 0.5 arcsec in any direction results in larger rms deviations. The number of matches is significantly higher than the expected number of chance coincidences. For the search radius of 2.0 arcsec the expectation value is ~ 8 with 37 matches found for USNO-B1.0 and ~ 3 with 18 matches found for GSC 2.2.

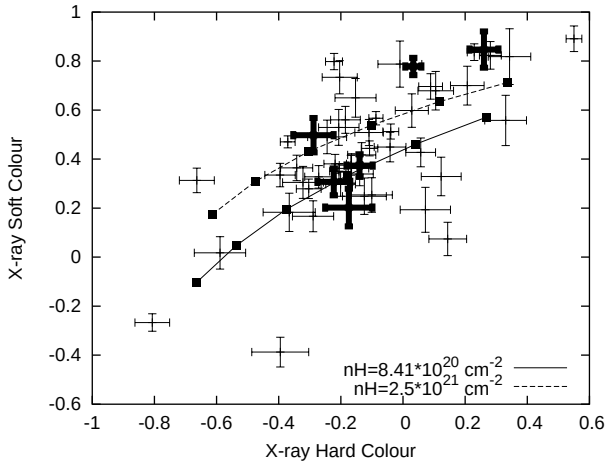

Figure 2.3: The color–color diagram of the brightest, > 200 counts, sources within 5 armin from the centre of Cen A. The sources coinciding with H_α-emitting regions are shown in bold. For reference, the two lines show the hardness ratios of power law spectra for two different values of absorption. The filled squares are at photon indices of 0.5, 1.0, 1.5, 2.0, 2.5, 3.0 from right to left. The hard and soft colours are defined as HC=(H-M)/(H+M), SC=(M-S)/(M+S), where S,M and H are the number of photons detected in the 0.5-1.0 keV, 1.0-2.0 keV and 2.0-8.0 keV energy range respectively.

For the actual identification of Chandra sources we used the results of the dedicated optical studies of the Cen A region by Peng et al. (2004), Minniti et al. (2003) and Woodley et al. (2005). Although the former three surveys were aimed specifically at globular cluster population of Cen A they also have identified a number of foreground stars, H_α emittors and several AGNs. We also used results of Graham & Fasset (2002). In total we identified 6 X-ray sources as foreground stars, leaving 266 sources of presumably extragalactic origin – either intrinsic Cen A sources or background AGNs. Of these, 37 were identified with the globular clusters in Cen A. The results of this work are presented in column 10 of Table 2.5.

About $\sim 2/3$ of the USNO and GSC matches were found to be globular clusters or likely globular clusters in Peng et al. (2004) and Minniti et al. (2003). The remaining 12 out of 37 sources do not appear in these papers. This is close to but slightly higher than the number of 8 random matches expected for the value of the search radius used in the analysis. Some of these sources also might be background AGNs or undetected globular clusters. Therefore we kept them all in the sample. We note that excluding them from the following analysis does not change our results in any significant way.

2.3.3 Hα-sources

Eight sources within 4 arcmin from the centre of Cen A coincide with Hα-emitting regions found in Minniti et al. (2003). All of them are located in the dust lanes region, have X-ray luminosities in the $10^{36} - 5 \cdot 10^{37}$ erg s^{-1} range and can potentially be associated with high-mass X-ray binaries. The optical magnitudes of the Hα sources

indicate that they may be young star clusters as well as individual X-ray binaries. In order to search for further indications of the high-mass X-ray binary (HMXB) nature of these sources we have compared their spectral properties with other sources and searched for periodic variability in their X-ray emission. As discussed in more detail below, no coherent pulsations were detected from any of the bright X-ray sources, although the upper limits are at a rather moderate level of $\sim$ 25 per cent pulsed fraction.

The accreting X-ray pulsars, constituting the vast majority of the neutron star HMXBs, are known to have notably harder spectra in the $\sim$ 1–20 keV energy range than LMXBs and often show significant intrinsic absorption. Therefore comparison of the spectral properties of the Hα objects with other X-ray sources (which in the central part of Cen A are mostly LMXBs, Sect. 2.4) can help to clarify the nature of the former. However, the X-ray colour-colour diagram of the sources within 5 arcmin from the centre of Cen A, shown in Fig 2.3, does not reveal systematic differences between Hα and other sources, nor have we found any systematic differences from the direct spectral fits of the brightest sources.

Comparing Fig 2.3 with Fig. 4 of Prestwich et al. (2003) and noting the slight difference in energy bands, it can be seen that the main part of our sources is located in the region corresponding to LMXBs. There is a small population of harder sources, of which two are Hα objects and also a few softer sources. From their position in the diagram, they could be HMXBs and thermal supernova remnants, respectively. Such identifications are not possible with to the colours alone for two reasons. One is that the absorption inside Cen A varies strongly with position, which has the effect of enhancing the scatter of LMXBs in the diagram. The second reason is that there is a contribution of CXB sources. This population is known to consist of two subpopulations, a hard and a soft one. These populations would be expected to coincide with the HMXBs and the supernova remnants, respectively, in the diagram.

As our results were not conclusive enough, we decided to keep the Hα sources in the sample, bearing in mind that their nature still needs to be clarified. Due to their relatively small number they do not significantly affect the following analysis of the spatial and luminosity distributions.

2.3.4 Globular cluster sources

37 X-ray sources coincide with known globular clusters. Interpreting this number, one should take into account that only $\sim 20 - 25$ per cent of the expected number of globular clusters in Cen A have been identified (Woodley et al., 2005). The identified sample is strongly biased, both with respect to the spatial distribution of the clusters and their luminosity distribution. Furthermore, the detection of the globular clusters is not independent of the X-ray observations, as X-ray source catalogues have been used to search for globular clusters (e.g. Minniti et al., 2003). It is therefore not possible to perform a rigorous comparison of the luminosity function and spatial distribution of the globular cluster X-ray sources with the sources residing outside globular clusters. Considering the sources brighter than $3{\cdot}10^{37}$ erg s^{-1} (i.e. unaffected by incompleteness effects) there are 15 known globular cluster X-ray sources, whereas the number of

sources outside globular clusters is 40. If the expected number of 22 CXB sources (see Sect. 2.4.3) is subtracted, we find 18 'field' LMXBs outside (or in undetected) globular clusters. Above this luminosity the XLF of globular cluster sources is similar to that of the field LMXBs. Below this luminosity the field LMXB XLF is much steeper than that of globular cluster sources. This can easily be caused by incompleteness effects, which cannot be corrected for without knowledge of the spatial distribution of the globular cluster sources (see section 2.A). We also note that in the outer region there are 7 globular cluster sources, with $L_X \geq 10^{37}$ erg s^{-1} whereas we expect ∼9 LMXBs in total (see Sect. 2.4.1.1).

2.3.5 Search for coherent pulsations

We searched for periodic variability in the light curves of the sources with more than 400 detected source counts and more luminous than $6.0{\cdot}10^{37}$ erg s^{-1} (24 sources in total). Each *CHANDRA* observation was tested separately. Events were extracted from the 4 sigma source ellipses in `wrecon` and the light curves with ≈ 3.2 sec time resolution were produced. The power spectra were calculated using the STARLINK[2] task `period`. Pulsations were searched for in the range of trial periods from $P \approx 6.4$ s, defined by the Nyquist frequency of the Chandra time series, to $P = 2000$ s. Except 3 sources showing variability due to the telescope dithering carrying them over the detector edge, in only one did the power exceeded the level corresponding to 99 per cent confidence. The period of 55.8 s was found for the source #135 (Table 2.5) in Obs 2978 and had a significance of 99.4 per cent. This significance takes into account the number of trial periods in one power spectrum but not the number of power spectra analyzed (74). In the other 3 observations of the source the power density spectrum did not show any signs of pulsations at this period. Given the total number of power spectra investigated it is likely that this detection is a result of a statistical fluctuation. Even for the most luminous sources, pulsed fractions of ∼25 per cent would be needed for detection at the 99 per cent confidence level.

2.4 Populations of X-ray sources in the field of Centaurus A

In the central $r < 10$ arcmin of Cen A (excluding the nucleus and the jet, Fig.2.1, Sect. 2.2) we detected 136 sources with $L_X > 10^{37}$ erg s^{-1} and 252 (≈ 321 after the incompleteness correction) sources with $L_X > 2 \cdot 10^{36}$ erg s^{-1} (Table 2.5, 2.3).

2.4.1 Expected numbers

2.4.1.1 Low mass X-ray binaries

LMXBs are related to the population of old stars, and there is therefore a correlation between their number and the stellar mass of a galaxy (Gilfanov, 2004). In order to estimate the expected number and luminosity distribuition of LMXBs we used a K-band image from the 2MASS Large Galaxy Atlas (Jarret et al., 2003) and integrated

[2]http://www.starlink.ac.uk

Table 2.3: Expected and observed numbers of point sources (section 2.4.1).

L_X	Predicted				Obs.
erg s^{-1}	LMXB	HMXB	CXB$^{(1)}$	Total$^{(1)}$	Total$^{(2)}$
$> 10^{37}$	81	10	34 (47)	125 (138)	136
$> 2 \cdot 10^{36}$	155	27	98 (135)	280 (317)	321

(1) – the CXB numbers are based on the soft (hard) band counts from Moretti et al. (2003), see Sect. 2.4.1.3; (2) – after the incompleteness correction

the flux emitted in the parts of Cen A analysed in this paper. This gives the K-band luminosity of $L_K = 8.6 \cdot 10^{10}\ L_\odot$. To convert it to the stellar mass we use the color-dependent K-band mass-to-light ratio from Bell & De Jong (2001). For the extinction corrected optical color of Cen A, $(B-V) \approx 0.88$, the mass-to-light ratio is $M_*/L_K \approx 0.76$. This gives the stellar mass of $5.5 \cdot 10^{10}\ M_\odot$, assuming that the absolute K-band magnitude of the sun is equal to $M_{K,\odot} = 3.39$. Using the results of Gilfanov (2004) we predict ≈81 LMXBs with $L_X > 10^{37}$ erg s^{-1}, and ≈155 with $L_X > 2 \cdot 10^{36}$ erg s^{-1}.

2.4.1.2 High mass X-ray binaries

Being young objects, HMXBs are associated with star formation and, as expected for an elliptical galaxy, are by far a less significant contribution to the population of X-ray binaries than LMXBs. In terms of absolute rates, star formation in Cen A is mostly associated with the dust disk. From their analysis of IRAS data, Marston & Dickens (1988) found the total far infra-red (FIR) luminosity of the Cen A disc to be $9.7 \cdot 10^9$ $L_\odot$ ($L_\odot = 3.8 \cdot 10^{33}$ erg s^{-1}). From this luminosity we subtracted the emission from the central region which is mostly due to the active nucleus, $1.5 \cdot 10^9\ L_\odot$, and corrected the distance from the 5 Mpc assumed in Marston & Dickens (1988) to the 3.5 Mpc adopted in this paper. This gives $L_{\rm FIR} \approx 4.0 \cdot 10^9\ L_\odot$. Assuming that the total infrared luminosity is $L_{\rm TIR} \approx 2 L_{FIR}$ and using the SFR calibration of Kennicutt (1998) we find SFR ≈ 1.4 M$_\odot$ yr^{-1}. We used the calibration of Grimm et al. (2003) to calculate the expected number of HMXBs (see comment in Shtykovskiy & Gilfanov 2005 regarding the normalization). From this we get the expectation of ≈10 HMXBs brighter than 10^{37} erg s^{-1}, and ≈27 sources brighter than $2 \cdot 10^{36}$ erg s^{-1}.

2.4.1.3 Background X-ray sources

To estimate the number of background sources we use the results of the CXB $\log(N) - \log(S)$ determination by Moretti et al. (2003). We use the source counts in the soft and hard bands (their Eq. 2) and convert the fluxes to the 0.5–8.0 keV band, assuming a powerlaw spectrum with a photon index of 1.4. For the total area of our survey of 0.079 deg^2 we obtain from the source counts in the soft band ≈34 CXB sources above the flux corresponding to 10^{37} erg s^{-1}, and ≈98 above 10^{36} erg s^{-1}. From the hard band counts the predicted numbers are ≈47 and ≈135 sources. The predictions based on

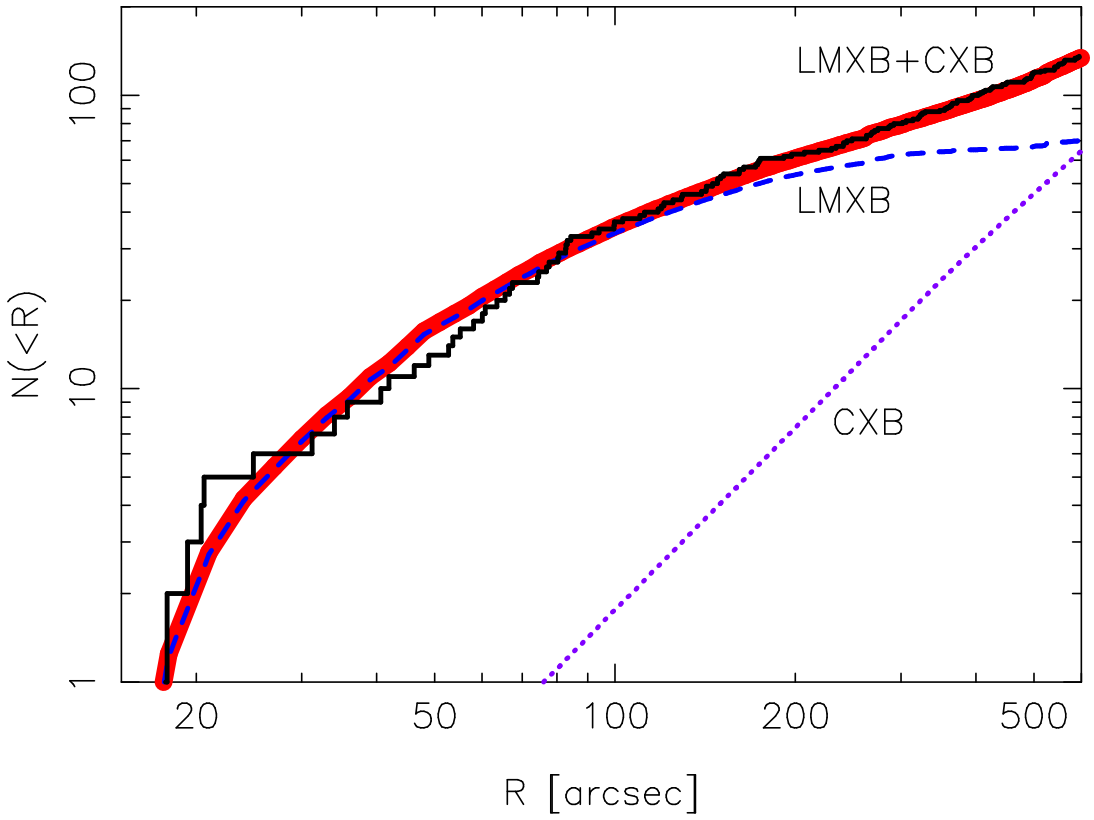

Figure 2.4: The radial distribution of observed sources (solid line), compared to the best fit model (thick grey line) and the contributions of LMXBs and CXBs

the soft and hard $\log(N) - \log(S)$ differ because of the well recognized fact that source counts in different energy bands and flux regimes are dominated by different types of sources. This is further discussed in Sect. 2.4.3. Furthermore the normalization of the CXB source counts is subject to uncertainy due to the cosmic variance. Its rms amplitude is $\sim 20 - 25\%$ (see e.g. Cappelluti et al., 2005).

The results of the above calculations are summarized in Table 2.3. For the total number of point sources, the agreement between observed and predicted values is surprisingly good, given the amplitude of uncertainties involved. In the following two subsections we derive from the data, and compare with the predictions, the abundances of individual types of X-ray sources. This is done in two independent ways – based on the radial distribution of the sources (Sect. 2.4.2) and on their flux/luminosity distribution (Sect. 2.4.3).

2.4.2 Spatial distribution of point sources

We begin with the azimuthally averaged radial profile (Fig.2.4). As it follows from the results of the previous section the two major contributiors to the population of

point sources in the field of Cen A are low-mass X-ray binaries ($\sim$ 1/2–2/3 of the sources, depending on the luminosity) and background AGNs ($\sim$ 1/3–1/2). Correspondingly, we model the observed distributions as a superposition of two functions, describing their respective contributions. The spatial distribution of the LMXBs has been shown (Gilfanov, 2004) to follow, to first approximation, the distribution of the stellar mass. The latter can be represented by the distribution of the K-band light and was computed using the K-band image of Cen A from the 2MASS Large Galaxy Atlas (Jarret et al., 2003). The density of the CXB sources can be assumed to be flat on the angular scales under consideration, therefore the CXB growth curve is proportional to the enclosed solid angle. In computing both radial profiles we took into account that some areas were excluded from the analysis (Fig.2.1). The only free parameter of the model is the ratio of normalizations of the LMXB and CXB distributions. The (unknown) distribution of HMXBs has not been included as it is unlikely to exceed 10% of the total number of sources (Sect. 2.4.1.2).

The model has been compared with the observed distribution of sources more luminous than 10^{37}erg s^{-1}. This value of the luminosity threshold was chosen in order to include as many sources as possible and, on the other hand, to keep incompleteness effects insignificant. The model adequately describes the data (Fig.2.4) as confirmed with the KS-test, with a probability of 96 per cent. The best fit LMXB fraction, determined from the Maximum Likelihood (M-L) fit to the the unbinned radial distribution data, is 51.7 ± 5.9 per cent, corresponding to 70.3 ± 10.0 LMXBs and 65.7 ± 9.8 CXB sources. Compared to Table 2.3, the abundance of LMXBs is surprisingly close to the expected value. The number of CXB sources, on the other hand, is higher than the expectation. This will be further discussed in Sect. 2.4.3.

The same LMXB+CXB model was also compared to the radially averaged azimuthal and two–dimensional distributions. The KS test of the unbinned two–dimensional distribution of the point sources (e.g. Press et al., 1992) gave a probability of 24%. The azimuthal distribution of the sources within 5 arcmin (to exclude the outer regions dominated by CXB) has the KS-probability of $10 - 20$ per cent depending on the starting point. Also we checked whether there was any azimuthal dependence on the radial profiles, by dividing the observations into two and three slices and comparing them using the KS-test. Trying a lot of different angles, we found no evidence for such a dependence. Due to the low number of sources, such evidence would not be found unless the effect was strong.

This analysis confirms that within the statistical accuracy of the data, the spatial distribution of the LMXBs is consistent with that of the K-band light. This implies, in particular, that no additional component corresponding to HMXBs is required by the data. However, this result is not very constraining, given the rather small expected number of HMXBs, ≈ 10.

2.4.2.1 Sensitivity of the spatial distribution analysis

In order to probe the sensitivity of the above analysis we performed the following test. The LMXB distribution was streched with respect to the center of the galaxy by some scale factor, the new best fit value of the CXB to LMXB ratio was found

using same method as before, and the consistency of new best fit model with the data was checked with the KS test. Then the range of values or the scale factor was found beyond which the KS probability decreased below 5 per cent indicating deteriorated quality of the approximation. The following ranges for the scale factor values were obtained: $0.4 \lesssim \eta \lesssim 1.9$ for the radial profile analysis and $0.2 \lesssim \eta \lesssim 2$ for the 2-dimensional image.

These numbers indicate a rather moderate sensitivity of the spatial distribution analysis. Sensitivity limitations of this kind are unavoidable when analysing individual galaxies. Further exposure of the inner 10 arcmin of the galaxy can improve the luminosity limit below which incompleteness effects have to be taken into account. Observations with the telescope pointing to the outskirts of the galaxy could be useful too, as they could help to constrain the local CXB normalization. Also a very careful study of the source distribution at luminosities where incompleteness is a problem could increase the sensitivity. Another approach is to study combined source density distributions for several (many) galaxies.

2.4.3 Source counts and the cosmic X-ray background source density

We divided Cen A into three annuli according to the ratio of predicted numbers of LMXBs and CXB sources: $r < 2.5$ arcmin, $r = 2.5 - 5$ arcmin, $r = 5 - 10$ arcmin). The inner and outer regions are expected to be dominated by LMXBs and CXB sources respectively, while the middle one contains comparable numbers of sources of both types (e.g. Fig.2.4). In analysing the luminosity functions and $\log(N) - \log(S)$ distributions we used the procedure described in section 2.A to correct for incompleteness effects.

We estimate the normalization of the CXB $\log(N) - \log(S)$ distribution from the source counts in the outer region. This region is far enough from the inner parts of the Cen A to keep the number of sources related to the galaxy low, while close enough to the aimpoints of the observations to have a reasonable sensitivity. In this region the incompleteness corrected number of sources with the 0.5–8 keV flux exceeding $2.7{\cdot}10^{-15}$ erg s^{-1} cm^{-2} (luminosity $4.0 \cdot 10^{36}$ erg s^{-1}) is 101.3 from which 13.4 are expected to be LMXBs. The implied number of CXB sources is ≈ 88, which we compare with the results of the radial profile analysis from the previous section and with results of dedicated CXB source counts. For this comparison we express the CXB normalization in units of the number of sources per deg^2 with 0.5–8.0 keV flux $S_X > 6.8 \cdot 10^{-15}$ erg s^{-1} cm^{-2}. The results of the CXB surveys are transformed to the 0.5–8.0 keV energy range assuming a power law spectrum with the photon index of 1.4. We used the source counts in both their soft (0.5–2.0 keV) and hard (2.0–8.0 keV) bands. The results are shown in the two columns in the upper part of Table 2.4. The last two lines in Table 2.4 present the results of the radial profile analysis and of the source counts in the $r = 5$ arcmin-10 arcmin ring. Note that although these two numbers are not statistically independent, they are obtained from different considerations. The radial profile analysis is based on sources with $L_X \geq 10^{37}$ erg s^{-1} in the entire $r \leq 10$ arcmin region and relies heavily on the assumption about the spatial distribution of the LMXB component. The source counts in the outer region

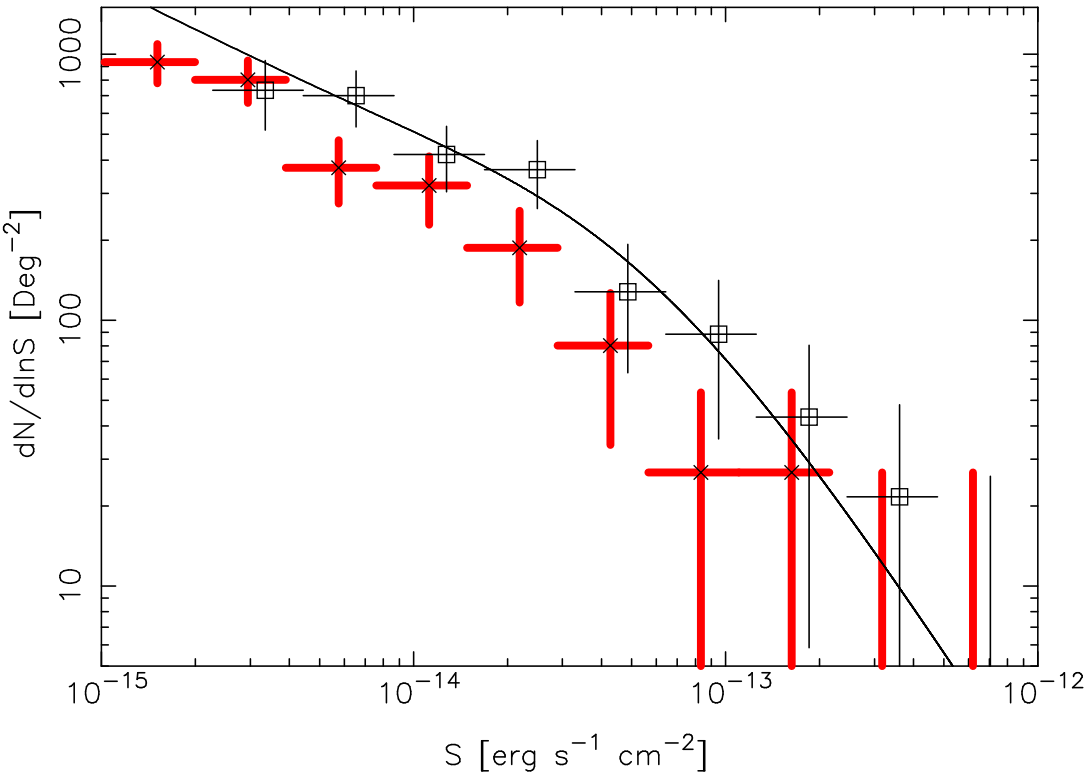

Figure 2.5: The source counts (open squares) in the outer region (5 arcmin$< r <$ 10 arcmin). The predicted contribution of LMXBs is subtracted. The thick solid line shows the CXB $\log(N) - \log(S)$ from Moretti et al. (2003). with best fit normalization from this paper. For comparison the source counts in the CDF-N Obs-ID 1671 are shown (crosses).

use all sources in the 5 arcmin$\leq r \leq$ 10 arcmin with a luminosity above 10^{36} erg s^{-1} and are significantly less dependent on the assumption of the LMXB spatial distribution.

As it has been already mentioned, there is a significant difference between the normalizations found from the hard and soft bands. This is related to the fact that different types of sources give dominant contributions to the hard and soft bands. Theoretically, the two bands can be reconciled using different spectral shapes for the the flux conversion, but this would introduce additional uncertainties and an investigation of this kind is beyond the scope of this paper. In addition, there is also a considerable spread in the CXB normalizations in the same energy band obtained in different surveys. This spread is partly due to the cosmic variance and partly it is likely to be caused by the difference in the analysis procedures and relative calibrations of different instruments.

In order to do a direct comparison with the empty fields source counts in the 0.5−8.0 keV energy band, we have analysed one observation from the CDF-N (Obs-ID 1671), using the same data analysis procedure as we used for Cen A. The column density of neutral hydrogen was set to $1.5{\cdot}10^{20}$ cm^{-2} (Dickey & Lockman, 1990). To avoid

Table 2.4: CXB normalization found in various surveys and in this paper.

Survey	soft band	hard band
CDF-S	332±70	686±71
CDF-N	437±80	791±73
Cappelluti et al., 2004	350±28	419±43
Cowie et al., 2002	–	456±30
Moretti et al., 2003	422	579
Obs–ID 1671 (CDF-N)	519 ± 71	
Radial profile (Cen A)	832 ± 124	
5 arcmin$< r <$ 10 arcmin counts (Cen A)	804 ± 86	

The normalization is expressed as the number of sources per deg^2 with 0.5–8.0 keV flux $S_X > 6.8 \cdot 10^{-15}$ erg s^{-1} cm^{-2}. The two columns give the numbers computed from the soft and hard band counts respectively. The for CDF-fields data listed in the upper part of the table are from Rosati et al. (2002), in the lower part – from this paper.

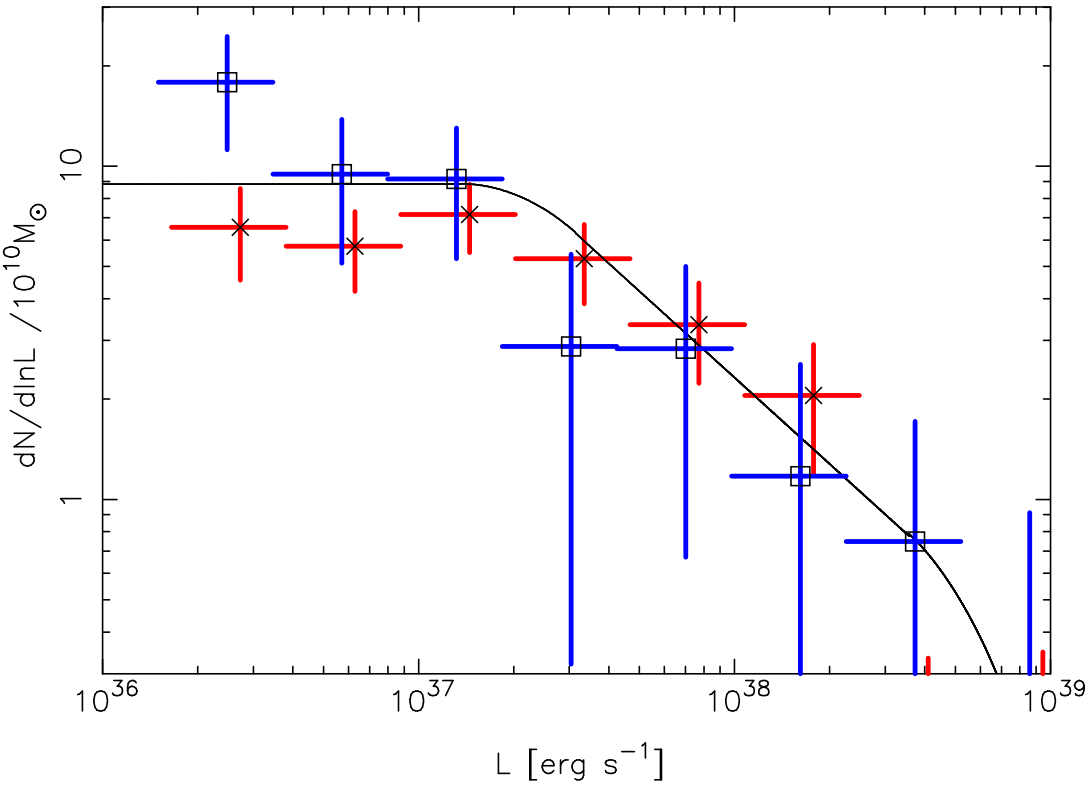

Figure 2.6: The differential luminosity functions of LMXBs in the innermost (stars) and middle (squares) annuli, normalized to 10^{10} $M_\odot$ of stellar mass. The CXB contribution is subtracted using the results of Sect. 2.4.3. The solid line shows the average LMXB XLF from Gilfanov (2004) smoothed with the boxcar filter with the logarithmically constant width equal to the bin width in the observed XLFs.

incompleteness effects, we only used sources observed in regions with exposure above $4.4 \cdot 10^7$ s cm^2. This limits the field to 0.058 deg^2. Above a flux of $2.7 \cdot 10^{-15}$ erg s^{-1} cm^{-2} (equal to the flux used to extimate the CXB normalization in the outer region of Cen A) we find 53 sources. This number can be directly compared with 88 CXB sources detected in the outer annulus in the Cen A field (by chance the two areas coincide). In order to facilitate comparison with the other CXB surveys, we transform this number to the units of Table 2.4, using the $\log(N) - \log(S)$ from the soft band of Moretti et al. (2003).

Even with the spread in values found from the various surveys, the CXB normalization in the Cen A field appears to be higher than the typical numbers obtained in the dedicated CXB studies, with the exception of the hard band counts of the Chandra Deep Fields, according to the analysis of Rosati et al. (2002). The latter two excluded, the density of CXB sources appears to be enhanced by a factor of $\sim 1.4-2$. Although this is larger than the rms variation between different fields typically quoted in the literature, $\sim 20-25$ per cent, the observed number is not exceptionally high and still lies within the spread of the CXB density values (e.g. Cappelluti et al., 2005).

2.4.4 LMXB X-ray luminosity function

The luminosity function of LMXBs determined from the two inner regions is shown in Fig.2.6. In subtracting the contribution of CXB sources we used the $\log(N) - \log(S)$ distribution from Moretti et al. (2003) with the normalization determined in the Sect. 2.4.3. While the CXB contribution is unimportant in the innermost region $r \leq 2.5$ arcmin, it accounts for about half of the sources in the middle region 2.5 arcmin $\leq r \leq 5$ arcmin. As is obvious from Fig.2.6, both distributions are consistent with each other and with the average LMXB XLF in the local galaxies determined by Gilfanov (2004), with the possible exception of the the lowest luminosity bin of the middle region, which deviates by $\sim 1.5\sigma$.

To further constrain the parameters of LMXB XLF in Cen A we fit the luminosity distribution in the inner region with a power law with two breaks, identical to the one used in Gilfanov (2004). Since there are no sources luminous enough to constrain the upper break and the slope beyond that, we have fixed them at the average values: $L_{b2} = 5.0 \cdot 10^{38}$ erg s^{-1}, $\alpha_3 = 4.8$. The best fit values of other parameters are: the low luminosity slope $\alpha_1 = 1.02^{+0.12}_{-0.13}$, a break at $L_{b1} = 5.0^{+1.0}_{-0.7} \cdot 10^{37}$ erg s^{-1} and a slope after the break $\alpha_2 = 2.6 \pm 0.4$. The slopes refer to the differential distribution, the parameter errors are 1σ statistical errors only. Notice that the break value found for differential XLFs is systematically higher than the break value found for cumulative XLFs, using the same data, see e.g. Kaaret (2002). These parameters are insensitive to whether the CXB component is accounted for or not.

A large uniformly analysed sample of the XLF of LMXBs in elliptical galaxies was presented by Kim & Fabbiano (2004). They find an average differential slope of 1.8 ± 0.2 in the luminosity range $L_X =$ a few $\times 10^{37}$ to 5×10^{38} erg s^{-1}. This is consistent with our results from the inner region. A KS-test gives 73 per cent probability that the observed luminosity distribution above $L_X = 1.0 \cdot 10^{37}$ erg s^{-1} could be produced by their LMXB XLF. On the other hand it is clear that at the faint end of the XLF

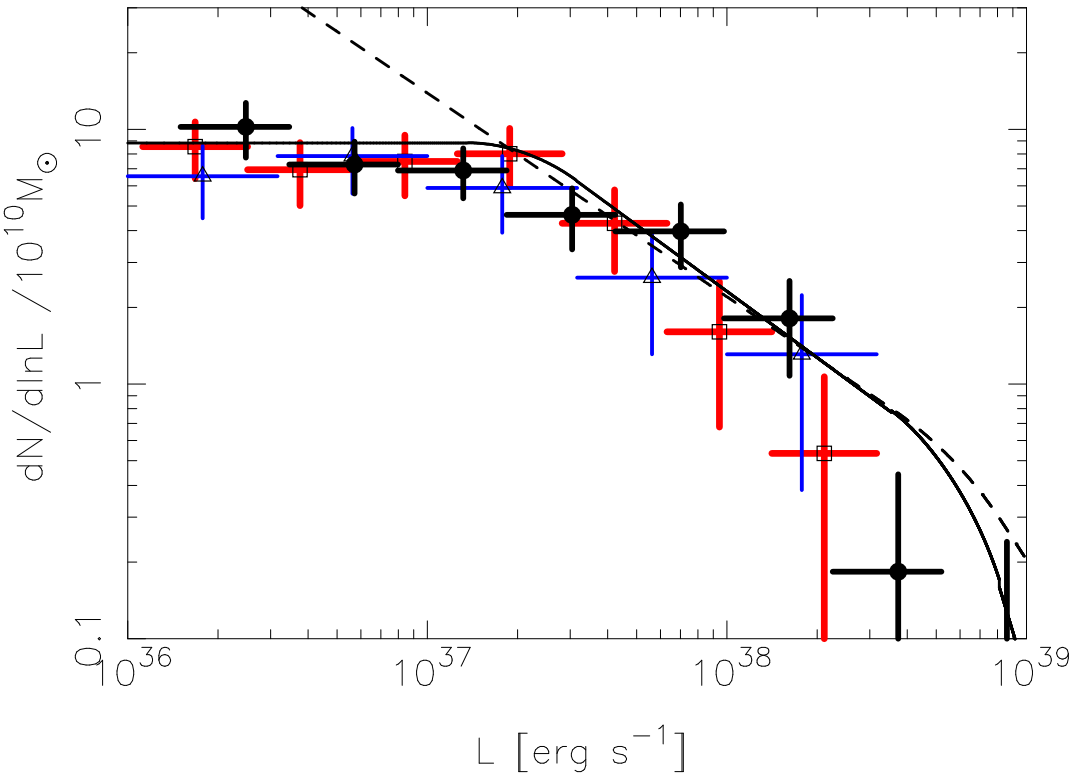

Figure 2.7: The luminosity function of LMXBs in the inner $r \leq 5$ arcmin of Cen A (the CXB contribution subtracted) in comparison with LMXB XLFs in the Milky Way (triangles) and M31 (squares) (from Gilfanov, 2004). The latter two are multiplied by constant factors of 1.7 and 0.6 respectively. The solid line shows the average LMXB XLF in the nearby galaxies as determined by Gilfanov (2004), the same as in Fig.2.6. The dashed line shows the average LMXB XLF from Kim & Fabbiano (2004) and its extrapolation towards low luminosities. Its normalization was chosen to approximately match our observations.

the extrapolation of their results is inconsistent with our observations. For sources more luminous than $L_X = 5.0 \cdot 10^{36}$ erg s^{-1}, a similar KS-test gives 3.4 per cent, and for lower luminosities the probability decreases further.

The LMXB XLF based on the combined data of $r \leq 5$ arcmin is plotted in Fig.2.7 along with luminosity distributions of LMXBs in the Milky Way and M31. This plot further illustrates the qualitative and quantitative similarity of the LMXB luminosity distributions in Cen A and bulges of spiral galaxies. This is the first study to extend the LMXB XLF in elliptical galaxies below $\sim$few$\times 10^{37}$ erg s^{-1}. Spiral and elliptical galaxies have different evolutionary histories and it could differ in the properties of their LMXB populations. As demonstrated here, the luminosity functions nevertheless seem very similar, except for the break luminosity which could be somewhat higher in Cen A than in the Milky Way and M31. Whether this reflects a systematic difference between LMXBs in galaxies of different type is yet to be investigated.

2.4.5 X/M_* ratios

In the inner (middle) region there are 53 (27) sources with $L_X > 10^{37}$ erg s^{-1}, with an integrated luminosity of $L_X = 2.3 \cdot 10^{39}$ ($1.3 \cdot 10^{39}$) erg s^{-1}. We expect the CXB contribution to be $N_{\rm CXB}$=3.8 (13.4), corresponding to a luminosity of $1.9 \cdot 10^{38}$ ($6.7 \cdot 10^{38}$) erg s^{-1}. From the K-band light we estimate that the stellar mass is $3.6{\cdot}10^{10}$ ($1.3{\cdot}10^{10}$) $M_\odot$, and this gives us the ratios N_X/M_*=13.7±1.9 (10.5±2.0) sources per 10^{10} $M_\odot$ and L_X/M_*=6.4 (4.8) $\times 10^{38}$ erg s^{-1} per 10^{10} $M_\odot$. The values for the two regions are consistent. They are also in a good agreement with the values for different nearby galaxies listed in Table 2 of Gilfanov (2004) as well as with the average values of $\langle N_X/M_* \rangle = 14.3$ and $\langle L_X/M_* \rangle = 8.0 \cdot 10^{38}$ erg/s per 10^{10} $M_\odot$.

The X/M_* ratios obtained in this paper are by a factor of 2 lower than the values for Cen A in Gilfanov (2004). He reported problems in approximating the multi-aperture K-band photometry data for Cen A galaxy. Indeed, we recomputed the K-band luminosity for the same region using the 2MASS K-band image and obtained ≈ 2 times larger number. This explains the lower values of N_X/M_* and L_X/M_* found in this paper. As these numbers are derived from the real K-band images rather than from extrapolation of the multi-aperture K-band photometry, they better represent the true values of the X/M_* ratios.

2.5 Summary and conclusions

We have used archival data of *CHANDRA* observations to study statistical properties of the point source population of Cen A. Our primary goal was to investigate the faint end of the LMXB luminosity distribution in an elliptical galaxy and to compare it with LMXB XLF in bulges of spiral galaxies.

To achieve this we assembled as deep a survey of the central part of the galaxy as permitted by the available data and implemented an adequate correction for the incompleteness effects.

Cen A is the closest giant elliptical galaxy and the only one with enough exposure time by *CHANDRA* to perform such a study. As Cen A is a merger remnant, the stellar and LMXB population might differ from those of less disturbed giant ellipticals. It is therefore important to further perform deep studies of the X-ray source population of more normal early-type galaxies.

Using a combined image of four ACIS observations (Table 2.1, Fig.2.1) with the total exposure time of 170 ks we have detected 272 point-like sources within 10 arcmin of the nucleus of Cen A. The luminosity of the weakest detected source is $\approx 9 \cdot 10^{35}$ erg s^{-1} (assuming a distance of 3.5 Mpc), while the source sample starts to be affected by the incompleteness effects below $\sim 10^{37}$ erg s^{-1} (Fig.2.8). After correction for incompleteness, the total number of sources with $L_X \geq 2 \cdot 10^{36}$ erg s^{-1} is ≈ 321. This number is in good agreement with the prediction based on the stellar mass, the star formation rate in Cen A and the density of CXB sources (Table 2.3). About half of the detected sources are expected to be X-ray binaries in Cen A, mostly LMXBs; the vast majority of the remaining sources are background galaxies constituting the resolved part of the CXB.

The spatial distribution of the detected sources can be well described by a sum of two components. Of these, one has a density proportional to the K-band light (Fig.2.4) and the other is uniform accross the Cen A field. We interpret this as that the former represents low-mass X-ray binaries in Cen A while the latter accounts for the resolved part of the CXB. The normalization of the LMXB component agrees well with the average value derived for the local galaxies by Gilfanov (2004). The normalization of the uniform component and source counts in the exteriors of the galaxy appear to indicate an overabundance of the CXB sources in the direction of Cen A by a factor of ~ 1.5 or, possibly, more (Table 2.4, Fig.2.5).

After applying the incompleteness correction and subtracting the contribution of CXB sources we were able to recover the the LMXB luminosity function in the inner $r \leq 5$ arcmin down to $L_X \sim 2 \cdot 10^{36}$ erg s^{-1} (Fig.2.6,2.7). This is by a factor of $\sim 5 - 10$ better than achieved previously for any elliptical galaxy (Kraft et al., 2001; Kim & Fabbiano, 2004). The shape of the luminosity distribution is consistent with the average LMXB XLF in nearby galaxies derived by Gilfanov (2004) and for the bright end by Kim & Fabbiano (2004). In particular, we demonstrate that the LMXB XLF in Cen A flattens at the faint end and is inconsistent with extrapolation of the steep power law with differential slope of $\approx 1.8-1.9$ observed above $\log(L_X) \sim 37.5-38$ in the previous studies of elliptical galaxies. Rather, the LMXB XLF in Cen A has a break at $L_X \approx (5 \pm 1) \cdot 10^{37}$ erg s^{-1} below which it follows the $dN/dL \propto L^{-1\pm0.1}$ law, similar to the behaviour found in the bulges of spiral galaxies.

Acknowledgements This reaserch has made use of *CHANDRA* archival data provided by the *CHANDRA* X-ray Center and data from the 2MASS Large Galaxy Atlas provided by NASA/IPAC infrared science archive. We would like to thank the referee for useful comments.

Bibliography

Bell, E., & De Jong, R. 2001, ApJ, 550, 212

Bildsten, L., & Deloye, C.J. 2004, ApJ, 607, L119

Cappelluti, N., Cappi, M., Dadina, M., et al., 2005, A&A, 430, 39

Colbert, E.J.M., Heckman, T.M., Ptak, A.F., Strickland, D.K., & Weaver, K.A. 2004, ApJ, 602, 231

Cowie, L.L., Garmire, G.P., Bautz, M.W., et al. 2002, ApJ, 566, L5

Dickey, J.M., & Lockman, F.J. 1990, ARA&A, 28, 215

Evans, D.A., Kraft, R.P., Worrall, D.M., et al. 2004, ApJ, 612, 786

Freeman, P.E., Kashyap, V., Rosner, R., & Lamb, D.Q. 2002, ApJ SS 138, 185

Gilfanov, M., 2004, MNRAS 349, 146

Graham, J.A., & Fasset, C.I. 2003, ApJ, 575, 712

Grimm, H-J., Gilfanov, M.R., & Sunyaev, R.A. 2003, MNRAS, 339, 793

Hardcastle, M.J., Worrall, D.M., Kraft, R.P., et al. 2003, ApJ 593, 169

Israel, F.P. 1998, A&A Rev., 8, 237

Jarret, T.H., Chester, T., Cutri, R., Schneider, S., & Huchra, J.P. 2003, AJ 125, 525

Kaaret, P. 2002, ApJ 578, 114

Karovska, M., Fabbiano, G., Nicastro, F., et al. 2002, ApJ, 577, 114

Kennicutt, R.C. 1998, ARA&A, 36, 189

Kim, D.-W.,& Fabbiano, G 2003, ApJ, 586, 826

Kim, D.-W.,& Fabbiano, G 2004, ApJ, 611, 846

Kraft, R.P., Kregenow, J.M., Forman, W.R., Jones, C., & Murray, S.S. 2001, ApJ, 560, 675

Kraft, R.P., Forman, W.R., Jones, C., et al. 2002, ApJ, 569, 54

Kraft, R.P., Vázquez, S.E, Forman, W.R., et al. 2003, ApJ, 592, 129

Marston, A.P., & Dickens, R.J. 1988, A&A, 193, 27

Minniti, D., Rejkuba, M., Funes, J.G., & Akiyama, S. 2003, ApJ, 600, 716

Monet, D.G., Levine, S.E., Canzian, B., et al. 2003, AJ, 125, 984

Moretti, A., Campana, S., Lazzati, D., & Tagliaferri, G. 2003, ApJ, 588, 696

Morrison, J.E., Röser, S., McLean, B., Bucciarelli, B., Lasker, B. 2001, AJ, 121, 1752

Peng, E.W., Ford, H.,C., & Freeman, K.C. 2003, ApJ SS, 150, 367

Postnov, K.A., & Kuranov, A.G. 2005, Astro. Lett., 31, 7

Press, W.H., Teukolsky, S.A., Vetterling, W.T., & Flannery, B.P. 1992, Numerical recipes in C. The art of scientific computing, University Press, Cambridge

Prestwich, A.H., Irwin, J.A., Kildgard, R.E., et al. 2003, ApJ 595, 719

Roeser, S., Bastian, U., & Wiese, K. 1991, A&A SS, 88, 277

Rosati, P., Tozzi, P., Giacconi, R., et al. 2002, ApJ, 556, 667

Schiminovich, D., van Gorkom, J.H., van der Hulst, J.M., & Kasow, S. 1994, ApJ, 423, L101

Shtykovskiy, P., & Gilfanov, M., 2005, A&A, 431, 597

Woodley, K.A., Harris, W.E., & Harris, G.L.H. 2005, AJ, 129, 2654

Appendix 2.A Correction for incompleteness

The variations of the diffuse background level and deterioration of the point spread function at large off-axis angles lead to variations of the point-source sensitivity accross the Chandra images. In the case where several observations with different pointing directions are combined, this effect is further amplified by the non uniform exposure of the combined image. As a result, the completness of the source sample at the faint end is compromised. A trivial solution to this problem is to define a conservative sensitivity limit, which is high enough to be achieved everywhere across the image. Although simple in implementation, this method has a disadvantage that a noticeable fraction of the source has to be thrown away. Nevertheless, it has been used, with few exceptions (e.g. Kim & Fabbiano, 2004; Shtykovskiy & Gilfanov, 2005), in the majority of the earlier studies of the point source populations in galaxies. A more effective approach to the problem is to define the correction function to the flux/luminosity distribution, which accounts for the sensitivity variations accross the image. For a uniform distribution of sources this correction function simply accounts for the dependence of the survey area upon the energy flux or count rate. This is the case, for example, in the

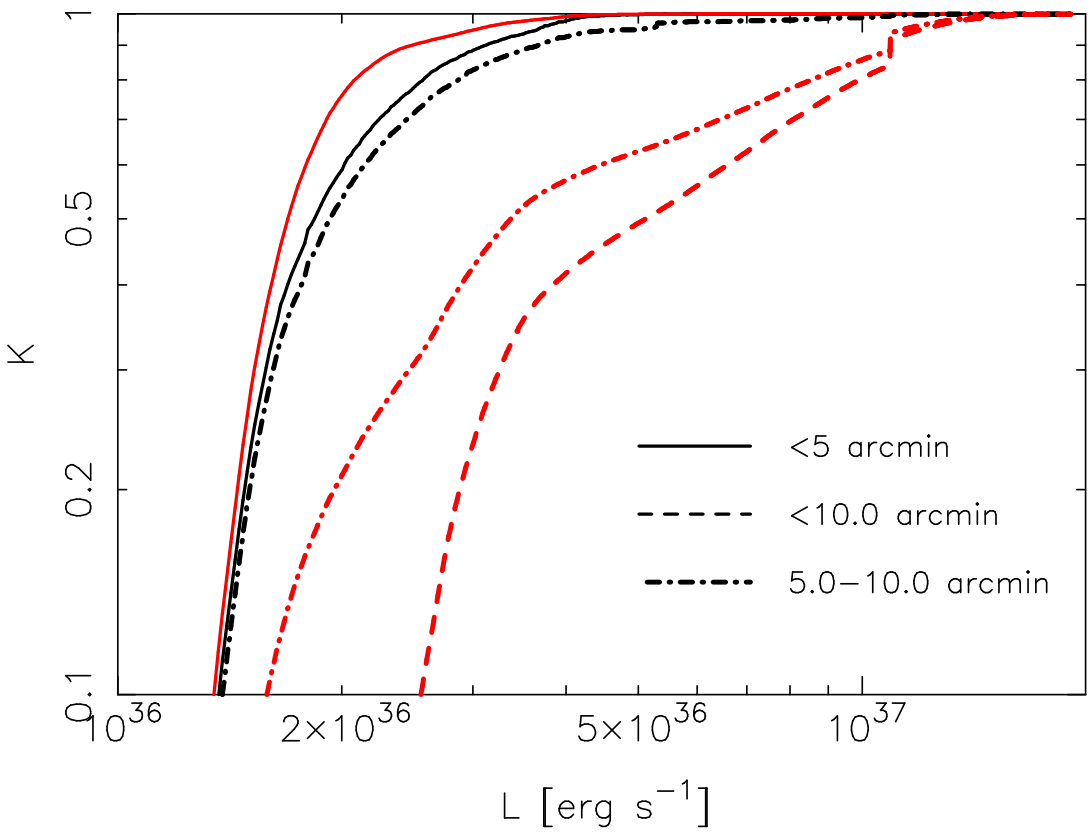

Figure 2.8: The sample incompleteness as a function of the luminosity for the inner (< 5 arcmin), outer (5–10 arcmin) and full region. The black lines are calculated using the source density proportional to the K-band light distribution. The grey lines are calculated assuming a uniform source density.

CXB studies. In a more complex case of a non-uniform distribution of point sources, the observed and real flux distributions are related via:

$$\left(\frac{dN}{dS}\right)_{\rm obs} = \int_{S_0 \le S} \frac{dN}{dS}\,\Sigma(x,y)\,dxdy \tag{2.1}$$

where $\Sigma(x,y)$ is the surface density distribution of point sources, and for given flux S the integration is performed over the part of the image where the local sensitivity $S_0(x,y)$ satisfies the condition $S_0(x,y) \le S$. If the flux distribution does not depend on the position, it can be easily recovered from the above equation. Importantly, knowledge of the spatial distribution of sources is required in order to recover the flux distribution and vice versa. If both flux and density distributions are unknown, the sample incompleteness can not be properly accounted for. The problem is further complicated by the contribution of the CXB sources, having a diferent spatial and flux distributions:

$$\left(\frac{dN}{dS}\right)_{\rm obs} = \int_{S_0 \le S} \left(\frac{dN}{dS}\right)_{\rm LMXB} \Sigma_{\rm xrb}(x,y)\,dxdy$$

$$+\int_{S_0\le S}\left(\frac{dN}{dS}\right)_{\rm CXB}\Sigma_{\rm cxb}(x,y)\,dxdy \qquad (2.2)$$

For the practical implementation of the correction procedure, knowledge of the source detection algorithm is of course required. The `wavdetect` task (Freeman et al., 2002) correlates the image with a Mexican Hat function and registers sources with the correlation value exceeding a threshold value. The latter is estimated numerically based on the user-specified threshold significance. For each of the used detection scales we computed the threshold sensitivity on a grid of the positions on the image (16 azimuthal angles, 40 radii from the centre of Cen A). At each image position the PSF was obtained from the CALDB PSF library for each of the four individual observations and then combined with the exposure times as weights. The local background levels were found from the normalized background maps created by `wavdetect`. The sensitivity for any given position on the image was found from interpolation of the grid values. The sample incompleteness is described by the incompleteness function:

$$K(L)=\sum_{L_0(i,j)\le L}\Sigma(i,j) \qquad (2.3)$$

where i,j are the pixel coordinates and $L_0(i,j)$ is the position-dependent sensitivity. Depending on the desired normalization of the $K(L)$, the the density distribution $\Sigma(i,j)$ can be normalized to unity or, for example, be given in the units of $M_\odot$ per pixel of the image.

If the CXB contribution can be neglected (eq.2.1), the corrected luminosity distribution can be obtained giving the weight $1/K(L)$ to a source of luminosity L. For the ML fits the model should be multiplied by the $K(L)$.

For the general case of eq.2.2, the incompleteness function $K(L)$ should be calculated for the CXB and LMXB components separately. For the LMXBs density distribution we used the K-band image, the CXB distribution was assumed to be uniform. The corresponding incompleteness functions are shown in Fig. 2.8. They demonstrate clearly importance of the spatial distribution of sources.

The results of one of our simulations are shown in Fig.2.9. In these simulations the background map from the `wavdetect` and the K-band image were azimutahlly averaged. The flux/luminosity distributions for the CXB sources and LMXBs were assumed in the form described in Sects. 2.4.3 and 2.4.4. In the simulations, the sources were randomly drawn from the assumed spatial and luminosity distributions and projected to the image using the PSF data from CALDB. The image of expectation values, containing the diffuse component and the point source contribution was then randomized assuming Poission statistics. The final image was analysed using the same chain of tasks as applied to the real images. The simulated and obtained luminosity distributions are shown in Fig.2.9.

The Figs.2.8 and 2.9 demonstrate that given the pattern of Chandra observations of Cen A, incompleteness effects are not of primary concern in the inner $r\lesssim 5$ arcmin region at the luminosoties above $\sim(2-3)\cdot 10^{36}$ erg/s. They should be taken into account, however, for the source counts in the entire image and in the outer ring.

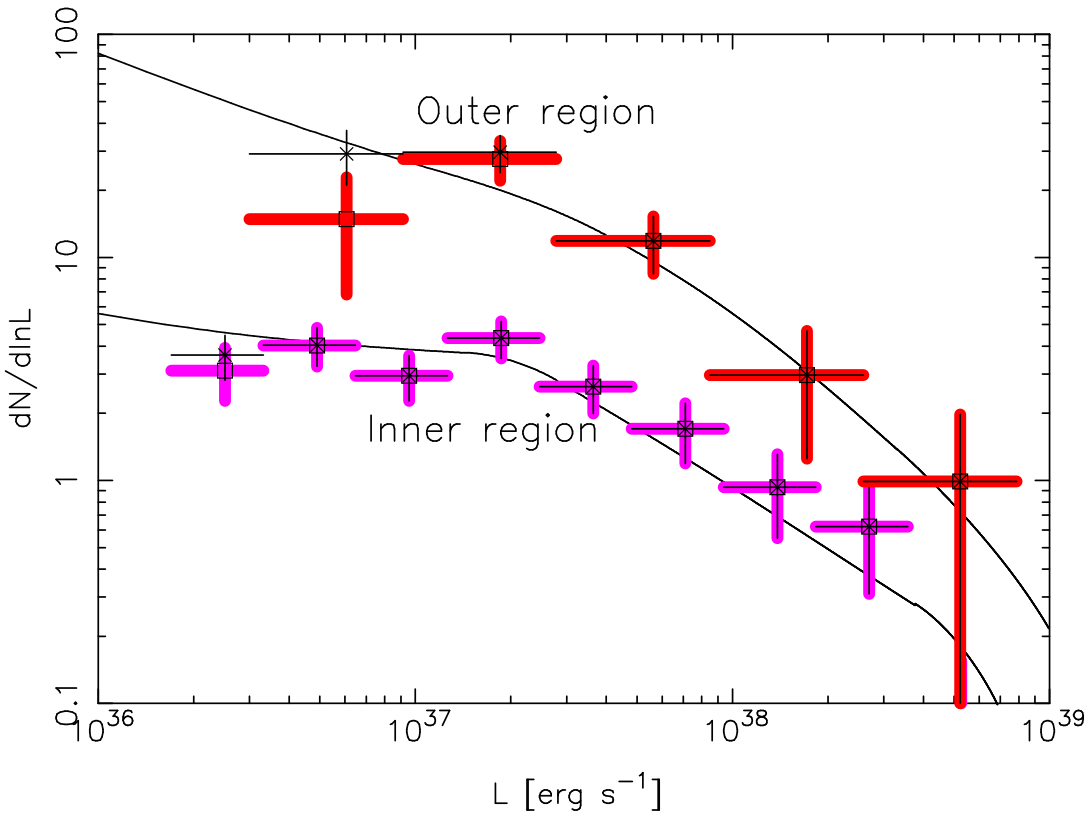

Figure 2.9: Simulated luminosity functions for the inner, $r \leq 5$ arcmin, and outer, $r \geq 5$ arcmin, regions. The input distributions (solid lines) are compared with the results obtained from the analysis of the images, done in the same way as the analysis of the real data. Both data corrected (asterisks) for incompleteness and uncorrected (squares) are shown. The normalization of the inner region has been divided by 10 for clarity.

2.A.1 Verification of the incompleteness correction

Although simulations described above show that the correction procedure is adequate for the analysis of Cen A, their accuracy is limited by the Poisonian statistics. Such accuracy limitations are intrinsic to full simulations of individual galaxies because the number of sources that can be put into a simulation is limited by the crowding effect. Another disadvantage of these simulation is that we used smoothed background maps produced by `wavdetect`, which, in addition, were azimuthally averaged.

In order to perform a more accurate and sensitive check of our incompleteness correction procedure we used a more direct, but also more computationally expensive, method, similar to the backward correction method suggested by Kim & Fabbiano (2003). In this method sources are placed one at a time on the real (unprocessed) observed image. For each simulated source the source detection and photometry are performed with the `wavdetect` task and then the original image is restored. As each source is put on the original undisturbed image, an arbitrarily large number of sources

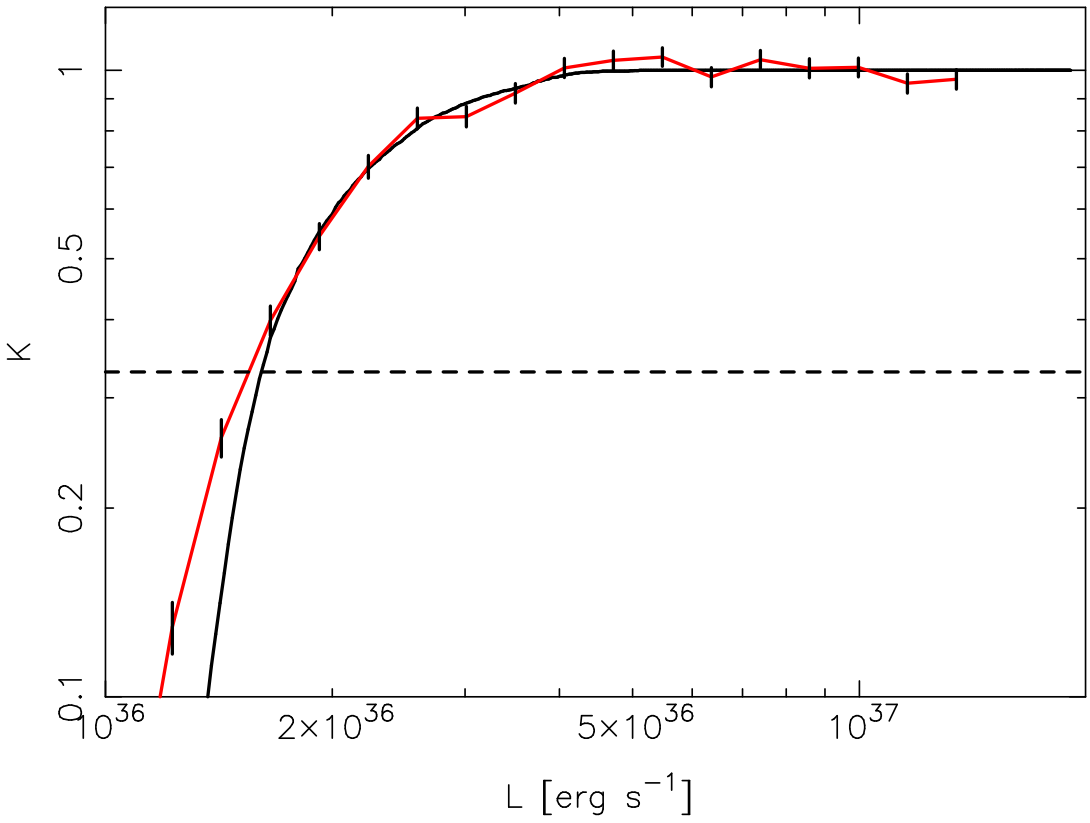

Figure 2.10: The incompleteness correction function for LMXBs within 5 arcmin from the centre of Cen A. The solid line is the function used throughout this paper, whereas the red line is found using the backward correction method of Kim & Fabbiano (2003). The dashed line marks the correction limit. Sources with a correction larger than this are not included in the analyses carried out in this paper.

can be simulated. The incompleteness function is given by the source detection efficiency and can be computed as a ratio of the flux distribution of the detected sources to the input flux distribution.

Using this method we checked the incompleteness correction for the region within 5 arcmin from the centre of Cen A, for the LMXB component. As above, the source distribution was assumed to follow the K-band light, and the differential luminosity function was chosen to follow 1/L. The sources were put on the image using the same method as in the simulations above, utilizing the CALDB PSF library together with the exposure map of the observations. To reduce statistical errors, we simulated 20,000 sources.

The resulting incompleteness correction, together with the correction function utilized throughout this paper, is shown in figure 2.10. As it can be seen from the figure, the two curves differ at low fluxes, corresponding to $L_X \lesssim 1.5 \cdot 10^{36}$ erg/s. The difference is caused by two effects. Firstly, the Eddington bias is neglected in our incompleteness correction calculations whereas it is automatically included in the

simulations. The second reason is that in the `wavdetect` task the source detection and countrate calculation are based on two different calculations. The source detection uses the correlation values of the wavelet transform to determine the source significance, whereas the photometry is performed on the original image. Although there is a linear relation between the expectation values of the source countrate and wavelet correlation, the measured numbers are subject to statistical fluctuations. This is ignored in the correction procedure, which uses the wavelet correlation values to both calculate the source significance and source flux. This effect is only important at low numbers of counts, where only a few sources are detected. These weak sources are excluded from our luminosity function analysis as we include only sources with the detection efficiency of $\geq 1/3$. For the weakest source used to plot Figs.2.5–2.7 the difference between two correction factors is 4.6%. In Fig. 2.7, for example, the lowest luminosity bin would decrease by $\sim 2\%$. This accuracy of the incompleteness correction is sufficient for the analysis presented in this paper.

Table 2.5: The list of point like X-ray sources within $r < 10$ arcmin from the center of Cen A.

ID (1)	CXO Name (2)	Dist (3)	R.A. (4)	Dec. (5)	T. Cts (6)	Src Cts (7)	Error (8)	Luminosity (9)	Type (10)	ID reference (11)
1	CXOU J132526.9-430052	17.5	13 25 27.0	-43 00 52.8	499	266.8	22.3	$2.36 \cdot 10^{37}$		
2	CXOU J132529.1-430114	18.1	13 25 29.2	-43 01 14.6	219	78.8	14.8	$7.17 \cdot 10^{36}$	H_α	mrfa-45
3	CXOU J132526.4-430054	19.1	13 25 26.5	-43 00 54.6	1905	1480.7	43.6	$1.28 \cdot 10^{38}$		
4	CXOU J132526.7-430126	19.7	13 25 26.8	-43 01 26.1	523	267.1	22.9	$2.29 \cdot 10^{37}$		
5	CXOU J132527.5-430128	19.8	13 25 27.5	-43 01 28.5	991	705.3	31.5	$5.99 \cdot 10^{37}$	GC	mrfa-053
6	CXOU J132529.4-430108	20.2	13 25 29.5	-43 01 08.3	498	297.4	22.3	$2.52 \cdot 10^{37}$	GC	mrfa-044
7	CXOU J132526.6-430129	23.3	13 25 26.6	-43 01 29.4	118	51.6	10.9	$5.25 \cdot 10^{36}$		
8	CXOU J132525.7-430056	23.8	13 25 25.8	-43 00 56.1	1862	1578.1	43.2	$1.35 \cdot 10^{38}$	GC	mrfa-017
9	CXOU J132525.2-430114	26.1	13 25 25.3	-43 01 14.3	105	61.7	10.2	$6.03 \cdot 10^{36}$		
10	CXOU J132529.6-430122	26.4	13 25 29.7	-43 01 22.5	68	31.3	8.2	$3.09 \cdot 10^{36}$		
11	CXOU J132525.5-430124	27.3	13 25 25.6	-43 01 24.2	259	110.3	16.1	$9.66 \cdot 10^{36}$		
12	CXOU J132528.4-430137	30.6	13 25 28.5	-43 01 37.9	96	42.9	9.8	$4.01 \cdot 10^{36}$		
13	CXOU J132525.1-430127	32.3	13 25 25.2	-43 01 27.1	741	565.7	27.2	$4.90 \cdot 10^{37}$	GC	mrfa-057
14	CXOU J132524.7-430125	34.9	13 25 24.8	-43 01 25.0	263	181.6	16.2	$1.66 \cdot 10^{37}$		
15	CXOU J132524.3-430110	35.8	13 25 24.4	-43 01 10.4	199	121.7	14.1	$1.09 \cdot 10^{37}$		
16	CXOU J132527.0-430030	38.7	13 25 27	-43 00 30.6	172	128.5	13.1	$1.15 \cdot 10^{37}$		
17	CXOU J132530.8-430128	40.5	13 25 30.9	-43 01 28.4	67	37.4	8.2	$3.54 \cdot 10^{36}$		
18	CXOU J132523.9-430059	41.5	13 25 23.9	-43 00 59.0	312	227.5	17.7	$2.00 \cdot 10^{37}$		
19	CXOU J132531.4-430057	43.9	13 25 31.5	-43 00 57.2	38	21.6	6.2	$2.05 \cdot 10^{36}$		
20	CXOU J132523.8-430127	45.2	13 25 23.9	-43 01 27.2	61	31.1	7.8	$3.24 \cdot 10^{36}$		
21	CXOU J132524.4-430141	47.6	13 25 24.4	-43 01 41.2	252	168.2	15.9	$1.51 \cdot 10^{37}$	H_α	mrfa-60
22	CXOU J132527.0-430159	50.9	13 25 27.1	-43 01 59.4	825	675.6	28.7	$5.76 \cdot 10^{37}$	H_α	mrfa-54
23	CXOU J132527.2-430016	52.9	13 25 27.3	-43 00 16.0	35	21.2	5.9	$2.23 \cdot 10^{36}$		
24	CXOU J132524.1-430145	53.0	13 25 24.2	-43 01 45.7	84	49.3	9.2	$4.74 \cdot 10^{36}$		
25	CXOU J132523.3-430043	53.1	13 25 23.4	-43 00 43.6	79	48.2	8.9	$4.61 \cdot 10^{36}$		
26	CXOU J132523.5-430138	53.9	13 25 23.5	-43 01 38.7	714	589.2	26.7	$5.15 \cdot 10^{37}$		
27	CXOU J132522.9-430125	54.2	13 25 22.9	-43 01 25.1	1947	1780	44.1	$1.53 \cdot 10^{38}$		
28	CXOU J132523.0-430134	56.1	13 25 23.1	-43 01 34.9	226	157.3	15	$1.46 \cdot 10^{37}$		
29	CXOU J132532.4-430134	58.9	13 25 32.5	-43 01 34.3	869	768.3	29.5	$6.41 \cdot 10^{37}$		
30	CXOU J132522.3-430122	59.1	13 25 22.4	-43 01 22.3	63	33.8	7.9	$3.37 \cdot 10^{36}$		
31	CXOU J132533.0-430108	59.9	13 25 33.1	-43 01 08.0	264	213.4	16.2	$1.80 \cdot 10^{37}$		
32	CXOU J132523.0-430145	61.9	13 25 23.1	-43 01 45.8	406	312.7	20.2	$2.77 \cdot 10^{37}$		
33	CXOU J132526.9-430004	64.4	13 25 26.9	-43 00 04.9	25	18.5	5.0	$4.84 \cdot 10^{36}$		
34	CXOU J132522.1-430132	65.0	13 25 22.1	-43 01 32.3	85	59.1	9.2	$6.00 \cdot 10^{36}$		
35	CXOU J132533.3-430053	65.0	13 25 33.4	-43 00 53.1	507	427.8	22.5	$3.64 \cdot 10^{37}$	H_α	mrfa-06
36	CXOU J132525.5-430210	65.5	13 25 25.6	-43 02 10.5	63	46	7.9	$4.54 \cdot 10^{36}$	GC	mrfa-055
37	CXOU J132527.4-430214	65.5	13 25 27.5	-43 02 14.3	1609	1496.2	40.1	$1.27 \cdot 10^{38}$		
38	CXOU J132531.3-430203	68.2	13 25 31.4	-43 02 03.3	22	18.8	4.7	$1.74 \cdot 10^{37}$		
39	CXOU J132527.6-430218	69.4	13 25 27.7	-43 02 18.2	288	227.8	17	$1.98 \cdot 10^{37}$	FS	mrfa-51
40	CXOU J132521.3-430046	72.1	13 25 21.4	-43 00 46.0	51	36.9	7.1	$3.72 \cdot 10^{36}$		
41	CXOU J132522.8-430017	72.9	13 25 22.9	-43 00 17.6	363	331.7	19.1	$3.02 \cdot 10^{37}$		
42	CXOU J132523.7-430009	73.0	13 25 23.7	-43 00 09.7	1835	1730	42.8	$1.50 \cdot 10^{38}$	H_α	mrfa-21
43	CXOU J132524.7-430002	73.2	13 25 24.8	-43 00 02.6	116	85.4	10.8	$7.40 \cdot 10^{36}$		
44	CXOU J132524.2-425959	78.5	13 25 24.2	-42 59 59.7	573	521.5	23.9	$4.55 \cdot 10^{37}$	H_α	mrfa-19
45	CXOU J132525.3-430223	78.8	13 25 25.3	-43 02 23.4	213	180.1	14.6	$1.63 \cdot 10^{37}$		
46	CXOU J132521.7-430154	78.8	13 25 21.7	-43 01 54.2	191	137.5	13.8	$1.22 \cdot 10^{37}$		
47	CXOU J132531.6-430003	78.9	13 25 31.6	-43 00 03.3	1023	962.6	32	$8.08 \cdot 10^{37}$	GC	pff-gc-210
48	CXOU J132528.7-425948	81.2	13 25 28.8	-42 59 48.6	1107	1034.7	33.3	$8.67 \cdot 10^{37}$		
49	CXOU J132521.2-430154	83.9	13 25 21.2	-43 01 55.0	212	189	14.6	$1.78 \cdot 10^{37}$		
50	CXOU J132523.5-430220	84.4	13 25 23.6	-43 02 20.8	465	421	21.6	$3.73 \cdot 10^{37}$		
51	CXOU J132521.2-430158	85.5	13 25 21.3	-43 01 58.9	223	174.4	14.9	$1.54 \cdot 10^{37}$		
52	CXOU J132521.5-430213	93.0	13 25 21.6	-43 02 13.8	146	124.7	12.1	$1.15 \cdot 10^{37}$		
53	CXOU J132520.8-430010	94.3	13 25 20.8	-43 00 10.8	27	20.3	5.2	$2.11 \cdot 10^{36}$		
54	CXOU J132532.0-430231	95.8	13 25 32.0	-43 02 31.5	535	490.7	23.1	$4.17 \cdot 10^{37}$	H_α	mrfa-40
55	CXOU J132525.8-425933	97.4	13 25 25.8	-42 59 33.4	33	17.4	5.7	$1.61 \cdot 10^{36}$		
56	CXOU J132530.3-425935	98.1	13 25 30.3	-42 59 35.2	136	89.8	11.7	$7.58 \cdot 10^{36}$	GC	pff-gc-209
57	CXOU J132518.9-430136	98.7	13 25 19.0	-43 01 37.0	67	48.6	8.2	$4.81 \cdot 10^{36}$		
58	CXOU J132529.0-425931	98.9	13 25 29.0	-42 59 31.1	95	59.8	9.7	$5.10 \cdot 10^{36}$		
59	CXOU J132536.6-430057	99.5	13 25 36.6	-43 00 57.6	303	233.9	17.4	$1.94 \cdot 10^{37}$		
60	CXOU J132518.5-430116	99.8	13 25 18.5	-43 01 16.3	578	523.1	24	$4.58 \cdot 10^{37}$	GC	mrfa-074
61	CXOU J132519.9-430203	100.4	13 25 19.9	-43 02 03.3	38	25	6.2	$2.69 \cdot 10^{36}$		
62	CXOU J132518.7-430141	102.7	13 25 18.7	-43 01 41.2	96	72.3	9.8	$7.04 \cdot 10^{36}$		
63	CXOU J132519.2-430158	104.6	13 25 19.2	-43 01 58.4	61	45.1	7.8	$5.07 \cdot 10^{36}$		
64	CXOU J132528.2-430253	105.0	13 25 28.2	-43 02 53.6	368	340.1	19.2	$2.98 \cdot 10^{37}$		
65	CXOU J132537.4-430131	110.2	13 25 37.4	-43 01 31.8	109	81.5	10.4	$6.81 \cdot 10^{36}$	GC	mrfa-033
66	CXOU J132526.7-430300	112.0	13 25 26.8	-43 03 00.4	188	159.4	13.7	$1.40 \cdot 10^{37}$		
67	CXOU J132518.7-430205	113.2	13 25 18.7	-43 02 05.8	41	27.3	6.4	$2.88 \cdot 10^{36}$		
68	CXOU J132522.2-430245	113.7	13 25 22.2	-43 02 45.8	126	116.9	11.2	$1.09 \cdot 10^{37}$	GC	pff-gc-121
69	CXOU J132520.6-425942	115.5	13 25 20.7	-42 59 42.1	22	12.7	4.7	$1.30 \cdot 10^{36}$		
70	CXOU J132530.4-425914	118.7	13 25 30.5	-42 59 14.3	496	435.8	22.3	$3.68 \cdot 10^{37}$		
71	CXOU J132535.2-430234	119.4	13 25 35.2	-43 02 34.1	150	120.8	12.2	$1.03 \cdot 10^{37}$		
72	CXOU J132517.8-430204	120.4	13 25 17.9	-43 02 04.4	209	181.6	14.5	$2.10 \cdot 10^{37}$		
73	CXOU J132531.9-430302	123.1	13 25 31.9	-43 03 02.5	56	38.2	7.5	$3.34 \cdot 10^{36}$		

Table 2.5: continued.

ID (1)	CXO Name (2)	Dist (3)	R.A. (4)	Dec. (5)	T. Cts (6)	Src Cts (7)	Error (8)	Luminosity (9)	Type (10)	ID reference (11)
74	CXOU J132527.8-425903	125.0	13 25 27.9	-42 59 03.9	43	26.5	6.6	$2.35 \cdot 10^{36}$		
75	CXOU J132528.4-430315	126.9	13 25 28.4	-43 03 15.4	251	211.5	15.8	$1.81 \cdot 10^{37}$		
76	CXOU J132535.5-425935	127.6	13 25 35.5	-42 59 35.3	609	549	24.7	$5.27 \cdot 10^{37}$	GC	pff-gc-214
77	CXOU J132538.3-430205	130.4	13 25 38.3	-43 02 05.8	2221	2158.8	47.1	$1.78 \cdot 10^{38}$		
78	CXOU J132539.4-430058	130.6	13 25 39.5	-43 00 58.9	39	22	6.2	$1.99 \cdot 10^{36}$		
79	CXOU J132517.0-430007	131.1	13 25 17.1	-43 00 07.5	46	33.9	6.8	$3.15 \cdot 10^{36}$		
80	CXOU J132533.3-425913	131.5	13 25 33.4	-42 59 13.6	101	78	10.1	$7.40 \cdot 10^{36}$		
81	CXOU J132515.7-430158	139.6	13 25 15.7	-43 01 58.2	58	44.7	7.6	$7.11 \cdot 10^{36}$		
82	CXOU J132533.6-430313	141.2	13 25 33.7	-43 03 13.3	188	159.3	13.7	$1.36 \cdot 10^{37}$		
83	CXOU J132514.8-430048	141.6	13 25 14.8	-43 00 48.7	42	21.3	6.5	$1.94 \cdot 10^{36}$		
84	CXOU J132540.5-430115	142.1	13 25 40.6	-43 01 15.2	638	587	25.3	$5.02 \cdot 10^{37}$		
85	CXOU J132538.2-430230	142.3	13 25 38.3	-43 02 30.5	15	9.4	3.9	$9.11 \cdot 10^{35}$		
86	CXOU J132523.6-430325	143.9	13 25 23.6	-43 03 25.9	256	221.8	16	$2.38 \cdot 10^{37}$		
87	CXOU J132533.9-425859	146.4	13 25 34.0	-42 58 59.9	558	514.4	23.6	$4.59 \cdot 10^{37}$	GC	pff-gc-159
88	CXOU J132520.0-430310	147.1	13 25 20.1	-43 03 10.4	367	317.4	19.2	$3.95 \cdot 10^{37}$	GC	mrfa-071
89	CXOU J132516.9-425938	147.9	13 25 16.9	-42 59 38.8	19	11.9	4.4	$1.18 \cdot 10^{36}$		
90	CXOU J132532.4-425850	148.1	13 25 32.4	-42 58 50.5	206	180.8	14.4	$1.80 \cdot 10^{37}$	GC	pff-gc-178
91	CXOU J132522.3-425852	148.2	13 25 22.4	-42 58 52.2	41	25.8	6.4	$2.34 \cdot 10^{36}$		
92	CXOU J132541.0-430126	148.6	13 25 41.1	-43 01 26.8	607	574.2	24.6	$4.95 \cdot 10^{37}$		
93	CXOU J132514.0-430121	149.6	13 25 14.0	-43 01 21.6	63	43.4	7.9	$6.44 \cdot 10^{36}$		
94	CXOU J132541.0-430037	150.0	13 25 41.0	-43 00 37.7	49	25.6	7	$2.21 \cdot 10^{36}$		
95	CXOU J132516.8-425932	152.7	13 25 16.8	-42 59 32.4	34	24.3	5.8	$2.29 \cdot 10^{36}$		
96	CXOU J132519.9-430317	153.5	13 25 19.9	-43 03 17.2	2263	2028.1	47.6	$2.10 \cdot 10^{38}$		
97	CXOU J132524.9-430341	155.2	13 25 24.9	-43 03 41.2	33	22.8	5.7	$2.46 \cdot 10^{36}$		
98	CXOU J132527.3-425829	159.2	13 25 27.3	-42 58 29.7	68	48.3	8.2	$4.29 \cdot 10^{36}$		
99	CXOU J132541.9-430142	161.0	13 25 42.0	-43 01 42.3	32	21.7	5.7	$1.98 \cdot 10^{36}$		
100	CXOU J132512.9-430114	161.4	13 25 12.9	-43 01 14.7	589	527.1	24.3	$7.40 \cdot 10^{37}$	GC	mrfa-082
101	CXOU J132520.6-425846	162.2	13 25 20.6	-42 58 46.0	712	676.3	26.7	$6.04 \cdot 10^{37}$		
102	CXOU J132516.4-430255	162.5	13 25 16.4	-43 02 55.4	290	262.1	17	$3.19 \cdot 10^{37}$		
103	CXOU J132538.6-425919	162.5	13 25 38.6	-42 59 20.0	99	70.5	10	$6.21 \cdot 10^{36}$	GC	pff-gc-164
104	CXOU J132512.4-430049	167.4	13 25 12.5	-43 00 49.4	56	39.5	7.5	$5.09 \cdot 10^{36}$		
105	CXOU J132512.0-430044	172.7	13 25 12.0	-43 00 44.6	343	302.3	18.5	$3.73 \cdot 10^{37}$		
106	CXOU J132540.0-430255	173.2	13 25 40.1	-43 02 55.5	45	27.1	6.7	$2.34 \cdot 10^{36}$		
107	CXOU J132527.9-430402	173.7	13 25 28.0	-43 04 02.5	194	167.4	13.9	$1.47 \cdot 10^{37}$	GC	mrfa-050
108	CXOU J132540.4-430251	174.4	13 25 40.5	-43 02 51.8	38	26.7	6.2	$2.37 \cdot 10^{36}$	H_α	mrfa-30
109	CXOU J132540.8-430247	175.0	13 25 40.8	-43 02 47.1	267	234.5	16.3	$1.97 \cdot 10^{37}$		
110	CXOU J132514.0-430243	175.8	13 25 14.1	-43 02 43.2	141	118.9	11.9	$1.29 \cdot 10^{37}$	GC	mrfa-080
111	CXOU J132535.7-430340	176.5	13 25 35.8	-43 03 40.9	44	33.7	6.6	$3.06 \cdot 10^{36}$		
112	CXOU J132512.0-430010	180.6	13 25 12.0	-43 00 11.0	473	441.9	21.7	$3.99 \cdot 10^{37}$	FS	mrfa-85
113	CXOU J132529.4-425809	180.6	13 25 29.4	-42 58 09.3	28	18	5.3	$1.96 \cdot 10^{36}$	GC	pff-gc-155
114	CXOU J132533.8-425821	180.8	13 25 33.9	-42 58 21.5	78	61.6	8.8	$5.72 \cdot 10^{36}$		
115	CXOU J132511.1-430132	182.7	13 25 11.1	-43 01 32.3	25	17.8	5	$2.54 \cdot 10^{36}$		
116	CXOU J132542.7-425943	186.6	13 25 42.8	-42 59 43.9	28	17.3	5.3	$1.60 \cdot 10^{36}$		
117	CXOU J132528.3-430416	187.9	13 25 28.3	-43 04 16.5	113	95.9	10.6	$8.55 \cdot 10^{36}$		
118	CXOU J132511.5-430226	192.1	13 25 11.6	-43 02 26.6	184	161.9	13.6	$1.74 \cdot 10^{37}$		
119	CXOU J132514.5-425858	193.9	13 25 14.5	-42 58 58.7	22	13.7	4.7	$1.37 \cdot 10^{36}$		
120	CXOU J132517.7-430350	194.4	13 25 17.8	-43 03 50.6	43	29.9	6.6	$3.45 \cdot 10^{36}$		
121	CXOU J132545.6-430115	197.9	13 25 45.7	-43 01 15.9	79	43.1	8.9	$3.62 \cdot 10^{36}$	GAL	whh-317
122	CXOU J132524.9-430425	199.1	13 25 24.9	-43 04 25.7	151	132.9	12.3	$1.58 \cdot 10^{37}$		
123	CXOU J132512.1-425918	201.8	13 25 12.2	-42 59 18.8	34	25.3	5.8	$2.57 \cdot 10^{36}$		
124	CXOU J132529.3-425747	201.8	13 25 29.3	-42 57 47.8	48	23.8	6.9	$2.18 \cdot 10^{36}$	GC	whh-22
125	CXOU J132514.8-425840	204.1	13 25 14.8	-42 58 40.8	33	23.2	5.7	$2.23 \cdot 10^{36}$		
126	CXOU J132542.1-430319	206.0	13 25 42.1	-43 03 20.0	52	30.5	7.2	$2.59 \cdot 10^{36}$	GC	mrfa-026
127	CXOU J132538.2-425815	208.6	13 25 38.2	-42 58 15.8	131	107	11.4	$9.14 \cdot 10^{36}$	GC	mrfa-003
128	CXOU J132532.8-430429	208.8	13 25 32.9	-43 04 29.4	173	146.6	13.2	$1.30 \cdot 10^{37}$		
129	CXOU J132546.4-430036	209.2	13 25 46.5	-43 00 36.7	54	31.1	7.3	$2.82 \cdot 10^{36}$		
130	CXOU J132519.0-425759	211.5	13 25 19.1	-42 57 59.3	55	42.9	7.4	$4.28 \cdot 10^{36}$		
131	CXOU J132524.4-425735	216.1	13 25 24.4	-42 57 35.6	12	7.1	3.5	$2.08 \cdot 10^{36}$		
132	CXOU J132513.1-425841	216.5	13 25 13.2	-42 58 41.2	23	17.2	4.8	$1.93 \cdot 10^{36}$		
133	CXOU J13257.82-430059	217.3	13 25 07.8	-43 00 59.8	24	15.9	4.9	$2.06 \cdot 10^{36}$		
134	CXOU J132532.3-430441	218.7	13 25 32.3	-43 04 41.3	49	34.3	7.0	$3.27 \cdot 10^{36}$		
135	CXOU J132507.6-430115	219.1	13 25 07.7	-43 01 15.5	2028	1873	45.0	$1.90 \cdot 10^{38}$	GC	whh-8
136	CXOU J132516.0-430411	222.1	13 25 16.0	-43 04 11.1	31	17.2	5.6	$2.14 \cdot 10^{36}$		
137	CXOU J132547.6-430030	223.0	13 25 47.7	-43 00 30.7	89	45	9.4	$4.18 \cdot 10^{36}$		
138	CXOU J132543.2-425837	228.5	13 25 43.2	-42 58 37.6	152	120.9	12.3	$1.04 \cdot 10^{37}$	GC	pff-gc-062
139	CXOU J132509.3-425917	229.0	13 25 09.4	-42 59 17.6	78	45.4	8.8	$4.13 \cdot 10^{36}$		
140	CXOU J132521.8-430451	231.3	13 25 21.8	-43 04 51.2	120	70.1	11	$7.33 \cdot 10^{36}$		
141	CXOU J132512.0-425830	233.2	13 25 12.0	-42 58 30.7	63	33.6	7.9	$3.02 \cdot 10^{36}$		
142	CXOU J132512.3-425824	234.6	13 25 12.3	-42 58 24.5	82	56.4	9.1	$5.12 \cdot 10^{36}$		
143	CXOU J132547.1-430243	234.7	13 25 47.2	-43 02 43.6	181	151.7	13.5	$1.32 \cdot 10^{37}$		
144	CXOU J132514.8-430418	235.4	13 25 14.8	-43 04 18.0	89	35.8	9.4	$3.89 \cdot 10^{36}$		
145	CXOU J132538.8-430432	237.9	13 25 38.9	-43 04 32.1	32	17.5	5.7	$1.63 \cdot 10^{36}$		
146	CXOU J132522.3-425717	238.4	13 25 22.4	-42 57 17.4	914	845.7	30.2	$7.37 \cdot 10^{37}$	GC	mrfa-208
147	CXOU J132546.3-430310	239.1	13 25 46.4	-43 03 10.8	406	356.8	20.1	$3.35 \cdot 10^{37}$	FS	mrfa-93

Table 2.5: continued.

ID (1)	CXO Name (2)	Dist (3)	R.A. (4)	Dec. (5)	T. Cts (6)	Src Cts (7)	Error (8)	Luminosity (9)	Type (10)	ID reference (11)
148	CXOU J132509.2-425859	239.7	13 25 09.2	-42 58 59.5	682	594	26.1	$5.21 \cdot 10^{37}$	GC	mrfa-215
149	CXOU J132506.3-430221	244.4	13 25 06.3	-43 02 21.2	974	818.5	31.2	$8.26 \cdot 10^{37}$		
150	CXOU J132515.8-425739	245.6	13 25 15.8	-42 57 39.9	141	106.5	11.9	$9.78 \cdot 10^{36}$		
151	CXOU J132505.0-430133	248.9	13 25 05.0	-43 01 33.5	292	239.9	17.1	$2.51 \cdot 10^{37}$		
152	CXOU J132534.2-425709	249.9	13 25 34.3	-42 57 09.7	47	25.2	6.9	$2.46 \cdot 10^{36}$		
153	CXOU J132547.6-425903	252.6	13 25 47.6	-42 59 03.8	56	36.4	7.5	$3.31 \cdot 10^{36}$		
154	CXOU J132529.2-430521	253.4	13 25 29.2	-43 05 21.5	32	19.4	5.7	$3.10 \cdot 10^{36}$		
155	CXOU J132548.5-430258	254.6	13 25 48.6	-43 02 58.4	33	18.8	5.7	$2.02 \cdot 10^{36}$		
156	CXOU J132527.5-430525	256.5	13 25 27.6	-43 05 25.3	55	37.2	7.4	$4.92 \cdot 10^{36}$		
157	CXOU J132538.5-425720	258.0	13 25 38.6	-42 57 20.5	102	57.5	10.1	$5.36 \cdot 10^{36}$		
158	CXOU J132518.8-425708	258.7	13 25 18.9	-42 57 08.5	91	61.5	9.5	$6.02 \cdot 10^{36}$		
159	CXOU J132523.5-425651	260.7	13 25 23.5	-42 56 52.0	204	170.4	14.3	$1.78 \cdot 10^{37}$		
160	CXOU J132504.4-430008	261.5	13 25 04.4	-43 00 08.2	94	69.8	9.7	$7.71 \cdot 10^{36}$		
161	CXOU J132545.5-425815	261.7	13 25 45.5	-42 58 15.9	242	179.5	15.6	$1.73 \cdot 10^{37}$		
162	CXOU J132533.6-430525	265.1	13 25 33.7	-43 05 25.4	86	63.8	9.3	$8.22 \cdot 10^{36}$	FS	HD 116647 fs
163	CXOU J132548.5-430322	265.6	13 25 48.5	-43 03 22.8	56	41.8	7.5	$5.83 \cdot 10^{36}$		
164	CXOU J132539.8-430501	268.9	13 25 39.8	-43 05 01.9	100	86.8	10	$2.20 \cdot 10^{37}$	GC	pff-gc-111
165	CXOU J132547.2-425825	270.0	13 25 47.2	-42 58 25.6	179	139.7	13.4	$1.22 \cdot 10^{37}$		
166	CXOU J132538.0-430513	270.4	13 25 38.1	-43 05 13.6	98	82.2	9.9	$2.00 \cdot 10^{37}$		
167	CXOU J132526.1-425636	272.5	13 25 26.2	-42 56 36.7	184	139.6	13.6	$1.25 \cdot 10^{37}$		
168	CXOU J132549.4-425858	273.2	13 25 49.5	-42 58 58.4	34	16.6	5.8	$1.62 \cdot 10^{36}$		
169	CXOU J132535.2-430529	273.3	13 25 35.2	-43 05 29.0	18	14.2	4.2	$4.67 \cdot 10^{36}$	GC	whh-17
170	CXOU J132527.5-430549	281.1	13 25 27.6	-43 05 49.9	59	35.1	7.7	$4.60 \cdot 10^{36}$		
171	CXOU J132503.5-425928	282.5	13 25 03.5	-42 59 28.8	29	17.2	5.4	$2.36 \cdot 10^{36}$		
172	CXOU J132539.1-425654	284.3	13 25 39.1	-42 56 54.0	352	297.3	18.8	$2.67 \cdot 10^{37}$		
173	CXOU J132507.4-430409	285.5	13 25 07.5	-43 04 09.3	6878	6474.7	82.9	$6.69 \cdot 10^{38}$	FS	Kraft
174	CXOU J132553.5-430134	285.7	13 25 53.6	-43 01 34.9	73	44.4	8.5	$3.95 \cdot 10^{36}$		
175	CXOU J132546.7-425752	287.1	13 25 46.7	-42 57 52.6	90	40.5	9.5	$3.51 \cdot 10^{36}$		
176	CXOU J132502.7-430243	289.0	13 25 02.7	-43 02 43.5	2412	2257.9	49.1	$2.45 \cdot 10^{38}$		
177	CXOU J132532.7-425624	290.1	13 25 32.8	-42 56 24.2	165	115.8	12.8	$1.01 \cdot 10^{37}$	GC	pff-gc-056
178	CXOU J132512.0-425713	291.2	13 25 12.0	-42 57 13.3	29	21.9	5.4	$9.13 \cdot 10^{36}$		
179	CXOU J132555.1-430119	301.8	13 25 55.1	-43 01 19.2	198	153.7	14.1	$1.31 \cdot 10^{37}$		
180	CXOU J132538.4-425630	302.2	13 25 38.4	-42 56 30.8	150	100.3	12.2	$8.94 \cdot 10^{36}$		
181	CXOU J132520.2-425615	304.3	13 25 20.3	-42 56 15.4	42	32.2	6.5	$1.02 \cdot 10^{37}$		
182	CXOU J132552.2-425830	312.9	13 25 52.2	-42 58 30.7	71	21.6	8.4	$1.86 \cdot 10^{36}$	GC	pff-gc-072
183	CXOU J132554.6-425925	313.4	13 25 54.6	-42 59 25.8	1500	1311.5	38.7	$1.10 \cdot 10^{38}$	GC	pff-gc-131
184	CXOU J132549.7-430430	315.7	13 25 49.8	-43 04 30.3	26	18.5	5.1	$5.02 \cdot 10^{36}$		
185	CXOU J132556.8-430044	321.8	13 25 56.9	-43 00 44.8	319	244.3	17.9	$2.07 \cdot 10^{37}$		
186	CXOU J132546.5-425703	321.8	13 25 46.6	-42 57 03.4	638	487.2	25.3	$4.56 \cdot 10^{37}$	GC	pff-gc-168
187	CXOU J132549.1-430447	321.9	13 25 49.2	-43 04 47.3	60	37.2	7.7	$8.91 \cdot 10^{36}$		
188	CXOU J132508.2-430511	322.2	13 25 08.3	-43 05 11.3	364	189.8	19.1	$2.11 \cdot 10^{37}$		
189	CXOU J132509.5-430529	327.5	13 25 09.6	-43 05 29.6	538	418.6	23.2	$4.66 \cdot 10^{37}$		
190	CXOU J132534.4-425549	327.6	13 25 34.5	-42 55 49.8	239	164.9	15.5	$1.48 \cdot 10^{37}$		
191	CXOU J132518.5-425547	336.0	13 25 18.6	-42 55 47.8	10	6.4	3.2	$3.11 \cdot 10^{36}$		
192	CXOU J132553.4-425806	336.9	13 25 53.4	-42 58 06.5	106	40.4	10.3	$3.50 \cdot 10^{36}$		
193	CXOU J132512.8-430606	338.8	13 25 12.9	-43 06 06.6	43	25.1	6.6	$3.07 \cdot 10^{36}$		
194	CXOU J132547.3-425647	339.5	13 25 47.4	-42 56 47.4	144	70.8	12	$6.87 \cdot 10^{36}$		
195	CXOU J132539.4-425546	347.6	13 25 39.4	-42 55 46.3	94	38.9	9.7	$3.44 \cdot 10^{36}$		
196	CXOU J132543.9-430610	350.1	13 25 43.9	-43 06 10.0	146	132.4	12.1	$5.91 \cdot 10^{37}$		
197	CXOU J132507.7-425630	353.6	13 25 07.7	-42 56 30.5	70	56.3	8.4	$2.80 \cdot 10^{37}$	GC	mrfa-216
198	CXOU J132510.1-425608	356.5	13 25 10.2	-42 56 08.0	39	30.2	6.2	$1.61 \cdot 10^{37}$		
199	CXOU J132545.2-425604	360.4	13 25 45.2	-42 56 04.5	95	31	9.7	$2.90 \cdot 10^{36}$		
200	CXOU J132456.1-430258	362.3	13 24 56.1	-43 02 59.0	144	80.9	12	$1.09 \cdot 10^{37}$		
201	CXOU J132557.2-425822	364.8	13 25 57.2	-42 58 22.3	414	291.8	20.3	$3.12 \cdot 10^{37}$		
202	CXOU J132510.6-430624	366.3	13 25 10.7	-43 06 24.5	398	299.5	20	$3.28 \cdot 10^{37}$		
203	CXOU J132522.7-425502	370.6	13 25 22.7	-42 55 02.1	109	92	10.4	$4.22 \cdot 10^{37}$		
204	CXOU J132601.4-430043	372.3	13 26 01.5	-43 00 43.5	109	37.9	10.4	$3.32 \cdot 10^{36}$		
205	CXOU J132554.6-425720	374.0	13 25 54.6	-42 57 20.8	38	16.1	6.2	$2.15 \cdot 10^{36}$		
206	CXOU J132531.4-430720	374.2	13 25 31.4	-43 07 20.7	33	26.6	5.7	$1.24 \cdot 10^{37}$		
207	CXOU J132529.1-425447	381.9	13 25 29.2	-42 54 47.3	22	15.5	4.7	$6.89 \cdot 10^{36}$		
208	CXOU J132545.2-425530	389.6	13 25 45.2	-42 55 30.6	96	36.9	9.8	$3.92 \cdot 10^{36}$		
209	CXOU J132552.6-430545	389.6	13 25 52.6	-43 05 45.5	45	38.1	6.7	$1.79 \cdot 10^{37}$	GC	pff-gc-129
210	CXOU J132503.1-425625	390.5	13 25 03.1	-42 56 25.5	43	29	6.6	$1.43 \cdot 10^{37}$	GC	pff-gc-157
211	CXOU J132557.2-430450	393.1	13 25 57.2	-43 04 50.5	68	44.2	8.2	$1.05 \cdot 10^{37}$		
212	CXOU J132558.6-430430	395.6	13 25 58.7	-43 04 30.4	1259	1180.4	35.5	$2.69 \cdot 10^{38}$		
213	CXOU J132510.0-430655	396.1	13 25 10.1	-43 06 55.1	137	90.2	11.7	$1.22 \cdot 10^{37}$		
214	CXOU J132529.0-430744	396.2	13 25 29.0	-43 07 44.7	23	16.5	4.8	$7.34 \cdot 10^{36}$		
215	CXOU J132549.6-430624	397.9	13 25 49.7	-43 06 24.7	18	10.5	4.2	$4.58 \cdot 10^{36}$		
216	CXOU J132510.2-425510	405.4	13 25 10.3	-42 55 10.8	80	65	8.9	$3.34 \cdot 10^{37}$		
217	CXOU J132513.9-430725	405.7	13 25 14	-43 07 25.9	222	168.2	14.9	$2.72 \cdot 10^{37}$		
218	CXOU J132548.7-425530	409.8	13 25 48.8	-42 55 31.0	76	47.7	8.7	$1.05 \cdot 10^{37}$		
219	CXOU J132557.8-425702	413.6	13 25 57.9	-42 57 02.5	393	296.1	19.8	$4.21 \cdot 10^{37}$		
220	CXOU J132521.2-425413	420.9	13 25 21.3	-42 54 13.7	113	98.8	10.6	$4.82 \cdot 10^{37}$		
221	CXOU J132606.3-430112	424.8	13 26 06.4	-43 01 12.3	35	19.7	5.9	$5.82 \cdot 10^{36}$		

Table 2.5: continued.

ID (1)	CXO Name (2)	Dist (3)	R.A. (4)	Dec. (5)	T. Cts (6)	Src Cts (7)	Error (8)	Luminosity (9)	Type (10)	ID reference (11)
222	CXOU J132545.4-425451	424.9	13 25 45.4	-42 54 51.4	119	80.3	10.9	$1.69 \cdot 10^{37}$		
223	CXOU J132533.2-430810	426.3	13 25 33.2	-43 08 10.6	38	28.1	6.2	$1.25 \cdot 10^{37}$		
224	CXOU J132522.7-430822	436.7	13 25 22.7	-43 08 22.2	20	13.3	4.5	$6.24 \cdot 10^{36}$		
225	CXOU J132501.0-430643	443.8	13 25 01.1	-43 06 43.8	971	853	31.2	$1.16 \cdot 10^{38}$		
226	CXOU J132511.1-430755	445.1	13 25 11.2	-43 07 55.9	144	101.4	12	$1.48 \cdot 10^{37}$		
227	CXOU J132506.8-430736	449.7	13 25 06.8	-43 07 36.5	86	43.1	9.3	$6.10 \cdot 10^{36}$		
228	CXOU J132601.2-430528	450.3	13 26 01.2	-43 05 28.0	949	919.9	30.8	$4.14 \cdot 10^{38}$		
229	CXOU J132544.1-430804	453.4	13 25 44.1	-43 08 04.5	146	135.7	12.1	$6.92 \cdot 10^{37}$		
230	CXOU J132540.4-430820	453.7	13 25 40.5	-43 08 20.1	18	11	4.2	$5.37 \cdot 10^{36}$		
231	CXOU J132550.3-425441	460.3	13 25 50.3	-42 54 41.9	82	34.4	9.1	$4.82 \cdot 10^{36}$		
232	CXOU J132459.0-430648	462.6	13 24 59.0	-43 06 48.9	74	34.9	8.6	$4.96 \cdot 10^{36}$		
233	CXOU J132450.4-430452	464.9	13 24 50.4	-43 04 52.3	106	55.9	10.3	$7.67 \cdot 10^{36}$		
234	CXOU J132557.5-425531	470.6	13 25 57.5	-42 55 31.5	73	38.2	8.5	$5.28 \cdot 10^{36}$		
235	CXOU J132504.0-425431	474.2	13 25 04	-42 54 31.5	107	44.1	10.3	$6.57 \cdot 10^{36}$		
236	CXOU J132609.9-430310	479.6	13 26 09.9	-43 03 10.5	32	17.3	5.7	$4.32 \cdot 10^{36}$		
237	CXOU J132557.5-430659	479.6	13 25 57.5	-43 06 59.2	23	16.7	4.8	$8.07 \cdot 10^{36}$		
238	CXOU J132513.9-425331	481.3	13 25 13.9	-42 53 31.5	344	283.6	18.5	$4.18 \cdot 10^{37}$		
239	CXOU J132548.1-430817	483.9	13 25 48.1	-43 08 17.2	43	29.7	6.6	$1.35 \cdot 10^{37}$		
240	CXOU J132511.3-430843	488.6	13 25 11.3	-43 08 43.5	51	34.2	7.1	$1.11 \cdot 10^{37}$		
241	CXOU J132542.0-425323	491.9	13 25 42.0	-42 53 23.1	26	16.6	5.1	$8.55 \cdot 10^{36}$		
242	CXOU J132510.3-425333	493.4	13 25 10.4	-42 53 33.2	415	334.4	20.4	$4.92 \cdot 10^{37}$		
243	CXOU J132611.8-430242	494.0	13 26 11.9	-43 02 42.9	280	247	16.7	$6.45 \cdot 10^{37}$		
244	CXOU J132535.1-425301	494.1	13 25 35.2	-42 53 01.7	246	233.2	15.7	$1.04 \cdot 10^{38}$		
245	CXOU J132546.7-425340	495.2	13 25 46.7	-42 53 40.1	209	118.5	14.5	$1.64 \cdot 10^{37}$		
246	CXOU J132502.9-425413	496.3	13 25 02.9	-42 54 13.2	307	211.7	17.5	$3.10 \cdot 10^{37}$		
247	CXOU J132605.5-425632	499.4	13 26 05.5	-42 56 32.5	191	132.7	13.8	$1.89 \cdot 10^{37}$	GC	pff-gc-122
248	CXOU J132555.4-430745	500.7	13 25 55.5	-43 07 45.8	29	20.6	5.4	$9.29 \cdot 10^{36}$		
249	CXOU J132614.1-430208	513.4	13 26 14.1	-43 02 08.6	73	55.6	8.5	$2.84 \cdot 10^{37}$		
250	CXOU J132511.0-425257	523.7	13 25 11.0	-42 52 57.8	50	26.5	7.1	$4.44 \cdot 10^{36}$		
251	CXOU J132527.3-430953	524.3	13 25 27.3	-43 09 53.1	61	48	7.8	$2.21 \cdot 10^{37}$		
252	CXOU J132458.9-430831	542.7	13 24 58.9	-43 08 31.3	167	86.8	12.9	$1.33 \cdot 10^{37}$		
253	CXOU J132456.7-430813	543.0	13 24 56.8	-43 08 13.7	798	594.6	28.3	$8.36 \cdot 10^{37}$		
254	CXOU J132539.2-430957	543.6	13 25 39.2	-43 09 57.3	38	24.9	6.2	$1.15 \cdot 10^{37}$		
255	CXOU J132615.9-425846	548.4	13 26 15.9	-42 58 46.8	530	392.4	23	$4.70 \cdot 10^{37}$		
256	CXOU J132546.4-430937	549.4	13 25 46.5	-43 09 38.0	119	102.7	10.9	$4.67 \cdot 10^{37}$		
257	CXOU J132450.4-430722	553.0	13 24 50.5	-43 07 22.9	271	151.4	16.5	$2.17 \cdot 10^{37}$		
258	CXOU J132557.4-425342	553.8	13 25 57.5	-42 53 42.2	282	136.4	16.8	$1.52 \cdot 10^{37}$	FS	GF Blue 1
259	CXOU J132525.9-425152	556.4	13 25 26.0	-42 51 52.7	160	96.2	12.7	$1.44 \cdot 10^{37}$		
260	CXOU J132549.3-425241	560.6	13 25 49.3	-42 52 41.4	897	757.4	30	$1.55 \cdot 10^{38}$		
261	CXOU J132503.1-430924	563.6	13 25 03.1	-43 09 24.3	163	85.2	12.8	$1.28 \cdot 10^{37}$		
262	CXOU J132510.9-425214	564.4	13 25 11.0	-42 52 14.8	109	56.3	10.4	$9.01 \cdot 10^{36}$		
263	CXOU J132534.0-431030	565.8	13 25 34.0	-43 10 30.2	46	34.5	6.8	$1.61 \cdot 10^{37}$		
264	CXOU J132613.0-425632	569.9	13 26 13.1	-42 56 32.9	142	68.8	11.9	$7.77 \cdot 10^{36}$		
265	CXOU J132620.4-425947	585.6	13 26 20.5	-42 59 47.2	142	78.6	11.9	$1.94 \cdot 10^{37}$		
266	CXOU J132619.7-430318	586.0	13 26 19.7	-43 03 18.8	75	52.7	8.7	$2.60 \cdot 10^{37}$		
267	CXOU J132454.4-425326	588.5	13 24 54.4	-42 53 26.8	65	35.2	8.1	$7.91 \cdot 10^{36}$		
268	CXOU J132541.7-425137	592.0	13 25 41.7	-42 51 37.3	24	18	4.9	$8.28 \cdot 10^{36}$		
269	CXOU J132541.9-431041	593.6	13 25 41.9	-43 10 41.4	642	610.1	25.3	$2.86 \cdot 10^{38}$	GC	pff-gc-188
270	CXOU J132544.2-425141	595.8	13 25 44.3	-42 51 41.7	18	12.9	4.2	$5.96 \cdot 10^{36}$		
271	CXOU J132548.4-425156	597.4	13 25 48.5	-42 51 56.9	25	20.8	5	$9.54 \cdot 10^{36}$		
272	CXOU J132531.0-431105	597.7	13 25 31.0	-43 11 05.3	152	139.1	12.3	$7.25 \cdot 10^{37}$	GAL	pff-qso-6

(1) – the sequence number; (2) – CXO source name, according to the *CHANDRA*-discovered source naming convention; (3) – distance from the center in arcsec; (4),(5) – right ascension and declination, J2000; (6) – total number of counts in the `wavdetect` source cell, source+background; (7) – number of source counts after background subtraction (8) – statistical error on the number of source counts after background subtraction; (9) – X-ray luminosity, 0.5–8 keV, assuming 3.5 kpc distance; (10) – source type: GC – confirmed globular cluster, FS – foreground star, GAL – background galaxy, H_α – H_α emmitter; (11) – precise identification and reference: pff – Peng et al. (2004), Tables 5 and 9; mrfa – Minniti et al. (2003), Tables 1 and 3; whh – Woodley et al. (2005) Tables 1 and 2 ; GF – Graham & Fasset (2002) Table 1; Kraft – Kraft et al. (2001) Sect. 5.1; HD – Roeser et al. (1991).

Comments: Source #121 was designated a globular cluster by Minniti et al. (2003), but according to Woodley et al. (2005) it is a background galaxy; Minniti et al. (2003) claim to have removed sources with H_α-emission from their list of globular clusters. However two sources (#54 and #108 in our source list) are both listed as H_α-emitters and globular clusters in their tables. We assume that they are H_α sources and designate them accordingly. Sources #146, #148 and #197 are included in the list of

globular clusters of Minniti et al. (2003), although no colours are available. They are marked as globular cluster in the Table.

3

A study of the population of LMXBs in the bulge of M31

Accepted by: Astronomy & Astrophysics, 2007 (astro-ph/0610649)

R. Voss & M. Gilfanov

Abstract

The purpose of this study is to explore the population of X-ray point sources in the bulge of M31, with the primary goal to contrast properties of various subpopulations, such as persistent and transient sources, primordial LMXBs and dynamically formed ones. Based on the data from 26 archival *Chandra* observations we study the source content and properties of various subpopulations of X-ray sources to a maximum distance of 12 arcmin from the centre of M31. To a limiting luminosity of $\sim 10^{35}$ erg s^{-1} we find 263 X-ray point sources, with $\sim 1/3$ of these being background galaxies. A study of the spatial distribution and the luminosity function of the X-ray sources shows that the distribution of primordial LMXBs is consistent with the distribution of the K-band light and that their luminosity function flattens below $\sim 10^{37}$ erg s^{-1} to the $dN/dL \propto L^{-1}$ law in agreement with the behaviour found earlier for LMXBs in the Milky Way and in Cen A. Within a radius of 12 arcmin, the luminosity function is independent of distance to the centre of M31 in contrast to earlier *Chandra* studies. The LMXBs located in globular clusters and within ~ 1 arcmin from the centre of M31 are presumably created via dynamical interactions. The dynamical origin of the $r < 1$ arcmin sources is strongly suggested by their radial distribution which follows the ρ_*^2 profile rather than the K-band light distribution. Their luminosity function shows a prominent fall-off below $\log(L_X) \lesssim 36.5$. Although the statistics is insufficient to claim a genuine low-luminosity cut-off in the luminosity function, the best fit powerlaw with a slope of -0.6±0.2 is significantly flatter than the $dN/dL \propto L^{-1}$ law. We also searched for transients and found 28 sources that varied by a factor larger than 20. Their spatial distribution follows the distribution of the persistent LMXBs within the accuracy allowed by the limited number of transients.

3.1 Introduction

With the advent of *Chandra*, X-ray point sources in nearby galaxies became a subject of intense study (see Fabbiano, 2006, and references therein). In spiral and starburst galaxies the X-ray luminosity function (LF) has been shown to be a powerlaw with a differential slope of ∼1.6 (Grimm et al., 2003), whereas the LF in elliptical galaxies seems to have a more complicated shape, being steep at the bright end, $\log(L_X) > 37.5$, with power law index in the $\sim$ 1.8-2.5 range, and flat below $\sim \log(L_X) < 37.0$ (Gilfanov, 2004; Voss & Gilfanov, 2006). There is, however, currently no consensus on the existence and position of the breaks, and on the slope below a few times 10^{37} erg s^{-1} (Kim, D.-W., et al., 2006).

While M31 is not an elliptical galaxy, the population of X-ray sources in the bulge mainly consists of low mass X-ray binaries (LMXBs), similar to the population of X-ray sources in elliptical galaxies. It is therefore fair to expect the X-ray LF to be similar to that of ellipticals (and perhaps even more interesting if differences show up). The LF can only be studied to a limiting luminosity of 10^{37} erg s^{-1} in the closest large ellipticals (Kim, D.-W., et al., 2006), except for Cen A (Voss & Gilfanov, 2006) that is both an unusual elliptical and suffers from contamination of X-rays from other sources than binaries. In contrast to this, the proximity of M31 makes it possible to study the LF down to 10^{35} erg s^{-1}.

M31 has been observed extensively both by *XMM-Newton* and *Chandra*, and the point source population has been analysed in a number of papers, see e.g. Kong et al. (2002); Kaaret (2002); Pietsch et al. (2005b); Williams et al. (2004a, 2006). In the central parts of M31 the point spread function (PSF) of *XMM-Newton* causes source confusion and therefore only *Chandra* observations are suited for studies of the weak sources in this region. The LF of the inner region of M31 has previously been studied with *Chandra* by Kong et al. (2002, 2003); Williams et al. (2004a). There are several good reasons to reinvestigate the LF in this region. The inner bulge of M31 has been observed a number of times after this study, significantly increasing the exposure, and also the previous study did not include the effects of incompleteness and contamination by background sources, which influences their conclusions significantly.

The paper is structured as follows. In section 3.2 we describe the data sets and the basic data preparation and analysis. Also the identification of sources in other wavelengths is discussed in this section. The properties of the population of X-ray binaries in the bulge of M31 are analysed in section 3.3, including the spatial distribution and analysis of incompleteness effects. The search for and analysis of transient sources is presented in section 3.4. The LFs of the source populations are analysed in section 3.5. We conclude the work in section 3.6.

Table 3.1: The specifications of the *Chandra* observations used in this paper. The corrections given in the last two columns are the corrections applied to the aspect files to align the observations and to achieve absolute astrometry. 1 pixel equals 0.492 arcsec.

Obs-ID	Date	Instrument	Exp. Time	R.A.	Dec.	Data Mode	Correction West	Correction North
0303	1999 Oct 13	ACIS-I	12.01 ks	00 42 44.4	+41 16 08.30	FAINT	+0.72 pixel	−0.29 pixel
0305	1999 Dec 11	ACIS-I	04.18 ks	00 42 44.4	+41 16 08.30	FAINT	−0.59 pixel	−0.16 pixel
0306	1999 Dec 27	ACIS-I	04.18 ks	00 42 44.4	+41 16 08.30	FAINT	−0.51pixel	−0.01 pixel
0307	2000 Jan 29	ACIS-I	04.17 ks	00 42 44.4	+41 16 08.30	FAINT	−0.34 pixel	+0.19 pixel
0308	2000 Feb 16	ACIS-I	04.06 ks	00 42 44.4	+41 16 08.30	FAINT	+0.77 pixel	+1.34 pixel
0309	2000 Jun 01	ACIS-S	05.16 ks	00 42 44.4	+41 16 08.30	FAINT	−0.41 pixel	+0.12 pixel
0310	2000 Jul 02	ACIS-S	05.14 ks	00 42 44.4	+41 16 08.30	FAINT	−0.40 pixel	+0.17 pixel
0311	2000 Jul 29	ACIS-I	04.96 ks	00 42 44.4	+41 16 08.30	FAINT	−1.29 pixel	−2.79 pixel
0312	2000 Aug 27	ACIS-I	04.73 ks	00 42 44.4	+41 16 08.30	FAINT	−0.90 pixel	+1.62 pixel
1575	2001 Oct 05	ACIS-S	38.15 ks	00 42 44.4	+41 16 08.30	FAINT	−0.97 pixel	+0.04 pixel
1577	2001 Aug 31	ACIS-I	04.98 ks	00 43 08.5	+41 18 20.00	FAINT	−2.79 pixel	−2.71 pixel
1581	2000 Dec 13	ACIS-I	04.46 ks	00 42 44.4	+41 16 08.30	FAINT	−0.62 pixel	+2.93 pixel
1582	2001 Feb 18	ACIS-I	04.36 ks	00 42 44.4	+41 16 08.30	FAINT	+1.65 pixel	+2.49 pixel
1583	2001 Jun 10	ACIS-I	05.00 ks	00 42 44.4	+41 16 08.30	FAINT	−0.50 pixel	−3.95 pixel
1585	2001 Nov 19	ACIS-I	04.95 ks	00 43 05.6	+41 17 03.30	FAINT	−1.28 pixel	−0.81 pixel
1854	2001 Jan 13	ACIS-S	04.75 ks	00 42 40.8	+41 15 54.00	FAINT	−0.74 pixel	+0.19 pixel
2895	2001 Dec 07	ACIS-I	04.94 ks	00 43 08.5	+41 18 20.00	FAINT	−0.49 pixel	+0.22 pixel
2896	2002 Feb 06	ACIS-I	04.97 ks	00 43 05.5	+41 17 03.30	FAINT	−0.20 pixel	+0.83 pixel
2897	2002 Jan 08	ACIS-I	04.97 ks	00 43 09.8	+41 19 00.72	FAINT	−0.44 pixel	+0.01 pixel
2898	2002 Jun 02	ACIS-I	04.96 ks	00 43 09.8	+41 19 00.72	FAINT	−0.56 pixel	−0.02 pixel
4360	2002 Aug 11	ACIS-I	04.97 ks	00 42 44.4	+41 16 08.90	FAINT	−0.19 pixel	−0.07 pixel
4678	2003 Nov 09	ACIS-I	04.87 ks	00 42 44.4	+41 16 08.90	FAINT	+0.06 pixel	−0.35 pixel
4679	2003 Nov 26	ACIS-I	04.77 ks	00 42 44.4	+41 16 08.90	FAINT	+0.00 pixel	−0.96 pixel
4680	2003 Dec 27	ACIS-I	05.24 ks	00 42 44.4	+41 16 08.90	FAINT	−0.36 pixel	−0.86 pixel
4681	2004 Jan 31	ACIS-I	05.13 ks	00 42 44.4	+41 16 08.90	FAINT	−0.59 pixel	−1.12 pixel
4682	2004 May 23	ACIS-I	04.93 ks	00 42 44.4	+41 16 08.90	FAINT	−0.64 pixel	−0.07 pixel

3.2 Data Analysis

The analysis in this paper is based on 26 *Chandra* ACIS observations, with aimpoints within 10 arcmin from the centre of M31 (RA 00 42 44.31, Dec +41 16 09.4). Information about the observations is listed in Table 3.1. The data preparation was done following the standard CIAO[1] threads (CIAO version 3.2.1; CALDB version 3.0.3), and limiting the energy range to 0.5-8.0 keV. The ACIS chips sometimes experience flares of enhanced background. For point source detection and luminosity estimation it is not necessary to filter out the flares, since the increased exposure time outweighs the increased background.

We used CIAO `wavdetect` to detect sources. The input parameters for the detection procedure are similar to those used in Voss & Gilfanov (2006). We detected sources within 10 arcmin of the aimpoint in each of the individual observations. Due to limitations of the absolute astrometry of *Chandra*, the observations have to be aligned before they are combined. We chose to align the observations to OBS-ID 1575, as this is the observation with highest exposure time. For each of the observations we determined the number of sources matching sources found in OBS-ID 1575, excluding all ambiguous matches, such as a source in one of the source lists being close to two sources in the other list. The source lists were shifted relative to each other, and the smallest rms-distance between the sources were found. This method made it possible to align the 25 observations with OBS-ID 1575 with a minimum of 40 matches. The corrections applied to the observations are listed in Table 3.1. All the observations were then reprojected into the coordinate systems of OBS-ID 1575 using CIAO `reproject_events`, and a merged observations were created. Notice that the steps above were taken in order to align and combine the observations, not to achieve good absolute astrometry. This will be dealt with using optical data in section 3.2.2.

An exposure map was created for each of the observations, assuming the energy distribution to be a powerlaw with photon index of 1.7 and Galactic absorption of $6.68\times10^{20}\mathrm{cm}^{-2}$. (Dickey & Lockman, 1990). In the following we use the same spectrum to convert the observed count rates to unabsorbed source flux. To calculate the luminosity of the sources, we assumed a distance of 780 kpc to M31 (Stanek & Garnavich, 1998; Macri, 2001).

To estimate the source counts we applied circular aperture photometry. The output count rate for each detected source is calculated inside a circular region centered on the source central coordinates given by `wavdetect`. The radius of the circle was determined individually for each source so that the encircled energy was 85%. To find this radius we extracted the PSF using CIAO `psfextract` task for each of the 26 observations, and the PSFs were combined using the values of the exposure maps as weights. For the background region we used a circle with radius 3 times the radius of the source region and the source region excluded, as well as the source regions of eventual nearby sources. The corrected source counts and errors were then found by the equations (Harnden et al., 1984):

$$S = \frac{C(b-d)d^{-1} - Q}{\alpha b d^{-1} - \beta} \tag{3.1}$$

[1] http://cxc.harvard.edu/ciao/

and

$$\sigma_S^2 = \frac{\sigma_C^2 (b-d)^2 d^{-2} + \sigma_Q^2}{(\alpha b d^{-1} - \beta)^2}. \tag{3.2}$$

Here S is the total number of counts from the source, C is the number of counts inside the source region and Q is the number of counts in the background region, α is the integral of the PSF over the source region, β is the integral of the PSF over the source and background regions, b is the area of the source and background regions and d is the area of the source region. For close sources the extraction regions can overlap. In this case a second iteration was performed. In this iteration the number of counts of the neighbouring sources, together with their PSF was used to find the contamination from nearby sources of the source and background regions of a source. This contamination from nearby sources was then subtracted from C and Q, and equation 3.1 was repeated. In all cases the effect of the contamination was small enough to justify the use of this method with only on iteration.

3.2.1 2MASS LGA

To compare the spatial distribution of the point sources with the distribution of mass in M31, we used a K-band image of the region from the 2MASS Large Galaxy Atlas (Jarret et al., 2003). The image has a resolution of 1 arcsec, and it is therefore possible to clearly see point sources. While many of the sources are objects inherent to M31, such as globular clusters, some of the sources may be foreground or background objects. In order to remove these objects, we correlate the image with the Revised Bologna catalogue of M31 globular clusters (Galleti et al., 2004), and thereby find the maximum K-band luminosity of a globular cluster, $\sim 2{\cdot}10^6 L_{K,\odot}$. All point sources more luminous than this are removed from the image (replaced with local background). This corresponds to 14 per cent of the luminosity in the outer part of the image (the annulus 9 arcmin-12 arcmin). Point sources with luminosities between $\sim 4{\cdot}10^5 L_{K,\odot}$ and $\sim 2{\cdot}10^6 L_{K,\odot}$ corresponds only to 2 per cent of the total luminosity, and most of these sources are GCs in M31. We therefore conclude that after our removal of the most luminous sources, contamination from point sources not in M31 is insignificant in the outer region. In the rest of the image the luminosity density of M31 is higher and contamination is therefore even less important.

3.2.2 Absolute astrometry

We used the 2MASS All-Sky Point Source Catalog (Skrutskie et al., 2006) to achieve better absolute astrometry. This catalog was chosen, due to the high number of (true) matches with our source list. The astrometric precision ranges from ~ 0.1 arcsec for brighter sources to 0.4 arcsec for the weakest sources. The X-ray sources were correlated with the 3132 2MASS point sources in the observed region and the X-ray image was shifted to give the smallest rms-distance for matches with a distance less than 1 arcsec. This gives a correction of -0.97 pixel west and $+0.04$ pixel north with 40 matches (<2 random matches expected). We note that after the corrections, our source coordinates are in good agreement with the coordinates given by previous studies (Kong et al., 2002; Williams et al., 2004a).

3.2.3 Source Identifications

For the identification of the detected sources we have used a variety of catalogues. For the identification of globular clustes we have used the Revised Bologna Catalogue of M31 globular clusters (Galleti et al., 2004) as well as the lists given by Magnier (1993) and Fan et al. (2005). GCs were divided into the categories confirmed GCs and candidate GCs, following (Galleti et al., 2004), and the GCs in Magnier (1993) and Fan et al. (2005) were all considered candidates. Planetary nebulae have been identified using Ciardullo et al. (1989), and supernova remnants using Magnier et al. (1995). Furthermore we have searched for sources coincident with stellar novae in Pietsch et al. (2005a). Stars were identified using Galleti et al. (2004) as well as GSC 2.2 (Morrison et al., 2003) and USNO-B1 (Monet et al., 2003) (the latter two catalogues gave only sources found in Galleti et al. (2004) as well). Finally we searched for possible counterparts using the NASA/IPAC Extragalactic Database (NED) and SIMBAD. A source was assumed to be a counterpart to the X-ray source if within a distance of 2.5 arcsec, except for supernova remnants for which the distance was 5 arcsec.

A number of objects have been excluded from the following analysis, 4 foreground stars, 3 SNRs and one extended source (which was detected as two sources). More sources have been identified with objects, as can be seen from our source list, but the number is small, and the meaning of the identifications is uncertain, and we have therefore chosen to keep them in the sample. For example we note that a detailed study of the planetary nebulae correlations (Williams et al., 2004b) suggested that most are not true counterparts. Also of the four novae correlations, only one (source 128) is a true counterpart (W. Pietsch, private communication).

Our final source list consists of 263 sources within a radius of 12 arcmin from the centre of M31 (table 3.4). Of these 9 sources are not included in the analysis below. Above 10^{37} erg s^{-1} there are 48 sources, and above 10^{36} erg s^{-1} (approximately the completeness limit), there are 136 sources included in the analysis. We expect $\sim$29 of the sources with luminosity $> 10^{36}$ erg s^{-1} and $\sim$89 of all the sources to be background sources, taking into account incompleteness, see sections 3.3.1.3 and 3.3.3. We find that 15 sources are coincident with GCs (0.25 random matches expected) and 14 with GC candidates (1 random match expected).

Table 3.2: The list of point like X-ray sources within a distance of 12 arcmin from the centre of M31. The full table will be available in the online version of the paper.

Number	distance	RA	DEC	cts	cor. cts	error	luminosity	type	id	name
(1)	(2)	(3)	(4)	(5)	(6)	(7)	(8)	(9)	(10)	(11)
1	1.0	00 42 44.37	41 16 08.7	2245	2580.7	58.0	7.08e+36			r1-10
2	2.2	00 42 44.38	41 16 07.4	2864	3308.2	65.4	1.08e+37			r1-9
3	4.0	00 42 44.38	41 16 05.4	1117	1233.9	41.3	5.32e+36			r1-21
4	4.6	00 42 44.30	41 16 14.0	316	344.9	22.6	1.52e+36			r1-22
5	5.4	00 42 43.86	41 16 11.1	225	244.1	19.2	1.07e+36			r1-27
6	7.4	00 42 43.87	41 16 03.9	709	811.6	33.1	3.53e+36			r1-23
7	9.7	00 42 44.68	41 16 18.2	906	1047.3	37.3	4.62e+36			r1-8
8	10.6	00 42 45.24	41 16 11.1	456	516.2	26.8	2.25e+36			r1-20
9	14.5	00 42 45.60	41 16 08.6	1026	1191.0	39.5	5.21e+36			r1-7
10	15.3	00 42 45.12	41 16 21.7	3098	3631.2	67.9	1.61e+37	RAD	S WSTB 37W135	r1-4
11	20.8	00 42 43.88	41 16 29.6	1293	1463.5	44.5	6.54e+36			r1-11
12	21.7	00 42 46.01	41 16 19.6	468	531.3	27.2	2.33e+36	t		r1-19
13	23.8	00 42 43.75	41 16 32.4	2329	2726.7	59.0	1.24e+37			r1-12
14	24.0	00 42 42.18	41 16 08.3	4525	5353.9	81.6	2.45e+37	t		r1-5
15	25.9	00 42 42.48	41 15 53.7	3077	3601.1	67.6	1.62e+37	PN	CIA 4	r1-14

(1) – The sequence number; (2) – Distance to the centre in arcsec; (3),(4) – Right ascension and declination of source; (5) – Source counts; (6) – Source counts after background subtraction; (7) – Statistical error on source counts after background subtraction; (8) – X-ray luminosity, 0.5-8 keV, assuming 780 kpc distance; (9) – Source Type: GC – confirmed globular cluster, GCC – globular cluster candidate, PN – planetary nebula, FGS – foreground star, NOVA – nova, EmO – emission line object, RAD – radio source, SNR – supernova remnant, EXT – extended source, t – transient source; (10) – precise identification and reference: Bol – Galleti et al. (2004), Fan – Fan et al. (2005), Mita – Magnier (1993), MLA – Meyssonnier et al. (1993), W2 – Williams et al. (2004b), CIA – Ciardullo et al. (1989), CFN – Ciardullo et al. (1987), PI – Pietsch et al. (2005a), SI – Shafter & Irby (2001), B68 – Börngen (1968), S – Simbad, GLG – Gelfand et al. (2004), B90 – Braun (1990), MG – Magnier et al. (1995), Cra – Crampton et al. (1984); (11) – Source name in Kong et al. (2002), Williams et al. (2004a) and Williams et al. (2006); Sources not included in these catalogues are marked with K if observed in Kaaret (2002), else with X, indicating that these are new sources.

3.3 Populations of sources in the bulge of M31

3.3.1 Expected numbers

3.3.1.1 Low mass X-ray binaries

LMXBs are related to the population of old stars, and there is therefore a correlation between their number and the stellar mass of a galaxy (Gilfanov, 2004). In order to estimate the expected number and luminosity distribution of LMXBs we used a K-band image from 2MASS Large Galaxy Atlas (Jarret et al., 2003) and integrated the flux emitted in the parts of M31 analysed in this paper (excluding luminous point sources not related to the galaxy, see Sect. 3.2.1). This gives a K-band luminosity of $L_K = 4.4 \cdot 10^{10}\ L_\odot$. To convert it to the stellar mass we use the color-dependent K-band mass-to-light ratio from Bell & De Jong (2001). For the extinction corrected optical color of the bulge of M31, $(B-V) \approx 0.95$ (Walterbos & Kennicutt, 1987), the mass-to-light ratio is $M_*/L_K \approx 0.85$. This gives the stellar mass of $3.8 \cdot 10^{10}\ M_\odot$, assuming that the absolute K-band magnitude of the sun is equal to $M_{K,\odot} = 3.39$. Using the results of Gilfanov (2004) we predict ≈55.7 LMXBs with $L_X > 10^{37}$ erg s^{-1}, and ≈128.9 with $L_X > 10^{36}$ erg s^{-1}.

3.3.1.2 High mass X-ray binaries

Being young objects, HMXBs are associated with star formation and, as expected for the bulge of a spiral galaxy, are by far a less significant contribution to the population of X-ray binaries than LMXBs. Star formation is mostly associated with the disk of M31. An investigation of the star formation rate of the disk has been conducted by Williams (2003), who find that the mean SFR over the last 60 Myr for 1.4 deg^2 of the M31 disk is 0.63±0.07 M$_\odot$yr^{-1} (in the range 0.1−100 M$_\odot$) with no drastic changes. Assuming a flat SFR density over the galaxy gives an SFR of ≈ 0.048 M$_\odot$yr^{-1} within the region analyzed in this paper. We used calibration of Grimm et al. (2003) to calculate the expected number of HMXBs (see comment in Shtykovskiy & Gilfanov, 2005, regarding the normalization). From this we get the expectation of ≈0.3 HMXBs brighter than 10^{37} erg s^{-1}, and ≈1.2 sources brighter than 10^{36} erg s^{-1}.

Alternatively we have estimated upper limits for the numbers of HMXBs from the Hα and FIR luminosities reported by Devereux et al. (1994). For Hα the combined luminosity from the nuclear region and from diffuse emission inside the star forming ring (which is at a radius of ∼ 50 arcmin, much larger than the maximum distance of 12 arcmin analysed in this paper) is 4.3· 10^{39} erg s^{-1} (corrected to our distance of 780 kpc). From Grimm et al. (2003) we find that this corresponds to 1.1 HMXBs with a luminosity above 10^{37} erg s^{-1}, and 4.4 HMXBs with a luminosity above 10^{36} erg s^{-1}. The FIR luminosity in this region is 5.25· 10^8 L$_\odot$, which corresponds to 2.0 HMXBs with a luminosity above 10^{37} erg s^{-1}, and 8.0 HMXBs with a luminosity above 10^{36} erg s^{-1}. It should be noted, however, that the region these luminosities are found from is much larger than the region containing our X-ray data, and that it is very likely that the main part of the light is not produced by star formation, as Devereux et al. (1994) found that for the central region the number of O-type stars is a factor of ∼

200 lower than what would be expected if the luminosities were due to star formation. We can therefore savely ignore the contribution of HMXBs in the following analysis.

3.3.1.3 Background X-ray sources

To estimate the number of background sources we use results of the CXB $\log(N) - \log(S)$ determination by Moretti et al. (2003). Namely, we use the source counts in the soft and hard bands (their Eq. 2) and convert the fluxes to the 0.5–8.0 keV band, assuming a powerlaw spectrum with a photon index of 1.4. For the total area of our survey of 0.126 deg^2 we obtain from the source counts in the soft band $\sim$1.8 CXB sources above the flux corresponding to 10^{37} erg s^{-1}, and $\sim$29 above 10^{36} erg s^{-1}. From the hard band counts the predicted numbers are $\sim$1.2 and $\sim$30.5 sources. The predictions based on the soft and hard $\log(N) - \log(S)$ differ slightly because of the well recognized fact that source counts in different energy bands and flux regimes are dominated by different types of sources, see Voss & Gilfanov (2006). To find the total number of background sources in our source list, we multiply the CXB LF with the incompleteness function found in section 3.3.3, and integrate over the observed luminosity range. We find the total number of CXB sources to be 89.

3.3.2 The spatial distribution of the point sources

To begin with we studied the azimuthally averaged radial distribution of the X-ray point sources. As the two main contributions of sources are the LMXBs and CXBs, we model the distribution as a superposition of two functions, representing these contributions. As the spatial distribution of the globular clusters in M31 is significantly different from the mass distribution in the inner parts of the bulge, we have accounted for the globular cluster sources separately. The distribution of LMXBs is assumed to follow the K-band light, and for this the image from the 2MASS LGA was used, whereas the density of CXBs can be assumed to be flat on the angular scales under consideration here. The only free parameter of the model is the ratio of normalizations of the LMXB and CXB fraction.

The model was compared to the observations for sources more luminous than 10^{36} erg s^{-1} (figure 3.1), as sources of such luminosity could be observed in the entire image without it being necessary to consider incompleteness effects. This analysis was presented in Voss & Gilfanov (2007), where the data was shown to deviate significantly from the model in the inner $r \lesssim 1$ arcmin. It was also shown that the discrepancy could be succesfully modelled by binaries created through dynamical interactions.

In this paper we adopt the normalizations of the primordial LMXBS and CXBs found in Voss & Gilfanov (2007). Above a luminosity of 10^{36} erg s^{-1} this corresponds to 29 CXBs and 64 primordial LMXBs, as well as $\sim$ 20 LMXBs created via dynamical interactions in the inner bulge and $\sim$ 20 LMXBs in GCs. The normalization of CXBs is consistent with the expectations. From this we find that the ratio of primordial LMXBs with luminosity above 10^{36} erg s^{-1} (10^{37} erg s^{-1}) to stellar mass is N_x/M_* is 17.0$\pm$1.8 (8.9$\pm$1.6) sources per 10^{10} $M_\odot$, and the ratio of primordial LMXBs to the K-band luminosity is N_x/L_K is 19.7$\pm$2.1 (10.3$\pm$1.9) sources per 10^{10} $L_{\odot,K}$. The normalization of the primordial LMXBs is about two times smaller than the number

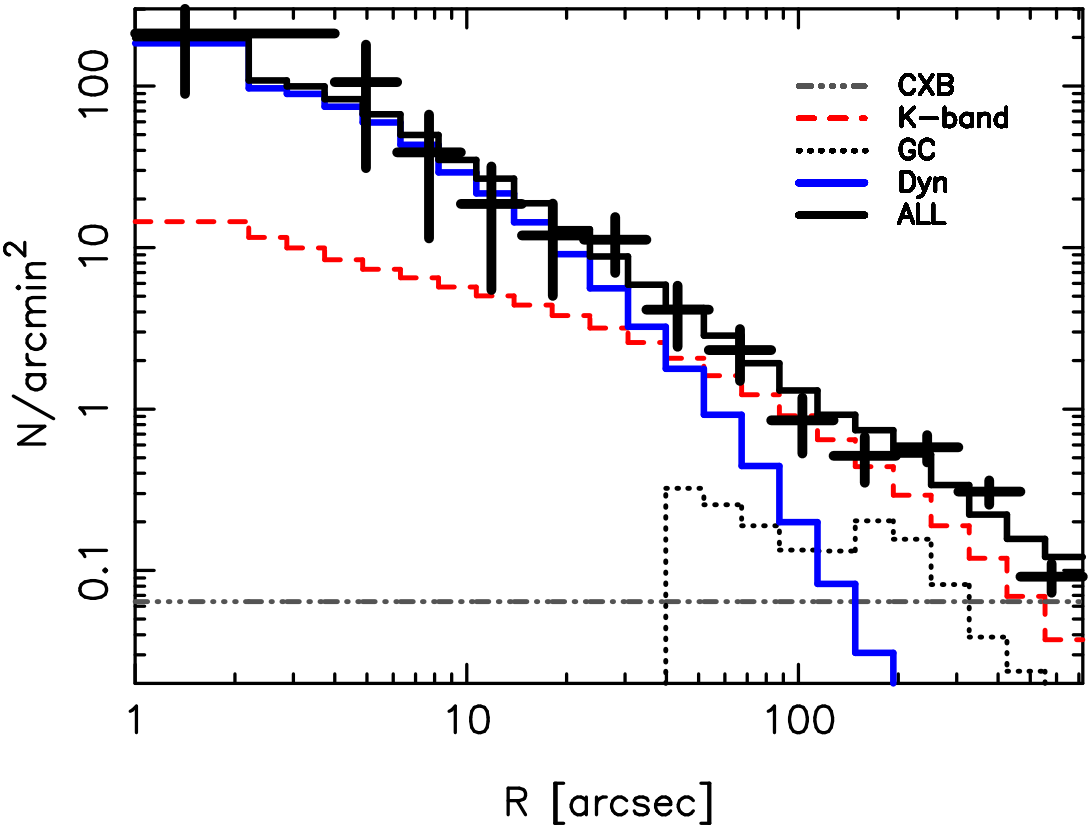

Figure 3.1: The spatial distribution of the point sources (crosses), compared to a model consisting of primordial LMXBs, CXB sources and LMXBs in GCs. The GC LMXB normalization was determined from the observed number of matches, and the primordial LMXB and CXB normalizations were found from a fit to the observed source distribution outside 1 arcmin. In the inner 1 arcmin the sources follow the expected distribution of LMXBs formed through dynamical interactions, ρ_*^2 (Voss & Gilfanov, 2007).

obtained by Gilfanov (2004). There are two reasons for this. 1) We removed LMXBs in GCs and in the inner bulge from the analysis, to only account for LMXBs thought to be primordial. This was not done by Gilfanov (2004). 2) We assumed the K-band mass to light ratio of the bulge of M31 to be 0.85, as compared to the ratio of 0.56 used in Gilfanov (2004).

3.3.3 Incompleteness

The variations of the diffuse background level and deterioration of the PSF at large off-axis angles lead to variations of the point-source sensitivity across the *Chandra* images. An image, in which observations with different pointings are combined has very non-uniform exposure. As a result there are strong incompleteness effects at the faint end of the luminosity function. We calculate the incompleteness function for each analysed area, using the method described in Voss & Gilfanov (2006), in which

the incompleteness function is calculated separately for LMXBs and for CXBs. A completeness limit is calculated for each pixel and weighted by the expected distribution of sources (using the same distributions as in section 3.3.2). In figure 3.2 the incompleteness function is shown for both LMXBs and CXBs in 3 regions. As in Voss & Gilfanov (2006) we verified our calculated incompleteness functions by simulations of the type used by Kim & Fabbiano (2004). In each of the simulations we used Monte Carlo techniques to simulate 10 000 point sources. Each of the sources was placed on the real image of M31, according to the expected spatial distribution of the source type (LMXBs or CXBs), and our observation pipeline was applied to the image to test if the source is detected, and if so, with which luminosity. This way, the observed number of sources in a luminosity range was compared to the simulated number to determine the detection efficiency. For more details on the method, see Voss & Gilfanov (2006). The results of the simulations are compared to the calculated functions for two regions in figure 3.3. We furthermore calculated the incompleteness function for GCs and GC candidates, by finding the detection limit at the position of each of the GCs, and assuming the probability of containing an LMXB to be the same for all the GCs. The incompleteness functions calculated in this section will be used in the analysis of the LF of the LMXBs in section 3.5.

3.4 Transient Sources

A large fraction of the sources in our sample are variable. For most of the sources, the luminosity varies within a factor of a few. In the combined image the luminosity is the average of the luminosities of the single observations, weighted by the exposure. For the sources with a low amplitude of the variability, this weighted average is adequate for the analysis carried out in this paper.

However, the study of Williams et al. (2006) have shown that, on average, there is $\sim$ one transient source per observation. In an image combined from many observations the effects of these sources on the normalization and shape of the LF are non-negligible. As the luminosity of a source is weighted by the exposure, it is straightforward that the more observations that are combined, the more transients there are, and the lower the average luminosity of each of them will seem to be. To find and investigate transient sources, we analysed each observation individually in the same way as the combined observation.

For each source it was noted for which of the observations it was found and with which luminosity. If the source was not found with `wavdetect` (and if the source region had any exposure) we put the source into one of two categories. The number of photons from the source region, N_{ps} (85 per cent of PSF centered on the observed coordinates of the full image), and background region N_{pb} (annulus with radius 1–3 times the source region) were counted. 95 per cent confidence limits C_{low} and C_{high} were calculated on the source counts (Gehrels, 1986). If C_{low} was larger than the number of expected background photons in the source region, scaled by exposure and numbers of pixels from the background region, we labelled it a low-significance source and used N_{ps}-N_{pb} as source photons to find the luminosity. If C_{low} was lower than the

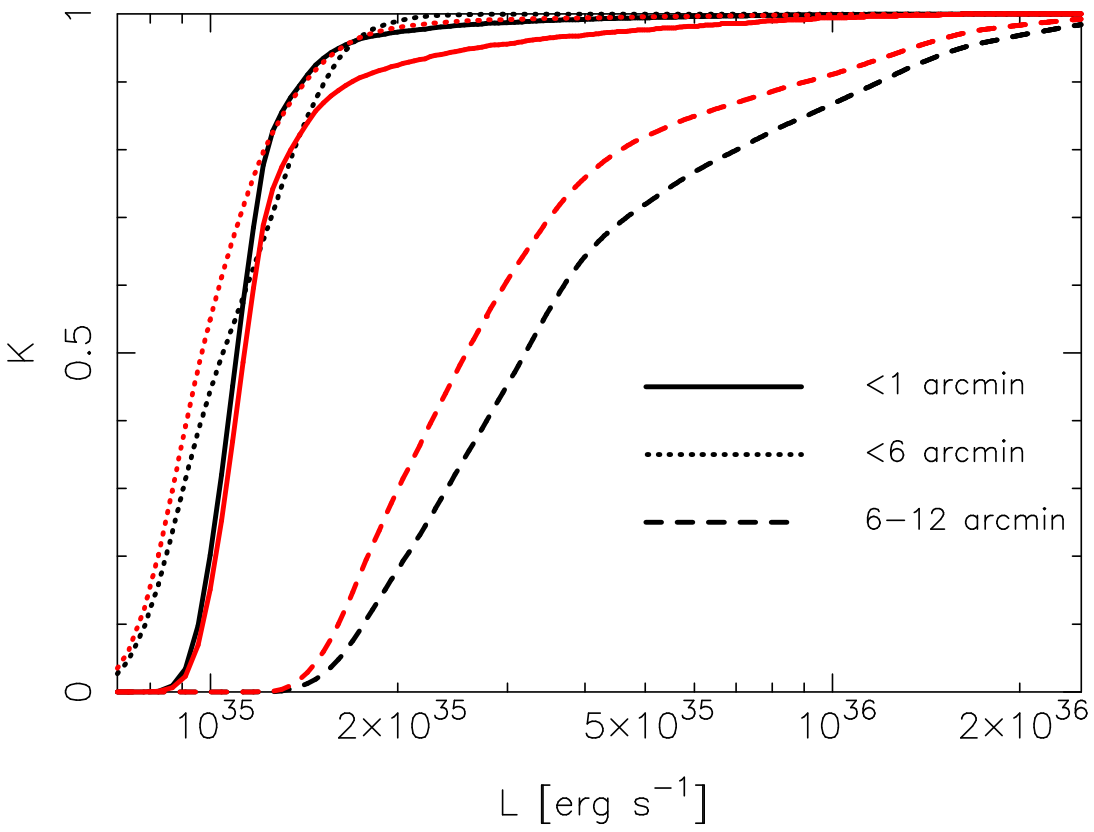

Figure 3.2: The incompleteness as a function of source luminosity for 4 regions of the bulge of M31. The red lines show the function for LMXBs, while the black lines show the functions for CXBs.

expectation of background photons, we calculated an upper limit to the luminosity from $C_{high} - N_{pb}$. Based on the considerations above we divided the sources into three types for each observation. Type 0 is a source observed with `wavdetect`, type 1 is a low-significance source, and type 2 is a source not observed, for which an upper limit is given. In table 3.3 the source type is given for the observation with lowest luminosity for each source.

The ratio between the highest and the lowest luminosity (or upper limit) was then noted for each of the sources. We chose to label sources with a ratio >20 as transients. This gave the 28 sources listed in table 3.3. Out of these, only one was actually observed at the lowest luminosity, indicating that the majority of these sources are real transients. For many of our sources, the ratio limit is set so high that if they are transients, they would not be labeled as such, due to lack of exposure. If the limit was set to be lower, however, there would be a large number of sources that are variable, but not transients, that would be included. It should be noted that amplitude of the variability of a source is artificially enhanced by statistics when the number of observations is large.

Recently a catalogue of transients in M31 was published by Williams et al. (2006),

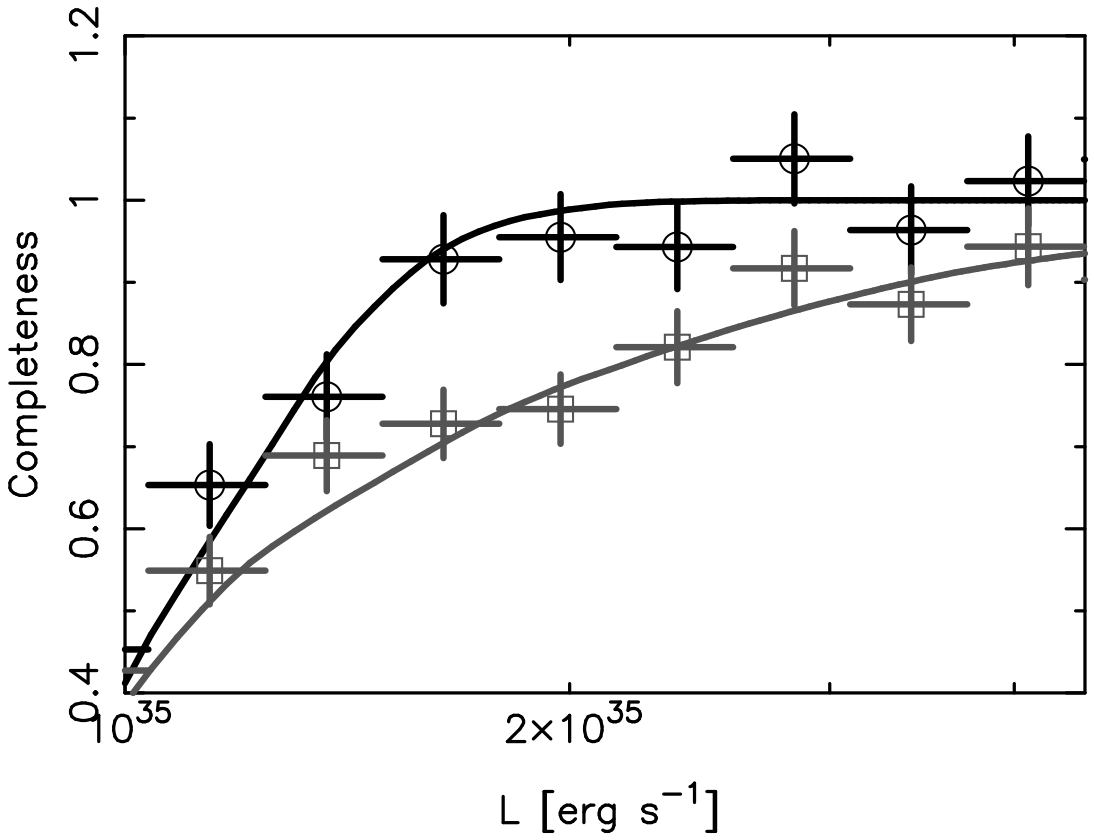

Figure 3.3: The results of incompleteness simulations compared to the calculated incompleteness functions of LMXBs. The black line and data points (circles) corresponds to the annulus with 3 arcmin-6 arcmin distance from the centre of M31, while the grey line and data points (squares) corresponds to the region within 12 arcmin. In both simulations 10 000 sources were simulated.

and 5 further transients were found in a series of papers by the same group (e.g. Williams et al., 2005). From their lists, 36 of the sources are within the region analysed in this paper. Of these, 18 coincide with sources in our transient list. We have therefore identified 10 new sources. Of the 18 sources remaining in their source list, 5 of them were detected in our observations, but did not live up to our criteria for being transients (they also had high/low ratios lower than 20 in Williams et al. (2006)). One source (source 214 in table 3.2) was labelled a transient in their paper with a high/low ratio of 96 but only varied by a factor of <10 in our observations. The last 12 sources from their source list are not active in our observations. Trudolyubov et al. (2006) detected 4 transients with *XMM-Newton*. 3 of these are not active in our observations, while the fourth (source 234 in table 3.2) was also found to be transient in our observations, as well as by Williams et al. (2005).

We investigated the spatial distribution of the transient sources. In figure 3.4 we compare their radial distribution with two models: 1) the distribution of the K-band light, representing the primordial LMXBs, and 2) the distribution of all the observed

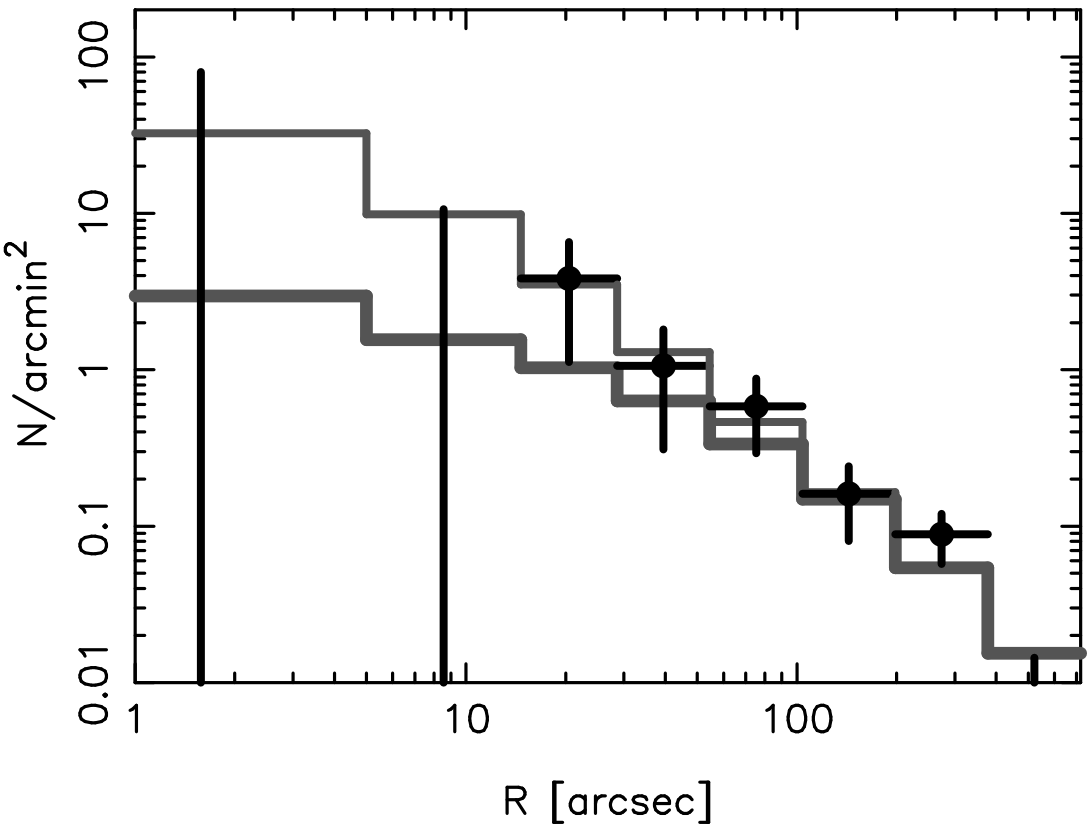

Figure 3.4: The spatial distribution of the transient sources, compared to two models, the distribution of primordial LMXBs (thick grey line) and the combined distribution of primordial LMXBs and LMXBs created through dynamical interactions in the inner bulge (thin grey line). The error bars are 1 σ.

LMXBs (all sources with CXBs subtracted). It can be seen that with the current set of observations, both models can explain the distribution. With more observations it might be possible to distinguish between the models, and thereby learn if the ratio of transient to persistent sources is different for primordial LMXBs and dynamically formed LMXBs. It is important to note that the number of individual observations and length of these varies strongly from region to region, and that this can have significant effects on the observed distribution. Also inside 5 arcsec the source density is so high, that transients could easily be missed.

3.5 The luminosity function of the point sources

The LF in the bulge of M31 has previously been studied with *Chandra* by Kong et al. (2002, 2003); Williams et al. (2004a), but for several reasons it is interesting to do further work on this. The exposure of the inner region has increased significantly since the previous studies, and methods for incompleteness correction have been developed.

Table 3.3: Highly variable sources with $L_{max}/L_{min} > 20$. Given here are (1) the source number from table 1, (2) the ratio of highest observed luminosity to the lowest observed luminosity (or upper limit), (3) the highest observed luminosity, (4) the observation in which the luminosity was highest, (5) the observation in which the luminosity was lowest, and (6) the observational type at lowest luminosity, see description in text. It is also noted in this column if the source belongs to a GC or GC candidate.

Source (1)	high/low (2)	max lum (3)	high obs (4)	low obs (5)	type (6)
12	22.0	7.61e+36	1585	310	2
14	468.8	7.28e+37	308	1575	2
23	50.3	1.26e+37	4682	305	1
29	126.2	4.42e+37	1575	310	2
32	65.2	1.37e+37	4681	1575	2
38	99.5	2.28e+37	4679	303	2
41	28.3	3.18e+36	303	1575	1
44	35.7	3.22e+36	303	1575	GCC,1
47	64.6	1.99e+37	4682	1575	2
51	87.1	1.11e+37	306	1575	2
59	589.0	4.75e+37	4682	1575	2
68	370.5	1.93e+37	310	1575	2
72	21.2	1.34e+37	309	4679	1
84	54.5	7.68e+36	1854	1575	2
85	79.0	2.56e+37	303	1585	1
90	58.6	5.36e+37	311	312	1
105	954.2	3.27e+38	1575	303	2
118	108.4	3.86e+37	4681	303	2
128	46.1	1.50e+37	2896	1575	2
130	104.4	1.49e+37	311	1575	2
136	92.2	4.55e+37	4682	305	GCC,2
146	212.4	3.77e+37	4681	1575	2
155	96.3	4.48e+37	1585	1575	GCC,0
212	65.2	2.68e+37	4682	1575	2
216	20.8	1.04e+37	1854	1575	2
234	66.9	1.18e+37	4682	2898	1
237	37.5	7.48e+37	2897	307	1
250	53.4	7.00e+37	2896	305	GC,2

It is therefore possible to probe the LF at much lower luminosities. Furthermore the previous studies neglected the contribution of background sources. This can be important for the outer parts of the bulge, where the density of LMXBs is comparable to the density of background objects, see figure 3.1.

Here we study the LF of the LMXBs in detail, statistically taking into account the CXBs, and correcting for incompleteness as described in section 3.3.3. The LMXB LFs presented in this section are corrected by subtracting the LF of CXBs multiplied by the incompleteness function of the CXBs. The normalization of the LF of CXBs was chosen as in 3.3.2. The LFs of the LMXBs was then corrected by dividing by the incompleteness function of the LMXBs. From figure 3.2 it can be seen that there is a factor of ∼10 difference between the sensitivity in the regions inside 6 arcmin and the regions outside. At the same time the density of X-ray sources is much higher in the inner region than in the outside region, making the CXB contribution less important. In the inner regions the LF can therefore be determined directly down to a few times 10^{35} erg s^{-1}. We choose to present the functions as differential LFs, as opposed to the cumulative LFs often used in the literature. The advantage of this is that bins are independent, and features in the LF are therefore more visible, and easier to interpret. The disadvantage is that it is necessary to bin the data. The LFs presented below are cut of at a lower luminosity. This luminosity corresponds to the limit, at which the incompleteness correction is > 2.5 for either the CXB LF or the LMXB LF. For this reason the LFs of the individual regions begin at different luminosities in figures 3.5-3.10. For each of the LFs, we give the number of sources included in the calculations. However it should be noted that due to the corrections for incompleteness and CXB sources applied to the LFs, the error bars in the figures provide better estimates for the precision of the functions.

In figure 3.5 we show the LF of the entire region within a distance of 12 arcmin from the centre of M31. The squares correspond to all the sources, whereas to produce the crosses, the transient sources (table 3.3) were excluded. There is a clear break at $\sim 2{\cdot}10^{37}$ erg s^{-1}, consistent with previous results obtained with *Chandra* (Kong et al., 2002, 2003; Williams et al., 2004a) as well as other X-ray telescopes (Primini et al., 1993; Shirey et al., 2001; Gilfanov, 2004).

As it can be seen in figure 3.5 the effect of transients is to artificially steepen the slope of the LF below $\sim 10^{37}$ erg s^{-1}. A maximum likelihood (ML) fit by a single powerlaw in the range $2 \cdot 10^{35} - 10^{37}$ erg s^{-1} gives a slope of -0.85 ± 0.12 and -0.7 ± 0.16 with and without transients, respectively. While the difference is not statistically significant in our sample, it is a systematic effect that should not be ignored in general when studying a large number of observations combined together. To avoid distortion of the LF due to transient sources they should be excluded from the analysis, and we have done so in the rest of the analyses presented in the paper.

After the transient source have been excluded, the faint end ($2 \cdot 10^{35} - 10^{37}$ erg s^{-1}) of the LF appears to be significantly flatter than L^{-1} powerlaw. This is caused by the sources located in globular clusters and in the inner bulge, thought to have dynamical origin, as the LF of these sources has a prominent fall-off at low luminosities (figure 3.6). Their relative contribution to the LF increases when the transient sources are excluded. As will be shown below, the LF of the primordial sources is consistent with the general shape found by Gilfanov (2004).

In figure 3.6 the LFs of the LMXBs thought to be created through dynamical interactions are presented. In this figure, the LMXBs from the inner 1 arcmin of the M31

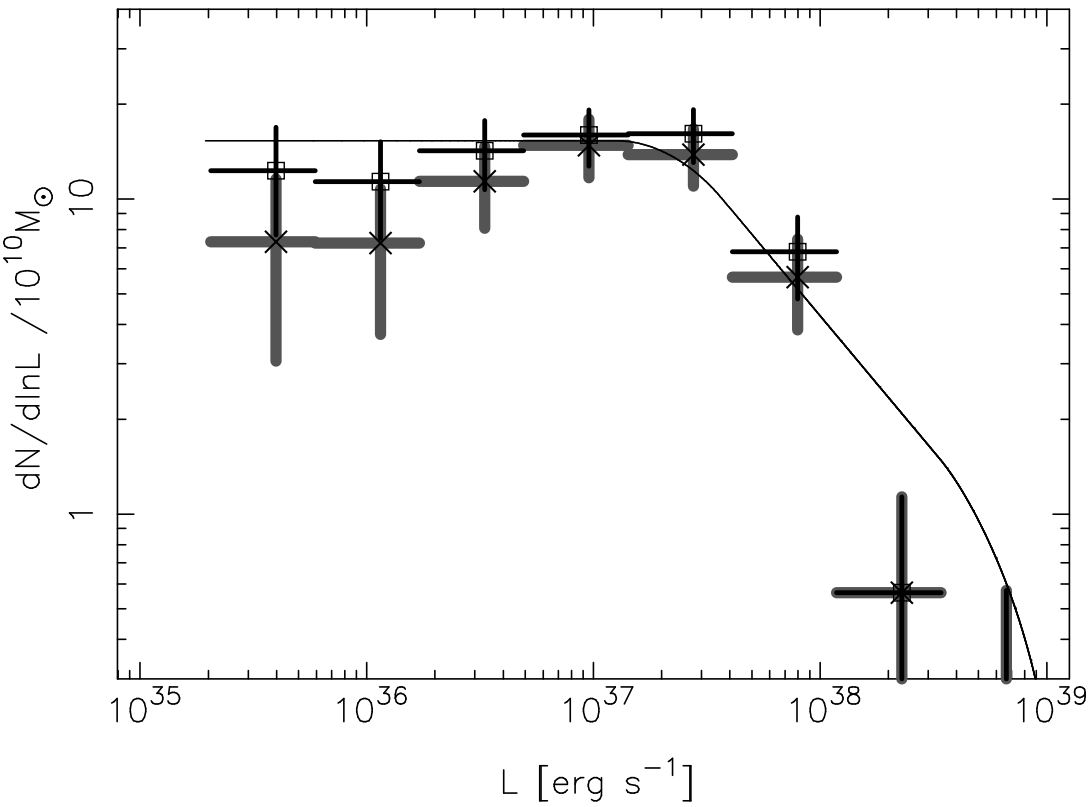

Figure 3.5: The LF of LMXBs within 12 arcmin of the centre of M31. Squares are obtained from all the observed sources (207 sources), whereas for the crosses, the transient sources are excluded (179 sources). Note that in the latter case the relative contribution of sources thought to have dynamical origin is increased, see the discussion in the text. The solid line is the average LF of LMXBs in nearby galaxies from Gilfanov (2004). The normalization is arbitrary, but the same on figures 5-10.

bulge are shown (crosses), compared to the LFs of LMXBs in confirmed GCs (squares) and GC candidates (triangles). The three LFs are consistent with each other, and for all three populations it is obvious that the number of LMXBs falls off at luminosities below $\log L_x \lesssim 36.0 - 36.5$. This is most significant in the bulge population, which can also be observed to the lowest luminosity level. For the GC candidate sources, the falling off at low luminosities is hardly significant, but it is known that the GC candidate list is contaminated by background galaxies (Galleti et al., 2004), and with the LF of CXB sources, the effect of such a contamination would exactly be to raise the lower end of the LF.

In the inner 1 arcmin of M31, as well as in the GCs the source density is so high, that the source blending can become a factor. We performed Monte Carlo simulations of the source population in the inner 1 arcmin of M31, similar to the ones performed to estimate incompleteness (see section 3.3.3). We assumed the average luminosity function of Gilfanov (2004), with the normalization according to our observed number

of sources in the region, and with a lower cut-off at 10^{36} erg s^{-1} as observed, and the spatial distribution of all sources in figure 3.1. From this we find that the fraction of blended sources (parameter b in section 3.A) is $\sim 3-4\%$. For an alternative luminosity function, in which the lower cut-off is set at 10^{34} erg s^{-1}, b ∼9-10%.
As only ∼20% of the GCs host LMXBs, the fraction of blended sources is also likely to be low here ($b \sim 4$ per cent, assuming that all GCs are identical, but the exact number depends on the distribution of GC properties relevant for the formation of LMXBs). For comparison one out of 12 GCs hosting LMXBs in the Galaxy has been shown to host two LMXBs (White & Angelini, 2001), corresponding to $b \sim 8-9$ per cent. In section 3.A we consider the effects of source blending on the observed LF, and we show that for the values of b in this range, the effect of blending is not important. Given the *Chandra* angular resolution, at the distance of M31, all X-ray sources in a GC will be blended into one point like source. As there are numerous sources of low luminosity $L_X \lesssim 10^{34}$ erg s^{-1}, this could possibly affect our analysis. This is not the case, however, as the luminosities of these sources are too low. For example the combined luminosity of the $\sim$ 300 observed sources in the massive Galactic GC 47 Tucanae is $\sim 5 \cdot 10^{33}$ erg s^{-1} (Heinke et al., 2005), i.e. less than 1% of the luminosity of a typical GC source observed in M31.

From a visual comparison of figure 3.5 and figure 3.6, it appears that the LF of the LMXBs of presumably dynamical origin is different from the average LF of all the LMXBs. We investigate this difference further in figure 3.8 where we compare the LF of the dynamically formed LMXBs (sources located in the inner 1 arcmin and in confirmed GCs), with the LF of all other sources in the 1 arcmin-9 arcmin annulus. These are, presumably, of primordial origin. This figure confirms qualitatively the difference between the two populations. It is obvious however that due to rather limited numbers of sources the LFs are not very tightly constrained. In particular, the statistics is insufficient to discriminate between a genuine low-luminosity cut-off in the LF of dynamically formed sources and its moderate flattening. To estimate the statistical significance we consider the numbers of sources in different sub-populations in the $1.5 \cdot 10^{35} - 10^{36}$ erg s^{-1} luminosity range (the lower boundary is defined by the low bound of the primordial LF, see discussion earlier in this section). There are two sources in this luminosity range in the population of the dynamically formed LMXBs, whereas 17.4 ± 4 would be expected if the source counts in the $10^{36} - 10^{37}$ erg s^{-1} range were extrapolated with a $dN/dL \propto L^{-1}$ law. Due to nearly identical normalizations of the two LFs above $\log(L_X) \gtrsim 36$ (cf. figure 3.8), these numbers can be directly compared with 32 ± 11 primordial sources (CXB contribution subtracted and incompleteness corrected) observed in the same luminosity range (20 ± 5.6 sources expected for L^{-1} extrapolation). In order to further quantify the difference between the two luminosity distributions we fit them by single powerlaw in the $1.5 \cdot 10^{35} - 10^{37}$ erg s^{-1} luminosity range, using ML fits. For the primordial sources we obtained a differential slope of -1.11 ± 0.18, while the LF of dynamicaly formed LMXBs has a slope of -0.6 ± 0.2. Although the difference between these two numbers is only marginally significant, the LF slope of the dynamically formed LMXBs is inconsistent with the value of -1 obtained for the average LMXB LF.

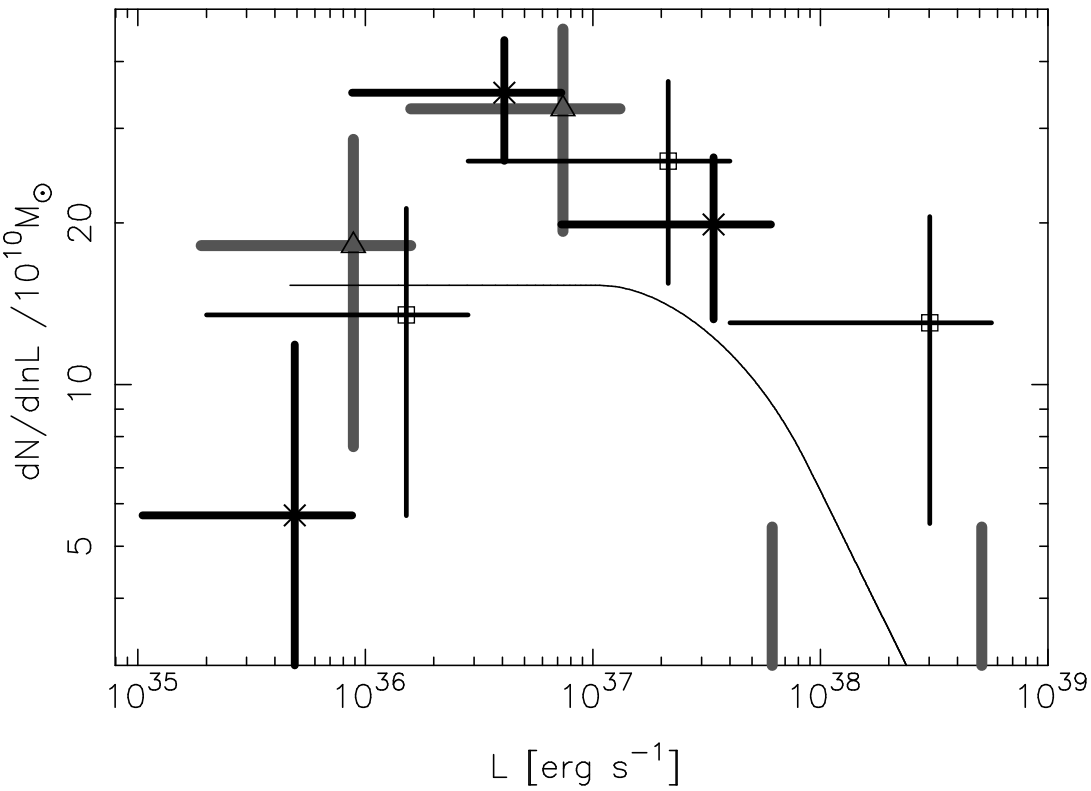

Figure 3.6: The LF of the sources in the inner 1 arcmin (crosses, 27 sources), the LF of the X-ray sources in confirmed GCs (squares, 12 sources) and the LF of the X-ray sources in GC candidates (triangles, 9 sources). The normalization of the LFs from GCs and GC candidates is arbitrary. The solid line is the average LMXB LF, with the same normalization in figures 5-10.

It is interesting to compare the results with the bright ($L_x \gtrsim 10^{35}$ erg s^{-1}) LMXBs in Galactic GCs. Currently 13 of such LMXBs have been observed in 12 GCs, and due to the proximity the sample is believed to be complete, except for possible future transients. While all of these sources have been observed with *Chandra*, there are not published luminosities for all of them, and analysis of the observations are beyond the scope of this paper. Instead we find the luminosities by averaging the lightcurves for each of the sources from *RXTE ASM*, over all of the observed time (until January 1st, 2007). The count rates were converted to fluxes in the 0.5-8.0 keV band, assuming a powerlaw spectrum with photon index 1.7, using `PIMMS`[2]. This gives a conversion factor of 1 count s^{-1} = $4.3 \cdot 10^{-10}$ erg cm^{-2} s^{-1}. In figure 3.7 the LF of the LMXBs in Galactic GCs is compared to the LF of LMXBs in confirmed GCs in M31, and it is shown that also in the Galaxy there is a clear cut-off at $\sim 10^{36}$ erg s^{-1}.

The difference between the LF of primordial and dynamically formed LMXBs is interesting for several reasons. It has recently been discussed whether most of the field

[2]http://cxc.harvard.edu/toolkit/pimms.jsp

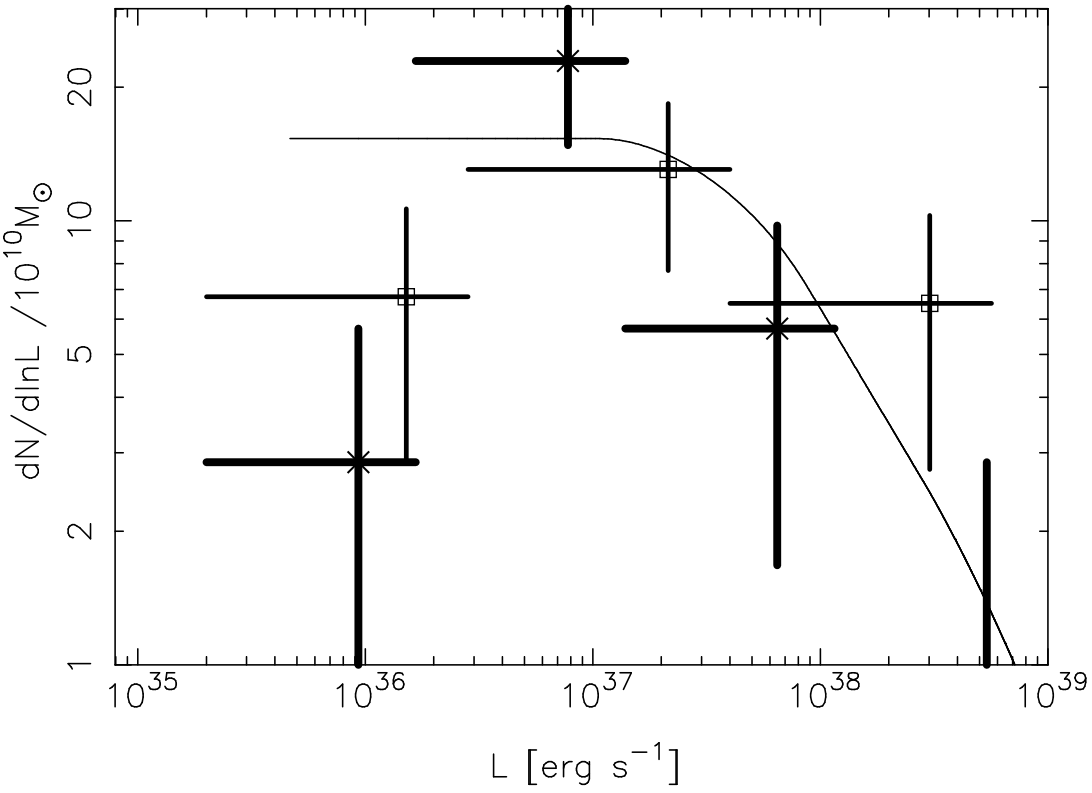

Figure 3.7: The LF of the LMXBs in Galactic GCs (crosses, 12 sources) compared to the LF of the LMXBs in confirmed GCs in M31 (squares, 12 sources). The solid line is the average LMXB LF, with the same normalization if figures 5-10.

LMXBs were actually formed in GCs (e.g. White et al., 2002; Juett, 2005). If the LFs of the field and GC LMXBs are different indeed, it is a strong indication that their origin is different as well. Moreover, the fact that the LF of the sources in the inner 1 arcmin is consistent with the LF of the GC sources and different from the LF of the field LMXBs reinforces the conclusion of Voss & Gilfanov (2007) that the surplus X-ray sources in the center of M31 are LMXBs created through dynamical interactions in high stellar density environment of the inner bulge. Differences between the LFs of dynamically formed LMXBs in the globular clusters and field LMXBs have previously been reported (Kong et al., 2002; Trudolyubov & Priedhorsky, 2004) but at larger luminosities, above 10^{37} erg s^{-1}. These have been disputed in a recent thorough study of six elliptical galaxies by Kim, E., et al. (2006), who concluded that the LFs of the two populations are consistent. We note that the differences found in the analysis of this paper occur at luminosities below the sensitivity threshold of Kim, E., et al. (2006), and our results do therefore not contradict theirs.

Various models for LMXB evolution exist, from which the shape of their luminosity distribution can be predicted. For a population of LMXBs with non-degenerate donors, the differential powerlaw slope of -1 at luminosities below $\sim 10^{37}$ can be nat-

urally obtained if the mass transfer is driven by gravitational radiation, as opposed to the steeper slope above $\sim 10^{37}$ erg s^{-1}, which can be explained by the magnetic braking driven systems (Postnov & Kuranov, 2005; Pfahl et al., 2003). Ultra-compact X-ray binaries (UCXB) have degenerate donor stars and the mass transfer is driven by gravitational radiation alone. In this case the reaction of the WD donor to mass loss is important for the mass transfer rates and therefore also for slope of the LF, and models have been succesful in explaining the bright end of the LMXB LF, near and above $\sim 10^{38}$ erg s^{-1} (Bildsten & Deloye, 2004). No modeling of the fainter end of luminosity distribution for UCXB population has been reported so far. Intuitively, one might expect that the luminosity distribution of these systems should fall off at low luminosities. Although the UCXB systems are very unlikely to contribute significantly to the bulk of fainter primordial LMXBs in the $\log(L_X) \lesssim 37$ luminosity domain, their importance increases dramatically in the entire luminosity range when considering the LMXBs of dynamical origin, especially those formed in the high velocity environment of the inner bulge (Voss & Gilfanov, 2007). This offers a plausible explanation of the rather peculiar shape of the luminosity distribution of the globular cluster sources and of the sources in the inner 1 arcmin of M31. As the reaction of the WD donor to mass loss depends on the chemical composition of the WD, modeling the luminosity function at low luminosities and comparing with observations of LMXB in the inner bulge and in globular clusters in M31 and other galaxies might reveal new information on the progenitors of the UCXBs and advance our understanding of binary evolution and dynamical interactions in dense stellar environments in general.

Another factor, potentially important at low mass transfer rates, is the thermal-viscous instability, which causes transient behaviour in LMXBs below some critical value of the mass accretion rate (van Paradijs, 1996). Consequently, the LF of persistent sources should be expected to have a break around this luminosity. The critical luminosity is somewhere in the $\lesssim 10^{35-36}$ erg s^{-1} domain, and depends, among other parameters, on the physical size of the accretion disk around the compact object (King & Ritter, 1998). In this picture, if the disk instability was the reason of the observed low luminosity cut-off observed in figure 3.6, the critical luminosity for UCXBs was expected to be lower than for LMXBs with non-degenerate donors. This prediction seems to be in contrast to the result of this paper, that the LF of the dynamically formed LMXBs (presumably having a significantly higher fraction of UCXBs) appears to be flatter (i.e. fewer faint systems) than the LF of the primordial LMXBs.

In the previous study of LMXBs in the bulge of M31 (Kong et al., 2002), it was found that their LF varied significantly with the distance from the centre, becoming progressively steeper with radius. We searched for the radial trend by comparing the LFs of the primordial LMXBs (that is, with LMXBs in GCs excluded) of the annuli 1 arcmin-3 arcmin, 3 arcmin-6 arcmin and 6 arcmin-12 arcmin (figure 3.9), and found no statistically significant variations. We suggest that the difference in the LF reported by them, especially between their regions 2 and 3, was caused by the contribution of CXB sources which becomes more important in the outer parts of the bulge (cf. figure 3.1). Note that this possibility was also considered by Kong et al. (2002).

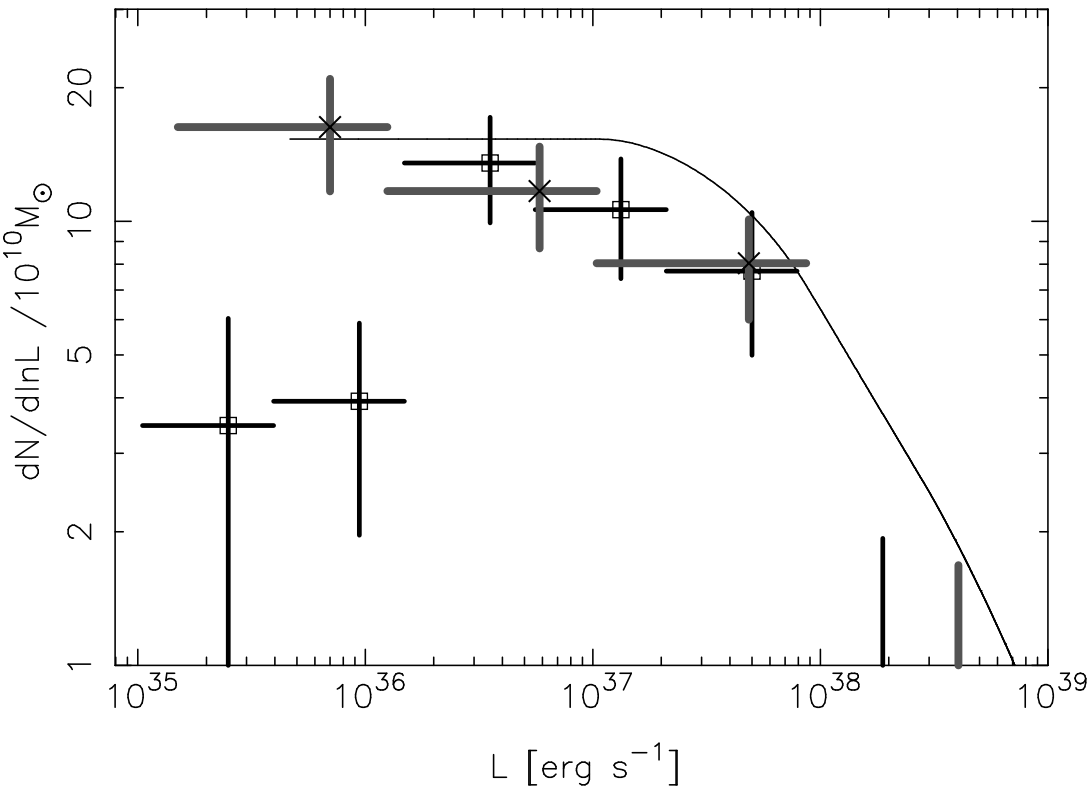

Figure 3.8: The LF of sources with a radial distance of 1 arcmin-9 arcmin from the centre of M31, excluding sources in GCs and GC candidates (crosses, 130 sources), compared to the LF of sources from the inner 1 arcmin and sources in confirmed GCs (squares, 40 sources). The normalization of the latter is arbitrary. The solid line is the average LMXB LF, with the same normalization in figures 5-10.

In figure 3.10, we show the LF of transient sources. As the average luminosity is meaningless, due to its dependence on the exposure time and pattern of the observations in which the sources were found, we have chosen to use the maximum of the observed luminosities in the individual observations for each source. It is interesting to see that the LF of these sources follows the average LF of LMXBs to a minimum luminosity of 10^{37} erg s^{-1}. Below this the observed distribution falls off quickly, but this is likely an artifact of the our selection criterium for transient sources, $F_{max}/F_{min} > 20$. For most sources with peak luminosities below 10^{37} erg s^{-1}, it is not possible to constrain the quiescent luminosity well enough to classify the sources as transients.

3.6 Conclusions

We have studied the X-ray point sources in the bulge of M31 ($r < 12$ arcmin) based on the archival *Chandra* data. Our study concentrated on statistical properties of the population, with emphasis on the spatial distribution and LFs of the various subpopulations. One of our primary goals was to contrast properties of different subpopulations of X-ray point sources, namely transient and persistent sources, primordial

LMXBs and the dynamically formed ones. To achieve this we combined 26 *Chandra* observations observations to get as much exposure as was possible at the time this project started and implemented an adequate correction for incompleteness effects, as well as for the contamination from background sources.

With a total exposure time of 201 ks, we detected 263 X-ray point sources within a distance of 12 arcmin from the centre of M31. Of these sources 64 were not observed previously. This allowed us to study the sources to a minimum luminosity of $\sim 10^{35}$ erg s^{-1}, whereas the sample is complete above $\sim 10^{36}$ erg s^{-1}. We found good agreement between the observed number of sources, and the expected number, predicted based on the K-band luminosity and average X-ray mass to light ratio for nearby galaxies. The radial distribution of the M31 sources (figure 3.1) can be interpreted as superposition of the following three components: (i) primordial LMXBs following the K-band light profile, (ii) LMXBs created through dynamical interactions in the inner bulge of the galaxy, with a distribution that follows the square of the stellar density ρ_*^2 and (iii) LMXBs dynamically created in the globular clusters, with a radial profile that follows the distribution of globular clusters in M31. Superimposed on these are the CXB sources, the distribution of which is flat on the angular scales under consideration.

After applying the incompleteness correction and subtracting the contribution of CXB sources, we were able to recover the LF of M31 sources down to the luminosity of $\sim$ few $\times 10^{35}$ erg s^{-1}, which is a factor of ~ 3 better than previous studies. The luminosity distribution of all X-ray sources in the bulge of M31 (Fig.3.5) is consistent with the average LMXB LF obtained by Gilfanov (2004), in particular, it follows the $dN/dL \propto L^{-1}$ law in the faint luminosity limit, in agreement with the behaviour found earlier for LMXBs in the Milky Way and in Cen A. It was furthermore possible to divide the LMXBs into two subpopulations – primordial LMXBs and dynamically formed ones, in order to study the differences in their luminosity distributions (figure 3.8). We found that the LF of the primordial LMXBs is consistent with the average LMXB LF, and is independent on the radial distance from the centre of M31, within the accuracy allowed by the statistics of our sample. The LMXBs thought to be of dynamical origin have a significantly different luminosity distribution – below $\log(L_X) \lesssim 36.5$ their LF shows a prominent decrease towards low luminosities (figure 3.6). The statistics is not sufficient to tightly constrain the shape of the LF, in particular to distinguish between a true low luminosity cut-off and a more moderate flattening of the luminosity function. It is however sufficient to claim that the low luminosity, $\log(L_X) < 37$, slope of the LF of these sources, -0.6 ± 0.2 is inconsistent with the $dN/dL \propto L^{-1}$ law.

We identified the population of transient sources and found that their radial distribution is consistent with the distribution of persistent sources. However the current statistics is insufficient to investigate differences between the fractions of transients in primordial and dynamically formed LMXBs, especially in the inner 30 arcsec, where the radial distribution of these two populations differ the most. It is interesting to note that above $\sim 10^{37}$ erg s^{-1} the LF of the maximum luminosity of the transients follow the average LMXB LF (figure 3.10).

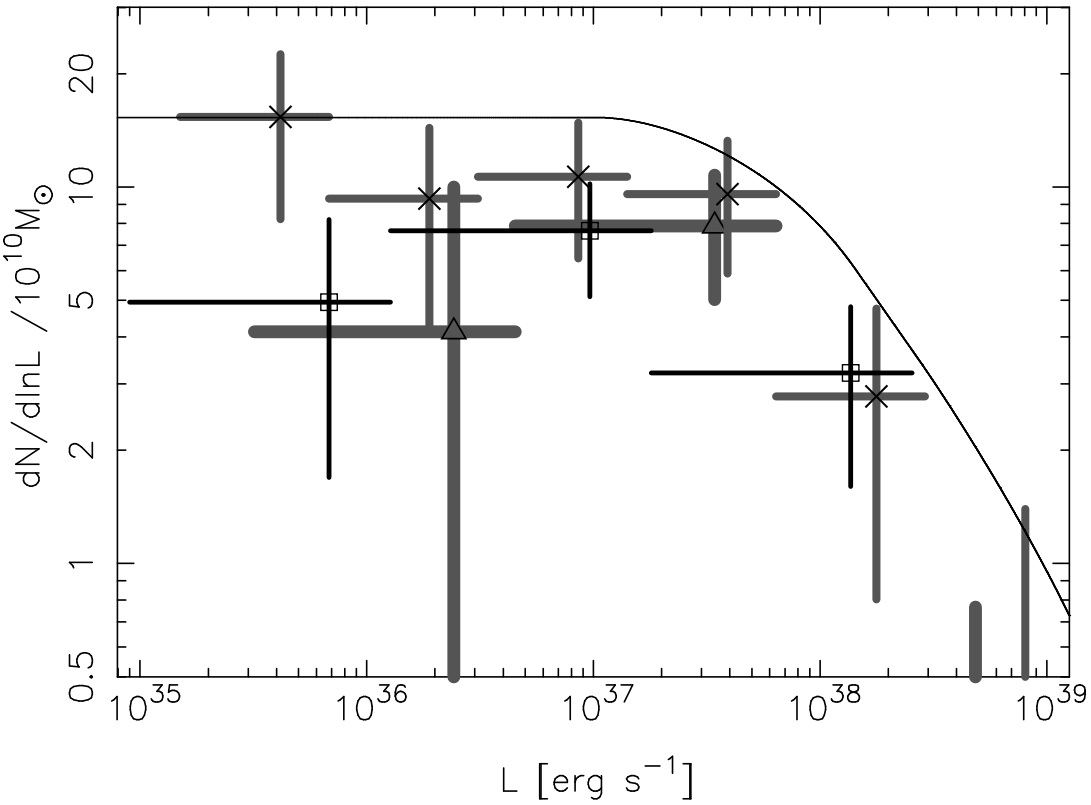

Figure 3.9: The LF of sources with a radial distance of 1 arcmin-3 arcmin (crosses, 28 sources), 3 arcmin-6 arcmin (squares, 56 sources) and 6 arcmin-12 arcmin from the centre of M31, excluding sources in GCs and GC candidates (triangles, 58 sources). The solid line is the average LMXB LF, with the same normalization if figures 5-10.

Acknowledgements

This reaserch has made use of *CHANDRA* archival data provided by the *CHANDRA* X-ray Center and data from the 2MASS Large Galaxy Atlas provided by NASA/IPAC infrared science archive, as well as *ASM/RXTE* data obtained through the HEASARC online service. We thank the referee for helpful remarks on the paper.

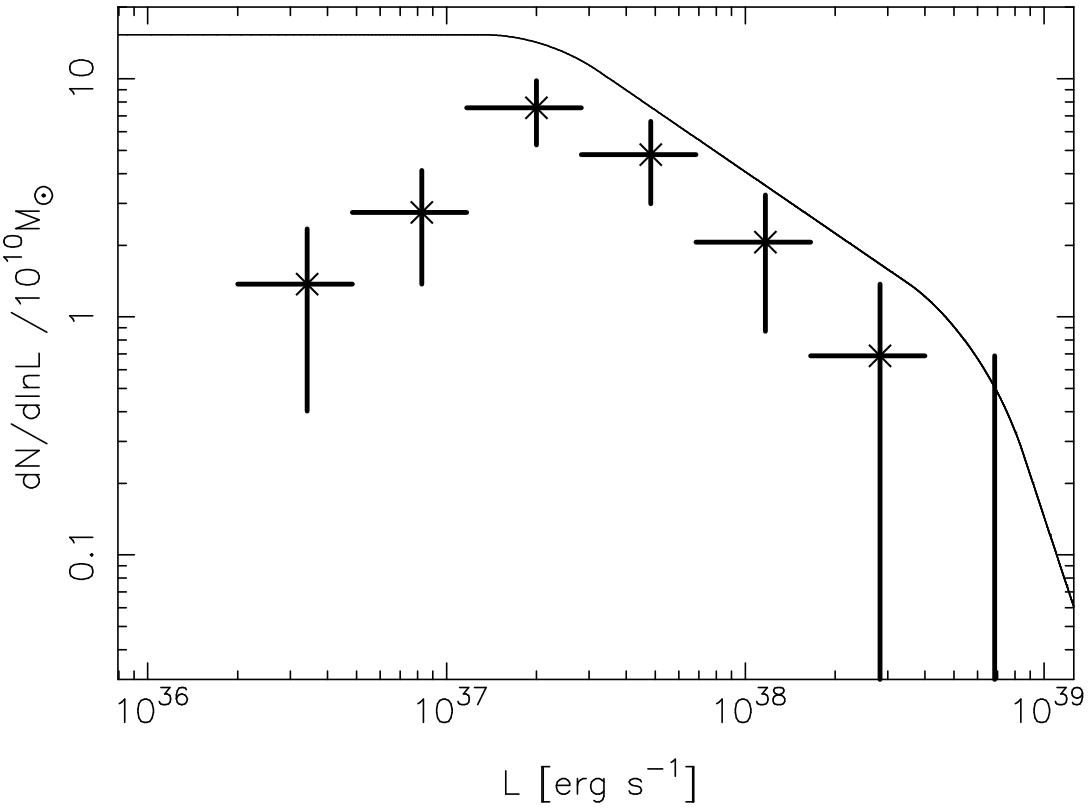

Figure 3.10: The LF of the maximum luminosity of the transients observed (28 sources). Note, that below $\sim 10^{37}$ erg/s it is subject to strong selection effects. The solid line is the average LMXB LF, with the same normalization in figures 5-10.

Bibliography

Bell, E., & De Jong, R. 2001, ApJ, 550, 212

Bildsten, L., Deloye, C.J. 2004, ApJ, 607, L119

Börngen, F. 1968, Astronomisch Nachrichten, 291, 19

Braun, R. AJS, 72, 761

Ciardullo, R., Ford, H.C., Neill, J.D., Jacoby, G.H., Shafter, A.W. 1987, ApJ, 318, 520

Ciardullo, R., Jacoby, G.H., Ford, H.C., Neill, J.D. 1989, ApJ, 339, 53

Crampton, D., Cowley, A.P., Hutchings, J.B., Schade, D.J., van Speybroeck, L.P. 1984, ApJ, 284, 663

Deloye, C.J., Bildsten, L. 2003, ApJ, 598, 1217

Devereux, N.A., Price, R., Wells, L.A., Duric, N. 1994, AJ, 108, 1667

Dickey, J.M., & Lockman, F.J. 1990, ARA&A, 28, 215

Fabbiano, G. 2006, ARA&A 44, 323

Fan, Z., Ma, J., Zhou, X., Chen, J., Jiang, Z., Wu, Z. 2005, PASP, 117, 1236

Galleti, S., Federici, L., Bellazzini, M., Fusi Pecci, F., & Macrina, S. 2004, A&A, 416, 917

Gehrels, N. 1986, ApJ 303, 336

Gelfand, J.D., Lazio, T.J.W., Gaensler, B.M. 2004, ApJS, 155, 89

Gilfanov, M. 2004, MNRAS, 349, 146

Grimm, H-J., Gilfanov, M.R., & Sunyaev, R.A. 2003, MNRAS, 339, 793

Harnden, F.R., Fabricant, D.G., Harris, D.E., Schwarz, J. 1984, SAO Special Report #393

Heinke, C.O., Grindlay, J.E., Edmonds, P.D., et al. 2005, ApJ, 625, 796

Jarret, T.H., Chester, T., Cutri, R., Schneider, S., & Huchra, J.P. 2003, AJ, 125, 525

Juett, A.M. 2005, ApJ, 621, L25

Kaaret, P. 2002, ApJ, 578, 114

Kim, D.-W., Fabbiano, G. 2004, ApJ, 611, 846

Kim, D.-W., Fabbiano, G., Kalogera, et al. 2006, astro-ph/0606008

Kim, E., Kim, D.-W., Fabbiano, G., Lee, M.G., Park, H.S., Geisler, D., Dirsch, B. 2006, ApJ, 647, 276

King, A.R., Ritter, H. 1998, MNRAS, 293, L42

Kong, A.K.H., Garcia, M.R., Primini, F.A., Murray, S.S., Di Stefano, R., McClintock, J.E. 2002, ApJ, 577, 738

Kong, A.K.H., Di Stefano, R., Garcia, M.R., Greiner, J. 2003, ApJ, 585, 298

Macri, L.M. 2001, ApJ, 549, 721

Magnier, E.A. 1993, Ph.D. thesis, MIT

Magnier, E.A., Prins, S., van Paradijs, J. Lewin, W.H.G., Supper, R., Hasinger, G., Pietsch, W., Truemper, J. 1995, A&AS, 114, 215

Meyssonnier, N., Lequeux, J., Azzopardi, M. 1993, A&AS, 102, 251

Monet, D.G., Levine, S.E., Canzian, B., et al. 2003, AJ, 125, 984

Moretti, A., Campana, S., Lazzati, D., & Tagliaferri, G. 2003, ApJ, 588, 696

Morrison, J.E., Röser, S., McLean, B., Bucciarelli, B., Lasker, B. 2001, AJ, 121, 1752

Pfahl, E., Rappaport, S., Podsiadlowski, P. 2003, ApJ, 597, 1036

Pietsch, W., Fliri, J., Freyberg, M.J., Greiner, J., Haberl, F., Riffeser, A., Sala, G. 2005a, A&A, 442, 879

Pietsch, W., Freyberg, M.J., Haberl, F. 2005b, A&A, 434, 483

Postnov, K.A., Kuranov, A.G. 2005, Astro. Lett., 31, 7

Primini, F.A., Forman, W., Jones, C. 1993, ApJ, 410, 615

Shafter, A.W., Irby, B.K. 2001, ApJ, 563, 749

Shirey, R., Soria, R., Borozdin, K., et al. 2001, A&A, 365, 195

Shtykovskiy, P., & Gilfanov, M., 2005, A&A, 431, 597

Skrutskie, M.F., Cutri, R.M., Stiening, R. et al. 2006, AJ, 131, 1163

Stanek, K.Z., & Garnavich, P.M. 1998, ApJ, 503, 131

Trudolyubov, S., Priedhorsky, W. 2004, ApJ 616, 821

Trudolyubov, S., Priedhorsky, W., Cordova, F. 2006, ApJ 645, 277

van Paradijs, J. 1996, ApJ, 464, L139

Voss, R., & Gilfanov, M. 2006, A&A, 447, 71

Voss, R., & Gilfanov, M. 2007, in preparation

Walterbos, R.A.M., & Kennicutt, R.C. 1987, A&AS, 69, 311

White, N.E., & Angelini, L. 2001, ApJL, 561, L101

White, R.E., Sarazin, C.L., Kulkarni, S.R. 2002, ApJ, 504, L31

Williams, B.F. 2003, AJ, 126, 1312

Williams, B.F., Garcia, M.R., Kong, A.K.H., Primini, F.A., King, A.R., Di Stefano, R., Murray, S.S. 2004a, ApJ, 609, 735

Williams, B.F., Garcia, M.R., McClintock, J.E., Kong, A.K.H. 2004b, AJ, 128, 1588

Williams, B.F., Garcia, McClintock, J.E., Primini, F.A., Murray, S.S., 2005, ApJ, 632, 1086

Williams, B.F., Naik, S., Garcia, M.R., Callanan, P.J. 2006, ApJ, 643, 356

Appendix 3.A The effects of source blending on the luminosity function

In densely populated regions of X-ray point sources, such as GCs or the very inner parts of a galaxy, a fraction of the observed point sources will in fact be a blend of two or more sources. Here we present a brief investigation of the effects of such source blending on the observed LF. If the distribution of luminosities of single sources is given by $P_1(L)$, then the distribution of luminosities $P_2(L)$ of a blend of two sources is given by

$$P_2(L) = \int_0^L P_1(\xi) P_1(L-\xi) d\xi \tag{3.3}$$

Ignoring blends of three or more sources, the observed luminosity distribution is then given by

$$P_d(L) = (1-b)P_1(L) + bP_2(L) \tag{3.4}$$

where b is the fraction of observed sources that are blends of two sources. In figure 3.11 we show the effects of source blending on the LMXB LF of Gilfanov (2004). The two models shown have different lower cut-off luminosities, below which the functions are set to zero, 10^{34} erg s^{-1} for the lower model and 10^{36} erg s^{-1} for the upper model (the assumed LFs are therefore equal to the LFs for which b was calculated in section

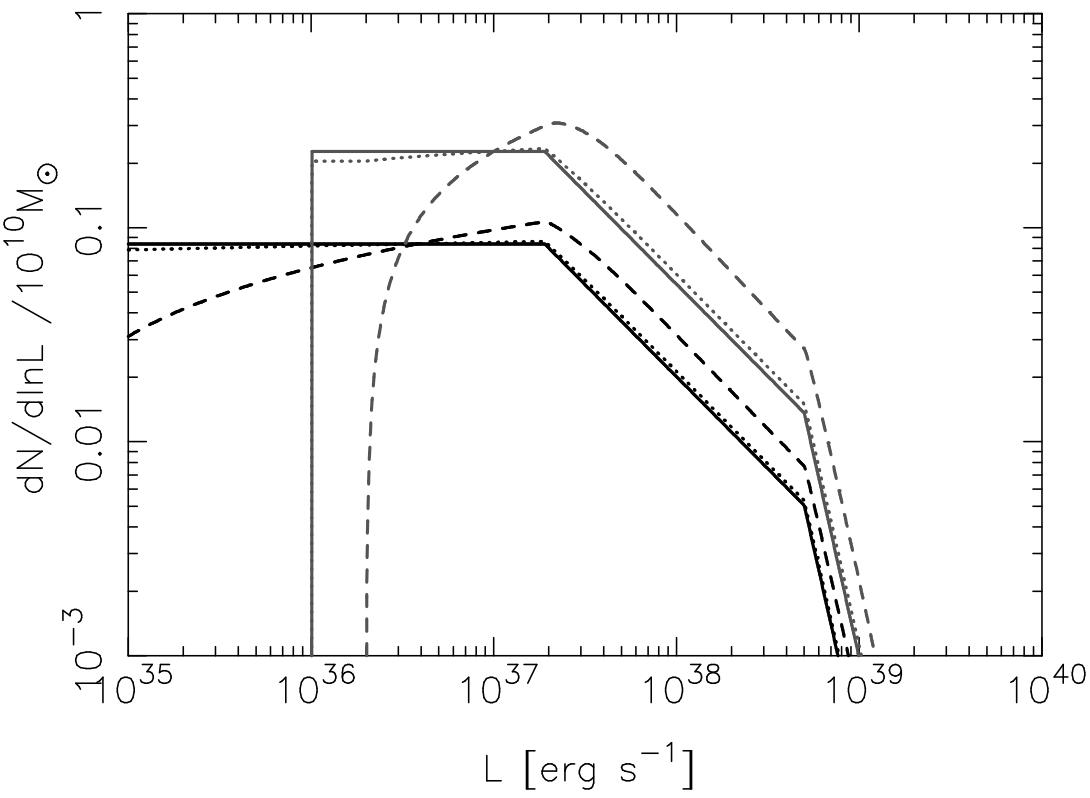

Figure 3.11: The effects of blending on the LMXB LF of Gilfanov (2004). The solid lines are the LFs without blending, whereas the dashed and dotted lines are the LFs assuming $b = 1$ and $b = 0.1$, respectively.

3.5). The solid lines give $P_1(L)$, whereas the dashed lines gives $P_2(L)$. The dotted lines gives $P_d(L)$, for $b = 0.10$. It is clear that for sources samples with $b \lesssim 0.10$ the effects on the observed LF are negligible, and even for samples with higher values of b, the effects are relatively small.

Table 3.4: The list of point like X-ray sources within a distance of 12 arcmin from the centre of M31

Number (1)	distance (2)	RA (3)	DEC (4)	cts (5)	cor. cts (6)	error (7)	luminosity (8)	type (9)	id (10)	name (11)
1	1.0	00 42 44.37	41 16 08.7	2245	2580.7	58.0	7.08e+36			r1-10
2	2.2	00 42 44.38	41 16 07.4	2864	3308.2	65.4	1.08e+37			r1-9
3	4.0	00 42 44.38	41 16 05.4	1117	1233.9	41.3	5.32e+36			r1-21
4	4.6	00 42 44.30	41 16 14.0	316	344.9	22.6	1.52e+36			r1-22
5	5.4	00 42 43.86	41 16 11.1	225	244.1	19.2	1.07e+36			r1-27
6	7.4	00 42 43.87	41 16 03.9	709	811.6	33.1	3.53e+36			r1-23
7	9.7	00 42 44.68	41 16 18.2	906	1047.3	37.3	4.62e+36			r1-8
8	10.6	00 42 45.24	41 16 11.1	456	516.2	26.8	2.25e+36			r1-20
9	14.5	00 42 45.60	41 16 08.6	1026	1191.0	39.5	5.21e+36			r1-7
10	15.3	00 42 45.12	41 16 21.7	3098	3631.2	67.9	1.61e+37	RAD	S WSTB 37W135	r1-4
11	20.8	00 42 43.88	41 16 29.6	1293	1463.5	44.5	6.54e+36			r1-11
12	21.7	00 42 46.01	41 16 19.6	468	531.3	27.2	2.33e+36	t		r1-19
13	23.8	00 42 43.75	41 16 32.4	2329	2726.7	59.0	1.24e+37			r1-12
14	24.0	00 42 42.18	41 16 08.3	4525	5353.9	81.6	2.45e+37	t		r1-5
15	25.9	00 42 42.48	41 15 53.7	3077	3601.1	67.6	1.62e+37	PN	CIA 4	r1-14
16	30.1	00 42 43.00	41 15 43.2	2424	2839.4	60.1	1.29e+37			r1-13
17	30.6	00 42 46.97	41 16 15.6	4037	4736.5	77.3	2.07e+37			r1-3
18	33.3	00 42 43.20	41 16 40.3	413	473.2	25.6	2.20e+36			r1-24
19	33.5	00 42 46.16	41 15 43.2	372	427.0	24.3	1.91e+36			r1-18
20	37.5	00 42 47.17	41 16 28.4	10653	12498.5	124.6	5.59e+37	PN	CIA 11	r1-2
21	41.0	00 42 42.65	41 16 45.9	38	33.6	8.8	1.58e+35			X
22	42.4	00 42 47.87	41 16 22.9	370	425.5	24.2	1.92e+36			r1-17
23	44.8	00 42 47.88	41 15 49.8	264	304.3	20.7	1.40e+36	t		r1-25
24	45.0	00 42 42.08	41 15 32.0	366	417.4	24.2	2.14e+36			r1-31
25	45.1	00 42 45.54	41 16 52.3	27	23.4	7.6	1.09e+35			X
26	47.0	00 42 45.09	41 15 23.2	386	441.1	24.8	2.05e+36	PN	CIA 18	r1-26
27	52.0	00 42 48.72	41 16 24.5	523	606.0	28.6	2.72e+36			r1-16
28	53.3	00 42 40.00	41 15 47.5	4068	4772.3	77.5	2.32e+37	RNova	SI 1997-06	r1-15
29	53.5	00 42 39.59	41 16 14.3	2967	3500.0	66.4	1.73e+37	t		r1-34
30	53.9	00 42 42.53	41 16 59.4	210	240.8	18.6	1.11e+36			r1-30
31	54.5	00 42 47.90	41 15 32.9	3265	3834.7	69.6	1.84e+37			r1-6
32	55.7	00 42 43.79	41 15 14.1	110	117.5	13.8	5.69e+35	t		r1-28
33	55.8	00 42 41.45	41 15 23.8	471	540.7	27.2	2.93e+36	GC	Bol B124	r1-32
34	64.7	00 42 38.59	41 16 03.7	27143	31287.2	198.7	1.54e+38			r2-26
35	67.8	00 42 48.53	41 15 21.2	12231	14353.6	133.8	6.74e+37			r1-1
36	72.2	00 42 50.62	41 15 57.1	35	23.7	8.5	1.15e+35	SNR	B90 101	r2-56
37	73.4	00 42 39.65	41 17 00.7	35	33.5	8.4	1.71e+35			K
38	73.6	00 42 45.22	41 17 22.3	675	783.9	32.2	3.63e+36	t		r2-16
39	75.5	00 42 50.82	41 15 51.6	25	22.1	7.4	1.08e+35	RNova	B68 27	X
40	75.7	00 42 38.80	41 15 26.2	35	29.8	8.5	1.50e+35			r2-54
41	76.0	00 42 42.73	41 14 55.5	46	47.2	9.4	2.55e+35	t		r2-20
42	81.9	00 42 46.14	41 17 28.6	21	20.7	6.8	9.45e+34			X
43	86.8	00 42 42.34	41 14 45.5	1868	2198.5	53.0	1.18e+37			r2-21
44	89.2	00 42 46.09	41 17 36.3	67	74.8	11.1	3.41e+35	GCC t	Bol BH16	r2-15
45	90.5	00 42 44.91	41 17 39.7	771	901.5	34.4	4.13e+36			r2-18
46	97.2	00 42 52.53	41 15 40.0	2740	3237.8	63.9	1.51e+37			r2-12
47	99.7	00 42 52.44	41 16 48.7	140	158.6	15.4	7.52e+35	t		X
48	107.5	00 42 49.15	41 17 42.0	90	103.4	12.6	4.75e+35			r2-41
49	113.5	00 42 44.63	41 18 02.8	21	19.9	6.8	9.00e+34			X
50	114.3	00 42 39.54	41 14 28.5	1169	1370.6	42.1	6.79e+36			r2-25
51	116.9	00 42 34.78	41 15 23.3	149	167.8	15.9	8.27e+35	t		r2-28
52	117.8	00 42 33.90	41 16 19.8	1217	1426.2	42.9	7.25e+36			r2-30
53	119.1	00 42 39.27	41 14 24.7	48	40.9	9.7	2.50e+35			r2-62
54	120.0	00 42 54.94	41 16 03.2	11609	13667.2	130.1	6.21e+37			r2-11
55	122.6	00 42 45.10	41 14 07.1	618	720.8	31.0	3.48e+36			r2-17
56	124.3	00 42 52.30	41 17 35.0	122	137.6	14.5	6.37e+35			r2-50
57	126.2	00 42 42.63	41 14 04.6	24	20.3	7.3	1.04e+35			X
58	130.6	00 42 36.05	41 17 41.0	15	13.0	6.0	6.04e+34	GCC	Bol B261	X
59	134.3	00 42 33.41	41 17 03.5	196	225.7	18.0	1.11e+36	t		r2-70
60	134.9	00 42 32.53	41 15 45.7	93	104.1	12.8	4.91e+35			r2-55
61	138.2	00 42 49.24	41 18 16.0	1627	1915.2	49.5	8.74e+36			r2-14
62	140.6	00 42 50.25	41 18 13.1	24	23.5	7.2	1.10e+35			r2-40
63	140.6	00 42 40.56	41 13 55.3	21	15.6	6.9	7.59e+34			r2-23
64	148.9	00 42 31.14	41 16 21.7	7403	8689.1	104.2	5.21e+37			r2-34
65	161.5	00 42 58.12	41 16 52.5	21	18.6	6.9	8.64e+34	GCC	Bol AU010	X
66	162.5	00 42 40.22	41 18 45.2	1090	1278.4	40.8	6.15e+36			r2-24
67	163.0	00 42 58.32	41 15 29.2	1537	1807.0	48.2	8.39e+36			r2-7
68	163.9	00 42 34.45	41 18 09.8	94	105.3	12.9	5.01e+35	t		r2-29
69	163.9	00 42 36.61	41 13 50.3	130	144.9	14.9	7.06e+35			r2-42
70	164.1	00 42 30.28	41 16 53.2	71	75.4	11.4	4.64e+35			r2-44
71	167.1	00 42 40.67	41 13 27.4	1530	1803.7	48.1	8.75e+36			r2-22
72	170.2	00 42 43.31	41 13 19.6	844	991.6	36.0	5.02e+36	t		r2-19
73	172.4	00 42 52.53	41 18 34.8	59	63.8	10.5	3.06e+35			r2-49
74	175.5	00 42 59.87	41 16 05.8	6988	8269.1	101.4	3.76e+37	GC	Bol B144	r2-5
75	177.1	00 42 50.72	41 13 27.8	20	18.4	6.7	9.03e+34			X
76	185.8	00 42 42.24	41 19 13.8	37	38.7	8.6	1.83e+35	RAD	B90 86	r2-53
77	186.3	00 42 52.64	41 13 28.5	60	61.4	10.6	2.98e+35			r2-38
78	189.2	00 42 52.53	41 18 54.4	13139	15495.8	138.6	7.47e+37			r2-13
79	191.2	00 42 55.19	41 18 36.1	635	744.8	31.5	3.58e+36			r2-10
80	192.4	00 42 54.36	41 13 33.9	30	28.1	7.9	1.36e+35			X
81	193.6	00 42 55.62	41 18 35.1	628	735.7	31.3	3.54e+36	FGS	Bol B138	r2-9

Table 3.4: continued.

Number (1)	distance (2)	RA (3)	DEC (4)	cts (5)	cor. cts (6)	error (7)	luminosity (8)	type (9)	id (10)	name (11)
82	195.7	00 42 29.84	41 17 57.5	19	16.7	6.6	1.01e+35	GC	Bol B103	X
83	204.1	00 42 51.66	41 13 02.9	260	297.7	20.6	1.51e+36			r2-39
84	204.5	00 42 27.49	41 14 53.0	76	81.3	11.7	4.54e+35	t		X
85	210.0	00 42 56.93	41 18 43.9	494	579.8	27.9	2.73e+36	t		r2-8
86	211.4	00 43 01.78	41 17 26.4	44	46.1	9.3	2.39e+35			r2-46
87	211.5	00 42 42.82	41 19 40.3	21	19.7	6.9	9.46e+34			X
88	215.2	00 43 02.94	41 15 22.6	4541	5335.8	82.2	2.52e+37	GC	Bol B146	r2-4
89	216.1	00 42 26.57	41 17 31.5	6	1.1	4.4	5.89e+33			X
90	217.3	00 43 03.22	41 15 27.8	6398	7511.3	97.2	3.57e+37	t		r2-3
91	217.5	00 42 58.09	41 13 37.3	39	36.6	8.9	1.72e+35			X
92	221.0	00 42 32.75	41 13 10.9	1005	1131.2	39.3	6.11e+36			r2-31
93	222.8	00 42 32.09	41 13 14.4	5162	6067.4	87.3	3.18e+37			r2-32
94	222.8	00 42 49.03	41 19 45.8	31	28.6	8.0	1.41e+35	RAD	S WSTB 37W138	r2-66
95	224.9	00 43 04.25	41 16 01.3	969	1139.6	38.6	5.62e+36	GCC	Fan 42	r2-1
96	229.2	00 42 24.19	41 15 36.9	35	26.1	8.5	1.50e+35			r2-52
97	229.6	00 42 32.09	41 19 13.1	37	35.0	8.7	1.70e+35			X
98	230.3	00 42 58.10	41 13 19.6	34	31.8	8.4	1.50e+35			X
99	232.6	00 43 01.71	41 18 14.5	31	26.6	8.0	1.33e+35			r2-47
100	234.4	00 43 01.12	41 13 51.6	242	270.6	19.9	1.27e+36			r2-37
101	235.1	00 42 30.96	41 19 10.1	104	117.9	13.5	6.95e+35			r2-43
102	240.7	00 42 24.24	41 17 31.5	44	38.9	9.3	2.19e+35			r2-57
103	243.2	00 42 22.96	41 15 35.3	13877	16254.1	142.4	9.59e+37			r3-39
104	244.6	00 43 01.72	41 18 35.5	28	24.1	7.7	1.24e+35			X
105	246.8	00 43 05.68	41 17 02.7	18818	21892.3	166.0	1.05e+38	t		r2-67
106	248.9	00 43 03.87	41 18 04.9	4658	5511.9	83.1	2.81e+37	GC	Bol B148	r2-2
107	251.0	00 42 44.40	41 11 58.4	488	571.2	27.7	4.36e+36			r3-30
108	253.7	00 42 47.24	41 11 57.9	159	181.2	16.4	1.34e+36			r3-27
109	254.3	00 42 24.16	41 14 15.3	22	19.9	7.0	1.21e+35			X
110	255.9	00 42 31.26	41 19 38.9	2884	3395.5	65.6	2.01e+37	GC	Bol B107	r2-33
111	256.9	00 42 59.66	41 19 19.3	6646	7851.7	98.9	3.94e+37	GC	Bol B143	r2-6
112	257.4	00 42 21.49	41 16 01.3	4270	5026.6	79.5	3.20e+37			r3-42
113	257.6	00 42 35.22	41 20 05.7	1496	1753.5	47.6	9.10e+36			r2-27
114	259.1	00 43 02.92	41 18 41.5	22	14.3	7.1	7.30e+34			X
115	260.3	00 42 21.29	41 15 48.8	21	15.5	6.9	1.09e+35	RAD	B90 65	X
116	262.3	00 42 25.15	41 13 40.6	614	712.8	31.0	4.44e+36			r2-45
117	262.5	00 42 21.80	41 15 02.7	32	29.1	8.1	1.89e+35			X
118	266.2	00 42 56.04	41 12 18.4	537	634.5	29.0	4.53e+36	t		r2-71
119	267.5	00 42 48.29	41 20 33.1	24	22.6	7.2	1.11e+35			X
120	267.9	00 42 23.16	41 14 07.5	1223	1435.2	43.2	8.95e+36			r3-38
121	269.0	00 42 59.52	41 12 42.3	173	191.7	17.1	9.62e+35			r2-48
122	270.0	00 42 54.79	41 20 12.2	21	17.9	6.9	8.95e+34			X
123	271.5	00 42 44.85	41 11 38.0	2955	3465.1	66.5	2.53e+37			r3-29
124	271.9	00 42 57.17	41 19 59.5	24	19.7	7.3	9.79e+34			X
125	277.1	00 42 26.05	41 19 15.0	1447	1697.3	46.9	9.40e+36	GC	Bol B096	r2-36
126	278.9	00 42 21.57	41 14 19.7	684	800.4	32.6	5.30e+36			r3-41
127	279.8	00 42 31.32	41 20 07.9	111	121.3	13.9	7.27e+35			r2-51
128	284.0	00 43 07.12	41 18 10.2	166	184.7	16.8	9.91e+35	Nova t	PI RJC 99 Jul 98	r3-115
129	285.4	00 42 20.85	41 17 56.7	33	31.4	8.2	1.85e+35			X
130	287.6	00 42 21.09	41 18 08.6	81	87.7	12.1	5.13e+35	t		r3-43
131	289.5	00 42 28.30	41 12 23.1	6286	7379.4	96.2	5.72e+37			r2-35
132	291.5	00 42 22.44	41 13 34.1	2253	2642.2	58.2	1.70e+37			r3-40
133	294.7	00 42 33.82	41 20 39.3	27	25.3	7.6	1.33e+35			X
134	297.5	00 42 58.61	41 11 59.5	28	26.5	7.7	1.72e+35			r2-59
135	297.6	00 42 41.65	41 21 05.5	450	522.2	26.7	3.64e+36			r3-31
136	298.2	00 42 47.83	41 11 13.9	168	189.4	16.8	1.50e+36	GCC t	Bol B128	X
137	300.6	00 42 59.02	41 11 58.8	33	32.8	8.2	2.14e+35			r2-58
138	301.6	00 42 20.85	41 13 44.5	27	23.2	7.6	1.62e+35			X
139	306.8	00 43 10.62	41 14 51.4	14308	16890.8	144.8	8.99e+37	GC	Bol B153	r3-15
140	307.1	00 42 50.02	41 11 09.1	93	98.7	12.9	7.51e+35			r3-24
141	308.9	00 42 41.12	41 11 02.6	30	25.9	8.0	2.07e+35			r3-32
142	311.2	00 42 46.94	41 21 19.2	214	243.8	18.8	1.71e+36			r3-28
143	311.9	00 42 18.43	41 17 59.6	8	0.8	4.9	5.37e+33			X
144	312.2	00 43 06.80	41 19 11.6	89	83.8	12.7	3.98e+35	EXT	Source 231	r3-67
145	312.9	00 42 16.55	41 16 10.7	30	27.5	7.9	1.90e+35			r3-75
146	313.5	00 42 17.04	41 15 08.2	261	299.0	20.6	2.19e+36	t		r3-46
147	314.6	00 43 06.75	41 19 16.6	100	97.3	13.3	4.73e+35	EXT	Source 160	r3-67
148	316.2	00 42 18.65	41 14 01.9	5388	6324.4	89.2	4.69e+37	GC	Bol B086	r3-44
149	318.6	00 42 16.09	41 15 53.3	37	36.6	8.6	2.80e+35			r3-76
150	318.9	00 42 47.88	41 10 53.1	54	56.4	10.1	4.71e+35			r3-26
151	320.1	00 43 02.44	41 12 03.1	54	55.6	10.1	4.05e+35			r3-68
152	321.4	00 42 20.48	41 13 13.2	34	27.6	8.4	2.03e+35			r3-89
153	327.9	00 43 11.37	41 18 09.9	317	360.6	22.7	1.93e+36			r3-14
154	330.4	00 42 15.69	41 17 21.0	2105	2476.8	56.2	1.69e+37			r3-47
155	335.1	00 43 09.85	41 19 00.9	1328	1559.0	45.0	8.29e+36	GCC t	Fan 44	r3-16
156	335.6	00 42 27.71	41 20 48.1	68	68.7	11.2	4.54e+35			r3-37
157	338.5	00 42 40.68	41 10 33.4	154	167.0	16.2	1.35e+36	GC	Bol B123	r3-34
158	339.3	00 43 13.88	41 17 12.2	70	64.0	11.4	3.59e+35			r3-12
159	340.2	00 43 08.64	41 12 48.4	1109	1292.5	41.2	6.86e+36			r3-17
160	341.1	00 42 57.91	41 11 04.8	4128	4861.9	78.4	3.65e+37			r3-22
161	341.5	00 43 14.38	41 16 50.2	119	121.6	14.5	6.61e+35			r3-11
162	343.1	00 42 50.76	41 10 34.1	48	46.0	9.7	3.58e+35	GCC	Bol BH18	r3-71
163	344.5	00 43 03.02	41 20 42.0	302	344.7	22.1	1.96e+36	PN	CIA 165	r3-21

Table 3.4: continued.

Number (1)	distance (2)	RA (3)	DEC (4)	cts (5)	cor. cts (6)	error (7)	luminosity (8)	type (9)	id (10)	name (11)
164	344.7	00 42 52.26	41 21 42.3	27	23.7	7.6	1.75e+35			X
165	346.2	00 42 15.24	41 18 01.3	190	210.4	17.8	1.48e+36			r3-49
166	348.8	00 43 13.23	41 18 13.5	418	473.5	25.8	2.67e+36	RNova	CFN 26	r3-13
167	350.4	00 42 16.98	41 18 56.4	54	51.6	10.2	3.24e+35			r3-91
168	350.6	00 42 33.46	41 21 38.0	49	45.2	9.8	3.83e+35	FGS	Bol B113	X
169	352.7	00 42 13.07	41 16 27.9	79	80.3	12.0	5.72e+35			r3-53
170	358.9	00 42 34.17	41 21 49.7	267	302.6	20.9	2.38e+36			r3-35
171	361.8	00 43 16.35	41 16 30.5	30	20.4	8.0	1.39e+35			X
172	362.0	00 43 07.50	41 20 19.9	550	632.5	29.4	3.51e+36	GCC	Bol B150	r3-18
173	366.3	00 42 40.73	41 10 05.3	33	25.8	8.3	2.24e+35			X
174	366.5	00 42 11.99	41 16 48.7	402	458.1	25.3	3.31e+36			r3-55
175	368.7	00 42 40.92	41 22 16.1	52	48.9	10.0	3.51e+35			r3-33
176	369.4	00 42 19.01	41 20 04.3	63	58.3	10.9	3.53e+35			r3-90
177	369.5	00 42 18.37	41 12 23.8	3119	3651.3	68.2	3.50e+37			r3-45
178	372.3	00 43 01.70	41 10 52.9	48	43.8	9.7	3.55e+35			r3-96
179	378.3	00 42 12.18	41 17 58.7	1554	1800.7	48.5	1.20e+37	GCC	Bol B078	r3-54
180	378.6	00 43 03.31	41 21 21.7	1486	1745.3	47.5	1.34e+37	FGS	Bol B147	r3-19
181	380.7	00 42 13.16	41 18 36.5	6027	7031.2	94.3	4.91e+37	FGS	Cra 13	r3-52
182	383.1	00 43 15.06	41 13 26.6	44	31.8	9.4	1.82e+35			X
183	385.5	00 43 14.18	41 13 02.0	51	35.7	10.0	2.04e+35			X
184	388.1	00 42 10.29	41 15 09.9	555	640.8	29.5	4.99e+36			r3-58
185	389.2	00 43 16.10	41 18 41.3	411	469.3	25.6	3.35e+36			r3-9
186	390.0	00 42 49.36	41 22 35.2	45	38.4	9.4	2.99e+35			X
187	392.9	00 42 15.14	41 12 34.6	2746	3194.3	64.2	2.67e+37			r3-50
188	393.2	00 42 25.35	41 10 39.4	33	16.3	8.4	1.59e+35			X
189	396.2	00 43 14.60	41 19 30.5	61	49.2	10.8	2.82e+35			X
190	403.9	00 42 09.51	41 17 45.6	1077	1244.1	40.6	8.92e+36	GCC	Mita 140	r3-59
191	404.3	00 42 54.26	41 09 41.0	29	22.5	7.9	1.91e+35			X
192	411.3	00 42 28.22	41 10 00.4	1989	2316.9	54.8	2.45e+37			r3-36
193	411.5	00 42 12.69	41 12 44.1	62	51.9	10.9	4.14e+35			r3-92
194	411.8	00 43 12.35	41 20 33.5	51	31.7	10.1	1.85e+35			X
195	412.7	00 43 03.13	41 10 15.6	561	643.6	29.7	5.25e+36	GCC	Fan 37	r3-20
196	417.2	00 42 15.51	41 20 31.5	570	655.6	29.9	4.67e+36	GCC	Fan 16	r3-48
197	420.2	00 43 21.57	41 15 57.4	52	37.0	10.1	2.37e+35			r3-104
198	425.4	00 42 07.10	41 17 20.1	140	145.1	15.5	1.10e+36			r3-79
199	426.1	00 42 11.00	41 12 48.3	270	296.3	21.0	2.34e+36			r3-57
200	426.6	00 43 21.08	41 17 50.5	724	826.5	33.6	5.02e+36			r3-7
201	430.6	00 42 07.77	41 18 14.9	4275	4995.6	79.7	3.72e+37			r3-61
202	432.2	00 43 17.06	41 12 25.1	28	19.9	7.8	1.75e+35			X
203	438.5	00 42 32.04	41 23 05.5	68	66.5	11.3	5.82e+35			r3-86
204	441.7	00 42 19.73	41 21 53.5	93	90.4	13.0	8.51e+35	GCC	Mita 166	r3-74
205	443.4	00 43 20.92	41 18 51.7	97	87.1	13.2	5.20e+35			r3-66
206	448.6	00 42 59.00	41 09 12.6	43	32.3	9.3	2.76e+35			X
207	448.9	00 43 19.98	41 12 50.2	50	32.3	10.	2.18e+35			X
208	451.6	00 43 15.42	41 11 25.3	167	182.8	16.8	1.57e+36	GC	Bol B161	r3-10
209	453.6	00 42 08.21	41 12 49.6	90	82.6	12.8	6.90e+35			r3-93
210	453.8	00 42 15.06	41 21 21.4	55	46.2	10.3	5.13e+35	GCC	Fan 15	r3-51
211	454.4	00 42 04.14	41 15 32.6	164	174.2	16.7	1.42e+36			r3-62
212	457.2	00 42 33.90	41 23 31.3	160	168.9	16.5	1.34e+36	t		X
213	458.9	00 42 09.62	41 20 09.8	76	68.7	11.9	5.43e+35	RAD	B90 34	r3-102
214	461.6	00 43 18.89	41 20 17.0	170	169.1	17.0	1.07e+36			r3-8
215	463.3	00 43 24.82	41 17 27.3	308	335.5	22.4	2.11e+36			r3-6
216	463.5	00 42 05.72	41 13 29.9	64	45.6	11.1	3.86e+35	t		r3-125
217	464.3	00 43 19.54	41 20 10.1	94	80.2	13.1	4.93e+35			X
218	468.0	00 43 06.65	41 22 43.9	87	87.3	12.6	7.83e+35	EmO	MLA 686	r3-83
219	468.4	00 43 18.39	41 11 41.8	38	29.3	8.8	2.69e+35			X
220	469.6	00 43 22.34	41 12 58.3	61	42.5	10.8	2.76e+35			r3-82
221	479.9	00 43 00.24	41 08 44.4	48	41.6	9.7	4.33e+35			X
222	480.5	00 43 17.95	41 11 14.7	42	33.0	9.2	3.33e+35			X
223	480.7	00 42 48.95	41 24 07.3	109	106.5	13.9	6.95e+35			r3-84
224	482.1	00 43 24.13	41 13 14.3	79	60.5	12.1	4.02e+35			r3-65
225	482.6	00 42 16.13	41 22 12.9	41	28.6	9.1	3.88e+35			X
226	484.8	00 42 09.10	41 20 48.0	698	799.3	33.0	7.81e+36			r3-60
227	487.2	00 42 11.78	41 10 49.0	386	430.9	24.9	6.10e+36			r3-56
228	493.0	00 43 18.73	41 21 13.8	48	41.3	9.7	4.07e+35			X
229	504.0	00 42 45.80	41 24 33.1	96	91.9	13.1	6.76e+35			r3-72
230	507.5	00 43 26.34	41 19 11.6	151	152.5	16.1	1.25e+36	RAD	GLG 005	r3-64
231	511.2	00 43 27.92	41 18 29.9	583	654.2	30.3	5.39e+36	SNR	B90 142	r3-63
232	513.6	00 42 05.90	41 11 33.7	85	75.6	12.5	1.10e+36			r3-80
233	521.7	00 42 24.51	41 24 01.1	58	43.6	10.6	4.12e+35			X
234	529.2	00 43 10.00	41 23 32.5	62	51.3	10.8	5.89e+35	PN t	CIA 350	r3-127
235	537.6	00 42 07.58	41 10 27.1	104	93.0	13.7	1.45e+36			r3-94
236	548.6	00 42 40.98	41 07 02.0	59	49.5	10.6	7.54e+35			r3-85
237	554.4	00 42 48.50	41 25 21.8	4302	5020.8	80.1	3.91e+37	t		r3-25
238	565.0	00 42 23.00	41 07 38.2	135	122.1	15.4	2.06e+36			r3-73
239	571.6	00 43 33.83	41 14 07.3	70	46.2	11.5	4.29e+35			X
240	575.9	00 42 49.41	41 06 36.3	54	42.5	10.2	7.28e+35			r3-98
241	585.2	00 43 08.89	41 07 34.2	38	34.9	8.8	8.72e+35			X
242	587.9	00 43 34.32	41 13 23.5	2185	2554.7	57.4	2.41e+37			r3-2
243	589.9	00 43 35.92	41 14 32.8	446	431.6	27.0	2.54e+36			X
244	590.7	00 42 53.68	41 25 50.6	313	322.0	22.6	3.66e+36	SNR	MG BA521	r3-69
245	600.3	00 42 55.40	41 25 56.5	1483	1696.3	47.6	1.84e+37			r3-23

Table 3.4: continued.

Number (1)	distance (2)	RA (3)	DEC (4)	cts (5)	cor. cts (6)	error (7)	luminosity (8)	type (9)	id (10)	name (11)
246	600.7	00 41 51.65	41 14 38.7	385	426.6	24.9	5.60e+36			r3-81
247	603.5	00 43 37.28	41 14 43.4	5112	5992.7	87.0	5.65e+37	GC	Bol B185	r3-1
248	617.2	00 42 26.26	41 25 52.2	581	660.6	30.2	9.26e+36	EmO	W2	r3-87
249	627.5	00 41 50.35	41 13 36.3	209	208.4	18.7	3.21e+36			r3-110
250	627.5	00 43 14.38	41 07 21.6	1405	1650.1	46.2	6.12e+37	GC t	Bol B158	r3-112
251	630.4	00 42 51.60	41 26 34.5	95	100.0	13.0	1.47e+36	RAD	GLG 011	r3-70
252	634.1	00 43 32.38	41 10 41.0	1298	1503.3	44.5	3.12e+37			r3-3
253	642.2	00 43 14.59	41 25 13.5	94	79.2	13.1	8.89e+35	GC	Bol B159	r3-105
254	645.6	00 43 33.58	41 21 39.1	70	73.3	11.4	1.38e+36			X
255	646.9	00 42 37.97	41 05 26.5	60	36.4	10.8	1.32e+36			r3-100
256	660.4	00 43 41.75	41 14 00.9	79	50.7	12.2	5.81e+35			X
257	669.7	00 42 32.82	41 27 06.5	26	18.0	7.5	3.02e+35			X
258	676.4	00 42 10.90	41 06 47.8	151	103.2	16.4	1.95e+36			r3-78
259	685.1	00 42 20.57	41 26 40.2	170	182.6	17.0	3.49e+36	EmO	W2	K
260	691.1	00 41 55.15	41 23 02.8	87	57.2	12.8	2.40e+36			r3-108
261	706.9	00 43 43.94	41 12 31.9	120	108.7	14.6	1.70e+36	RAD	B90 166	X
262	715.3	00 42 28.98	41 04 35.4	785	807.6	35.1	2.45e+37			r3-111
263	718.2	00 42 44.29	41 28 07.6	84	71.5	12.4	1.17e+36			X

(1) – The sequence number; (2) – Distance to the centre in arcsec; (3),(4) – Right ascension and declination of source; (5) – Source counts; (6) – Source counts after background subtraction; (7) – Statistical error on source counts after background subtraction; (8) – X-ray luminosity, 0.5-8 keV, assuming 780 kpc distance; (9) – Source Type: GC – confirmed globular cluster, GCC – globular cluster candidate, PN – planetary nebula, FGS – foreground star, Nova – nova, Rnova – Nova (random match), EmO – emission line object, RAD – radio source, SNR – supernova remnant, EXT – extended source, t – transient source; (10) – precise identification and reference: Bol – Galleti et al. (2004), Fan – Fan et al. (2005), Mita – Magnier (1993), MLA – Meyssonnier et al. (1993), W2 – Williams et al. (2004b), CIA – Ciardullo et al. (1989), CFN – Ciardullo et al. (1987), PI – Pietsch et al. (2005a), SI – Shafter & Irby (2001), B68 – Börngen (1968), S – Simbad, GLG – Gelfand et al. (2004), B90 – Braun (1990), MG – Magnier et al. (1995), Cra – Crampton et al. (1984); (11) – Source name in Kong et al. (2002), Williams et al. (2004a) and Williams et al. (2006); Sources not included in these catalogues are marked with K if observed in Kaaret (2002), else with X, indicating that these are new sources.

4

Dynamical formation of X-ray binaries in the inner bulge of M31

Submitted to: Monthly Notices of the Royal Astronomical Society, 2007
(astro-ph/0702580)

R. Voss & M. Gilfanov

Abstract

The radial distribution of luminous ($L_X > 10^{36}$ erg s^{-1}) X-ray point sources in the bulge of M31 is investigated using archival *Chandra* observations. We find a significant increase of the specific frequency of X-ray sources, per unit stellar mass, within 1 arcmin from the centre of the galaxy. The radial distribution of surplus sources in this region follows the ρ_*^2 law, suggesting that they are low-mass X-ray binaries formed dynamically in the dense inner bulge. We investigate dynamical formation of LMXBs, paying particular attention to the high velocity regime characteristic for galactic bulges, which has not been explored previously. Our calculations suggest that the majority of the surplus sources are formed in tidal captures of black holes by main sequence stars of low mass, $M_* \lesssim 0.4 M_\odot$, with some contribution of NS systems of same type. Due to the small size of the accretion discs a fraction of such systems may be persistent X-ray sources. Some of sources may be ultra-compact X-ray binaries with helium star/white dwarf companions. We also predict a large number of faint transients, both NS and BH systems, within ~ 1 arcmin from the M31 galactic centre. Finally, we consider the population of dynamically formed binaries in Galactic globular clusters, emphasizing the differences between these two types of stellar environments.

4.1 Introduction

It is a well known fact that the ratio of the number of low mass X-ray binaries (LMXBs) to stellar mass is $\sim$ two orders of magnitude higher in globular clusters (GCs) than in the Galactic disc (Clark, 1975). With the advent of *Chandra* and *XMM-Newton*, studies of X-ray point sources in external galaxies have become possible, and have shown that also there globular clusters are especially abundant in LMXBs. This is attributed to dynamical processes, through which LMXBs are formed in two-body encounters. Due to the ρ_*^2 dependence on the stellar density such encounters are frequent in globular clusters and are negligible in the field. Currently, there are 13 LMXBs (Liu et al., 2001) in the 150 globular clusters (Harris, 1996) known in the Galaxy.

In the central parts of massive galaxies, the stellar densities can reach values similar to the densities in less luminous GCs. Except for the very inner parts, these densities are still an order of magnitude smaller than the densities found in the most luminous GCs, where the LMXBs are preferentially found. However, the large volume compensates for the smaller density and LMXBs can be formed near the galactic centres in two-body encounters in non-negligible numbers. Whereas dynamical interactions in globular clusters have been intensively investigated, the parameter range typical of galactic centres remains unexplored. Due to an order of magnitude higher stellar velocities, the character of the dynamical interactions and relative importance of different formation channels in the galactic centres differ from those in globular clusters.

Due to the large stellar mass contained in the central region of a galaxy, a number of "primordial" LMXBs formed through the standard evolutionary path exist there too. Although these can not be easily distinguished from the binaries formed in two-body encounters, an argument of the specific LMXB frequency (per unit stellar mass) can be employed, in the manner similar to the one that led to the discovery of dynamical formation of binaries in globular clusters. The volume density of the primordial LMXBs follows the distribution of the stellar mass in a galaxy (Gilfanov, 2004) whereas the spatial distribution of the dynamically formed binaries is expected to obey the ρ_*^2/v law (Fabian et al., 1975). Hence the latter should be expected to be much more concentrated towards the centre of the host galaxy and reveal themselves as a population of "surplus" sources near its centre. M31 is the closest galaxy with a bulge density large enough to host a number of LMXBs formed through dynamical interactions. At a distance of 780 kpc (Stanek & Garnavich, 1998; Macri et al., 2001) X-ray sources can be easily resolved with *Chandra*, even near the centre of the galaxy. It has been studied extensively with *Chandra* and we use these observations to explore the radial distribution of bright X-ray point sources in the bulge. The results of this study are presented in the Section 4.2 where it is demonstrated that the specific frequency of X-rays sources increases sharply inside $\approx$ 1 arcmin. The possible nature of surplus sources is discussed in section 4.3. The details of dynamical formation of binaries in dense stellar environments and dependence on the stellar velocity dispersion are considered in the section 4.4. The results of this section are applied to the inner bulge of M31 and to the Galactic globular clusters in sections 4.5. Our conclusions are presented in the section 4.6.

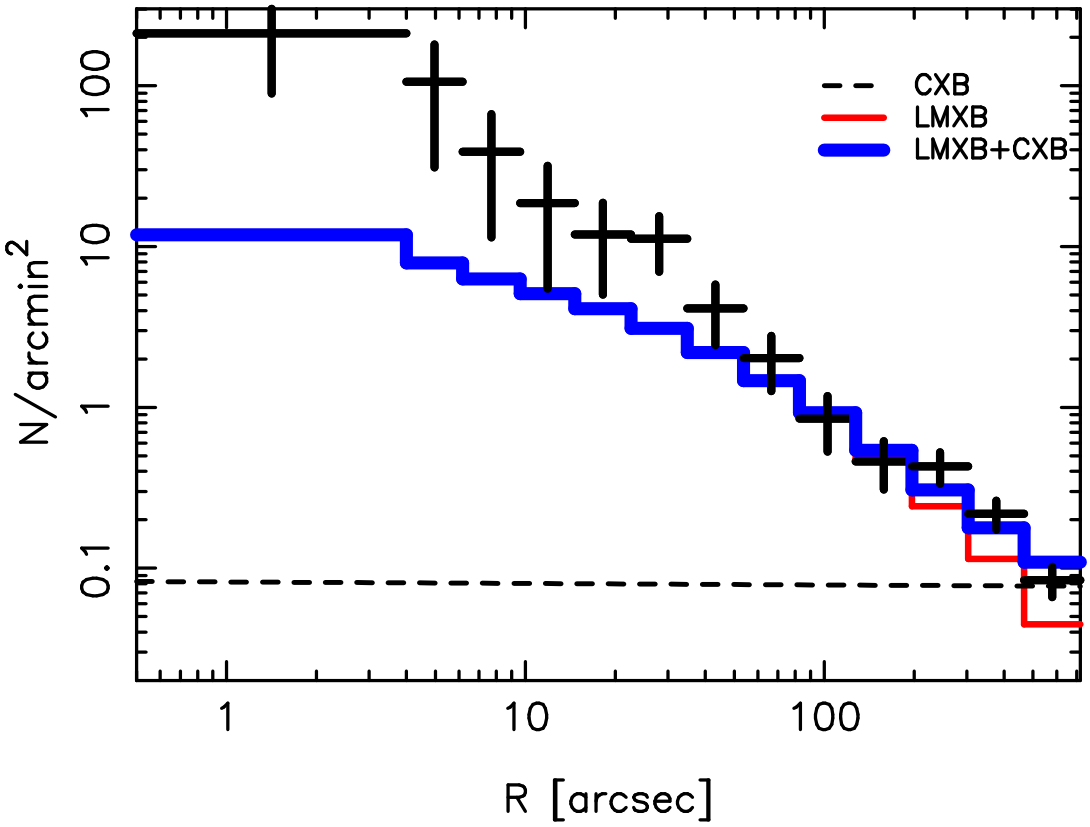

Figure 4.1: The radial distribution of the X-ray point sources in M31, excluding globular cluster sources. The histograms show the total distribution and individual components of the model: flat distribution of CXB sources and primordial LMXB sub-population tracing the stellar mass distribution. The normalizations of the individual components are from the best fit to the data outside 1 arcmin.

4.2 Radial distribution of the X-ray point sources

With the currently available *Chandra* data it is possible to study the spatial distribution of the X-ray point sources in the bulge, without being affected by incompleteness, down to the limiting lumionosity of 10^{36} erg s^{-1}. We restrict our analysis out to a distance of 12 arcmin from the centre and combine 26 ACIS observations with telescope pointings within the central 10 arcmin region of the M31 bulge for a total exposure time of 201 ks. Details of the data analysis, the source lists and the luminosity functions of various sub-populations in the bulge are presented in Voss & Gilfanov (2007).

We model the radial distribution of the X-ray sources by a superposition of primordial LMXBs and CXB sources, as in Voss & Gilfanov (2006). The spatial distribution of the former is assumed to follow the stellar mass distribution of the galaxy, as traced by the K-band light (Gilfanov, 2004). We used the K-band image of M31 provided by 2MASS LGA (Jarret et al., 2003). The distribution of CXB sources is assumed to be flat on the angular scales of interest. Before proceeding with the fit we removed the contribution the from sources other than primordial LMXBs and background galaxies.

Firstly, we removed 4 identified foreground sources, 1 supernova remnant and one extended source. Secondly, we excluded X-ray binaries associated with globular clusters, as their origin and spatial distribution are different from the "field" LMXBs.

Among our X-ray sources 13 are coincident with confirmed GCs from Galleti et al. (2004) and 8 with GC candidates. We estimated the number of random matches by displacing the sources by 10 arcsec in 4 directions. We found an average of 0.25 coincidences with confirmed GCs and 1.0 with GC candidates. It is well known that the inner parts of M31 are depleted of GCs, suggesting that the GC list might be affected by incompleteness. Barmby & Huchra (2001) estimate that 70 per cent of the GCs in the central parts of M31 have been detected, leaving the room for only a relatively small number of undetected GCs. As only a small fraction, $\sim 1/5$, of the GCs contain LMXBs it is reasonable to neglect the possible contribution of missing GCs. A large fraction of the GC candidates are not real globular clusters. However, an association with an X-ray source raises the probability of the GC candidates actually being GCs considerably. We therefore remove these sources from our source list too, noting that all conclusions of this paper remain unchanged if the analysis is performed with a source list in which these sources are included.

We fit the relative normalizations of the LMXBs and CXBs, using the maximum likelihood (ML) test. The best fit is given by a model, in which the normalization of CXBs is zero, meaning that all the sources are LMXBs. As an alternative, we performed a χ^2-fit on the binned data, with > 15 sources in each bin, and obtained the same result. The probability that the data can be a realization of the model is 0.06 using the Kolmogorov-Smirnov (KS) test, and $6 \cdot 10^{-4}$ for the χ^2 test. The KS test is less sensitive to deviations at the end of a distribution, and therefore the result of the χ^2-test is more restrictive. We conclude that the LMXB+CXB model is rejected.

The visual examination of the data (Fig. 4.1) suggests that the reason for the rejection of the model is an overdensity of sources in the inner 1 arcmin region of M31. Motivated by this we did a χ^2 fit of the same model to the distribution outside 1 arcmin. The best fit value of the normalization of the CXB component gives the total number of 26±9 sources CXB sources in the entire $r < 12$ arcmin. This value is consistent with the expectation of 29 background galaxies, estimated from the soft band of Moretti et al. (2003), using the method described in Voss & Gilfanov (2006). We therefore fix the normalization of the CXB component at the value corresponding to 29 sources. This gives a total number of the LMXBs of 64±7 in the entire $r < 12$ arcmin image. The χ^2-value is 2.63 for 3 degrees of freedom. The best fit model is shown in Fig. 4.1 together with the observed distribution.

Using the best-fit model it is possible to investigate the distribution of sources in the inner 1 arcmin and quantify the excess in the surface density of the sources. The total number of sources detected in the the $r < 60$ arcsec region is 29. The extrapolation of the best fit model into this region predicts 8.4±0.9 sources, and therefore the number of surplus sources is 20.6±5.5. The error in the latter estimate accounts for the Poissonian uncertainty in the total number of sources inside 60 arcsec and for the uncertainty of the best fit model normalization. As it is obvious from Fig.4.1, the contrast between the observed number of sources and that predicted from the K-band light distribution increases towards the centre of the galaxy. Inside $r < 15$ arcsec, for example, 9 sources

are detected with only 1.1 sources predicted. The formal probability of such an excess to happen due to statistical fluctuation is $\sim 3 \cdot 10^{-6}$, assuming Poissonian distribution.

4.3 Origin of the surplus binaries

Non-uniform extinction, peaking at the centre of M31, could cause the distribution of the K-band light to deviate from the distribution of stellar mass. This possibility can be excluded, however, as the extinction towards the centre of M31 is low, A_V=0.24 mag and A_I=0.14 mag (Han, 1996), which extrapolated to the K-band gives A_K=0.03 (Binney & Merrifield, 1998). Moreover, a non-uniform extinction distribution would also cause non-uniformity in the apparent colours of the stellar population, which is not observed (Walterbos & Kennicutt, 1987).

The surplus sources can be high-mass X-ray binaries associated with star formation in the inner bulge of M31. We derive upper limits for the star formation rate and the number of HMXBs from the Hα and FIR luminosities reported by Devereux et al. (1994). The combined Hα luminosity of the nuclear region and from diffuse emission inside the star forming ring (which lies at a radius ∼50 arcmin, i.e. much larger than the region analysed in this paper) is $4.3 \cdot 10^{39}$ erg s^{-1} (transformed to the distance of 780 kpc used in this paper). From Grimm et al. (2003) we find that this corresponds to 3.2 HMXBs with a luminosity above 10^{36} erg s^{-1}. The FIR luminosity in this region is $5.25 \cdot 10^8$ L$_\odot$, which corresponds to 5.9 HMXBs with a luminosity above 10^{36} erg s^{-1}.

It should be stressed out, that the region these luminosities refer to is almost 20 times larger than the region analysed in this paper. Moreover it is very likely that the main part of the Hα and FIR emission is not associated with star formation, as the number of O-type stars is a factor of $\sim$ 200 lower than what would be expected otherwise (Devereux et al., 1994). To conclude, the HMXB nature of the sources in the inner bulge can be excluded.

The surplus sources could have been created in globular clusters that remain undetected. In the catalogue of Galleti et al. (2004) there are 64 confirmed GCs hosting 13 LMXBs in the region we analysed. The fraction of GCs containing X-ray sources is therefore 0.2. This number is larger than what is found in other galaxies (Sarazin et al., 2003; Maccarone et al., 2003), but consistent with the results for the inner parts of galaxies in Kim et al. (2006). Attributing the $\approx$ 20 surplus sources to undetected GCs would therefore indicate that $\sim$ 100 unobserved GCs exist in the inner 1 arcmin region of M31. This is much larger than allowed by the completeness level of the present studies of GC population in M31, consistent with only a few undetected globular clusters in this region (Barmby & Huchra, 2001).

In a related scenario, the surplus sources could have been created in globular clusters at larger distances from the centre of M31. Due to the mass segregation the globular clusters drift towards the centre of the bulge, where they are destroyed, leaving behind remnant LMXBs. This scenario has been motivated by Fig.4.2 where the radial distribution of surplus sources is compared with that of the globular clusters. Indeed, for a GC of mass $10^5 M_\odot$ the mass segregation timescale is $\sim 10^9$ yr at a radius of 5 arcmin and $\sim 10^{10}$ yr at a radius of 12 arcmin (Spitzer, 1969). Assuming that a neutron star turns accreted matter into radiation with an efficiency of $\sim$ 0.2, the lifetime of

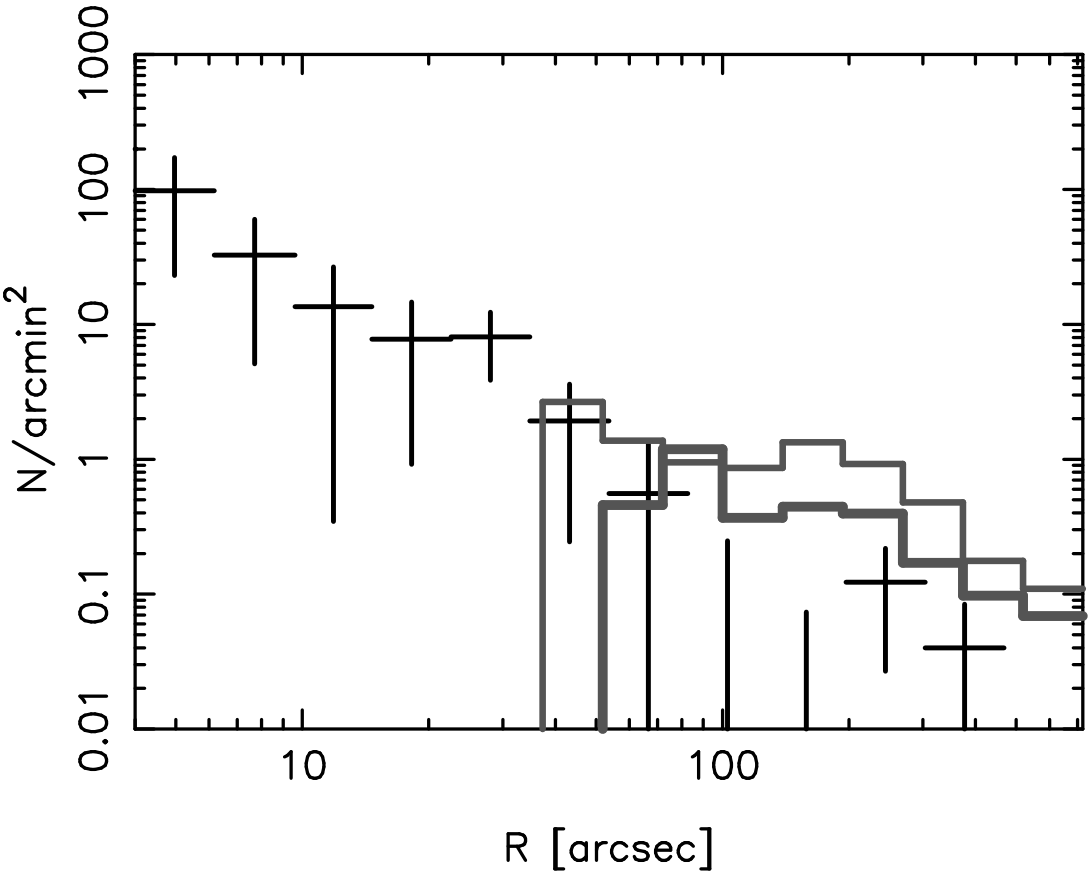

Figure 4.2: The radial distribution of the "surplus" X-ray sources, computed as a difference between the data and best fit model shown in figure 4.1. The histograms show distributions of the confirmed globular clusters (thick grey line) and globular cluster candidates (thin grey line).

an LMXB is $\lesssim 10^9 m_d/L_{37}$ yr, where m_d is the mass of the donor star at the onset of mass transfer expressed in solar masses, and L_{37} is the average luminosity of an LMXB in units of 10^{37} erg s^{-1}. Taking into account that on average $\sim 1/5$ of GCs in M31 contain LMXBs, a destruction rate of ~ 100 globular clusters per Gyr is required to explain ≈ 20 sources observed near the centre of M31. This number is comparable to the total number of GCs within the entire region analysed in this study, and is $\sim$ 30 per cent of the total number of GCs in M31. As GCs are not continually formed in large numbers in M31, the globular cluster system of this galaxy will not be able to sustain such a destruction rate and, consequently, the population of X-ray sources observed in the inner bulge, for any significant length of time.

Finally, the stellar density in the central part of the M31 bulge, $\sim 10^4$ M$_\odot$/pc^3, is high enough that LMXBs can be formed through dynamical interactions in the same manner as in globular clusters. In the following sections we investigate this possibility, and apply it to the population of X-ray sources in the inner bulge of M31 and in globular clusters in the Milky Way.

4.4 Dynamical interactions in dense stellar environments

We begin with consideration of two-body encounters involving a neutron star. The results of this section are extended to formation of black hole binaries in the section 4.4.4. There are three main channels of dynamical LMXB formation operating in dense stellar environments:

1. In a tidal capture of a neutron star (NS) by a non-degenerate single star, a close passage of the two stars induces oscillations in the non-degenerate star, and the energy for this is taken from the orbital energy. If the energy of the oscillations exceeds the originally positive orbital energy, the stars are captured in a bound orbit (Fabian et al., 1975).

2. A collision between an NS and an evolved single star on the subgiant or red giant branch (RGB) or the asymptotic giant branch (AGB) can lead to the formation of an X-ray binary, in which the donor star is a white/brown dwarf or a helium star, depending on the evolutionary stage of the evolved star before the collision (Ivanova et al., 2005b). In the case of a white dwarf donor an ultra compact X-ray binary is formed. In this scenario, orbital energy is transferred to the envelope of the evolved star, which is expelled, leaving the NS and the core of the evolved star in a bound orbit (Verbunt, 1987).

3. In an exchange reaction, an NS exchanges place with a star in a pre-existing binary during a close binary-single encounter (Hills, 1976).

In the following we compute cross-sections and rates of these three processes, consider their dependence on the velocity dispersion of the stars and discuss various factor affecting their efficiency in the high velocity regime.

Each of the processes depends on the rate of encounters between two types of objects, which in a unit volume is given by $n_1 n_2 \gamma$, where

$$\gamma = \int_0^\infty F(v_{rel}, \sigma_v)\sigma(v_{rel}, M_1, M_2)v_{rel}dv_{rel} \tag{4.1}$$

where n_1 and n_2 are the number densities and M_1 and M_2 are the masses of object type 1 and 2, respectively, $\sigma(v_{rel})$ is the cross-section of the encounter, and $F(v_{rel})$ is the distribution of relative velocities at infinity. Assuming that the velocity distributions of the two kinds of objects are both Maxwellian and have the same three-dimensional velocity dispersion σ_v, the distribution of relative velocities is given by

$$F(v_{rel})dv_{rel} = \left(\frac{4\pi}{3}\right)^{-3/2} \sigma_v^{-3} exp\left(-\frac{3v_{rel}^2}{4\sigma_v^2}\right) 4\pi v_{rel}^2 dv_{rel} \tag{4.2}$$

Due to the effect of gravitational focusing, the cross-section for two objects to pass within a distance D of each other is given by

$$\sigma(v_{rel}) = \pi D^2 \left(1 + \frac{2G(M_1 + M_2)}{Dv_{rel}^2}\right) \tag{4.3}$$

In most cases, the gravitational focusing (the second term in the brackets) dominates. Only for very fast encounters (large D and/or v_{rel}) is $Dv_{rel}^2 > 2G(M_1 + M_2)$. If D is independent on the relative velocity, $\gamma \propto \rho^2/v_{rel}$ for slow encounters, and $\gamma \propto \rho^2 v_{rel}$ for the fast ones.

Several remarks are in place, concerning the subsequent evolution of the newly created binary system with a compact object.

Capture of a neutron star in a bound orbit with a companion will lead to formation of an X-ray binary provided that the companion star will fill its Roche lobe and mass transfer will commense within a reasonable time, shorter than $\sim 5 - 10$ Gyr. If the initial binary separation is too large for this to occur immediately after the capture, it can be decreased in the course of evolution of the binary. There are 3 main mechanisms, which affect the orbital separation: (i) magnetic braking, (ii) gravitational braking and (iii) binary-single interactions. The former two are familiar from the standard theory of the binary evolution (see van den Heuvel, 1992, for a review). For the companion mass in the $0.4 - 1.0 M_\odot$ range they will bring the system in to the Roche lobe contact within 5 Gyr if the initial orbital separation does not exceed $\sim 3.0 - 7.0 R_\odot$ and $\sim 2.5 - 3.0 R_\odot$ respectively. The braking mechanism due to interaction of the binary with single "field" stars is specific for high stellar density environments. Its properties are briefly summarized below.

When considering evolution of a binary due to binary-single interactions it is conventional to divide the binaries into soft and hard, depending on the ratio of their binding energy to the kinetic energy of the single star at infinity (Heggie, 1975). Soft binaries have relatively wide orbits, and interactions with single stars tend to widen the orbit further or to ionize the binary. Hard binaries, on the contrary, are on average hardened by encounters with single stars (Hut & Bahcall, 1983). The effect of this is that over time most binaries with a separation above a critical value are disrupted, while the compact ones become more compact. The boundary between soft and hard binaries depends on the stellar velocity dispersion and the mass ratios and ranges from $a \sim 300 - 1000 R_\odot$ in a typical globular cluster to $a \sim$ few $R_\odot$ in the high velocity environment of the M31 bulge. Due to a linear dependence of the crossection on the binary separation the collisional braking is mostly important at wide binaries, where magnetic braking and gravitational radiation, decreasing as inverse power of the binary separation, are inefficient.

The initial orbital separation in the binaries produced through tidal captures and collisions with RGB/AGB stars is small and a large fraction of this systems will start mass transfer (i.e. become X-ray sources) soon after their formation. Only a small fraction of them ($\lesssim$20 per cent in GCs and $\lesssim$ 2 per cent in M31) will experience close encounters with single stars significantly affecting thery semimajor axis, therefore binary-single interactions are not an important factor in their evolution. Binaries created through exchanges, on the contrary, typically have wider orbits, and the effects of encounters can be important.

If the initial binary separation is large and the braking mechanisms are insufficient to start Roche-lobe overflow, this can occur when the donor star evolves off the main sequence, as a result of its expansion during the giant phase. In these systems the accretion disc is large and X-ray emission from vicinity of the NS is insufficient for the

irradiation to keep the entire disc ionized, and they are therefore transient (King et al., 1997). Furthermore, mass transfer can only occur while the donor is on the RGB, which makes the lifetime of such systems short. While they may account for bright sources detected in massive elliptical galaxies (Piro & Bildsten, 2002), they are too rare to make a significant contribution to our sample. The NSs in these systems are spun up to become millisecond pulsars, and in the Galactic GCs a large number of these have been observed (Lorimer, 2005). After the outer layers of the giant star have been ejected, a binary consisting of a white dwarf and an NS remains. However for the vast majority of the systems the binary separation is too large for mass transfer to begin, and they will therefore not become observable in X-rays.

4.4.1 Single-single encounters

The formation rates of LMXBs due to tidal captures and stellar collisions can be found by integrating the encounter rate, given by equation 4.1, over the relevant parts of the mass function of stars $f(M)$. We assume that the latter follows the form of Kroupa (2001), a broken powerlaw with slope 1.3 from 0.1-0.5$M_\odot$ and slope 2.3 above 0.5 $M_\odot$, and is normalized according to

$$\int_{M_{co}}^{M_{max}} f(M)dM = 1.0 \tag{4.4}$$

where M_{max} is the maximum initial mass of stars that have not yet evolved to become stellar remnants at present, and M_{co} is the lower cut-off mass. The number density of stars is then given by $n_* = \frac{\rho_*}{<M>}$, where ρ_* is the stellar mass density. We assume the mass of all neutron stars to be $1.4M_\odot$, and that they are formed from stars with initial mass in the range $8.0 - 30.0M_\odot$. The number density of these can then be expressed as $n_{ns} = f_{ns}\frac{\rho_*}{<M>} = f_{ns}n_*$, where $f_{ns} = \int_{8M_\odot}^{30M_\odot} f(M)dM$ (for $M_{co} = 0.1M_\odot$ and $M_{max} = 1.0M_\odot$ $f_{ns} = 0.0068$). We define the rate integrated with the mass function

$$\Gamma = \int \gamma f(M)dM \tag{4.5}$$

where integration is performed in the relevant initial mass range (see below) and γ is from equation 4.1. With this definition $n_* n_{ns}\Gamma$ gives the rate of encounters in s^{-1} cm^{-3}. For the calculation of Γ it is necessary to know the current radius of a star $R(M)$ as a function of its initial mass, as well as its evolutionary stage, which is used to define the mass limits of the integral. These informations we take from stellar isochrones of Girardi et al. (2002).

4.4.1.1 Collisions

We define an encounter between two stars as a collision if the stars come so close that considerable amounts of material is exchanged between them, and hydrodynamical effects become important. For the collisions with NSs, that are relevant for dynamical formation of LMXBs, we distinguish between collisions with main sequence (MS) or horizontal branch (HB) stars and with evolved stars on the RGB or AGB. Due to

the different structure of the stars, the outcome of a collision with a NS is different. Simulations indicate that collisions between an NS and an MS star tend to destroy the MS star (Davies et al., 1992). We expect the same to happen to stars on the HB, as their structure is similar to that of MS stars (Dorman, 1992). Collisions of this type are not interesting from the point of view of formation of X-ray binaries. As the envelope of stars on the RGB or AGB is less strongly bound to the core, a collision with an NS can lead to the envelope being expelled. The outcome is a short period binary consisting of the core of the evolved star and the NS. If the evolved star had a degenerate core, an ultra-compact X-ray binary (UCXB) with a white dwarf donor will be formed (Verbunt, 1987; Ivanova et al., 2005b; Lombardi et al., 2006). In either case an X-ray binary can be created.

The maximum value of distance at periastron R_{coll}, for which significant amounts of material can be exchanged in an encounter of an NS with a non-degenerate star (with radius R_*) is between R_* and the orbital separation at which the star fills its Roche-lobe (Eggleton, 1983):

$$a_{fill} = \frac{R_*}{0.49}\left[0.6 + q^{-2/3}\ln\left(1 + q^{1/3}\right)\right] \tag{4.6}$$

where $q = M_*/M_{NS}$. For encounters with NSs, this separation ranges from $\sim 5.4R_*$ to $\sim 2.8R_*$ for stars with masses in the $0.1 - 1.0M_\odot$ range. SPH Simulations of stellar encounters have shown that for $M_* \simeq 1M_\odot$, the value of $R_{coll}/R_* \sim 1.8$ (Davies et al., 1992), which we adopt as the standard value. The value of R_{coll}/R_* given, the encounter rate can be calculated from equations 4.1-4.3 and 4.5 (but see below regarding the choice of integration limits in equation 4.1).

When considering collisions between NSs and evolved stars, it is important to note that the envelope of a star on the RGB/AGB is loosely bound to the core, and the orbital energy of the two stars at infinity can be comparable to the binding energy of the envelope. It is therefore possible that the envelope is expelled without carrying off enough energy to leave a bound system, or that in the high-velocity encounters, the duration of the interaction is too short for enough energy to be transferred from the NS to the envelope. While simulations indicate that the RG envelope is promptly disrupted, instead of ejected through a common envelope (CE) evolution (Rasio & Shapiro, 1991; Lombardi et al., 2006), the energy considerations are similar. Adopting the formalism of Webbink (1984) and de Kool (1990), we assume that the envelope of the RG is ejected, and that energy for this (the binding energy of the envelope E_{bind}) is taken from the orbital energy of the two stars which is therefore changed by ΔE_{orb}. Allowing energy to be lost, e.g. as radiation or as some of the envelope is ejected with a velocity higher than the escape speed, an efficiency parameter α_{ce} is defined, so that $E_{bind} = \alpha_{ce}\Delta E_{orb}$. The binding energy of the RG is given by $E_{bind} = -\frac{1.0}{\lambda}\frac{GM_{env}M}{R}$, where M and R is the mass and radius of the RG, respectively, and M_{env} is the mass of the envelope of the RG. λ is a factor that relates the simplified equation to a precise integral of the gravitational binding energy and internal energy in the envelope of the RG, see e.g. Dewi & Tauris (2000). The change in orbital energy needed to reach an orbit with a separation a_f is given by $\Delta E_{orb} = \frac{1}{2}\frac{MM_{ns}}{M+M_{ns}}v_{rel}^2 + \frac{GM_{core}M_{ns}}{2a_f}$, where M_{core} is the core mass of the RG, M_{ns} is the mass of the NS and v_{rel} is the relative velocity

of the two stars at infinity.

For a given encounter velocity, we can now find the final separation of the binary by solving

$$\frac{GM_{env}M}{R} = \alpha_{ce}\lambda\left(\frac{1}{2}\frac{MM_{ns}}{M+M_{ns}}v_{rel}^2 + \frac{GM_{core}M_{ns}}{2a_f}\right) \tag{4.7}$$

When we calculate the rate of collisions with evolved stars, γ_{coll}, the integral over velocities (equation 4.1) is only carried out for velocities $V_{rel} < V_{max,c}$, defined such that the final separation $a_f < 5R_\odot$ (this choice of the maximum separation ensures that the gravitational braking will be efficient on the formed binary)

$$\gamma_{coll} = \int_0^{v_{max,c}} F(v_{rel},\sigma_v)\sigma_{coll}v_{rel}dv_{rel} \tag{4.8}$$

where σ_{coll} is the collisional cross-section defined by equation 4.3 with $D = R_{coll}$. In figure 4.3 we compare the formation rates of UCXBs due to collisions between RGB+AGB stars and NSs for different values of $\alpha_{ce}\lambda$. The rates were calculated by integrating over all evolutionary stages of stars on the RGB/AGB, using the isochrones of (Girardi et al., 2002). The details of the calculations are given below in section 4.4.3. It is obvious that the choice of $\alpha_{ce}\lambda$ is very important in the bulge of M31, with an order of magnitude difference between the rates of the highest and the lowest value, while the difference is relatively small in GCs.

SPH simulations indicate that the effectivity in standard CE evolution is $\alpha_{ce} \lesssim 0.5$ (see Taam & Ricker, 2006, and references therein), and in population synthesis studies, values of $\lambda\alpha_{ce}$ in the range 0.1-1.0 are most often assumed (Portegies Zwart & Yungelson, 1997; Fryer & Woosley, 1999; Hurley et al., 2002; Voss & Tauris, 2003; Belczynski et al., 2005), and this seems to give a good fit to the observed properties of the post-CE binary population.

However there are differences between the standard CE evolution and the collisions considered here. In the former, the stars are already in a bound orbit, and the energy can therefore be transferred to the envelope over a longer period of time during a large number of orbital revolutions. On the other hand, in a collision, enough energy has to be transferred from the NS to the envelope during the first periastron passage, so that the two stars remain bound. Especially for high velocity encounters, the CE formalism might not be directly applicable, as the timescale for the first passage can be so short that the NS passes through the envelope without transferring much energy to this. While the low-velocity regime has been well investigated using SPH simulations (Davies et al., 1992; Lombardi et al., 2006), showing that a value of $R_{coll}/R_* = 1.8$ is adequate, no investigation of the high-velocity regime has been performed. We assume that $\alpha_{ce}\lambda$ is in the range 0.1–1.0 (1.0 can be considered a very conservative estimate, giving the minimum rate of LMXB formation through this process, whereas 0.1 may be a rather optimistic value), with 0.5 being our chosen standard value for calculations below.

4.4.1.2 Tidal captures

At periastron distances above R_{coll}, and up to a few times R_*, tidal capture can happen. Press & Teukolsky (1977) provided a way of calculating the energy absorbed

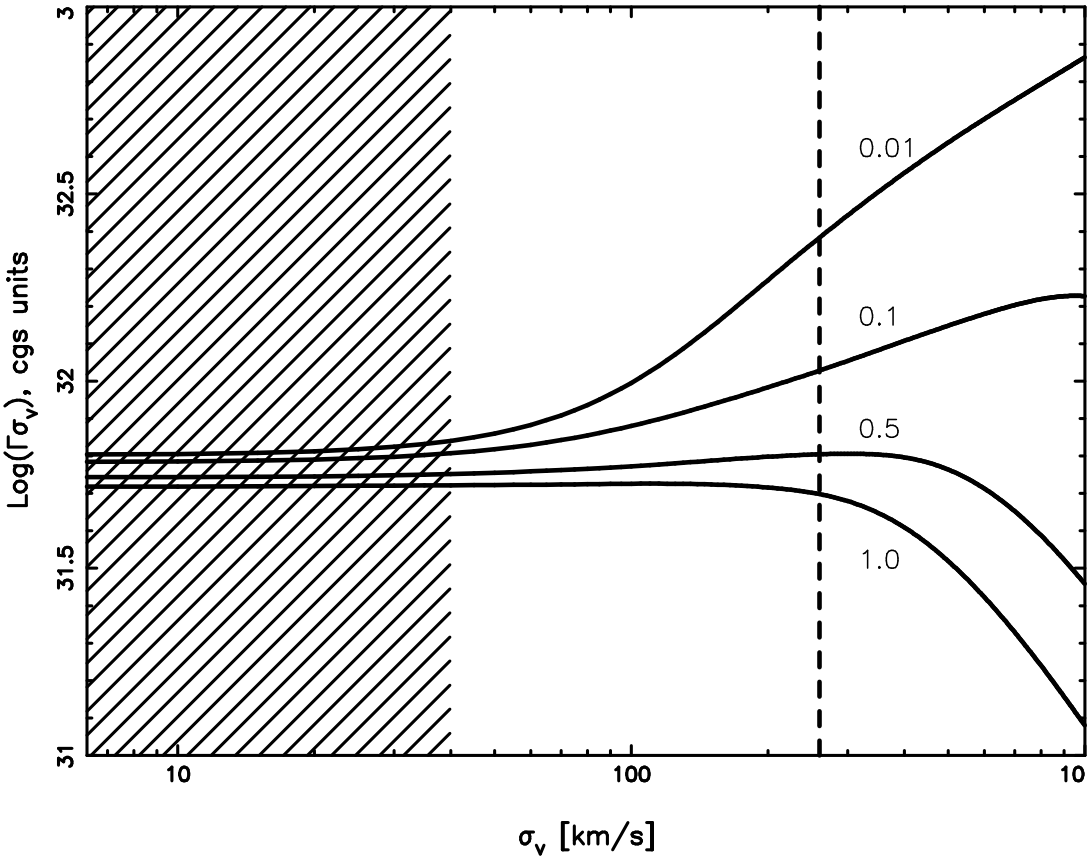

Figure 4.3: The rate γ of NS-RGB/AGB encounters that lead to the formation of a binary as a function of the 3D velocity dispersion for 4 values of $\alpha_{ce}\lambda$ (equation 4.7). The values are 0.01,0.1,0.5,1.0 from the top to the bottom. The shaded area corresponds to the range of velocity dispersions in the central parts of GCs, wheras the vertical dashed line corresponds to the velocity dispersion in the bulge of M31.

by the stars assuming $n = 3/2$ polytropes and Lee & Ostriker (1986) extended these calculations to other polytropic indices. In this formulation, the energy of oscillations induced in the non-degenerate star of mass M_* during an encounter with a neutron star is

$$\Delta E_1 = \left(\frac{GM_*}{R_*}\right)^2 \left(\frac{M_{ns}}{M_*}\right)^2 \sum_{l=2,3} \left(\frac{R_*}{R_p}\right)^{2l+2} T_l(\eta) \tag{4.9}$$

where R_p is the distance of closest approach. Only the spherical harmonic indices $l = 2$ (quadrupole) and $l = 3$ (octupole) are included, as higher indices give negligible contributions to the energy (Lee & Ostriker, 1986). The parameter η is defined as

$$\eta = \left(\frac{M_*}{M_* + M_{ns}}\right)^{1/2} \left(\frac{R_p}{R_*}\right)^{3/2} \tag{4.10}$$

With the tabulated overlap integrals of Lee & Ostriker (1986), for polytropic indices $n = 3/2$ and $n = 3$, we use the numerical method described by Press & Teukolsky (1977) to calculate $T_l(\eta)$. From equation (4.9) it is then possible to calculate the maximum value of R_p (we call this R_{tid}) for which capture will occur, when the mass of the star and the relative velocity at infinity is known. We use this method for the case where the non-degenerate star is on the MS. A polytropic index of $n = 3/2$ is assumed for the fully convective stars of mass, $M_* < 0.4\ M_\odot$, and $n = 3$ for stars $M_* > 0.4\ M_\odot$ having radiative core. For stars on the red giant branch, we use the results of McMillan et al. (1990), who calculated R_{tid} for captures of a neutron star by a $0.8\ M_\odot$ star at various evolutionary stages along the RGB. This mass is close to the MS turn-off masses for the Galactic globular clusters (GCs), whereas the turn-off mass in M31 is higher, $\sim 1\ M_\odot$. We use their results directly in both cases. As tidal captures by evolved stars give a negligible contribution to the overall binary formation rates we did not attempt to perform a more accurate computation for the case of M31. We neglect tidal captures during the subsequent evolutionary stages. The structure of stars on the AGB is similar to those on the RGB, but the time spent there is much shorter. The tidal capture rate must therefore be lower. The time spent on the HB is also very short, compared to the MS lifetime, and although the tidal capture rate may be comparable to the RGB rate, it is much smaller than the MS capture rates.

The tidal capture rate γ_{tidal} is computed as a rate of encounter with the periastron distance $R_{coll} < R_p < R_{tid}$, i.e. contribution of very close encounters resulting in collisions is subtracted:

$$\gamma_{tidal} = \int_0^{v_{max,t}} F(v_{rel}, \sigma_v)[\sigma_{tidal} - \sigma_{coll}] v_{rel} dv_{rel} \tag{4.11}$$

The upper integration limit $v_{max,t}$ is defined as the velocity at which $R_{coll} = R_{tid}$ i.e. the term in square brackets is required to be positive inside the integration limits. The σ_{tidal} is calculated from equation 4.3 with $D = R_{tid}$.

Important for the following evolution of tidal capture binaries is the timescale on which the tidally induced oscillations are dissipated. If this timescale is short (as argued by Kumar & Goodman, 1996), so that a large fraction of the energy is thermalized within one orbital revolution of the binary, new oscillations will be induced at each periastron passage. The binary quickly becomes circularized with the final orbital separation (from conservation of angular momentum):

$$a = \frac{(\sqrt{2G(M_* + M_{ns})R_p} + v_{rel}R_p)^2}{G(M_* + M_{ns})} \tag{4.12}$$

For slow encounters (low v_{rel} or small R_p), $a \simeq 2R_p$. If the dissipation time scale is too short, the quick conversion of the energy (of the order of few per cent of the binding energy of the star) may cause the star to expand and lead to a merger. The outcome of the dissipation process depends on the thermalization timescale and the region of the star where the energy is deposited, both factors being unkown (Podsiadlowski, 1996). Alternatively, if the dissipation is inefficient, coupling of the orbital motion with oscillation can cause large fluctuations in the orbital energy, substantially extending the circularization process and potentially scattering a fraction of the binaries to wider

orbits (Kochanek, 1992; Mardling, 1995). The details and the final outcome of this processes are poorly understood. In the following we assume that all binaries become circularized with the final separation given by equation 4.12.

Equation 4.11 defines the total tidal capture rate, irrespective of the subsequent evolution of the tidally formed binary. In order to calculate the rate of encounters, leading to formation of an LMXB, one needs to account for the finite braking time scales. For this, R_{tid}, used to calculate σ_{tidal} in equation 4.11, is replaced by $\min(R_{tid}, R_{brake})$, where R_{brake} depends on the mass of the star and is chosen so that the braking time scale for the tidal capture binary is shorter than 5 Gyr. Due to small values of the tidal capture radius R_{tid}, this does not affect the final rates significantly.

4.4.2 Binary-single interactions

The rate of exchange reactions between a binary (M_1, M_2, a) and a star M_3 is:

$$\gamma_{exch}(M_3, \sigma_v) = \int f(M_1) dM_1 \int p(q) dq \times \int_{a_{min}}^{a_{max}} \gamma(M_1, M_2, M_3, a, \sigma_v) \frac{dn}{da} da \tag{4.13}$$

where $f(M)$ is the distribution of mass of one of the stars in the binary, q is the binary mass ratio and $p(q)$ its probablity distribution, dn/da is the binary semimajor axis distribution and $\gamma(M_1, M_2, M_3, a, \sigma_{rel})$ is the exchange rate of a star M_3 into a binary (M_1, M_2, a) computed from the equation 4.1. In the context of LMXB formation the third star M_3 is an NS or a black hole.

4.4.2.1 Monte-Carlo simulations

Theoretically, one could use one of the semi-analytical approximations to the exchange crossection available in the literature (e.g. Heggie & Hut, 1993) and compute the rates from equations 4.1 and 4.13. However, the semimajor axis distribution is a function with a complex time evolution, depending on a number of processes and parameters. Another factor, which is even more difficult to account for in an analytical calculation is the effect of mergers during the binary-single interactions. Furthermore, unlike in collisions with red giants and in tidal captures, the binary separation of the exchange binary is large and one would have to take into consideration the subsequent evolution of the binary parameters, before the Roche lobe contact is achieved.

				without collisions					with collisions				
CO	σ_v (1D)	n_*	f_{ns}	N_{bin}	Total	MS-NS	RG-NS	γ_{ex}	N_{bin}	Total	MS-NS	RG-NS	γ_{ex}
NS	3	$5 \cdot 10^4$	0.0025	1120790	3157	318	816	$1.41{\cdot}10^{32}$	2739700	3093	77	277	$1.39{\cdot}10^{31}$
NS	15	$3 \cdot 10^5$	0.0025	467000	1256	163	277	$2.89{\cdot}10^{31}$	1027400	1328	27	108	$2.17{\cdot}10^{30}$
NS	150	10^4	0.0068	$1.68 \cdot 10^{8\dagger}$	1625	66	165	$1.02{\cdot}10^{29\dagger}$	$8.87 \cdot 10^{7\dagger}$	604	3	46	$8.76{\cdot}10^{27\dagger}$
BH	150	10^4	0.0012	$8.10 \cdot 10^{7\dagger}$	10938	82	739	$1.49{\cdot}10^{30\ \dagger}$	$8.10 \cdot 10^{7\dagger}$	9557	13	559	$2.37{\cdot}10^{29\dagger}$

† This simulation was performed for a limited range of orbital separations and γ_{ex} have been corrected for this.

Table 4.1: Parameters and results for the three simulations of exchange reactions. The parameters are: the velocity dispersion σ_v in km s^{-1}, the number density of single stars n_* in pc^{-3}, the NS fraction in the population of single stars f_{ns} and the number of binaries simulated N_{bin}. The results are: the total number of NS binnaries formed through exchanges of a neutron star in to a binary (Total) and the numbers of LMXBs formed in the simulations – with MS (MS-NS) and RG (RG-NS) donors. The formation rate γ_{ex} calculated from equation 4.15 (cgs units), is given for LMXBs with MS donors. The other rates can be computed by scaling with the numbers of formed systems. The two groups of columns present results with and without account for stellar collisions.

For these reasons we chose to use Monte-Carlo simulations in order to estimate the rate of LMXB formation due to exchange reactions. In these simulations we follow the evolution of binaries in an environment of single stars, with special emphasis on interactions between the single stars and the binaries. The outcome gives a reasonable indication of the importance of this process, compared to the two paths of dynamical formation of LMXBs from single-single encounters discussed above. The simulations are based on the FEWBODY code of Fregeau et al. (2004). FEWBODY numerically integrates the orbits of the stars during the interaction, and automatically classifies and terminates calculations as soon as the outcome is unambiguous, which makes it well suited for carrying out large sets of binary interactions.

All binaries and single stars are assumed to be formed at the same time, and the simulation of the binaries begins 0.5 Gyr after the star formation episode. The masses of single stars are assumed to follow the initial mass function of Kroupa (2001). Only main sequence stars and neutron stars are included, and the main sequence turn-off mass evolves with the age of the population (as given by Girardi et al., 2002). The number density of single stars is kept constant during the simulation.

The initial binaries are drawn randomly from a population with properties typical of binary population synthesis studies. The mass distribution of the primary stars (M_p) was chosen to be the same as the mass function of single stars, while the mass of the secondary chosen from a flat mass ratio distribution. The distribution of orbital separations a was assumed flat in $\log a$ between a minimum separation corresponding to one of the stars filling its Roche-lobe, and a maximum separation of $10^4 R_\odot$. The initial eccentricity of the binaries was set to 0. Each binary is evolved for 15 Gyr in the single star environment, taking into account stellar evolution and evolution of the binary orbit due to magnetic braking and gravitational radiation. as well as encounters with single stars.

The binaries are evolved in timesteps of maximally 0.01 times the average time between encounters with single stars, where an encounter is assumed to happen if a star comes closer than 6 orbital separations. For each timestep binary parameters are adjusted according to gravitational wave emission (Landau & Lifshitz, 1962; Peters, 1964) and magnetic braking (Rappaport et al., 1983). We assumed the disrupted magnetic braking model, where magnetic braking is ineffective when the MS star is totally convective (Rappaport et al., 1983; Spruit & Ritter, 1983). This is the case when the mass of the star is below $\sim 0.4\ M_\odot$. The probability of an encounter between the binary and a single star within a timestep of length Δt is given by a weighted average over the distribution of relative velocities and over the mass function of single stars.

$$P_{enc} = \Delta t\ n_* \int_M \gamma f(M) dM \tag{4.14}$$

Here n_* is the number density of single stars, γ is given by equation 4.1, with the cross-section found from equation 4.3 with $D = 6a$, where a is the orbital separation of the binary. Random numbers are drawn to see whether an encounter occurs. If this is the case, the parameters of the encounter are drawn from their respective probability distributions. The mass of the single star is drawn from the mass function (allowing for neutron stars also). The probability of an encounter distance D is proportional to $\frac{d\sigma}{dD}$

(where σ is given by equation 4.3) out to the maximum distance of 6 orbital separations of the binary. The distribution of encounter velocities v_{rel} is given by equation 4.2. The encounter is then solved for using the `binsingle` program of FEWBODY. Binary phase and encounter angle is chosen randomly by FEWBODY from a flat and an isotropic distribution, respectively. The simulation of a binary is terminated when one of the following occurs: (1) the binary is disrupted, (2) one of the stars evolves off the main sequence or (3) Roche-lobe contact is reached. If one of the binary components is an NS, possibility 3 leads to the formation of an LMXB. Possibility 2 also leads to Roche-lobe overflow, but as discussed above, such RGB-NS systems are shortlived and transient X-ray sources.

The simulations are performed with several simplifying assumptions. We discuss the most important of them below. Encounters between binaries are ignored. As most wide binaries are quickly destroyed, the binary fraction decreases fast and binary-binary encounters should only matter at early times. Moreover, in most binary-binary encounters, two or more of the stars merge (Fregeau et al., 2004). Secondly we have neglected the effect of tidal interaction in the evolution of the binaries (Zahn, 1989a,b). This will tend to lock the rotation of the stars to the orbit and to circularize the orbit, thus decrease somewhat the time it takes for a system to achieve Roche-lobe contact. The significance of this effect is difficult to estimate, for its implementation in population synthesis codes see Belczynski et al. (2005). Evolved stars were not included in the simulations. For the single star population this should not be a problem, as an encounter between an evolved star and a binary will probably lead to a merger of some sort due to the large radius of the evolved star. The net effect of such encounters will most likely be a decreased binary fraction. As for the evolved stars in the binaries, they will lead to Roche-lobe overflow. It is unlikely that a neutron star can be exchanged into such a system without the occurrence of a physical collision. We verified with test simulations that close encounters between tight binaries and single stars in which one of the stars is evolved in almost all cases lead to merger of two or all three stars, in accordance with the conclusions of Fregeau et al. (2004).

4.4.2.2 Results of simulations

We performed three simulations with different velocity dispersions and densities, to cover the environment in both M31 and in GCs. Parameters and results of the simulations are summarized in table 4.1. Presented in the table are the numbers of neutron star binaries created in the simulations – the total number and the numbers of Roche-lobe filling systems. The latter is divided into the following two categories: the binaries in which Roche-lobe overflow occurs due to evolution of the binary orbit, while the companion star is on the MS (MS-NS) and the systems in which the mass transfer is initiated due to the evolution of the companion star off the main sequence (RG-NS).

We convert the numbers into γ_{ex} rates, which can be directly compared to the single-single interaction rates computed in the previous section, using

$$\gamma_{ex} = \frac{\Gamma}{n_{bin} n_{ns}} = \frac{N}{T_{sim} n_{ns} N_{bin}} \tag{4.15}$$

where n_{bin} and n_{NS} are the number densities of binaries and neutron stars, N_{bin} is

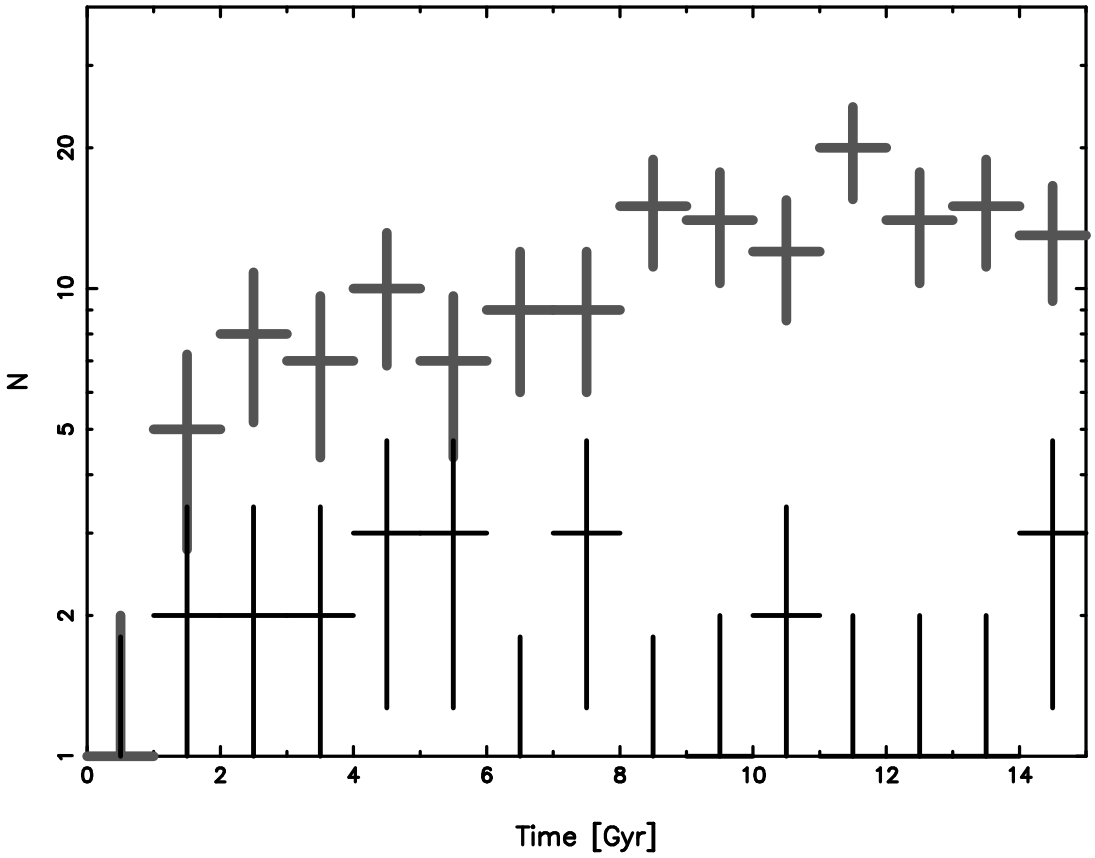

Figure 4.4: The evolution of the dynamical formation rate of LMXBs due to exchange reactions in a low velocity environment of a globular cluster ($\sigma_v = 15$ km s^{-1}). The plot shows the number of systems in which Roche-lobe contact was reached, per time bin, as a function of time from the start of the simulation. Results of simulations without and with account for mergers are shown with thick grey and thin black crosses respectively.

the total number of binaries in the simulation and T_{sim} is the simulations time span. Note, that with the above definition, N_{bin} is the total number of binaries simulated, i.e. n_{bin} has the meaning of the primordial volume density of binaries. The rates for MS-NS systems are given in the Table 4.1. The other rates can be computed from these by scaling according to numbers of binaries. The Monte-Carlo uncertainties can be estimated assuming a Poissonian distribution for the numbers of binaries. In the M31 simulations (the largest value of σ_v) we simulated binaries in a limited range of separations, as wide binaries are quickly ionized and do not contribute to the LMXB production rates. The final value of the exchange rates given in Table 4.1 has been corrected correspondingly.

In the initial simulations the radii of stars were set to zero, i.e. the possibility of stellar collisions was not accounted for. We performed a second set of simulations, in which two stars with radii R_1 and R_2 were assumed to collide if the distance of closest approach was $D < 1.8(R_1 + R_2)$. We assumed that collisions lead to a merger and removed from simulations all binaries that experience such events. With these

assumptions, the rates of LMXB formation decrease dramatically, by about an order of magnitude, i.e. in $\sim 90\%$ of binary-single interactions which could potentially lead to an exchange of the neutron star into the binary, two or more of the stars collide. This result is in agreement with Fregeau et al. (2004) and demonstrates that mergers are a determining factor in the formation of exchange LMXBs.

Figure 4.4 illustrates the time dependence of the formation rate of exchange LMXBs in a low velocity environment of a typical globular cluster (simulation with $\sigma_v = 15$ km s^{-1}). Shown in the figure is the number of binaries per time bin, in which the Roche-lobe overflow was initiated during the given time bin, irrespective of the time when the neutron star was exchanged into the binary. There is an obvious increase with time, due to the fact that in a low velocity dispersion environment most MS-NS binaries are created with relatively large orbital separations and need to be hardened by further collisions in order to become LMXBs. This is in contrast to M31 (large velocity dispersion), where the rate is constant, due to the fact that almost all exchange LMXBs there are formed from binaries with small orbital separations, $a \lesssim 10 R_\odot$. For such binaries, binary-single interactions are not an important factor in their further evolution towards Roche-lobe overflow. Also shown in the plot by thin crosses is the result of simulations with account for mergers.

4.4.3 Comparison of the rates

The results of this section are summarized in figure 4.5 where we compare the rates for the three main LMXB formation processes, involving neutron stars, as a function of the stellar velocity dispersion. In computing the rates for the tidal capture and collisions with evolved stars we assumed an environment (IMF, age metallicity etc.) similar to the bulge of M31, as described in section 4.5. The exchange LMXB rates are from the simulations of the previous subsection, without and with account for mergers. It should be noted, that low and high velocity parts of these simulations were tailored for GC and M31 environment respectively, therefore were performed for different values of the stellar density, main sequence cut-off mass M_{co}, age and metallicity. For this reason, although they do correctly illustrate the general trend of the exchange rates with the stellar velocity dispersion, they should not be used to study the exact dependence. One should also keep in mind, that in order to convert the formation rates into the numbers of X-ray sources, the LMXB life-time considerations should be taken into account, as discussed in the section 4.4.5.

Figure 4.5 illustrates significant velocity dependence of the relative importance of different LMXB formation channels and suggests that the relative contributions of different subclasses of LMXBs should be different in GCs and in the galactic centres. In the low velocity environment of a GCs all three processes make comparable contributions to the LMXB production rates (but not to the numbers of X-ray sources observed in any given time, see below), with some prevalence of tidal captures by the main sequence stars, depending on the exact value of the velocity dispersion. In the high velocity environment of a galactic bulge, on the contrary, the tidal capture by main sequence stars with $M_* > 0.4 M_\odot$ and exchange reactions are unimportant and the LMXB formation rates are dominated by the collisions with evolved stars and

tidal captures by very low mass stars. However, the comparison between globular clusters and M31 is more complex than comparison of the velocity dependent rates, as these environments also differ in other properties of the stellar populations, such as the present day mass function, metallicity, binary fraction etc. This is considered in detail in section 4.5.

Finally, the total rate of encounters in volume V can be obtained as:

$$R = \int_V \left(\frac{\rho_*}{< M >}\right)^2 f \int \gamma(M, M_{ns}, \sigma_v) f(M) dM dV \tag{4.16}$$

where $f = f_{ns}, f_{bh}, f_{bin}$. Note, that the former two coefficients refer to the present day values, while the latter is the primordial binary fraction, as clarified in the previous subsection.

4.4.4 Black hole encounters

The discussion above was limited to the formation of LMXBs in which the compact object is an NS. Of course, the same processes are relevant for black holes (BHs), and these are considered below. We assume that stars with initial masses in the $30-100 M_\odot$ range become BHs, with a canonical mass of 10 $M_\odot$. The rates of tidal captures and and collisions with evolved stars can then be found from the equations of the previous sections, replacing M_{ns} with M_{bh} and f_{ns} with f_{bh}. With the initial mass function of Kroupa (2001), $f_{bh} = 0.17 \cdot f_{ns}$. Note that although there are ≈ 6 times fewer BHs than NSs, this is countered by the the gravitational focusing term (equation 4.3) which makes the encounter cross-section $\sim$5 times larger for a BH. As for the neutron stars, we assume that $R_{coll}/R_* = 1.8$. We note, however, that from equation 4.6 it might be expected that R_{coll} may be larger for the very small mass ratios considered here.

When considering various aspects of single-single encounters on the basis of the total energy arguments it should be noted that the kinetic energy at infinity in the centre-of-masses frame is defined by the reduced mass $\mu = M_1 M_2/(M_1 + M_2)$ which, for the low mass stars, only depends weakly on the compact object mass. Therefore, even if the energy equipartition is inefficient and the NS and BH velocity dispersions are comparable, as is the case in the M31 bulge, the kinetic energy at infinity, $\mu v_{rel}^2/2$, will not be much higher in the case of a black hole.

For this reason the energy considerations in collisions with evolved stars (section 4.4.1.1, eq.4.7), will not change significantly and the fraction of collisions expected to lead to a bound systems for a given velocity dispersion depends only weakly on the mass of the compact object.

For tidal captures, the energy of the oscillations induced in the non-degenerate star is roughly $\propto M_{NS,BH}^2$ (see equation 4.9), and the capture distance is therefore larger for BHs than for NSs. At low velocities, this can enhance the rate by a moderate factor of $\lesssim$2. At large velocities, on the contrary, $R_{tid} \sim R_{coll}$, and even a small increase in R_{tid} can drastically increase $\sigma_{tid} - \sigma_{coll}$ and thereby the overall tidal capture rate. As the total energy to be dissipated in the interaction depends weakly on the compact object mass, the impact of the tidal oscillation on the thermal state of the normal star does not become more severe for the black hole. Therefore, if a tidal capture is possible at all, it is possible for black holes as well as for neutron stars.

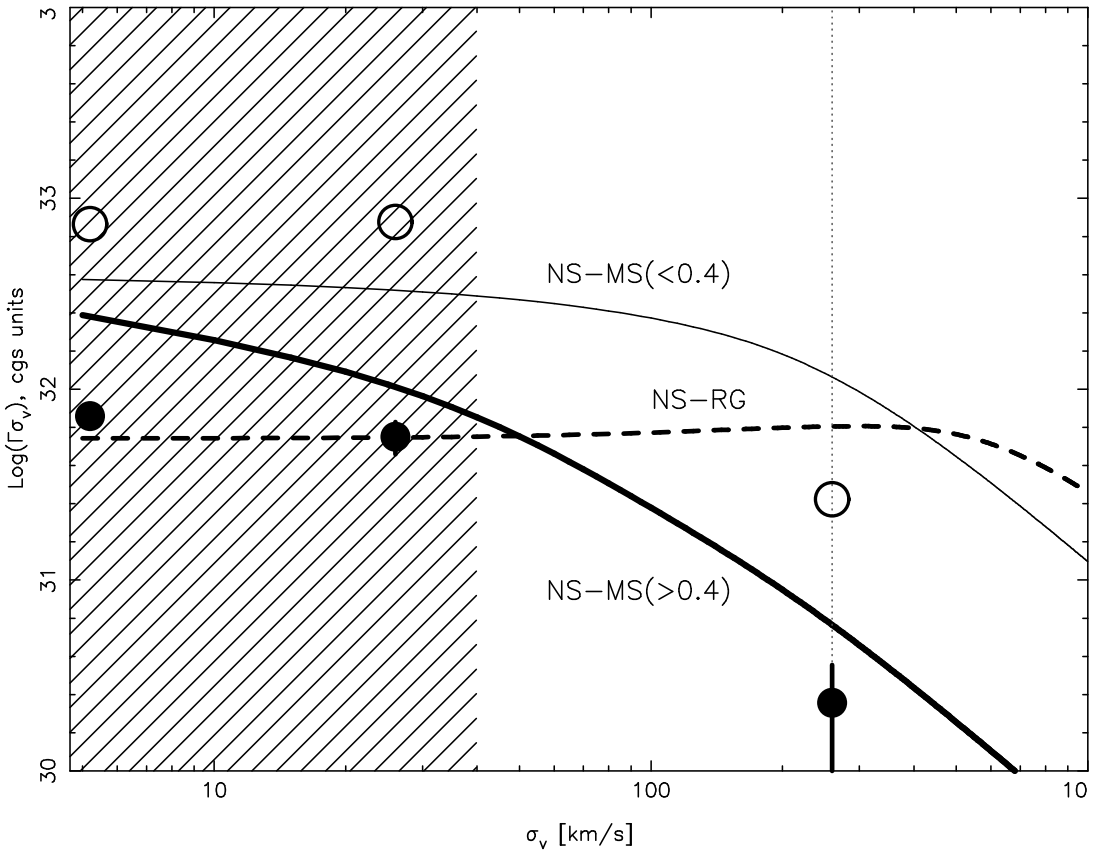

Figure 4.5: Comparison of NS LMXB dynamical formation rates as a function of the stellar velocity dispersion. Shown are the rates $\gamma\sigma_v$ for tidal captures by main sequence stars $> 0.4M_\odot$ (thick solid line) and $< 0.4M_\odot$ (thin solid line), collisions with evolved stars (assuming $\lambda\eta = 0.5$, dashed line) and exchange reactions (circles with error bars). For the exchange reactions, results are shown for simulations without (open symbols) and with (filled symbols) account for collisions. Error bars are only shown if they are larger than the circles. The hatched area shows the velocity dispersion range typical for globular clusters, the dotted line for the inner bulge of M31.

There is one important difference between BHs and NSs, namely that the retention factor for black holes in globular clusters is close to zero (O'leary et al., 2006). For this reason, black holes do not contribute to dynamical LMXB formation in globular clusters. In M31, however, the black hole fraction should be close to the IMF-based estimate given above, due to much longer energy equipartition time scale than in globular clusters.

In figure 4.6 we compare the LMXB formation rates in single-single encounters involving black holes and neutron stars. Obviously, black holes can make sizable contribution to the LMXB formation rates, especially in the high velocity regime.

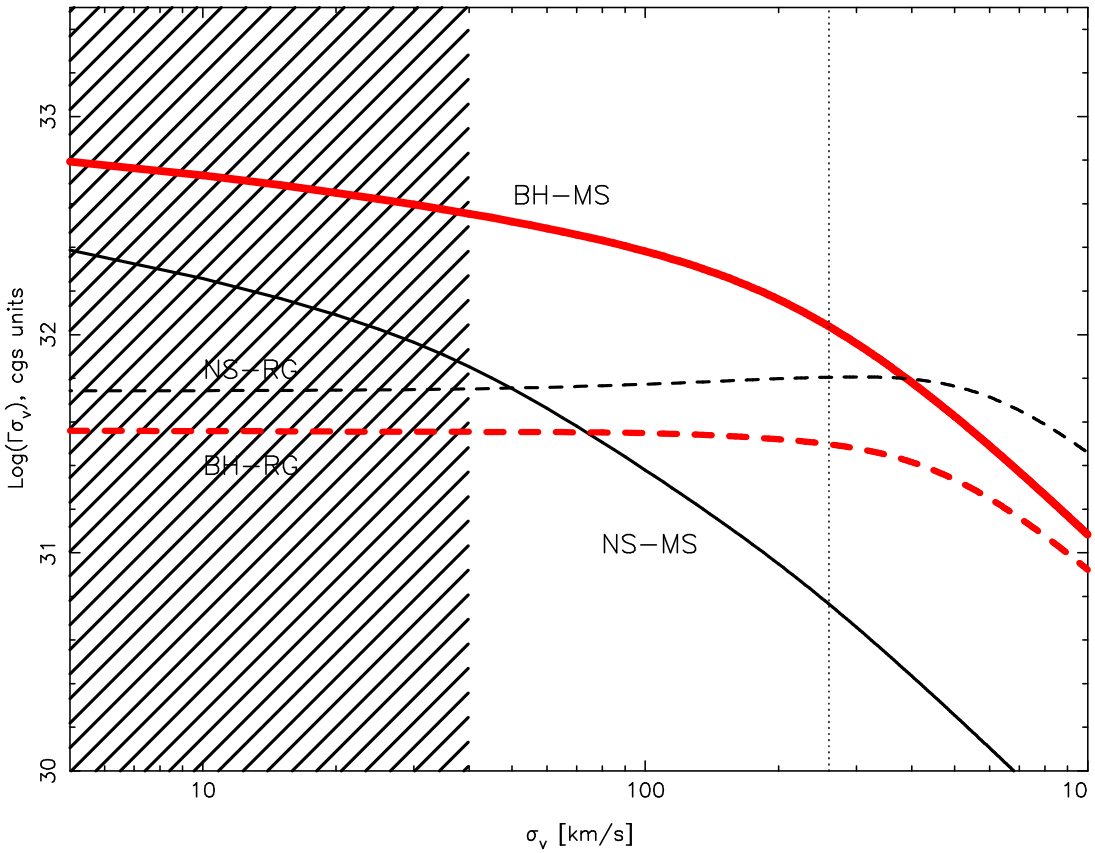

Figure 4.6: Comparison of the LMXB formation rates in encounters with neutron stars (thin lines) and black holes (thick lines). Shown are tidal captures by main sequence stars of mass $> 0.4 M_{\odot}$ (solid lines) and collisons with RGB/AGB stars (dashed lines). The normalization of the BH rates have been multiplied with f_{bh}/f_{ns}.

4.4.5 Numbers of X-ray sources

In order to convert the encounter rates to the numbers of X-ray sources observed at any given moment of time, one needs to consider the evolution of a binary through the X-ray phase. A definitive answer can be obtained from proper population synthesis calculations, which is beyond the scope of this paper. In a simpler approach one may consider characteristic life times τ_X of binaries at different phases of its evolution. The number of X-ray sources N_X can be then related to the corresponding encounter rate: $N_X \sim \gamma\,\tau_X$. Taking into account dependence of the τ_X on the mass and evolutionary status of the donor star and their mass distribution, we obtain an expression, similar to the equation 4.16 for overall encounter rate:

$$N_X \approx \int_V \left(\frac{\rho_*}{< M >}\right)^2 f \int \tau_X(M)\,\gamma(M, M_{ns}, \sigma_v) f(M)\,dM dV \qquad (4.17)$$

where f is defined as in eq.(4.16) and $\tau_X(M) = \Delta M_d/\dot{M}$, $\Delta M_d = M_i - M_f$, M_i is the initial mass of the donor star and M_f its final mass in the given evolution stage

(e.g. for a star with initial mass $> 0.4M_\odot$, $M_f = 0.4M_\odot$ – the mass corresponding to the period gap). In case of an LMXB powered through the Roche-lobe overflow, the $\dot{M}$ is defined by the orbital braking mechanism and the mass-radius relation for the donor star. The stability of the mass transfer in the accretion disc should be also taken into account in order to identify persistent/transient nature of the binary. The integral in eq.(4.17) is taken over the range of the masses relevant to the given type of X-ray binaries.

Below we examine evolution and characteristic values of $\dot{M}$ of X-ray binaries formed formed via different dynamical processes considered in in this paper. We accept the standard prescriptions for the magnetic braking (Rappaport et al., 1983) and gravitational radiation (Landau & Lifshitz, 1962; Peters, 1964) and the transiency criterium in the form published by Dubus et al. (1999) for irradiated discs. One should keep in mind that these simple presciptions predict time averaged quantities but may fail to explain the momentary values of luminosity, which may vary significantly on the timescales of days–months–years. The dependences of the mass accretion rate on the mass of the donor star for NS and BH binaries are shown in figure 4.7. These dependences were computed based on standard formulae for a Roche lobe filling secondary (van den Heuvel, 1992) assuming that the secondary is in the thermal equilibrium. As was demonstrated by Stehle et al. (1996), this assumption gives sufficiently accurate results for the main sequence donor. For the mass-radius relation we used the 10 Gyr isochrones of Baraffe et al. (2003) and Baraffe et al. (1998) for stars $M < 0.1M_\odot$ and $M > 0.1M_\odot$, respectively. Also shown in figure 4.7 are transiency limits for different types of compact object. The NS and BH masses were assumed 1.4 and 10 $M_\odot$ respectively. The spike in $\dot{M}$ at $\approx 0.07M_\odot$ is caused by the shape of mass-radius relation near the end of the nuclear burning, as given by the isochrones. It is less pronounced in the 1 Gyr isochrones (shown in figure 4.7 by thin solid lines) which might be more appropriate for the thermal state of a mass-losing brown dwarf. We did not investigate the reality of this spike and note, that its presence or absence does not significantly affect our conclusions.

Collisions with evolved stars. In a collision with a red giant, an ultra-compact X-ray binary (UCXB) with a He white dwarf donor is formed. The white dwarf mass equals approximately the mass of the red giant's core (Lombardi et al., 2006), i.e. is in the 0.1-0.4 $M_\odot$ mass range, depending on the evolutionary stage of the red giant. The evolution of such a system includes a very fast initial stage of very short, $\sim$ minutes, orbital period and very high, super-Eddington $\dot{M}$. During this period the white dwarf donor is quickly reduced to a $\sim 0.06M_\odot$ after which a more "normal" UCXB with $P_{orb} \sim 10$ min and $L_X \lesssim 10^{38}$ erg/sec emerges, similar to the ones observed in our Galaxy. Overall, such a system will spend ~ 0.1 Gyr with the luminosity $10^{36} - 10^{38}$ erg/sec, before the white dwarf is depleted below $\approx 0.02M_\odot$. Somewhere around this mass the sources will cross the stability threshold and will become transient (Deloye & Bildsten, 2003; Bildsten & Deloye, 2004).

The cores of less evolved, sub-giant stars are not fully degenerate and/or hydrogen-depleted. In this case a collision will result in a binary with He or brown dwarf donor, depending on the core mass and chemical composition. Such a binary is also driven by gravitational radiation, but due to the larger radius the period minimum is higher,

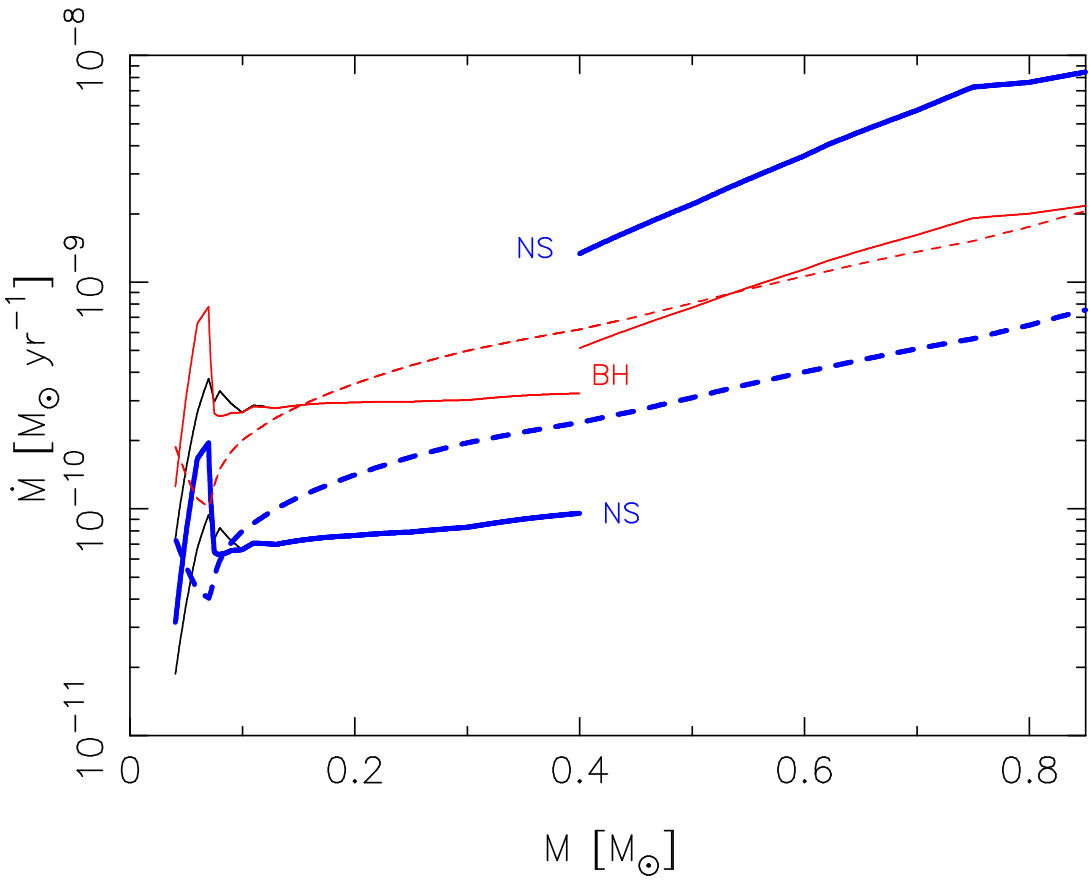

Figure 4.7: Dependence of the mass accretion rate $\dot{M}$ in a Roche-lobe filling system on the mass of the donor star. The curves for a neutron star and a black hole binary are shown by thick and thin lines. The calcultaions based on 10 and 1 Gyr isochrones give identical result down to $\sim 0.1 M_\odot$, below which the 10 Gyr isochrones give more pronounced spike in $\dot{M}$. The transiency limits are plotted by respective dashed lines. The method of calculations and assumptions are described in section 4.4.5

$\sim 20 - 30$ minutes, and super-Eddington mass transfer does therefore not occur. For such systems, a life time of $\sim 200 - 300$ Myrs may be expected (N.Ivanova, private communication). In order to make a crude estimate of their fraction we assume that the core of an RGB star becomes fully degenerate, when the central density exceeds $\rho_c \gtrsim (5 - 10)\,\rho_{crit}$, where ρ_{crit} is the critical density above which electron gas is degenerate ($\rho_{crit} \sim 2.4 \cdot 10^{-8} \mu_E T^{3/2}$ g cm^{-3}). We estimated from the Padova stellar tracks that this occures at stellar radii of $R \sim (3 - 5) \times R_\odot M/M_\odot$. As discussed in section 4.4.1.1, given the high stellar velocities in M31, only RGBs with rather small radii can effectively capture a compact object through collisions, and we expect that in a large fraction, $\sim 50 - 80$ per cent, of X-ray sources created through this mechanism the donor star is not fully degenerate. In the low velocity environment of globular clusters this fraction is smaller, $\sim 25 - 40$ per cent.

Tidal captures by main sequence stars with $M > 0.4 M_\odot$ lead to formations of "usual"

LMXBs, similar to the ones constituting the majority of systems with main sequence donors observed in the Galaxy. These sources are driven by the magnetic braking and luminosities of $\sim 10^{36.5-38.0}$ erg/sec and lifetimes of $\sim 0.1-0.5$ Gyr should be expected. Note, that these estimates depend critically on the magnetic braking prescription, the weak magneting breaking predicting up to several times smaller luminosities and longer life times (Ivanova & Kalogera, 2006). All black hole systems are expected to be transient, in agreement with BH binaries statistics in the Milky Way.

Tidal captures by main sequence stars of very low mass, $M < 0.4M_{\odot}$. For these fully convective very low mass stars the magnetic braking is believed to be inefficient, therefore the accretion is driven by the gravitational radiation. Given that the orbital periods of these systems are in the ∼hours range, gravitational radiation can provide luminosities of $\sim 10^{36.0-36.5}$ and $\sim 10^{36.5-37.0}$ erg/s for NS and BH systems respectively. The systems with $M \gtrsim 0.15M_{\odot}$ will be transient, these constraints being more severe for the NS binaries. The life times during the persistent phase are ~ 300 Myr. The life times during the transient phase are ~ 1 and ~ 4 Gyrs for BH and NS systems respectively.

It is interesting to consider the final stage of evolution of these systems, after the donor star is reduced to $\lesssim 0.1M_{\odot}$, below the nuclear burning limit. As these are descendants of very low mass stars, whose nuclear time scale is much longer than the cosmological time, they will become brown dwarfs of mass $\sim 0.05M_{\odot}$. Given the mass-radius relation for brown dwarfs, the $\dot{M}$ drops quickly (Fig.4.7) and these systems become transients, similar to some of the accreting msec pulsar systems, observed in our Galaxy.

We note that in the binary systems with very low mass ratios, q$\lesssim 0.02$, the circularization radius exceeds the tidal truncation radius (e.g. Paczynski, 1977). It is therefore not entirely clear whether the stable mass transfer is possible, see e.g. discussion in Yungelson et al. (2006) (section 3.3). Such low mass ratios can be reached for the most low mass black hole systems.

4.5 M31 and the Milky Way globular clusters

Below we compute rates of dynamical formation of LMXBs and their expected numbers in M31 and in Galactic GCs. For this, we need to specify velocity dispersion, initial and present day mass functions, age, metallicity and stellar isochrones. These parameters are different in GCs and galactic centres. The difference in stellar velocities is an important one, as discussed in section 4.4.3, but several other properties of stellar populations play equally significant roles in shaping the population of dynamically formed binaries. The factor of prime importance is highly efficient mass segregation in GCs. Its two most significant consequences are:

1. The present day mass function. Due to efficient mass segregation, the inner regions of the GCs, where most of the encounters happen, are depleted of low mass stars, to the degree that the mass function is essentially flat (e.g King et al., 2005; de Marchi & Paresce, 1997; Albrow et al., 2002). This is not the case for a galactic bulge, where the mass distribution of main sequence stars is sufficiently

well represented by the Kroupa IMF (Zoccali et al., 2000). As a result, the tidal captures by very low mass stars, dominating the binary formation processes in M31 (Fig.4.5), are significantly less important in GCs.

2. Abundance of BHs. GCs are believed to be completely depleted of black holes (O'leary et al., 2006), due to mass segregation and BH-BH encounters. Therefore tidal captures of BHs do not play any roles in globular clusters as opposite to the case of M31. Note that in the latter case the role of black holes is further enhanced by the velocity dependence of the tidal capture cross-section, as discussed in section 4.4.4 and shown in figure 4.6.

Among other factors, leading to further quantitative differences, the following should be mentioned: (i) Due to supernova kicks, large fraction of neutron stars escape the parent cluster, with the NS retention factor being in the $\sim 0.1-0.2$ range (Pfahl et al., 2002). On the other hand, the mass segregation of the remaining NSs may increase their density near the globular cluster centres, thus compensating for the low retention fraction. (ii) Binary fractions are different in globular clusters and galactic centres, due to different rates of binary-single processes, caused by difference in velocities and stellar densities. This is important for exchange rates and is taken into account in our simulations automatically. (iii) Finally, different ages and, especially metallicities result in different mass-to-light ratios, the main sequence turn-off mass and duration of the red giant phase, as discussed in section 4.5.2.

For these reasons the comparison between globular clusters and M31 is more complex than comparison of the velocity dependent rates, shown in figure 4.5. It is the subject of this section.

4.5.1 M31

For the stellar models we used an ischrone with a metallicity ~ 1.5 times solar and an age of 12 Gyr (isochrone file isoc_z030.dat from Girardi et al., 2002). This gives a main sequence turn-off mass of 0.9532 $M_\odot$ and a mass at the tip of the AGB of 1.0081 $M_\odot$ (initial masses). Stars more massive than this have all turned into stellar remnants.

The velocity dispersion (3D) was assumed to be constant, σ_v=260 km s^{-1} (McElroy, 1983; Widrow et al., 2003). The density structure of M31 was constructed using the model of Riffeser et al. (2005), based on the Gunn-r band photometry presented by Kent (1989). In this model the total R-band luminosity of the bulge out to a distance of 12 arcmin from the centre of M31 is $1.18 \cdot 10^{10} L_{\odot,R}$. We normalized the density by requiring the integrated R-band luminosity over the mass function (giving a mass-to-light ratio of $(M/L)_R$=3.27) to match the R-band luminosity of the model, giving the bulge a total mass of $3.9 \cdot 10^{10} M_\odot$ of stars in the 0.1-1.0081 $M_\odot$ range. The projection of this model agrees with the mass distribution inferred from the K-band light, which was used to model the LMXB distribution in Voss & Gilfanov (2007). The observed K-band luminosity of the region is $4.4 \cdot 10^{10} L_{\odot,K}$, and integrating over the isochrone, we find a mass-to-light ratio of $(M/L)_K$=0.76, giving a total mass of $3.4 \cdot 10^{10} M_\odot$, compatible with the R-band estimate.

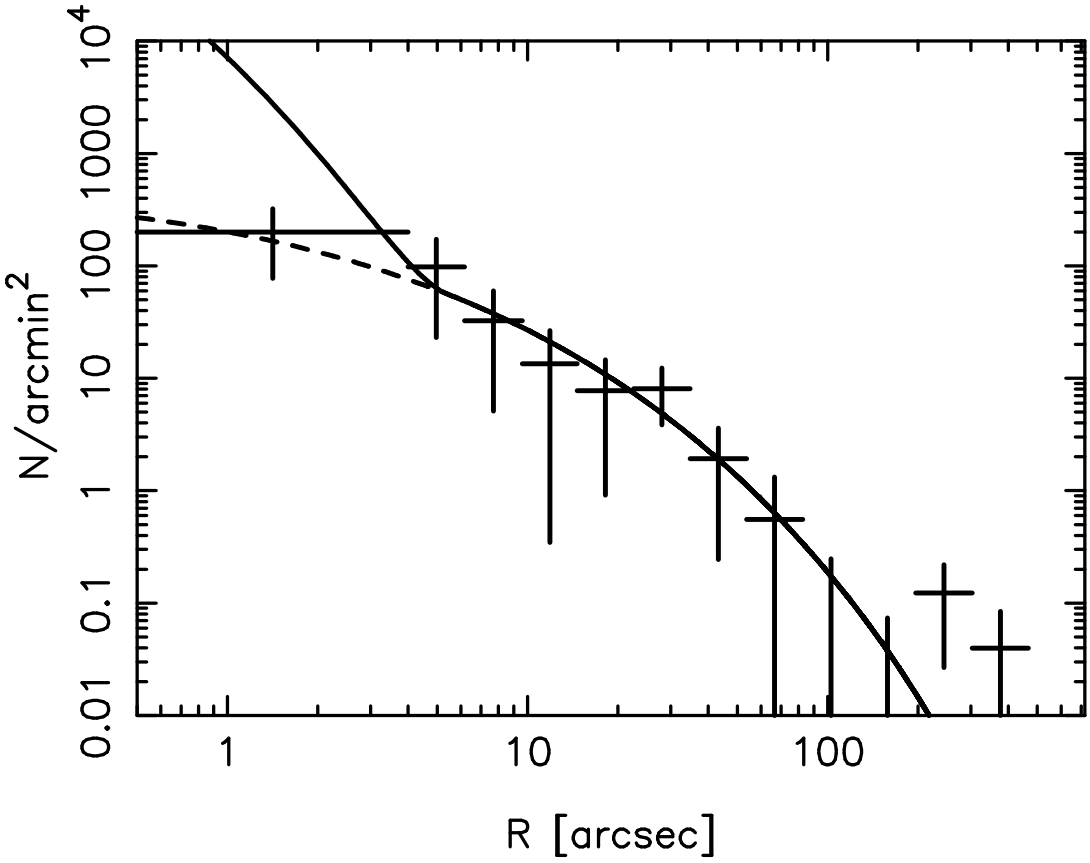

Figure 4.8: The radial distribution of "surplus" X-ray sources computed as a difference between the data and best fit model in figure 4.1. The solid line shows the projected ρ_*^2 distribution, computed from the original mass model of the M31 bulge from Riffeser et al. (2005). The dashed line was computed from the mass distribution with the circumnuclear stellar disc excluded. Both model distributions are normalized to the observed number of surplus sources outside 4 arcsec.

As a consistency check, we estimate the mass, using the mass-to-light ratios of Bell & de Jong (2001). With the bulge colour $(B\text{-}V)$=0.95 (Walterbos & Kennicutt, 1987), we find a bulge mass of 3.75 and 3.73 $\cdot 10^{10} M_\odot$ from the R-band and the K-band, respectively. In figure 4.8 the ρ_*^2 profile, integrated over the line of sight, is compared to the observed distribution of surplus sources, which was calculated by subtracting the best-fit model of LMXBs and CXBs from the observed radial distribution of X-ray sources (section 4.2, figure 4.1). It is obvious that the distributions agree well everywhere outside $\sim$ 4 arcsec. In the innermost 4 arcsec of M31 the mass model of Riffeser et al. (2005) features a sharp increase in density, absent in the distribution of X-ray sources. This increase is due to a stellar disc of high density surrounding the central super-massive black hole (Bender et al., 2005). In this paper we do not try to model the environment in this region and exclude the disc component.

Object	Type	MS($< 0.4M_\odot$)	MS($> 0.4M_\odot$)	RGB	HB	AGB	Exchange
(1)	(2)	(3)	(4)	(5)	(6)	(7)	(8)
NS	Tidal capture	**15.1** (15.7)	**0.8** (0.9)	0.01	-	-	3.5
NS	Collisions	36.6	46.6	**6.5-13.3**	5.2	**0.01-0.67**	**0.3**
BH	Tidal capture	**65.3** (65.3)	**14.2** (14.2)	0.09	-	-	8.8
BH	Collisions	37.7	38.0	**3.1-5.8**	2.0	**0.00-0.06**	**1.0**

Table 4.2: Formation rates of LMXBs in M31, per Gyr. The entries in bold are expected to lead to the formation of LMXBs. The columns are: (1) The type of compact object; (2) the capture process; (3) rate of interactions with MS stars of mass $< 0.4M_\odot$, only those initiating Roche-lobe overflow within 5 Gyr are included (full number is given in the parenthesis); (4) rate of interactions with MS stars of mass $> 0.4M_\odot$, same criteria as (3); (5) rate of interactions with stars on the RGB, for collisions only those with $a_f < 5R_\odot$ are included for $\eta\lambda = 0.1 - 1.0$; (6) rate of interactions with stars on the HB, tidal captures were not calculated; (7) rate of interactions with stars on the AGB, tidal captures were not calculated, same criteria as (5); (8) LMXBs created through exchange reactions, estimated from simulations without collisions (in tidal capture rows) and with collisions (in collision rows).

Metallicity	Type	MS($< 0.4M_\odot$)	MS($> 0.4M_\odot$)	RGB	HB	AGB	Exchange
0.2 solar	Tidal capture	**12.9** (17.2)	**24.8** (25.7)	7.0	-	-	203.4
	Collisions	10.5	51.3	**24.3-27.7**	4.6	**0.4-1.1**	**15.3**
0.02 solar	Tidal capture	**8.6** (10.8)	**14.3** (14.7)	2.9	-	-	117.3
	Collisions	6.6	28.6	**10.1-11.7**	2.0	**0.3-0.6**	**8.8**

Table 4.3: Total encounter rates for 140 Galactic globular clusters from Harris (1996) for which sufficient structural parameters are known, calculated assuming metallicity of 0.2 and 0.02 solar. Entries in bold indicate paths expected to lead to the formation of LMXBs. The rates are given in LMXBs/Gyr. These 140 GCs contain the 13 LMXBs observed in the Galactic GC system. The notation is the same as in table 4.2

Population	LMXBs observed	Type	MS($< 0.4M_\odot$)	MS($> 0.4M_\odot$)	RGB	HB	AGB	Exchange
Red GCs	8	Tidal capture	**4.1** (5.2)	**6.5** (6.7)	1.6	-	-	53.3
		Collisions	3.4	16.8	**7.9-9.2**	1.5	**0.1-0.4**	**4.0**
Blue GCs	5	Tidal capture	**5.9** (7.6)	**10.5** (10.8)	2.2	-	-	86.1
		Collisions	4.4	19.2	**6.8-7.8**	1.3	**0.2-0.4**	**6.5**

Table 4.4: Total encounter rates calculated separately for red and the blue Galactic globular cluster subsystems, assuming metallicity of 0.2 and 0.02 solar respectively. Bold entries indicate paths expected to lead to formation of LMXBs, and the rates are given as LMXBs/Gyr. The notation is the same as in table 4.2.

The stellar model used for computation of the encounter rates is described by the following distribution:

$$\rho_{bulge} = \rho_0 10^{-0.4(7.1 a_{bulge}^{1/4} + 0.61)} \tag{4.18}$$

where

$$a_{bulge} = \frac{0.254 z_0^2 + \sqrt{0.254^2 z_0^4 + 4(x_0^2 + y_0^2 + 1.11) z_0^2}}{2} \tag{4.19}$$

with a_{bulge}, x_0, y_0 and z_0 expressed in arcmin. The inclination of the bulge coordinate system is assumed to be 77°, and $\rho_0 = 4.34 \cdot 10^4 M_\odot$ pc^{-3} (using our mass to light ratio $(M/L)_R = 3.27$). This gives a bulge mass (within 12 arcmin from the centre) of $3.87 \cdot 10^{10} M_\odot$ and

$$\int \rho_*^2 dV = 4.6 \cdot 10^{11} M_\odot^2 \text{ pc}^{-3} \tag{4.20}$$

It is now straightforward to calculate the rates of tidal captures and collisions. Following the equations of section 4.4 the rates are given by

$$R_{M31} = \int_{bulge} \left(\frac{\rho_*}{< M >} \right)^2 dV \cdot f_{ns} \int_{M_{low}}^{M_{high}} f(M) \gamma dM \tag{4.21}$$

where $M_{low} - M_{high}$ is the initial mass range for the type of stars for which the rates are calculated. The rates for different types of encounters are summarized in Table 4.2. For clarity the channels expected to lead to the formation of LMXBs are written in bold font.

4.5.1.1 Numbers of X-ray sources

We turn now to the numbers of of dynamically formed X-ray sources. As it is obvious from Table 4.2 (column 4), the number of "normal" presistent LMXBs with a neutron star accreting from a main sequence companion $M_* > 0.4 M_\odot$, which constitute the majority of the primordial LMXBs, is negligibly small (BH capture products with $M_* > 0.4 M_\odot$ donors are expected to be transients and are discussed below). The two main contributions to the population of dynamically formed sources come from the tidal captures of black holes and neutron stars by very low mass MS stars, and from collisions of compact objects with RGB stars (columns 3 and 5). In computing the numbers of sources from equation 4.17 we take into account that the the evolutionary timescales of all types of dynamically formed X-ray sources are much shorter than the life time of the bulge. Therefore the systems formed via tidal capture by $M_* > 0.4 M_\odot$ stars will pass through the phase of the very low mass companion in the end of their life time, adding to the numbers of persistent and transient sources of this type. Similarly, a capture product of, for example, a $0.3 M_\odot$ star will go through the transient phase in the beginning of its X-ray active phase and will become a persistent source after the donor star is depleted below $\sim 0.10 - 0.15 M_\odot$. We thus predict ~ 24 and ~ 5 persistent X-ray sources with black holes and neutron stars respectively, accreting from the very low mass stars. To this number should be added the number of ultra-compact X-ray binaries produced via collisions of compact objects with red giants, which is ~ 3. The total number of predicted persistent sources is compatible with, albeit somewhat larger

than the observed number of surplus sources, ~ 21. Given the number and magnitude of uncertainties involved in the calculations and the simplifications made, we consider this as a good agreement.

Based on the range of the donor masses corresponding to unstable mass transfer (figure 4.7), we predict ~ 30 BH and ~ 22 NS transient sources with very low mass donors $M_* < 0.4 M_\odot$, as well as ~ 3 BH transient sources with MS donors $> 0.4 M_\odot$. Furthermore, exchange reactions might contribute with a number of LMXBs with RGB donor stars, that are also transient, but duration of their active phase is restricted by the life time of the red giant donor. The number of transients observed at any given moment in time depends on their duty cycle. Taking Galactic black hole transients with the main sequence donor as an example, one could expect a duty cycle of $\sim 1/50$, giving one bright transient in ~ 15 years. As for the transients with very low mass donors, one can use the accreting msec pulsars as an example of NS systems. SAXJ1808.4-3658 has outbursts lasting for $\sim 2-3$ weeks every ~ 2 years, and the duty cycle is therefore $\sim$0.03. Assuming crudely that it is the same for BH and NS systems, we would expect 1.5 transient sources at any given time. The outbursts of accreting msec pulsars in our Galaxy are characterized by low peak luminosities, $\log(L_X) \lesssim 36 - 36.5$. Therefore many, if not most, of outbursts from these sources will be missed in a Chandra survey of the type reported in Voss & Gilfanov (2007) which detects mostly brighter transients, with the peak luminosity of $\log(L_X) \gtrsim 36.5$. This explains why Voss & Gilfanov (2007) have not found any excees in the number of transient sources close to the galactic center – the fraction of transients detected inside 1 arcmin from the center (5 out of 28 in 29 Chandra observations with the time span of ~ 5 years) agrees with the fraction of stellar mass contained in this region. On the other hand Chandra observations of our Galactic Center, having much better sensitivity, have indeed revealed overabundance of faint transients (Muno et al., 2005).

4.5.2 Globular Clusters

Due to high efficiency of the mass segregation in globular clusters the (retained) neutron stars will be much more centrally concentrated than low mass stars. Assuming that stellar density and velocity dispersion are approximately constant over the region occupied by the neutron stars, one can approximately write:

$$\int_V n_{ns} n_* \Gamma \, dV \simeq n_* \Gamma \int_V n_{ns} \, dV = k N_{ns} \, n_* \Gamma \tag{4.22}$$

where N_{ns} is the total number of neutron stars in the globular cluster under consideration, n_* is the central density of stars and $k \lesssim 1$ is a constant accounting for inaccuracy of this approximation. Assuming that the distribution of normal stars follows the analytic King model (Lugger et al., 1995; Grindlay et al., 2002), and that the NSs are in thermal equilibrium with the stars at turn-off (0.80-0.85 $M_\odot$), we estimated that $k \sim 0.2 - 0.3$. Total thermal equilibrium is generally not reached, the value of k is therefore slightly lower. In the following we will use a value of $k = 0.2$ for all globular clusters.

We use the catalogue of Harris (1996) for the globular clusters parameters required to estimate the formation rates of LMXBs in the Galactic GCs. Of the 150 GCs included

in the catalogue, the parameters are missing for 10, and we ignore these. The stellar populations in the GCs were modelled using the isochrones of Girardi et al. (2002), with an age of 11 Gyr (Salaris & Weiss, 2002). The N_{ns} for each GC was computed as follows. Assuming the initial mass function of Kroupa (2001), we used the integrated light of the isochrones to compute the present day mass-to-light ratio and from the total V-band luminosity of the GCs computed the IMF normalization. Assuming further that all stars with the initial mass in the range of $8-30\,M_{\odot}$ have become neutron stars and retention factor of 10 per cent (Pfahl et al., 2002) we finally compute the present day number of the neutron stars in each globular cluster, N_{ns}. On the other hand, we assumed that the present day mass function in the GC centers is flat. With this mass function we again use the integrated V-band light of the isochrones to calculate n_* from the V-band luminosity density ρ_V given in Harris (1996). For the 56 GCs in Pryor & Meylan (1993) we use their central velocity dispersions v_0 needed to compute the encounter rates. The remainong GCs were dealt with as follows. ¿From the virial theorem we expect that $v_0 \sim Kr_c\sqrt{\rho_0}$, where r_c is the core radius of the GCs, and ρ_0 is the central density; we further assumed that $\rho_V \propto \rho_0$. We performed the least square fit to the known central velocity dispersions in 56 GCs and found $K = 0.18$ km s^{-1} and 0.17 km s^{-1} for the metal-rich and metal-poor GCs respectively (assuming that r_c is in pc and ρ_V in $M_{\odot,V}$ pc^{-3}). These values have been used to find v_0 for the remaining 84 GCs.

4.5.2.1 Metallicity effects

In order to study the metallicity dependence of the encounter rates, we compute the cumulated rates for two metallicities, 20 per cent, and 2 per cent of the solar value (files `isocz004.dat` and `isocz0004.dat` from Girardi et al. (2002)) which are representative of the red and blue GC populations, respectively. The results are presented in table 4.3 and show a ∼1.5-2.5 increase in the encounter rates for the higher metallicity case.

The metallicity dependence in our calculations is mainly due to two factors. (1) As noted by Bellazzini et al. (1995) the radii of metal-rich stars are larger, and therefore the rates of tidal captures and collisions are higher. Furthermore the duration of the RG phase is longer for metal-rich stars. As demonstrated by Maccarone et al. (2003) this effect can maximally lead to an enhancement of the cross-sections and rates by $\lesssim 60$ per cent, and most likely ~ 30 per cent. Our results are consistent with this, showing a ~ 20 per cent increase in tidal captures by MS stars ($> 0.4M_{\odot}$) and ~ 50 per cent increase in collisions with RGB/AGB stars. For exchange reactions the effect is negligible. (2) Theoretical isochrones predict that the V-band mass-to-light ratio of the metal-rich population is higher than that of the metal-poor population. As the stellar densities are given in Harris (1996) in the form of V-band luminosity density, the encounter rate is proportional to $\rho_*^2 \propto (M/L)^2$. This could result in an additional ~ 60 per cent increase in the rates. It is however unclear, whether this is the case for real globular clusters – observations indicate that the the central mass-to-light ratio might be independent on the metallicity (McLaughlin, 2000). This could be due to the fact that the red GCs typically are more dynamically evolved (but not

older) than the blue ones and therefore have a flatter mass function in their cores (McClure et al., 1986; Vesperini & Heggie, 1997; Piotto & Zoccali, 1999). Moreover, these structural differences may be the true reason for the observed metallicity dependence of the abundance of dynamically created sources in globular clusters as also noted by Bregman et al. (2006).

Thus our calculations do indicate a moderate metallicity dependence of the encounter rates. It is however insufficient to explain observations. Indeed, there are ∼3 times as many LMXBs in red GCs as in blue GCs of the same size in the Galaxy (Grindlay, 1993; Bellazzini et al., 1995), where 8 out of 13 LMXBs are observed in the red GC system containing 46 out of the total number of 140 GCs with known metallicities (assuming a division at [Fe/H]=-1). Similar trend is observed in in other galaxies (Kundu et al., 2002; Sarazin et al., 2003; Kim et al., 2006).

4.5.2.2 Predicted rates and numbers of X-ray sources

To predict the total rates of LMXBs formation in the Galactic GCs, we divide the GCs into two subpopulations depending on metallicity, red (46 GCs) and blue (94 GCs). The cumulative rates for these two subpopulations are then calculated as above, assuming all red GCs to have 0.2 solar metallicity and all blue ones to have 0.02 solar metallicity. The results are given in table 4.4. As it can be expected from figure 4.5, all three processes give comparable contributions.

For metal-rich clusters, these rates predict ~ 0.5 X-ray binaries with the companion mass $> 0.4M_\odot$ due to tidal captures, with an additional $0.5 - 1.0$ such binaries from exchange reactions, ~ 1.5 UCXBs and ~ 3 fainter LMXBs with very low mass companion. Corresponding to ~ 6 sources overall, this is in a good agreement with the total number of LMXBs observed in metal-rich clusters (8). On the other hand, we do overpredict the numbers of X-rays sources in the metal-poor GCs by a factor of ~ 1.5 – although our calculations do show the expected metallicity dependence, it is compensated by the larger number of metal-poor clusters. Note that the number of bright sources with $M_d > 0.4M_\odot$ main sequence companion dependes critically on the rate of magnetic braking. The above numbers have been computed with the standard prescription of Rappaport et al. (1983). The weaker variants of magnetic braking (e.g. Ivanova & Taam, 2003) may give upto a factor $\sim 5 - 10$ longer lifetimes and, consequently, larger numbers of LMXBs with $M_d > 0.4M_\odot$ donors. This can change the overall numbers for globular clusters, but is insignificant factor in the M31 bulge calculations, due to negligible contribution of these systems there.

It is interesting to compare the numbers of ultra-compact systems. Considering metal rich clusters only, 2 of the 8 LMXBs have measured orbital periods $\lesssim 1$ h and are therefore most likely UCXBs (Benacquista, 2006). Of the 6 others 4 have undetermined periods and could therefore be either UCXBs or traditional LMXBs. The final 2 have orbital periods > 5 h. Thus, there may be from 2 to 6 short period systems. We predict ~ 1.6 UCXBs formed in the collisions with red giants. In addition, the LMXBs with the very low mass donor stars, $M_d \lesssim 0.15M_\odot$, for which the predicted number is ~ 2.4, will also have short orbital periods and faint optical counterparts and may contribute to the observed statistics of UCXBs, giving a prediction of ~ 4 short

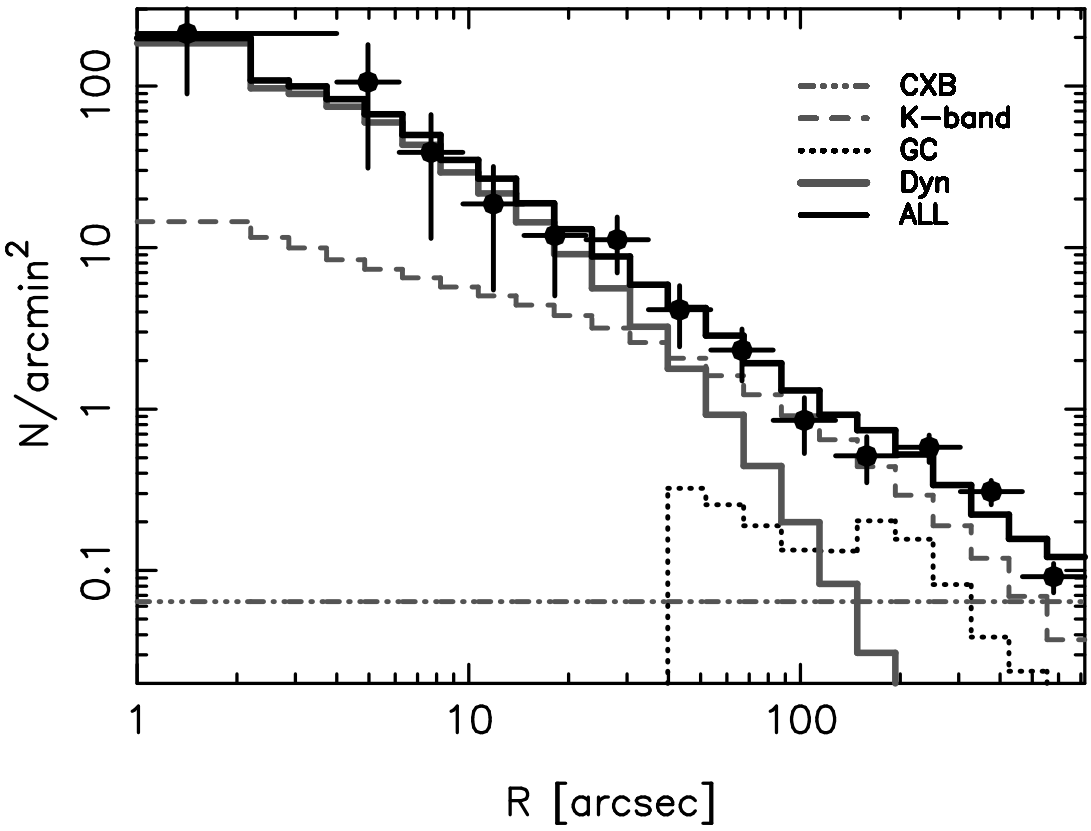

Figure 4.9: The observed radial distribution of the X-ray sources in the bulge of M31, compared with the expected contributions of different sub-populations of low-mass X-ray binaries: primordial, binaries in globular clusters and binaries formed through dynamical interactions in the inner bulge of M31. The dash-dotted horizontal line shows contribution of the background AGN. The total numbers of sources are summarized in table 4.5.

Type	Number
Background sources	29
Primordial LMXBs	64
LMXBs in globular clusters	21
LMXBs dynamically formed in the bulge	21

Table 4.5: Numbers of X-ray sources of different origin in the bulge of M31, $r < 12$ arcmin, $L_X > 10^{36}$ erg/s

period systems in total.

4.6 Conclusions

We have studied the spatial distribution of the luminous X-ray point sources ($L_x > 10^{36}$ erg s^{-1}) in the bulge of M31. We show that there is a significant increase in the specific frequency of sources, per unit stellar mass, in the inner ≈ 1 arcmin. This behaviour is similar, although smaller in the magnitude, to that observed in globular clusters. The radial distribution of the surplus sources follows the ρ_*^2 profile. All these suggest that the surplus sources are dynamically created in stellar encounters in the high stellar density environment of the inner bulge of M31. This is further confirmed by the peculiarity of their luminosity distribution, which resembles that of the globular cluster sources in M31 and our Galaxy (Voss & Gilfanov, 2007).

It has long been known that dynamical interactions are responsible for the relatively large number of X-ray sources observed in globular clusters, but this is the first evidence of the dynamical formation of LMXBs in the vicinity of a galactic center. The stellar velocities in bulges are higher than in globular clusters by a factor of $\sim 5-10$. We therefore performed a detailed study of the velocity dependence of the three main dynamical processes leading to the formation of LMXBs: tidal captures of a compact objects by main sequence stars, collisions between evolved stars and compact objects and the exchange of a compact object into an already existing binary. Another major factor affecting the overal encounter rates and the numbers of dynamically formed LMXBs is the high efficiency of the mass segregation in globular clusters, which modifies significantly the spatial distributions of objects of different mass and affects the present day mass function in different parts of a globular cluster. In addition, due to the relative shallowness of the potential well, the populations of compact objects are significantly depleted in globular clusters.

We found that while exchange reactions are potentially the dominant formation channel in globular clusters (although stellar collisions might decrease the importance of this channel significantly), this process is relatively unimportant in M31. Similarly, tidal captures of NSs by main sequence stars of mass $> 0.4M_\odot$ are important in globular clusters, but not in M31. Instead the main formation channel is tidal captures of compact objects by low mass ($< 0.4M_\odot$) stars, with some contribution from collisions between red giants and compact objects. While the geometrical collision rate is high enough to explain the total number of sources from the latter channel, the majority of the collisions are unlikely to lead to the formation of a binary system, as the binding energy of the envelopes of most RGB/AGB stars is too low to capture a compact object in a high velocity environment. We conclude that the majority of the sources in M31 are short-period binaries, and in contrast to globular clusters many of them have BH accretors. We note that the BH binaries with a very low mass companion may become persistent X-ray sources after the donor star is depleted below, $M_d \lesssim 0.15M_\odot$, due to small size of the accretion disc and the positive dependence of the gravitational breaking rate on the mass of the primary. We also predict for M31 a large number of faint transients, similar to the accreting msec pulsars in our Galaxy. Overall, we have been able to explain the spatial distribution and absolute numbers of surplus sources detected in the inner bulge of M31 as a well as the statistics of LMXBs in the metal rich globular clusters. However, we overpredict by a factor of ~ 1.5 the population of

LMXBs in the metal poor clusters.

Finally, the sub-populations of low-mass X-ray binaries in the bulge of M31 are summarized in Fig.4.9 and Table 4.5.

Acknowledgements The authors would like to thank Natasha Ivanova for numerous discussions and useful comments on the initial version of the manuscript.

Bibliography

Albrow M. D., De Marchi G., Sahu K. C., ApJ, 579, 660

Baraffe I., Chabrier G., Barman T. S., Allard F., Hauschildt P. H., 2003, A&A, 402, 701

Baraffe I., Chabrier G., Allard F., Hauschildt P. H., 1998, A&A, 337, 403

Barmby P., Huchra J. P., 2001, AJ, 122, 2458

Belczynski K., Kalogera V., Rasio F. A., Taam R. E., Zezas A., Bulik T., Maccarone T. J., Ivanova N., 2005, preprint (astro-ph/0511811)

Bell E. F., de Jong R. S., 2001, ApJ, 550, 212

Bellazzini M., Pasquali A., Federici L., Ferraro F. R., Fusi Pecci F., 1995, ApJ, 439, 687

Benacquista M. J., 2006, LRR, 9, 2

Bender R., et al., 2005, ApJ, 631, 280

Bildsten L., Deloye C. J., 2004, ApJ, 607, L119

Binney J., Merrifield M., 1998, Galactic Astronomy, Princeton Univ. Press, Princeton, NJ

Bregman J. N., Irwin P. S., Seitzer P., Flores M., 2006, ApJ, 640, 282

Clark G. W., 1975, ApJ, 199, L143

Davies M. B., Benz W., Hills J. G., 1992, ApJ, 401, 246

de Kool M., 1990, ApJ, 358, 189

de Marchi G., Paresce F., 1997, ApJ, 476, L19

Deloye C. J., Bildsten L. 2003, ApJ, 598, 1217

Devereux N. A., Price R., Wells L. A., Duric N., 1994, AJ, 108, 1667

Dewi J. D. M., Tauris T. M., 2000, A&A, 360, 1043

Dorman B., 1992, ApJS, 80, 701

Dubus G., Hameury J., Charles P., 1999, MNRAS, 303, 139

Eggleton P. P., 1983, ApJ, 268, 368

Fabian A. C., Pringle J. E., Rees M. J., 1975, MNRAS, 172, 15

Fregeau J. M., Cheung P., Portegies Zwart S. F., Rasio F. A., 2004, MNRAS, 358, 572

Fryer C. L., Woosley S. E., 1999, 526, 152

Galleti S., Federici L., Bellazzini M., Fusi Pecci F., Macrina S., 2004, A&A 416, 917

Gilfanov M., 2004, MNRAS, 349, 146

Girardi L., Bertelli G., Bressan A., Chiosi C., Groenewegen M. A. T., Marigo P., Salasnich B., Weiss A., 2002, A&A, 391, 195

Grimm H-J., Gilfanov M. R., Sunyaev R. A., 2003, MNRAS, 339, 793

Grindlay J., ASP conf. Ser. 48, The Globular Clusters-Galaxy connection, ed. G. H. Smith & J. P. Brodie (San Francisco:ASP), 156

Grindlay, J. E., Camilo, F., Heinke, C. O., Edmonds, P. D., Cohn, H., Lugger, P. 2002, ApJ, 581, 470

Han C., 1996, ApJ, 472, 108

Harris W. E., 1996, AJ, 112, 1487

Heggie D. C., 1975, MNRAS, 173, 729

Heggie D. C., Hut, P., 1993, ApJS, 85, 347

Hills J. G., 1976, MNRAS, 175, 1

Hurley J. R., Tout C. A., Pols O. R., 2002, MNRAS, 329, 897

Hut P., Bahcall J. N., 1983, ApJ, 268, 319

Ivanova, N., Taam, R., 2003, ApJ, 599, 516

Ivanova N., Rasio F. A., Lombardi J. C., Dooley K. L., Proulx Z. F., 2005, ApJ, 621, L109

Ivanova N., Kalogera V., 2006, ApJ, 636, 985

Jarret T. H., Chester T., Cutri R., Schneider S., Huchra, J. P. 2003, AJ, 125, 525

Kent S.M., 1989, AJ, 97, 1614

Kim E., Kim D.-W., Fabbiano G., Lee M. G., Park H. S., Geisler D., Dirsch B., 2006, ApJ, 647, 276

King A. R., Frank J., Kolb U., Ritter H., 1997, ApJ, 484, 844

King I. R., Sosin C., Cool A. M., 1995, ApJ, 452, L33

Kochanek C. S., 1992, ApJ, 385, 604

Kroupa P., 2001, MNRAS, 322, 231

Kumar P., Goodman J., 1996, ApJ, 466, 946

Kundu A., Maccarone T. J., Zepf S. E., 2002, ApJ, 574, L5

Landau L. D., Lifshitz E. M., 1962, The Classical Theory of Fields, Addison-Wesley, Reading, Massachusetts

Lee H. M., Ostriker J. P., 1986, AJ, 310, 176

Liu Q. C., van Paradijs J., van den Heuvel E. P. J., 2001, A&A, 368, 1021

Lombardi J. C., Proulx Z. F., Dooley K. L., Theriault E. M., Ivanova N., Rasio F. A., 2006, ApJ, 640, 441

Lorimer D.R., 2005, LRR, 8, 7

Lugger P.M., Cohn H.N., Grindlay J.E., 1995, ApJ, 439, 191

Maccarone T. J., Kundu A., Zepf S. E., 2003, AJ, 586, 814

Macri L. M., et al., 2001, ApJ, 549, 721

Mardling R. M., 1995, ApJ, 450, 732

McClure R. D., et al., 1986, ApJ, 307, L49

McElroy D. B., 1983, AJ, 270, 485

McLaughlin D.E., ApJ, 539, 618

McMillan S. L. W., Taam R. E., McDermott P. N., 1990, ApJ, 354, 190

Moretti A., Campana S., Lazzati D., Tagliaferri G., 2003, ApJ, 588, 696

O'leary R. M., Rasio F. A., Fregeau J. M., Ivanova N., O'shaugnessy R., 2006 ApJ, 637, 937

Muno M.P., Pfahl E., Baganoff F.K., Brandt W.N., Ghez A., Lu J., Morris M.R., 2005, ApJ, 622, L113

Paczynski B., 1977, ApJ, 216, 822

Peters P. C., 1964, Phys. Rev., 136, B1224

Pfahl E., Rappaport S., Podsiadlowski P., 2002, ApJ, 573, 283

Piotto G., Zoccali M., 1999, A&A, 345, 485

Piro A. L., Bildsten L., 2002, ApJ, 571, 103

Podsiadlowki P., MNRAS, 279, 1104

Podsiadlowki P., Rappaport S., Pfahl E. D., 2002, ApJ, 565, 1107

Portegies Zwart S. F., Yungelson L. R., 1997, A&A, 332, 173

Press W. H., Teukolsky S. A., 1977, ApJ, 213, 183

Pryor C., Meylan G., 1993, in ASP Conf. Ser. 50, Structure and Dynamics of Globular Clusters, ed. S. G. Djorgovski & G. Meylan (San Francisco:ASP), 357

Rappaport S., Verbunt F., Joss P. C., 1983, ApJ, 275, 713

Rasio F. A., Shapiro S. L., 1991, ApJ, 377, 559

Riffeser A., Fliri J., Seitz S., Bender R., 2005, ApJS, 163, 225

Salaris M., Weiss A., 2002, A&A, 388, 492

Sarazin C. L., Kundu A., Irwin J. A., Sivakoff G. R., Blanton E. L., Randall S. W., 2003, AJ, 595, 743

Spitzer L., 1969, ApJ, 158, L139

Spruit H. C., Ritter H., 1983, A&A, 124, 267

Stanek K. Z., Garnavich P. M., 1998, APJ, 503, L131

Stehle R., Ritter H., Kolb U., 1996, MNRAS, 279, 581

Taam R.E., Ricker, P.M, 2006, Preprint (astro-ph/0611043)

van den Heuvel, E. P. J., 1992, in Saas-Fee advanced course 22, Interacting Binaries, ed. H. Nussbaumer & A. Orr (Springer-Verlag), 263

Verbunt F., 1987, ApJ, 312, L23

Vesperini E., Heggie D. C., 1997, MNRAS, 289, 898

Voss R., Gilfanov M., 2006, A&A, 447, 71

Voss R., Gilfanov M., 2007, Preprint (astro-ph/0610649)

Voss R., Tauris T. M., 2003, MNRAS, 342, 1169

Walterbos R. A. M., Kennicutt R. C., 1987, A&AS, 69, 311

Webbink R. F., 1984, ApJ, 277, 355

Widrow L. M., Perrett K. M., Suyu S. H., 2003, ApJ, 588, 311

Yungelson L. R., Lasota J.-P., Nelemans G., et al. 2006, A&A, 454, 559

Zahn J.-P., 1989, A&A, 220, 112

Zahn J.-P., 1989, A&A, 223, 112

Zoccali M., Cassisi S., Frogel J. A., Gould A., Ortolani S., Renzini A., Rich M. R., Stephens A. W., 2000, AJ, 530, 418

5 Conclusions

The goal of the observational part of the research was to study the faint end of the LF and the spatial distribution of LMXBs with *Chandra* in Cen A and Andromeda. Due to the large angular size of nearby galaxies, the samples of LMXBs in these are strongly contaminated by background sources, except for the innermost regions. Another problem is that at the faint end of the LF, incompleteness effects can be important. In order to study the populations to the faintest possible limit, we therefore developed methods to correct for these effects statistically.

With a distance of ∼3.5 Mpc, Cen A is the only massive elliptical galaxy for which the luminosity function can be studied below $L_x \sim 10^{37}$ erg s^{-1}, with moderate observing times. By combining 4 *Chandra* ACIS observations with a total exposure time of 170 ks, it was possible to perform a detailed study of the spatial distribution of the sources to a limiting luminosity of $L_x \sim 10^{37}$ erg s^{-1} and the LF down to $L_x \sim 2 \cdot 10^{36}$ erg s^{-1}. This is by a factor of $\sim 5 - 10$ better than achieved previously for any elliptical galaxy. After correction for incompleteness, the total number of sources, inside a 10 arcmin radius of the centre, with $L_x \geq 2 \cdot 10^{36}$ erg s^{-1} is ≈ 321. This number is in good agreement with the prediction based on the stellar mass, the star formation rate in Cen A and the density of CXB sources. About half of the detected sources are expected to be X-ray binaries in Cen A, mostly LMXBs; the vast majority of the remaining sources are background galaxies constituting the resolved part of the CXB.

We showed that the spatial distribution of LMXBs was consistent with the distribution of the K-band light as observed by 2MASS, and that their luminosity function is consistent with the average LMXB LF in nearby galaxies. In particular, we demonstrate that the LMXB LF in Cen A flattens at the faint end and is significantly flatter than extrapolation of the steep power law with differential slope of $\approx 1.8-1.9$ observed above $\log(L_x) \sim 37.5 - 38$ in the previous studies of elliptical galaxies. Rather, the LMXB LF in Cen A has a break at $L_x \approx (5\pm1)\cdot 10^{37}$ erg s^{-1} below which it follows the

$dN/dL \propto L^{-1\pm0.1}$ law, similar to the behaviour found in the bulges of spiral galaxies.

Thanks to the low distance to M31 ($\sim$ 780 kpc), it is possible to study the properties of the LMXBs down to a limiting luminosity of $\sim 10^{35}$ erg s^{-1}. To do this, we combined 26 individual *Chandra* ACIS observations of the bulge with a total exposure time of 201 ks. We found good agreement between the observed number of sources, and the expectation based on the K-band luminosity and average X-ray mass to light ratio for nearby galaxies. We demonstrated that the LMXBs in M31 can be divided into 3 subpopulations. (1) Primordial LMXBs with a spatial distribution following the mass distribution of the bulge as modelled by the K-band light. (2) LMXBs formed through dynamical interactions in globular clusters. (3) LMXBs formed through dynamical interactions in the inner 1 arcmin of the bulge, with a spatial distribution following ρ_*^2, where ρ_* is the stellar density. Superimposed on these are the CXB sources, the distribution of which is flat on the angular scales under consideration. After applying the incompleteness correction and subtracting the contribution of CXB sources, we were able to recover the LF of M31 sources down to the luminosity of $\sim$ few $\times 10^{35}$ erg s^{-1}, which is a factor of $\sim$ 3 better than in previous studies. The luminosity function of all X-ray sources in the bulge of M31 is consistent with the average LMXB LF of nearby galaxies, in particular, it follows the $dN/dL \propto L^{-1}$ law in the faint luminosity limit, in agreement with the behaviour found earlier for LMXBs in the Milky Way and in Cen A. It was furthermore possible to divide the LMXBs into two subpopulations – primordial LMXBs and dynamically formed ones, in order to study the differences in their luminosity distributions. Within 12 arcmin from the centre, there are $\sim$ 21 dynamically formed LMXBs in the central parts of the bulge and $\sim$ 21 in globular clusters, while there are 64 primordial LMXBs (with $L_x \gtrsim 10^{36}$ erg s^{-1}). While the LFs of the two types of sources are consistent above $\sim 10^{36}$ erg s^{-1}, where they follow the average LMXB LF of nearby galaxies. Below this luminosity there is a significant difference, with the LF of the dynamically formed LMXB falling off sharply.

The detection of population (3) in the bulge of M31 was the first observational evidence for the dynamical formation of LMXBs in a bulge environment. We conducted a theoretical study of the dynamical formation of LMXBs, with special emphasis on the differences between the environment in GCs (with velocity dispersions of up to $\sim$ 15 km s^{-1}) and in the inner bulge of M31 (with velocity dispersions of $\sim$ 150 km s^{-1}). There are three possibly important channels of dynamical formation of LMXBs: We estimated the rates of different channels of dynamical formation of LMXBs in the Galactic globular clusters and in the centre of M31, based on realistic models of the stellar environments. For the exchange reactions we furthermore simulated the evolution of a large number of binaries ($\sim 10^6$ for a globular clusters and $\sim 10^8$ for the bulge) in an environment of single stars. This was done using numerical scattering calculations for each encounter between a single star and a binary with the program `FEWBODY`, and taking into account the most important processes of binary evolution.

We found that while exchange reactions are potentially the dominant formation channel in globular clusters (although stellar collisions might decrease the importance of this channel significantly), this process is relatively unimportant in M31. Similarly, tidal captures of NSs by main sequence stars of mass $> 0.4 M_\odot$ are important in glob-

ular clusters, but not in M31. Instead the main formation channel is tidal captures of compact objects by low mass ($< 0.4 M_{\odot}$) stars, with some contribution from collisions between red giants and compact objects. While the geometrical collision rate is high enough to explain the total number of sources from the latter channel, the majority of the collisions are unlikely to lead to the formation of a binary system, as the binding energy of the envelopes of most RGB/AGB stars is too low to capture a compact object in a high velocity environment. We conclude that the majority of the sources in M31 are short-period binaries, and in contrast to globular clusters many of them have BH accretors. We note that the BH binaries with a very low mass companion may become persistent X-ray sources after the donor star is depleted below, $M_d \lesssim 0.15 M_{\odot}$, due to small size of the accretion disc and the positive dependence of the gravitational breaking rate on the mass of the primary. We also predict for the inner bulge of M31 a large number of faint transients, similar to the accreting msec pulsars in our Galaxy. Overall, we have been able to explain the spatial distribution and absolute numbers of surplus sources detected in the inner bulge of M31 as a well as the statistics of LMXBs in the metal rich globular clusters.